The Dissertation Committee for Muhammad Sohaib Alam
certifies that this is the approved version of the following dissertation:

Phase Transitions in Holographic QCD and Instanton Crystals

Committee:

Vadim Kaplunovsky, Supervisor

Sonia Paban

Can Kilic

Jacques Distler

Andrew Neitzke

Phase Transitions in Holographic QCD and Instanton Crystals

by

Muhammad Sohaib Alam, B.A.; M.A.

DISSERTATION
Presented to the Faculty of the Graduate School of
The University of Texas at Austin
in Partial Fulfillment
of the Requirements
for the Degree of

DOCTOR OF PHILOSOPHY

THE UNIVERSITY OF TEXAS AT AUSTIN
August 2014

Dedicated to my parents, Badar-e-Alam and Bushra Nasim.

Acknowledgments

Where to even begin. First and foremost thanks goes to my committee members, my intellectual parents – Vadim Kaplunovsky, Sonia Paban, Jacques Distler, Can Kilic and Andy Neitzke. Quite simply put, no amount of words can ever do justice to express my gratitude for the gift of knowledge you have bestowed upon me. There is a saying where I come from, attributed to Imam Ali, "I am a slave of whoever teaches me even a single word". Well if this is true, then surely I am in your bondage forever! Vadim, my advisor, it was glorious battling to reach the standard of intellectual rigour you demanded of me, I have grown in more ways under your watchful guidance than you will ever know.

Immeasurable thanks also goes to my professors and mentors from Franklin & Marshall College. Annalisa Crannell, you have been more than just a mentor, thanks for giving me an early introduction to the joys and rewards of research, I still think back fondly to our math paper. Greg Adkins, Calvin Stubbins, Michael McCooey, Ken Krebs, you had a huge role to play in inculcating and encouraging my interest in physics at a time when I was too distracted by other liberal arts subjects, I cannot thank you enough.

I could not have gotten through grad school without the support and camaradarie of my friends and peers in and outside the Theory Group. You know who you are, I certainly hope this is not the last we see or hear of each other.

Jan Duffy, you never failed to make life easier for someone so often lost and clueless at paperwork and other such bureaucratic stuff as I.

JP's Java, you have been a veritable friend, it is sad to hear you are closing down soon. Epoch Coffee, some of the most wondrous realizations about the beauty and mysteries of the universe have unfolded at your location.

Last, but certainly not the least, my parents – to whom this thesis is dedicated. And Safa, for her love.

Phase Transitions in Holographic QCD and Instanton Crystals

Publication No. __________________

Muhammad Sohaib Alam, Ph.D.
The University of Texas at Austin, 2014

Supervisor: Vadim Kaplunovsky

We investigate phase transitions in holographic models of QCD. In chapter I, we explore the effect of constant external $U(1)$ fields on the physics of chiral symmetry breaking, as realized in the $D3/D7$ model. We discover that this model exhibits the phenomenon of magnetic catalysis, which is what one would expect from a weakly coupled field theory intuition. In chapter II, we continue exploring the effect of external $U(1)$ fields but now on the backreacted $D3/D7$ model, where the backreaction is obtained via a smearing procedure. We again find the magnetic catalysis effect, however the results differ from the previous case depending on the backreaction parameters. In chapter III, we investigate lattices of instantons in the $D4/D8$ model of chiral symmetry breaking. These instanton lattices can change dimensionality, and in particular we investigate the $1D \rightarrow 2D$ transition as a simpler case of the more complicated $3D \rightarrow 4D$ transition which is conjectured to be holographically dual to the baryonic to quarkyonic phase transition. Besides this interpretation, one could also view this as a hypothetical condensed matter system. We have a lattice of instantons dominated by two-body forces, whose interactions depend not only on their mutual distance in physical space but also on their relative orientations in the internal isospace. We obtain a rich variety of instanton crystals whose description could serve to be useful beyond holography.

Table of Contents

List of Figures

Chapter 1

Chiral Symmetry Breaking and External Fields in the Kuperstein-Sonnenschein Model

1.1 Introduction

[1] With the advent of holography, and more specifically the gauge-gravity duality[53, 55, 54] (for a review, see [4]), we have been provided with a remarkable tool to study a large class of strongly coupled large N_c gauge theories. Within these class of theories, much effort has been spent trying to construct holographic models which share some of the key features of QCD at strong coupling, such as the confinement/deconfinement transition, chiral symmetry breaking and numerous other properties which are of recent phenomenological interests. See *e.g.* the review [5] for more details. The hope is any lesson learnt using these models will teach us useful lessons about QCD in some universal (and at least qualitative) sense.

In this chapter we will focus entirely on the physics of chiral symmetry breaking. In the holographic construction the fundamental matter fields are introduced by considering N_f "flavour branes" in the background of N_c "colour branes" and the global symmetry associated with these flavour branes is identified with the chiral symmetry. In an analogue of the quenched approximation, the problem simplifies in the probe limit where $N_f \ll N_c$ and thus the gravi-

---

[1] This chapter is based on previous work done with Vadim Kaplunovsky and Arnab Kundu.

tational backreaction of the flavour branes can be safely ignored. The dynamics of the probe branes is then simply determined by the Dirac-Born-Infeld (DBI) action (supplemented by the Chern-Simons action when necessary) in the given gravitational background. This was initially done in [58] by considering probe D7-branes in the background of N_c D3-branes. The background geometry there is given by $\mathrm{AdS}_5 \times S^5$ and the dual field theory is the $\mathcal{N} = 4$ super Yang-Mills. However, the global flavour symmetry in [58] is only a $U(1)$ and does not resemble the chiral symmetry group in QCD. Besides, the D7-brane embeddings are $\frac{1}{2}$-BPS which necessarily implies that the chiral condensate identically vanishes and there is no spontaneous chiral symmetry breaking. We will refer to this as the $\mathrm{D3} - \mathrm{D7}$ model.[2]

The Sakai-Sugimoto model[106, 10], on the other hand, is based on considering D8 and $\overline{\mathrm{D8}}$-branes in the non-extremal D4-brane background. This brane–anti-brane pair is separated in the UV which gives rise to an $U(N_f)_L \times U(N_f)_R$ flavour symmetry, very similar to the chiral symmetry group in QCD. In the IR, these branes merge together smoothly spontaneously breaking the chiral symmetry to a diagonal $U(N_f)$. This model gives a simple and elegant geometric realization of the chiral symmetry breaking in QCD.

Recently a similar geometric mechanism of spontaneous chiral symmetry breaking has been introduced in [56] by considering D7/$\overline{\mathrm{D7}}$-branes in the conformal Klebanov-Witten background[59]. We will call this the Kuperstein-Sonnenschein model. The D7/$\overline{\mathrm{D7}}$-branes wrap a three cycle in the internal manifold $T^{1,1} \cong S^2 \times S^3$ and is extended along the rest of the conifold $\mathbb{R}^+ \times S^2$. At zero temperature the brane–anti-brane pair has no choice but to dynamically join in the IR,

---

[2] If we embed a probe D7-brane in a deformed confining D3-brane geometry (*e.g.* the Constable-Myers background), then the axial $U(1)$ (corresponding to the rotation in the directions transverse to the D7-brane) can be broken spontaneously[7]. This further allows one to compute the mass of the ρ-meson in terms of the mass of the π-meson, see *e.g.* [8].

which realizes spontaneous breaking of chiral symmetry: $U(N_f)_L \times U(N_f)_R \rightarrow U(N_f)_{\rm diag}$. Since the background is conformal, the two branches corresponding to the brane and the anti-brane produce an asymptotic angle separation of $\Delta\phi_\infty = (\sqrt{6}/4)\pi$ which is independent of the IR point where the brane–anti-brane pair joins. This asymptotic angle separation corresponds to the coupling of the corresponding operator introduced in the dual gauge theory.

It is worth remarking on the differences between this model and the Sakai-Sugimoto model. First, the Sakai-Sugimotmo model contains a running dilaton which diverges in the UV and one needs to worry about the UV completion of the theory. Second, the Sakai-Sugimoto model is built upon D4-branes compactified on a spatial circle which is dual to a $(4+1)$-dimensional gauge theory at energies bigger than the compactification scale. The Kuperstein-Sonnenschein model avoids these two drawbacks rather simply: the dilaton does not run and by construction this is dual to an honest $(3+1)$-dimensional gauge theory. Thus the Kuperstein-Sonnenschein model has certain advantages over the Sakai-Sugimoto model.

Within the probe approximation, it is possible to further study the physics of chiral symmetry breaking in the presence of external parameters, such as temperature, constant electromagnetic field *etc.* In this article, we study the effect of finite temperature and a constant electromagnetic field in the Kuperstein-Sonnenschein model. Having a finite temperature corresponds to introducing a black hole in the bulk geometry. This corresponds to having the AdS-Schwarzschild$\times T^{1,1}$-background. The physics at finite temperature is rather simple because of the underlying conformal invariance. Since there is no other scale, chiral symmetry is restored as soon as any temperature is turned on.

At finite temperature, we introduce a constant electromagnetic field by exciting gauge fields on the worldvolume of the probe brane. This gauge field, in the probe limit, does not modify the background; it only affects the probe. Thus the electromagnetic field we consider couples only to the flavour sector and results in a non-trivial phase structure for the flavours. Recall that at zero temperature and vanishing external fields the coupling in the dual field theory $\Delta\phi_\infty$ has a fixed value. When we introduce these external parameters we do not insist that the coupling remain fixed at this value. If we have well-defined UV theory for a given coupling, then changing this coupling would imply we change the theory as well, which may not be desirable.[3] However, as pointed out in [56] the operator corresponding to $\Delta\phi_\infty$ in the dual field theory is not completely understood. Our approach, thus, is entirely guided by the holographic construction and is more in the spirit of condensed matter physics where one allows various couplings in the theory to depend on the external parameters introduced in the system and scans the space of possible phases as the couplings change.

Phase diagrams with similar external parameters have been studied in the $\mathrm{D3}-\mathrm{D7}$ model in [96, 97, 91, 16, 17] and in the Sakai-Sugimoto model in [18, 98]; for a comparative account of these studies see *e.g.* [20].[4] It has been found that the magnetic field promotes the spontaneous breaking of the global flavour symmetry and results in a non-trivial phase diagram in the temperature vs magnetic field plane. This effect is widely recognized as the *magnetic catalysis* in chiral symmetry breaking[23, 24, 25]. The key physics behind this phenomenon is an effective dimensional reduction of the problem in the presence of a magnetic field. In a strong magnetic field, the lowest Landau level plays an important role and reduces the dynamics from d-spatial dimensions to $(d-2)$-spatial dimensions. From the holographic point of view, this catalysis effect is seen as a magnetic field-induced bending of the probe flavour brane. An electric field

---

[3] We thank Anatoly Dymarsky for raising this point.

[4] For more recent studies involving the $\mathrm{D3}-\mathrm{D7}$ model, see *e.g.* [21, 22].

on the other hand favours symmetry restoration and drives a current[90, 91, 18]. This current is non-zero even in the absence of finite chemical potential or charge density. The key physics behind this is simple: charge carriers are created from the vacuum via thermal and quantum fluctuations. The holographic realization of this effect is rather elegant. In the presence of a constant electric field, the probe brane excites an appropriate gauge field on its worldvolume which is dual to a boundary current carried by the fundamental flavours. In the T-dual picture, having a constant electric field on the worldvolume of the probe brane is equivalent to considering the brane with some angular velocity, as considered in *e.g.* [27, 28]. In such a case, due to gravitational red-shift, the local speed of propagation on the probe brane can exceed the speed of light near the infrared region of the bulk geometry. To prevent such superluminal propagation the probe brane can develop a non-trivial profile along another transverse direction. When we T-dualize back to our original configuration, this "extra" profile maps to a gauge field living on the worldvolume of the D7-brane which is holographically dual to a current in the boundary theory.

In this chapter we demonstrate that a similar *magnetic catalysis* effect exists in the Kuperstein-Sonnenschein model. At vanishing magnetic field, the finite temperature immediately restores the symmetry without undergoing any phase transition. At non-zero magnetic field, there is a first order phase transition at some critical temperature below which chiral symmetry is broken and beyond which it is restored. This happens at a critical value of the coupling $\Delta\phi_\infty$ in the boundary theory. As we increase the magnetic field, the critical coupling increases and at infinitely large magnetic field approaches a finite constant value. We also study the thermodynamics associated with this first order phase transition.

The thermal physics in the presence of an electric field is more subtle. The presence of a current in the boundary theory implies that we are dealing with a steady-state system rather than an equilibrium system. The identification of a thermodynamic free energy and hence to determine the corresponding phase diagram in this case becomes more subtle. Previous works in *e.g.* [91, 18] have made use of a "Maxwell construction" to determine the phase transition point. However, we believe this is inappropriate. The "insulating" phase has vanishing current and the "conducting" phase has a non-zero current. The current jumps to a constant non-vanishing value across the phase transition, but we do not see the "metastable" states where the current smoothly interpolates between zero and the non-vanishing constant value across the phase transition. To count the energetics properly, the Maxwell construction relies on the presence of these metastable states. We circumvent this issue by proposing a definition of the thermodynamic free energy in the conducting phase in terms of the probe brane's on-shell action. The prescription is: we first need to supplement the usual DBI piece with a boundary term in order to have a well-defined variational problem. Then we need to put an IR cut-off at a radial position which we call the "pseudo-horizon" that emerges as a natural radial scale in the problem. We argue that this cut-off is natural since the open string degrees of freedom effectively see a horizon at this position.

Using our proposal of the thermodynamic free energy we then explore the rich phase diagrams when both electric and magnetic fields are present. We choose two representative configurations: perpendicular electric and magnetic fields and parallel electric and magnetic fields. In both these cases the qualitative features of the phase diagrams are similar and conforms to our general intuition of temperature and electric field favouring chiral symmetry restoration and a magnetic field promoting symmetry breaking. We also argue that when both electric and magnetic fields are present, the corresponding phase diagrams have non-trivial structure only when the electric field is smaller than the magnetic field. In the regime where the electric field is greater than the magnetic field, we do not have any chiral symmetry broken phase.

This chapter is organized as follows: We briefly review the Kuperstein-Sonnenschein model in section 2. In section 3, we briefly discuss the physics at finite temperature. We introduce a magnetic field in section 4 and in section 5 we study the effect of both temperature and magnetic field. In section 6, we introduce an electric field and discuss the subtleties associated in identifying a free energy and conjecture a proposal to do sensible thermodynamics. We use this proposal in section 7 to study the detailed phase structure in the presence of both perpendicular and parallel electric and magnetic fields. Finally we conclude in section 8 with open questions and future directions. Some relevant details have been relegated to three appendices.

1.2 The Kuperstein-Sonnenschein Model

Let us begin by briefly reviewing the Kuperstein-Sonnenschein model introduced in [56]. We start with the $AdS_5 \times T^{1,1}$ background (first obtained in [29] and then explored in the context of AdS/CFT in [59]) which is the near-horizon limit of a stack of N_c D3-branes placed on the tip of a conifold. The metric is

$$\begin{aligned} ds^2 &= \frac{r^2}{R^2} dx_\mu dx^\mu + \frac{R^2}{r^2} ds_6^2 \,, && (2.1) \\ ds_6^2 &= dr^2 + r^2 ds^2_{T^{1,1}} && (2.2) \\ &= dr^2 + \frac{r^2}{3}\left(\frac{1}{4}\left(f_1^2+f_2^2\right) + \frac{1}{3}f_3^2 + \left(d\theta - \frac{1}{2}f_2\right)^2 + \left(\sin\theta d\phi - \frac{1}{2}f_1\right)^2\right) \,, \end{aligned}$$

the dilaton is constant, and there is a self-dual 5-form RR flux

$$F_5 = \frac{4r^3}{g_s R^4}\, dr \wedge d^4x \; - \; \frac{R^4}{27 g_s} \sin\theta \, d\theta \wedge d\phi \wedge f_1 \wedge f_2 \wedge f_3 \,. \tag{2.3}$$

In our notations x^μ are the four Minkowski directions, r is the AdS-radial coordinate, and $(f_1, f_2, f_3, \theta, \phi)$ represent the $T^{1,1}$ as a local $S^3 \times S^2$ trivialization — the $f_{1,2,3}$ are unit differentials on the S^3 while θ and ϕ are spherical coordinates on the S^2. Furthermore, R is the AdS radius — which obtains as

$$R^4 \;=\; \frac{27\pi}{4} N_c g_s \alpha'^2 \;=\; \lambda \alpha'^2 \tag{2.4}$$

where g_s is the string coupling, $2\pi\alpha'$ is the inverse string tension, and λ is the 't Hooft coupling of the dual 4D gauge theory; later in this paper we shall use a related coupling

$$\bar{\lambda} \;=\; \frac{\pi^2}{4} \lambda \; . \tag{2.5}$$

The field theory dual to this background was constructed in [59]: it is an $\mathcal{N} = 1$ superconformal quiver gauge theory with a gauge group $SU(N_c) \times SU(N_c)$ and two bi-fundamental chiral superfields usually denoted by $A_{1,2}$, $B_{1,2}$. These fields transform in the $(N_c, \bar{N_c})$ and $(\bar{N_c}, N_c)$ representations of the gauge group $SU(N_c) \times SU(N_c)$. This theory has a further global $SU(2) \times SU(2) \times U(1)_{\mathrm{R}}$ symmetry. Under these two $SU(2)$ symmetries the bi-fundamentals transform as a doublet of one of the $SU(2)$'s and as a singlet of the other one.

Following [56] we place the D7 and anti D7-brane along the Minkowski and the S^3-directions, and restrict to the equatorial embedding denoted by $\theta = \pi/2$, $\phi = \phi(r)$. The brane–anti-brane pair is separated in the ϕ-direction at the UV boundary (at $r \to \infty$). This configuration preserves one of the global $SU(2)$'s of the background. The corresponding DBI action is given by

$$S = -\tau_7 \int d^8\xi \sqrt{-\det P[G]} = -\mathcal{N} \int dt dr r^3 \left[1 + \frac{r^2}{6} (\phi')^2\right]^{1/2} = -\mathcal{N} \int dt dr \mathcal{L} \; , \tag{2.6}$$

$$\mathcal{N} = \tau_7 V_{\mathbb{R}^3} \frac{8\pi^2}{9} \; . \tag{2.7}$$

In the above equation, τ_7 denotes the tension of the D7-brane, ξ denotes the D7-brane worldvolume coordinates, $P[G]$ denotes the pull back of the background metric on the probe brane, $\mathcal{L}$ is the Lagrangian density. Here $V_{\mathbb{R}^3}$ is the volume of the spatial $\mathbb{R}^3$.

The equation of motion resulting from the action in (2.6) is given by

$$\frac{(r^5/6)\phi'}{\left(1+\frac{r^2}{6}(\phi')^2\right)^{1/2}} = c \ , \tag{2.8}$$

where c is the constant of motion. The large r behaviour of the profile is

$$\phi(r) = \frac{\Delta\phi_\infty}{2} - \frac{3c}{2r^4} + \dots \ , \tag{2.9}$$

where $\Delta\phi_\infty$ is the asymptotic angle separation between the brane–anti-brane pair. It is clear from the asymptotic behaviour of the profile function that $\Delta\phi_\infty$ is the non-normalizable mode (corresponding to source/coupling in the boundary theory) and c is the normalizable mode (corresponding to VEV/condensate in the boundary theory).

We can integrate the equation of motion in (2.8) analytically and the full solution is given by[56]

$$\cos\left(\frac{4}{\sqrt{6}}\phi(r)\right) = \left(\frac{r_0}{r}\right)^4 \ , \quad \text{with} \quad \phi'(r_0) \to \infty \qquad \Longrightarrow c = \frac{r_0^4}{\sqrt{6}} \ . \tag{2.10}$$

The boundary condition $\phi'(r_0) \to \infty$ ensures that the brane–anti-brane smoothly join at r_0. We have two branches of solutions with $\phi \in [0, \pi/2]$ and $\phi \in [-\pi/2, 0]$. The first branch corresponds to the D7-brane and the second one to the $\overline{\text{D7}}$-brane. As $r \to \infty$, we see that $\Delta\phi_\infty = \frac{\sqrt{6}}{4}\pi$. Thus, in fact, one gets a family of solutions (with the same asymptotic angle separation) parametrized by r_0 where the brane–anti-brane pair joins. For future references we call these profiles as the "U-shaped" embeddings. It is easy to see that since there is no natural place for the brane–anti-brane pair to end separately, they must join together. We will see at finite temperature this is not the case any more. There is a special solution for $r_0 = 0$ given by $\phi_\pm = \pm(\sqrt{6}/8)\pi$. Each branch of the family of solutions with $r_0 \neq 0$ is non-holomorphic and thus breaks supersymmetry completely. The two branches of the solution with $r_0 = 0$ also break supersymmetry completely since they are not antipodal[56]. The qualitative shapes of the brane–anti-brane profile have been demonstrated in fig. 1.1.

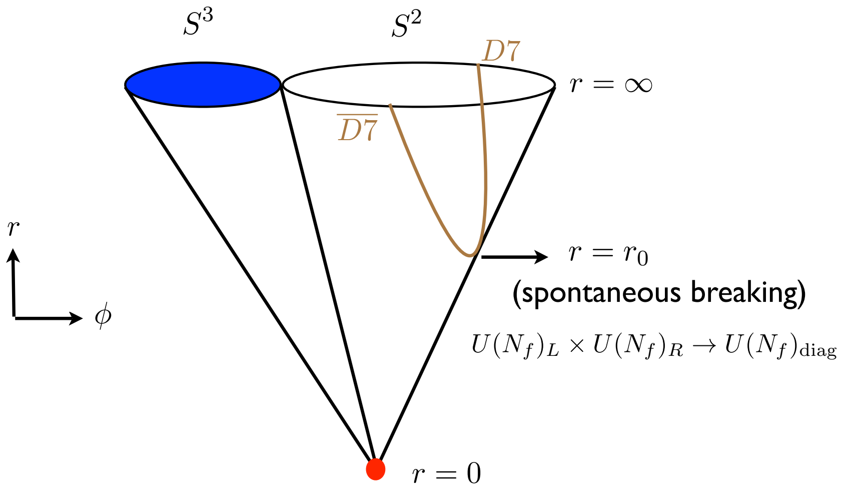

Figure 1.1: A schematic diagram showing the shape of the profile (in grey) of the brane–anti-brane pair. The red dot located at $r = 0$ represents the conifold singularity. The brane–anti-brane pair joins at $r = r_0$ realizing the spontaneous breaking of chiral symmetry.

Introducing probe D7 and $\overline{\text{D7}}$ implies that we have introduced matter fields in the fundamental representation in the dual gauge theory. As argued in [56], adding the D7/$\overline{\text{D7}}$-brane corresponds to introducing left-handed/right-handed Weyl fermions in the dual gauge theory. Thus, in the UV where the D7 and the $\overline{\text{D7}}$ are separate, we have a global $U(N_f)_L \times U(N_f)_R$

flavour symmetry, where N_f is the number of flavours.[5] This global flavour symmetry is dynamically broken to a diagonal $U(N_f)$ in the infrared where the brane–anti-brane pair joins. The asymptotic angle separation $\Delta\phi_\infty$ corresponds to the coupling of an operator in the dual gauge theory.[6] One would be tempted to identify the constant c with the quark condensate corresponding to the breaking of the chiral symmetry, however since the corresponding operator is not well-understood at this moment we will make no such precise claim. Nonetheless, it is fair to say that the constant c serves the purpose of an order parameter for the breaking of the chiral symmetry.

1.3 Introducing Finite Temperature

Let us now discuss the physics at finite temperature. The finite temperature background is given by AdS_5-Schwarzschild$\times T^{1,1}$. Also, we need to Euclideanize the time direction and periodically identify along a circle. The temperature is then simply given by the inverse period. In Euclidean signature this background is explicitly given by

$$ds^2 = \frac{r^2}{R^2}\left(f(r)dt_E^2 + dx_i^2\right) + \frac{R^2}{r^2}\frac{dr^2}{f(r)} + R^2 ds^2_{T^{1,1}} \ , \quad f(r) = 1 - \left(\frac{r_H}{r}\right)^4 \ , \tag{3.11}$$

where t_E is the Euclidean time direction, x_i with $i = 1,2,3$ represent the spatial 3-directions, r_H is the location of the horizon and the temperature is given by $T = r_H/(\pi R^2)$. Furthermore, $ds^2_{T^{1,1}}$ represents the metric on the $T^{1,1}$ which is given in (2.1). This background corresponds to the phase of the dual gauge theory where the adjoint matter is deconfined.

---

[5] Strictly speaking, here we take $N_f = 1$.

[6] It is not completely clear at present what the corresponding operator is; in fact the quiver diagram of this theory (after introducing the fundamental matter) is not completely understood. Part of the complications arise from breaking supersymmetry completely, which means we can no longer use the technology of supersymmetric field theories to "fix" various terms in the Lagrangian. Some thoughts and proposals on this are given in [56].

Now, we introduce the D7 and $\overline{\rm D7}$ pair along the same directions as in the zero temperature case. In this case the DBI action[7] is given by

$$S = \tau_7 \int d^8\xi \sqrt{{\rm det} P[G]} = \mathcal{N}_T \int dr r^3 \left(1 + \frac{r^2}{6} f (\phi')^2\right)^{1/2} , \tag{3.12}$$

$$\mathcal{N}_T = \frac{\mathcal{N}}{T} . \tag{3.13}$$

Note that the definition of $\mathcal{N}_T$ in this case differs from the zero temperature case by a factor of the temperature. The resulting equation of motion is given by

$$\frac{(r^5/6) f \phi'}{\left(1 + \frac{r^2}{6} f (\phi')^2\right)^{1/2}} = c , \tag{3.14}$$

where c is the constant of motion. The equation (3.14) is not analytically solvable. There are two possible classes of solutions to the equation (3.14): the U-shaped ones for which we have $c = \frac{r_0^4}{\sqrt{6}} f(r_0)^{1/2}$, where r_0 is the point where the brane–anti-brane pair smoothly joins; the second class of solutions are the ones where the brane and the anti-brane separately end on the horizon. These are given by $\phi_\pm = \pm{\rm const}$ (corresponding to $c = 0$) which we henceforth call the "$\|$ embedding". The ± sign corresponds to the D7 and the $\overline{\rm D7}$-brane respectively. As before, the U-shaped embeddings correspond to spontaneous breaking of chiral symmetry and the $\|$ embeddings correspond to chiral symmetry restoration. Clearly r_0 and r both have the following range: $r_H \leq r_0, r \leq \infty$. In fig. 1.2 we have pictorially demonstrated various possible profiles.

In a situation like this, one would typically expect as we vary the temperature the system undergoes a first order phase transition and at some critical temperature chiral symmetry is

---

[7] Note that there is a relative -ve sign between the DBI action at finite temperature and the one at zero temperature. This simply stems from the fact that in the finite temperature case we are working in an Euclidean signature.

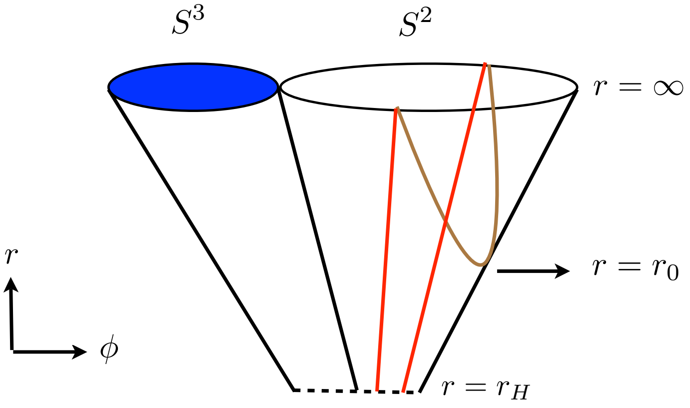

Figure 1.2: A schematic diagram showing the qualitative shapes of the probe brane–anti-brane pair when a non-zero temperature has been introduced. We have two classes of embeddings: the U-shaped ones (in grey) and the parallel ones (in red). The singularity of the cone is hidden behind the horizon located at $r = r_H$.

restored. However, we started with a conformal background and so far temperature is the only scale in the system. We do not have any other scale in terms of which such a critical temperature can be measured.[8] The conclusion therefore must simply be: If there exists a temperature that can restore the chiral symmetry, then the $\|$ embeddings will always be energetically favoured.

Let us elaborate a bit more on this issue. As we have seen, the chiral symmetry broken phase measures a non-zero value of c and the chiral symmetry restored phase has $c = 0$. Thus the constant c serves the purpose of an order parameter of this symmetry breaking, although it should not be confused with the chiral condensate. Thus we have the canonically conjugate variables $\{\Delta\phi_\infty, c\}$ and we should be able to see the signature of a first order phase transition (if it exists) in this plane. A numerical plot is shown in Fig. 1.3. To have a first order phase transition we would expect to see a turn-around behaviour of $\Delta\phi_\infty$ as c is increased. However, here $\Delta\phi_\infty$ only approaches the value $(\sqrt{6}/4)\pi$ from below as $c \to \infty$. Hence we can conclude that this system does not have any first order phase transition.

To conclusively decide which embedding is favoured, we consider the following energy difference

$$\Delta S = S_U - S_\| = \mathcal{N}_T r_0^4 \left(\int_1^\infty dy y^3 \left[\left(1 + \frac{f(1)}{y^8 f(y) - f(1)} \right)^{1/2} - 1 \right] - \int_{y_H}^1 dy y^3 \right) \ , \tag{3.15}$$

where we have defined

$$y = \frac{r}{r_0} \ , \quad y_H = \frac{r_H}{r_0} \ , \quad f(y) = 1 - \left(\frac{y_H}{y} \right)^4 \ . \tag{3.16}$$

---

[8] Note that r_0 where the brane–anti-brane pair joins seems to provide another scale in the system. However, in reality this is a modulus of the problem and this modulus is only perceived as the dimensionless asymptotic angle separation at the boundary, but not a scale in the system.

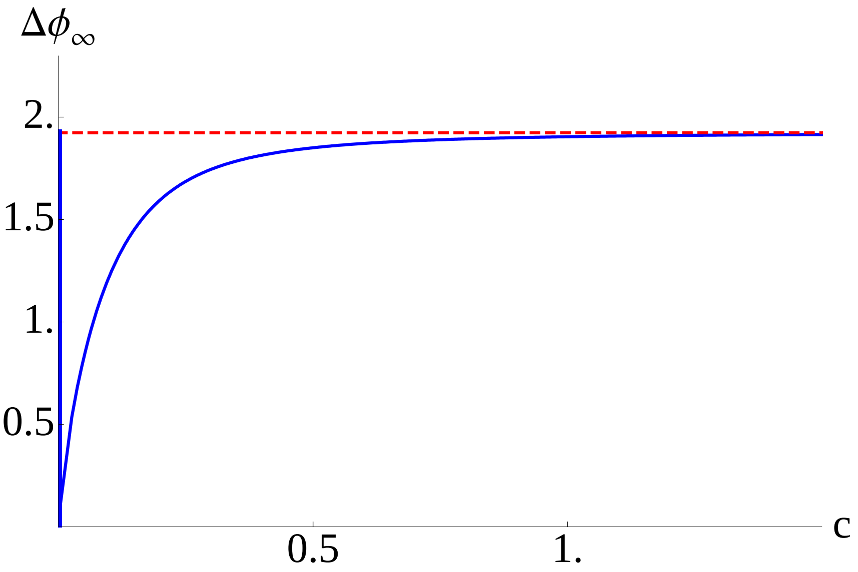

Figure 1.3: $\Delta\phi_\infty$ as a function of c. The red dashed line is the asymptotic boundary value at zero temperature. The blue curves (including the vertical line at $c = 0$) correspond to the space of solutions.

Now it is sufficient to check the sign of ΔS for any value of y_H, since every temperature is identical. We can perform a Taylor expansion of the integrand in the limit $y_H \to 0_+$ and at the leading order in y_H obtain

$$\Delta S = (\mathcal{N}_{\mathcal{T}} r_0^4) \frac{y_H^4}{8} > 0 \ . \tag{3.17}$$

This clearly implies that the $\|$ embeddings are favoured. Thus finite temperature restores chiral symmetry.

1.4 Introducing a Magnetic Field

Let us first discuss the case of vanishing temperature. The relevant background is given in (2.1). Now we want to introduce a constant magnetic field on the worldvolume of the probe D7 and $\overline{\text{D7}}$-brane. Recall that the DBI action is given by

$$S = -\tau_7 \int d^8\xi \sqrt{-\det\left(P[G+B] + (2\pi\alpha' F)\right)} \ , \tag{4.18}$$

where B is the background NS-NS field (which is zero in this case) and F is the electromagnetic 2-form on the worldvolume of the probe brane.

Here we want to introduce a Minkowski gauge field, specifically a constant magnetic field, on the probe brane worldvolume. This can be achieved by simply exciting a gauge field of the form:[9] $A_3 = Hx^2$ which gives a constant field strength $F_{23} = H$. This corresponds to having a constant magnetic field along the x^1-direction on the probe brane worldvolume. Since we are in the probe limit, this gauge field does not affect the 10-dimensional background. Thus in the

---

[9] It can be checked *a posteriori* that this ansatz for the gauge field does satisfy the equations of motion resulting from the DBI action itself.

dual field theory the adjoint matter is insensitive to this external field and only the fundamental matter couples to it. Our purpose here will be to investigate the effect of this constant field on the physics of chiral symmetry breaking.

With this gauge field, the action for the D7/$\overline{\text{D7}}$ is given by[10]

$$\begin{aligned} S &= -\mathcal{N}\int dtdr\mathcal{L} = -\mathcal{N}\int dtdr r^3\left(1+\frac{r^2}{6}(\phi')^2\right)^{1/2}\left(1+\frac{h^2}{r^4}\right)^{1/2} , && (4.19)\\ h &= 2\pi\alpha' R^2 H \ , \quad \mathcal{N} = \tau_7 V_{\mathbb{R}^3}\frac{8\pi^2}{9} \ . && (4.20)\end{aligned}$$

Introducing the magnetic field introduces a scale in the theory which is denoted by h. Thus we break conformal invariance explicitly even in the zero temperature case. The equation of motion resulting from this action is given by

$$\frac{r^3\left(1+h^2/r^4\right)^{1/2}(r^2/6)\phi'}{\left(1+(r^2/6)(\phi')^2\right)^{1/2}} = c \ , \tag{4.21}$$

where c is the constant of motion. The asymptotic behaviour of the profile $\phi(r)$ is the same as given in (2.9).

This equation of motion can be solved analytically and the solution is given by

$$\begin{aligned} &\cos\left(\frac{4}{\sqrt{6}}\phi(r)\right) = \left(\frac{r_0}{r}\right)^4\frac{1}{h^2+2r_0^4}\left[h^2\left(2-\frac{r^4}{r_0^4}\right)+2r_0^4\right] , && (4.22)\\ &\text{with} \quad \phi'(r_0)\to\infty \quad \Longrightarrow \quad c = \frac{r_0^4}{\sqrt{6}}\left(1+\frac{h^2}{r_0^4}\right)^{1/2} , && (4.23)\end{aligned}$$

where r_0 is the point where the brane–anti-brane pair smoothly joins. In the limit $h\to 0$, we recover the known result in (2.10). In fig. 1.4, we have shown a schematic diagram of the shape of the probe brane profile.

---

[10] It can be checked that there is no contribution coming from the Chern-Simons term.

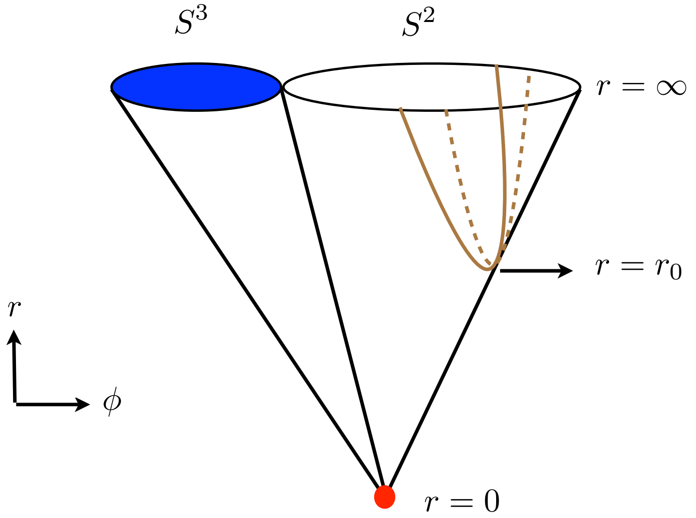

Figure 1.4: A schematic diagram showing the qualitative features of the brane–anti-brane profile in the presence of a non-zero magnetic field at zero temperature. The dashed grey curve represents the corresponding profile at zero magnetic field. The red dot again represents the conifold singularity located at $r = 0$.

A few comments on the asymptotic angle separation are in order. Considering the limit $r \to \infty$, from the solution in (4.22) we get

$$\Delta\phi_\infty = \frac{\sqrt{6}}{4}\pi + \frac{\sqrt{6}}{2}\alpha \ , \quad \alpha = \sin^{-1}\left(\frac{h^2}{h^2 + 2r_0^4}\right) \ . \tag{4.24}$$

As a consequence of the explicit breaking of conformal invariance, the asymptotic angle separation is now promoted to a function of h and r_0; in fact, it depends only on the dimensionless ratio h/r_0^2. It is clear from this expression that in the limit $h \to 0$, we recover the known result $\Delta\phi_\infty \to (\sqrt{6}/4)\pi$ and as $h \to \infty$, we get $\Delta\phi_\infty \to (\sqrt{6}/2)\pi$; for any intermediate value of h, $\Delta\phi_\infty$ interpolates between these two limiting values. The special solution for $r_0 = 0$ (which corresponds to $c = 0$) is identified with the solution obtained at $h \to \infty$ limit and is simply given by: $\phi_\pm = \pm(\sqrt{6}/4)\pi$.

For a more thorough investigation we obtain the following integral formula for the asymptotic angle separation

$$
\begin{aligned}
\Delta\phi_\infty(x_h) &= 2\sqrt{6}\int_1^\infty \frac{dy}{y}\frac{(1+x_h)^{1/2}}{\left[y^8(1+x_h/t^4)-(1+x_h)\right]^{1/2}} \\
&= \sqrt{6}\tan^{-1}\left(\sqrt{1+x_h}\right) , \qquad (4.25) \\
y &= \frac{r}{r_0} , \quad x_h = \frac{h^2}{r_0^4} . \qquad (4.26)
\end{aligned}
$$

This is a monotonically increasing function of x_h. The dependence is explicitly demonstrated in Fig. 1.5. From this monotonicity we can conclude that for a given r_0, $\Delta\phi_\infty(x_h) > \Delta\phi_\infty(0)$ which in turn implies that the magnetic field helps the brane–anti-brane pair to join. Since this

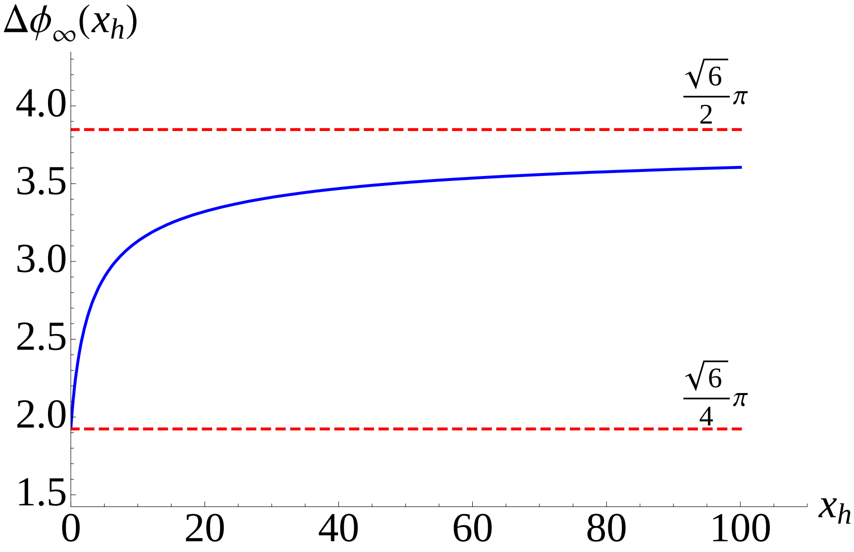

Figure 1.5: $\Delta\phi_\infty$ as a function of x_h. The range of allowed values are given by: $(\sqrt{6}/4)\pi \leq \Delta\phi_\infty \leq (\sqrt{6}/2)\pi$.

is the basic mechanism leading to chiral symmetry breaking we expect that the magnetic field is further promoting this spontaneous symmetry breaking. We will find that this is indeed the case at finite temperature in the next section.

1.5 Temperature and Magnetic Field

Let us now consider the case where both temperature and magnetic field are present. For this we consider the background in (3.11) and we place the probe D7/$\overline{\text{D7}}$-brane similarly as before. The magnetic field is again realized as a gauge field on the worldvolume of the probe brane. The action is

$$\begin{aligned} S &= \tau_7 \int d^8\xi \sqrt{-\det\left(P[G+B] + (2\pi\alpha' F\right)} = \mathcal{N}_T \int dr \mathcal{L} \\ &= \mathcal{N}_T \int dr r^3 \left(1 + \frac{h^2}{r^4}\right)^{1/2} \left(1 + \frac{r^2}{6} f(r)(\phi')^2\right)^{1/2} . \end{aligned} \tag{5.27}$$

The equation of motion is

$$\frac{r^3\left(1+h^2/r^4\right)^{1/2}(r^2/6)f\phi'}{\sqrt{1+\frac{r^2}{6}f(\phi')^2}} = c . \tag{5.28}$$

This equation is not analytically solvable anymore. As in the pure finite temperature case, we have two different classes of solutions: the U-shaped ones and the $\|$ ones. The U-shaped ones are characterized by the position r_0 where the brane–anti-brane pair smoothly join which gives

$$c = \frac{r_0^4}{\sqrt{6}} f(r_0)^{1/2} \left(1 + \frac{h^2}{r_0^4}\right)^{1/2} . \tag{5.29}$$

The $\|$ solutions are simply given by: $\phi_\pm(r) = \pm\text{const}$ (which gives $c = 0$). These solutions corresponds to $0 \le \Delta\phi_\infty \le 2\pi$.

On the other hand, for the U-shaped profiles the asymptotic angle separation is given by

$$\Delta\phi_\infty(y_H, x_h) = 2\sqrt{6}\int_1^\infty \frac{dy}{y}\sqrt{\frac{f(1)}{f(y)}}\frac{(1+x_h)^{1/2}}{\left[y^8(1+x_h/y^4)f(y)-(1+x_h)f(1)\right]^{1/2}} , \tag{5.30}$$

$$x_h = \frac{h^2}{r_0^4} , \tag{5.31}$$

where the ranges of the parameters are given by: $0 \le y_H \le 1$ and $0 \le x_h \le \infty$. In the limit $y_H \to 0_+$, $x_h \to 0_+$, we can analytically evaluate this integral to be given by

$$\begin{aligned}\Delta\phi_\infty(y_H, x_h) &= \frac{\sqrt{6}}{4}\left[\left(\pi + x_h - \frac{1}{2}x_h^2 + \mathcal{O}(x_h^3)\right)\right.\\ &+ \left.\left(\frac{2-\pi}{4}x_h + \frac{2\pi-3}{8}x_h^2 + \mathcal{O}(x_h^3)\right)y_H^4\right] + \ldots\end{aligned} \tag{5.32}$$

We can also evaluate this integral analytically in the limit $y_H \to 0_+$ and $x_h \to \infty$ to be given by the following

$$\Delta\phi_\infty(y_H, x_h) = \sqrt{\frac{3}{2}}\left[\left(\pi - \frac{2}{\sqrt{x_h}} + \mathcal{O}(x_h^{-3/2})\right) + \left(-\frac{\pi}{4} + \frac{1}{\sqrt{x_h}} + \mathcal{O}(x_h^{-1})\right)y_H^4\right] + \ldots . \tag{5.33}$$

It is clear from both the expansions in (5.32) and (5.33) that $\Delta\phi_\infty$ approaches the respective constant values that we encountered in sections 1.2 and 1.4. In the limit $y_H \to 1$, however, it can be shown that this angle separation approaches zero as $\Delta\phi_\infty \sim (1-y_H)^{1/2}$.

For a generic point in the $\{y_H, x_h\}$ parameter space, we have to resort to numerics. Now $\Delta\phi_\infty$ depends on two variables y_H and x_h and generates a 3-dimensional plot, but we can take various constant y_H or constant x_h-slices. Some such slices are shown in Fig. 1.6.

Before proceeding to determine the phase structure, let us analyze the possible phases closely. Since our underlying theory is conformal, the only meaningful quantity that we can vary is a dimensionless ratio constructed from the temperature and the magnetic field, for example

$$\frac{h}{r_H^2} = \frac{H}{\sqrt{\lambda}T^2} \tag{5.34}$$

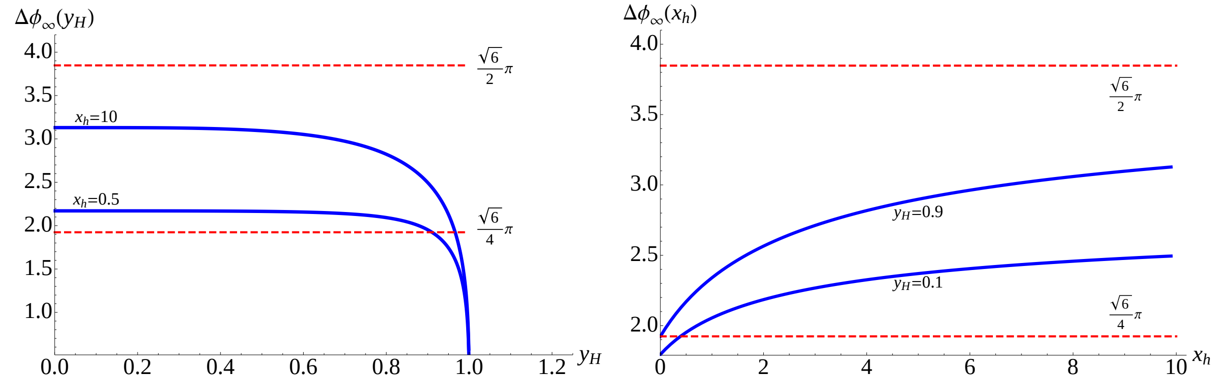

(a)

(b)

Figure 1.6: We have shown the dependence of $\Delta\phi_\infty$ as a function of y_H (for a given value of x_h) on the left and as a function of x_h (for a given value of y_H) on the right. It is clear from these plots that when we have both y_H ad x_h present, the allowed range is given by: $0 \leq \Delta\phi_\infty \leq (\sqrt{6}/2)\pi$ for the whole parameter space. Note that $\Delta\phi(y_H) \to 0$ as $y_H \to 1$, which is suggestive from the plot on the left.

where $h = (2\pi\alpha' R^2)H$ and $\bar{\lambda} = (\pi^2/4)\lambda_{\rm t\,Hooft}$; we shall use this particular ratio in this and following sections. Introducing a magnetic field (in the presence of a temperature) ultimately gives rise to the possibility of a first order phase transition. This can be best understood by looking at the $\{\Delta\phi_\infty - c\}$ plot as before. This is shown in Fig. 1.7. The main qualitative difference as compared to the purely thermal case presented in Fig. 1.3 is the bending of the curves for large enough values of c, which encodes the possibility of a first order phase transition.

It is clear from Fig. 1.7 that the maximum value of $\Delta\phi_\infty$ depends on the value of $H/(\sqrt{\bar{\lambda}}T^2)$. For a given $H/(\sqrt{\bar{\lambda}}T^2)$, beyond the maximum value of $\Delta\phi_\infty$, there is no chiral symmetry broken phase. On the branch where $(\partial\Delta\phi_\infty)/(\partial c) > 0$, increasing r_0 will increase the asymptotic angle separation and thus a small perturbation will either push the brane–anti-brane pair all the way up to infinity or pull them all the way down to the horizon. Thus the branch corresponding to $(\partial\Delta\phi_\infty)/(\partial c) > 0$, although possesses the U-shaped embeddings, is thermodynamically unstable. There is no chiral symmetry broken stable phase here. The only window where chiral symmetry broken phase can appear is for values of $\Delta\phi_\infty$ which lies in between its maximum value and the asymptotic value (as $c \to \infty$, demonstrated in Fig. 1.8), where both the U-shaped and the parallel shaped embeddings are available and are thermodynamically stable. Within this window we need to compute the free energies of the corresponding phases to decide which embedding is thermodynamically favoured.

Now we check which embedding is picked by thermodynamic energy considerations within the window discussed above. To analyze what happens to the chiral symmetry, we need to evaluate the free energy difference which is given by (up to a factor of temperature) the difference

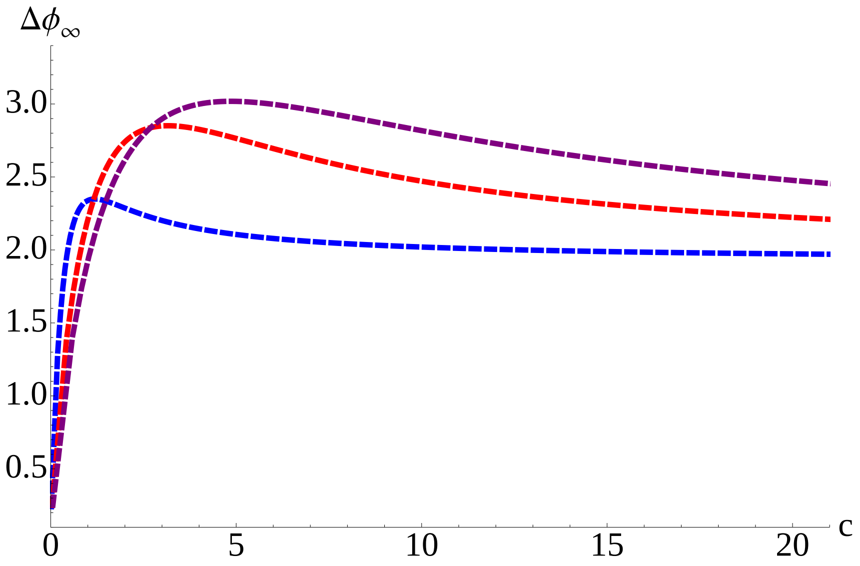

Figure 1.7: We have shown the dependence of $\Delta\phi_\infty$ as a function of c for fixed values of $H/(\sqrt{\lambda}T^2) = 2, 5, 7$ corresponding to blue, red and maroon curves. The asymptotic (as $c \to \infty$) value of $\Delta\phi_\infty$ for any value of $H/(\sqrt{\lambda}T^2)$ approaches the constant value of $(\sqrt{6}/4)\pi$.

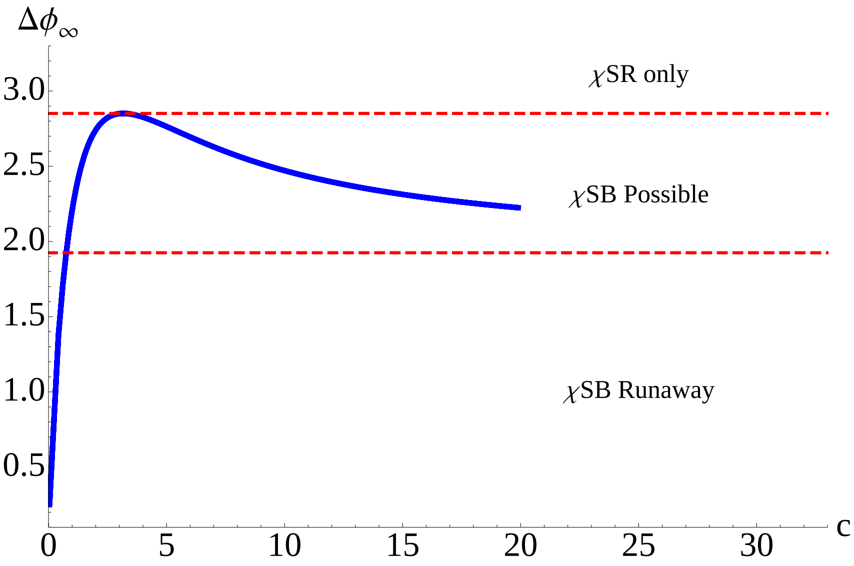

Figure 1.8: We have shown the dependence of $\Delta\phi_\infty$ as a function of c for fixed values of $H/(\sqrt{\lambda}T^2) = 5$. The asymptotic (as $c \to \infty$) value of $\Delta\phi_\infty$ for any value of $H/(\sqrt{\lambda}T^2)$ approaches the constant value of $(\sqrt{6}/4)\pi$, which is marked by the lower horizontal red dashed line and the blue solid curve asymptotes to this line. We have marked the various possible phases for various ranges of the angle separation.

of the on-shell Euclidean actions for the corresponding embedding

$$\begin{aligned}\Delta S &= S_U - S_{\|}\\ &= \mathcal{N}_T r_0^4 \int_1^\infty dy y^3 \left(1+\frac{x_h}{y^4}\right)^{1/2} \left[\left(1+\frac{(1+x_h)f(1)}{y^8\left(1+x_h/y^4\right)f(y)-(1+x_h)f(1)}\right)^{1/2} - 1\right]\\ &- \mathcal{N}_T r_0^4 \int_{y_H}^1 dy y^3 \left(1+\frac{x_h}{y^4}\right)^{1/2} = \mathcal{N}_T r_0^4 \mathcal{I}(y_H, x_h)\ . \end{aligned} \tag{5.35}$$

We can argue that the right hand side of (5.35) changes sign for a given y_H as we vary x_h. This can be seen from fixing the value of y_H to be some very small non-zero number such that $y_H \ll 1$. Now in the limit $x_h \to 0_+$, we get $\Delta S \sim x_h \log y_H < 0$. On the other hand, in the limit $x_h \to \infty$ we get $\Delta S \sim \sqrt{x_h} y_H^2 > 0$, thus clearly indicating that ΔS goes through zero. Note that even for a small magnetic field ΔS starts off being negative which implies that the chiral symmetry broken phase is favoured. This broken symmetry now gets restored at some critical value of temperature. Thus our primary analysis indicates that the magnetic field is *catalyzing* in chiral symmetry breaking.

Finding the zeroes of the right hand side of (5.35) in the full parameter space will give a curve $y_H(x_h)$ which corresponds to the phase boundary between a chiral symmetry broken and a chiral symmetry restored phase. This phase boundary in the $\Delta\phi_\infty$ vs $H/(\sqrt{\lambda}T^2)$-plane can be obtained numerically and the result is shown in Fig. 1.9.

In Fig. 1.9 if we take the strict limit $H \to 0$, then there is no phase transition at all and all we have is the chiral symmetry restored phase for any given temperature. For a non-zero magnetic field the system undergoes a first order phase transition at some critical value of temperature for the range within the red dashed curves. For a fixed finite value of $H/(\sqrt{\lambda}T^2)$, we get a critical $\Delta\phi_\infty$ below which the chiral symmetry broken phase is favoured and above which

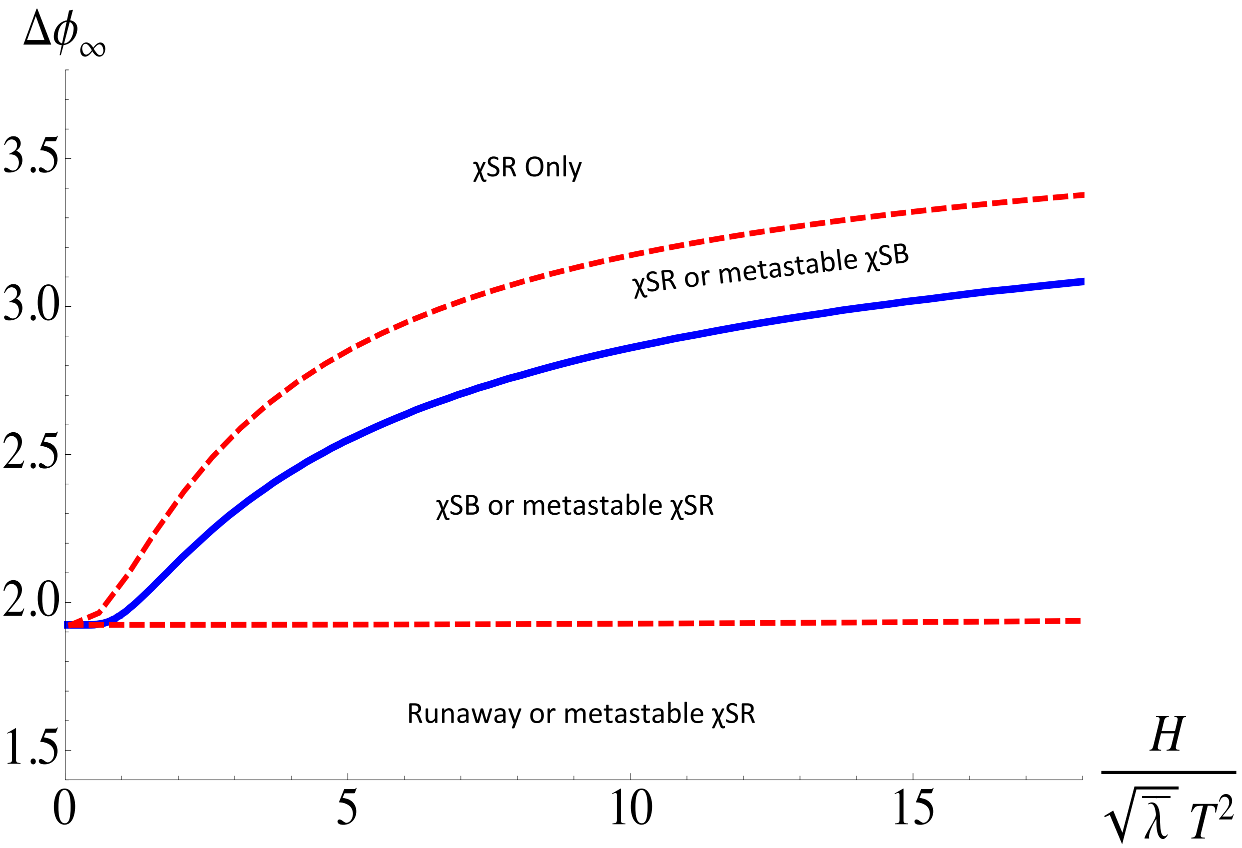

Figure 1.9: The phase diagram in the $\Delta\phi_\infty$ vs $H/(\sqrt{\lambda}T^2)$ plane. The upper red dashed curve corresponds to the maximum value of $\Delta\phi_\infty$ and the lower dashed red curve corresponds to the asymptotic (as $c \to \infty$) value of $\Delta\phi_\infty$. Below the red dashed line, we only have chiral symmetry restored phase for all values of $\Delta\phi_\infty$. We have not shown the complete range of this for aesthetic reasons.

chiral symmetry is restored. As we increase the magnetic field, *i.e.* increase the ratio $H/(\sqrt{\lambda}T^2)$, this critical coupling monotonically increases and in the strict $H \to \infty$ limit approaches the value $(\sqrt{6}/2)\pi$. Thus the external magnetic field indeed *catalyzes* the chiral symmetry breaking.

The appropriate thermodynamic potential for our system is the Helmholtz free energy given by

$$d\mathcal{F} = -\mathcal{S}dT - \mu dH \ , \quad \mathcal{F} = \frac{S}{T} \ , \tag{5.36}$$

where $\mathcal{F}$ is the Helmholtz free energy, $\mathcal{S}$ is the entropy, μ is the magnetization and S is the on-shell Euclidean action of the brane/anti-brane. The first order phase transition is associated with a non-zero latent heat and a relative change in magnetization given by

$$\begin{aligned} \mathcal{S}_{\|} - \mathcal{S}_U &= \Delta\mathcal{S} = -\frac{\partial}{\partial T}\left(\mathcal{F}_{\|} - \mathcal{F}_U\right)\Big|_{T_c} \ , \quad C_{\rm latent} = T_c\Delta\mathcal{S} \ . \\ &= \mathcal{N}_T r_0^3 \pi R^2 \left(\frac{\partial\mathcal{I}}{\partial y_H}\right)\Big|_{T_c} \ , & (5.37) \\ \mu_{\|} - \mu_U &= \Delta\mu = -\frac{\partial}{\partial H}\left(\mathcal{F}_{\|} - \mathcal{F}_U\right)\Big|_{T_c} = 2\mathcal{N}_T r_0^2 R^2 \left(\sqrt{x_h}\frac{\partial\mathcal{I}}{\partial x_h}\right)\Big|_{T_c} \ . & (5.38) \end{aligned}$$

where $\mathcal{I}$ has been defined in (5.35). The absolute free energy is a formally divergent quantity, however the change in free energy is finite. The same is true for the magnetization. Thus instead of calculating the absolute quantities for each of these phases we focus on the relative ones.[11] From simple scaling arguments it can be argued that both $C_{\rm latent} \sim T_c^4$ and $\Delta\mu \sim T_c^4$. Their dependence on the magnetic field is more involved and we have shown the numerical results in

---

[11] To obtain the finite action for each phases, one needs to add proper counter terms to cancel the divergences. In this particular case, the free energy has two sources for divergences: one is a power law divergence which comes from the infinite volume of AdS and the other is a log-divergence supported by a non-zero electromagnetic field strength.

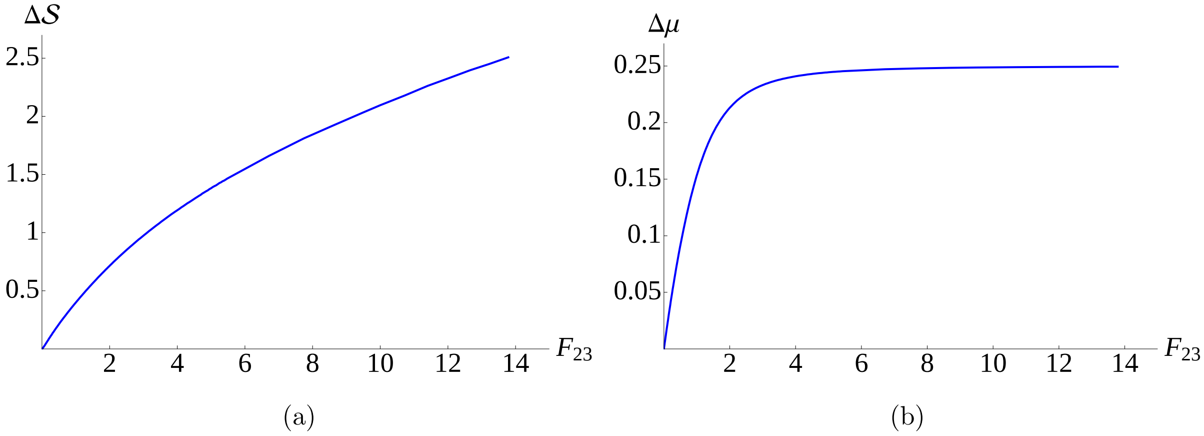

Figure 1.10: We have shown the dependence of the change in entropy and in magnetization associated with the first order phase transition. The entropy is measured in units of $\mathcal{N} r_0^3 \pi R^2$, the magnetization is measured in units of $2\mathcal{N} r_0^2 R^2$ and the magnetic field is measured in units of $(2\pi\alpha')(r_0/R)^2$.

Fig. 1.10. Clearly the change in entropy increases with increasing magnetic field. The relative magnetization initially increases, but then seems to saturate an upper bound. The fact that $\Delta\mu > 0$ is intuitively clear: the chiral symmetry restored phase is more *ionized* than the chiral symmetry broken phase.

On the other hand, the log-divergence supported by the external field in the free energy is quadratic in the field strength. Thus any quantity obtained from taking the second derivative of the free energy with respect to the field strength can be regulated rather simply. One such thermodynamic quantity is the magnetic susceptibility. We define the regularized magnetic susceptibility as below[18]

$$\chi = -\frac{\partial^2 \mathcal{F}}{\partial H^2} + \left.\frac{\partial^2 \mathcal{F}}{\partial H^2}\right|_{H=0} . \tag{5.39}$$

and compute the corresponding susceptibilities in each phases. For the chirally symmetric phase, the magnetic susceptibility (as defined in (5.39)) can be evaluated analytically to be given by

$$\chi_{\|} = -2\mathcal{N}R^4\left[1 - \frac{y_H^2}{\sqrt{y_H^4 + x_h}} - 2\log(y_H) + \log\left(\frac{y_H^2 + \sqrt{y_H^4 + x_h}}{2}\right)\right] \ . \tag{5.40}$$

For the symmetry broken phase, the integral is not analytically tractable. The dependence of the magnetic susceptibility in both these phases has been shown in Fig. 1.11, which shows the non-linear monotonic dependence with the magnetic field. As expected, we also observe that the symmetry restored phase has higher susceptibility than the symmetry broken phase.

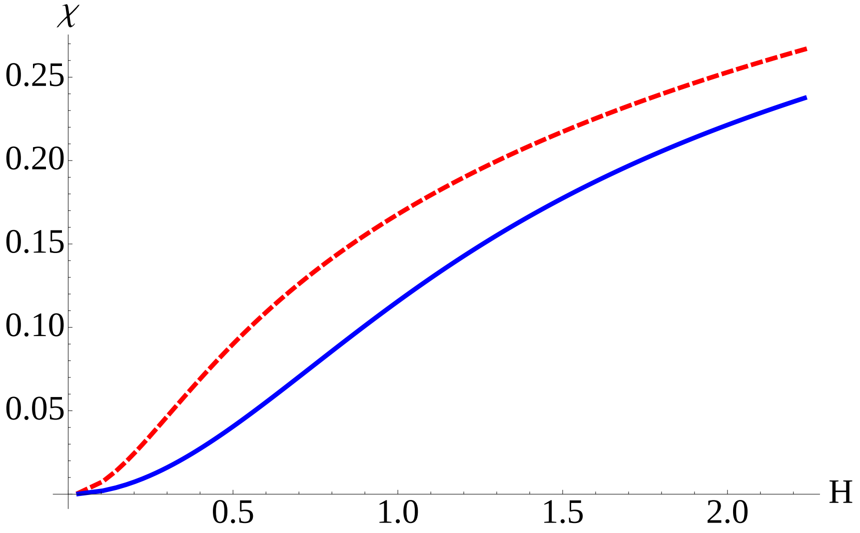

Figure 1.11: The dependence of the magnetic susceptibility with the applied magnetic field in the chiral symmetry broken (blue solid curve) and chiral symmetry restored (red dashed curve) phases. The magnetic susceptibility is measured in units of $(4\mathcal{N}R^4)$ and the magnetic field is measured in units of $(2\pi\alpha')(r_0/R)^2$.

1.6 Introducing an Electric Field

We can include the effect of an external electric field in a similar manner. The gauge potential that we excite in this case is simply given by[90, 91]

$$A_x = -Et + A(r) \ , \tag{6.41}$$

where E is the strength of the electric field along the x^1-direction.[12] Note that we have also included a function $A(r)$ in the ansatz for the gauge field. In the presence of an electric field we must also include the possibility of a flavour current. This function encodes this information of the current.

The Euclideanized[13] DBI action takes the following form

$$\begin{aligned} S &= \mathcal{N}_T \int dr r^3 \left[\left(1 - \frac{e^2}{f r^4}\right) \left(1 + \frac{r^2}{6} f(\phi')^2\right) + f(a')^2 \right]^{1/2} \ , \\ &= \mathcal{N}_T \int dr \mathcal{L}(a', \phi', r) \ , \qquad (6.42) \\ e &= (2\pi\alpha' E) R^2 \ , \quad a = 2\pi\alpha' A \ . \qquad (6.43) \end{aligned}$$

From the structure of the action in (6.42) it is clear that for any non-trivial $\phi(r)$, the action is minimized for $a' = 0$. The equation of motion for the profile function $\phi(r)$ is given by

$$\left(1 - \frac{e^2}{r^4 f(r)}\right)^{1/2} \frac{(r^5/6) f(r) \phi'}{\left(1 + (r^2/6) f(r) \phi'^2\right)^{1/2}} = c = \frac{r_0^4}{\sqrt{6}} \left(1 - \frac{e^2}{r_0^4 f(r_0)}\right)^{1/2} \ , \tag{6.44}$$

---

[12] Note that the ansatz for the gauge field contains the time coordinate t explicitly. At the horizon (when a black hole is present in the background), this coordinate is ill-defined. A better coordinate system is the ingoing Eddington-Finkelstein coordinates. However, since the Poincaré coordinate is well-defined everywhere except at the horizon, it will not affect the physics we study here. For an analysis involving the Eddington-Finkelstein coordinates, see *e.g.* [30].

[13] After Euclideanization, the gauge field will take the form: $A_x = -iEt_{\rm E} + A(r)$, where $t_{\rm E}$ is the Euclidean time obtained by $t \to it_{\rm E}$.

where r_0 is the point where the brane–anti-brane pair joins. The reality condition of the constant c imposes an upper bound for the electric field: $e^2 < r_0^4 f(r_0) = e_{\rm max}^2$. The existence of this maximum value of the electric field simply tells us that before we reach $e_{\rm max}$, the chiral symmetry restored phase should become energetically favourable. A similar effect has been discussed in [18] for the Sakai-Sugimoto model. In our case, this is trivially true: at finite temperature the U-shaped embeddings are already energetically disfavoured. We expect an electric field will tend to restore the chiral symmetry, therefore our intuition tells us that at finite temperature and non-zero electric field, the parallel embeddings must be the thermodynamically preferred phase. We can check this explicitly by evaluating the corresponding on-shell actions; however, there are subtleties we need to address.[14]

Any non-trivial $a'(r)$ is supported only for the parallel embedding for which $\phi' = 0$. For this class of embeddings, let us examine the action in (6.42) carefully. The variation of this action yields

$$\delta S = \mathcal{N}_T \left[\frac{\partial \mathcal{L}}{\partial a'} \delta a \bigg|_{r_{\rm min}}^{\infty} - {\rm EOM} \right] , \tag{6.45}$$

where $r_{\rm min}$ is the IR boundary. Usually this $r_{\rm min}$ should be identified with the location of the black hole horizon; however, we will argue this is not the case here. To have a well-defined variational problem the boundary term in (6.45) must vanish. We have the freedom to choose $\delta a(\infty) = 0$, but generically $\delta a(r_{\rm min}) \neq 0$. Thus in this case, we need to supplement the action in (6.42) with an additional boundary term at $r_{\rm min}$. This boundary term does not affect the equation of motion, but it will have a non-trivial effect when we evaluate the free energy by evaluating the on-shell action.

---

[14] We are grateful to Oren Bergman and Gilad Lifschytz for a very fruitful discussion on this issue.

Before including this boundary term, let us look at the equation for the gauge field

$$\frac{\partial \mathcal{L}}{\partial a'} = \frac{r^3 f a'}{\left[\left(1 - \frac{e^2}{f r^4}\right) + f (a')^2\right]^{1/2}} = j \ , \tag{6.46}$$

$$a' = \pm \frac{j}{r^2 f} \sqrt{\frac{r^4 f - e^2}{r^6 f - j^2}} \ , \quad \Longrightarrow \quad a(r)|_{r \to \infty} = \mp \frac{j}{2r^2} + \ldots \tag{6.47}$$

where j is a constant. It is clear that $a(r) \to 0$ as $r \to \infty$. We have to decide on the sign of the solution for a' above. This can be fixed by imposing an "ingoing" boundary condition at the horizon (meaning any energy-momentum flow at the horizon only flows into the horizon and not the other way round). This condition picks up the solution with the +ve sign.

Now let us go back to the action with the boundary term subtracted. This can be written as

$$S = \mathcal{N}_T \left[\int_{r_{\min}}^{\infty} dr \mathcal{L}(a', r) - j \int_{r_{\min}}^{\infty} a' dr \right] \ , \tag{6.48}$$

where we have used the fact that $a(r) \to 0$ as $r \to \infty$. From now on, in the presence of an electric field we will work with this action for the parallel embeddings.

From the perspective of the boundary theory, the response current is given by

$$\langle J_{x^1} \rangle = \lim_{\epsilon \to 0} \frac{1}{\sqrt{-\gamma}} \frac{1}{\epsilon^4} \frac{\delta S_{\text{ren}}}{\delta A_{x^1}} \bigg|_{\epsilon} \ , \tag{6.49}$$

where ϵ is the UV cut-off (in our notation $\epsilon \sim 1/r$) and γ denotes the pull-back metric on the $r = 1/\epsilon$ cut-off surface and S_{ren} is the renormalized action after adding the appropriate counter-terms. Following [90], it can be easily shown that $\langle J_{x^1} \rangle \sim j$.

Let us now comment on the choice of $r_{\min}$ when we want to identify the on-shell action as the thermodynamic free energy. A natural choice is clearly $r_{\min} = r_H$. However there is an issue with this choice. The integral of $(j \cdot a')$ yields a contribution of the form $(j \cdot e)\tau$, where τ is some typical time-scale. This time-scale τ has an IR log-divergence coming from the horizon

$$\tau = \frac{1}{4r_H} \log\left(r - r_H\right) \quad \text{with} \quad r \to r_H \ . \tag{6.50}$$

From the bulk point of view, τ can be identified with the time light rays take to travel from the boundary (at $r = \infty$) to the horizon (at $r = r_H$)[31]. On the other hand, from the gauge theory point of view, the existence of $(j \cdot e)\tau$ can be interpreted as the total energy dissipated to maintain the current j from time $t = 0$ to time $t = \tau$.

The process of switching on an electric field and the onset of flow of charges is a time-dependent one. The electric field creates fundamental matter anti-matter pair via the Schwinger mechanism and accelerates them. This results in a deposition of energy into the background thermal bath of the adjoint matter. In the probe limit, the energy density of the fundamental sector is suppressed by a factor of N_f/N_c and thus the background does not heat up. Finally the fundamental matter reaches a steady-state where a constant current flows.

Thus what we have here is not a stationary equilibrium state. Clearly, the energy dissipated to maintain the current should not be included in the thermodynamic free energy of the corresponding phase. The physics is telling us the choice of $r_{\min} = r_H$ is incorrect as far as the computation of the thermodynamics goes and there has to be another radial scale naturally arising in this problem. This is indeed the case.

The parallel branes go all the way to the horizon. Thus the on-shell action in this case is given by

$$S = \mathcal{N}_T \left[\int_{r_H}^{\infty} dr \left\{ r^3 \left(1 - \frac{e^2}{r^4 f(r)}\right)^{1/2} \left(1 - \frac{j^2}{r^6 f(r)}\right)^{-1/2} - j a' \right\} \right] \ . \tag{6.51}$$

This action must remain real. This reality condition imposes two algebraic conditions. These conditions determine the constant j in terms of e and r_H

$$e^2 = r_*^4 f(r_*) \quad \text{and} \quad j^2 = r_*^6 f(r_*) \quad \text{for the same } r_* \ , \tag{6.52}$$

hence

$$r_*^4 = r_H^4 + e^2 \tag{6.53}$$

and

$$j = e \times \sqrt[4]{r_H^4 + e^2} \ . \tag{6.54}$$

Thus we obtain the analogue of an Ohm's law where the conductivity depends non-linearly on the electric field. This result is in precise agreement with the one obtained in [90, 91] by considering a completely different kind of D7-brane embedding in AdS-Schwarzschild$\times S^5$ background.[15] This conductivity depends entirely on the non-compact part of the background metric (which is AdS_5 here) and is insensitive to the details of how the probe brane is embedded along the compact internal directions. Although the dual gauge theories are different in these cases, this fact tells us that the finite temperature transport properties (such as the conductivity) are insensitive to such differences.

The above algebraic constraints do more for us than to just determine the conductivity; they give us another natural radial scale denoted by r_*. Following [91], we will call this the "pseudo-horizon". We will argue momentarily that this radial scale acts as a natural "cut-off" as far as thermal properties are concerned, which is otherwise usually played by the event-horizon. Note that at this radial position nothing special happens to the background; moreover the induced

---

[15] This corresponds to adding $\mathcal{N} = 2$ hypermultiplets to the $\mathcal{N} = 4$ super Yang-Mills.

metric on the probe D7-branes is also ignorant about the location of the pseudo-horizon. As we will argue now, it is only the flavour degrees of freedom which are sensitive to the existence of the pseudo-horizon.

Before doing so, let us remind ourselves some important facts on the physics at finite temperature. At finite temperature, we identify the Euclidean on-shell action of the probe with its thermodynamic free energy (up to a factor of temperature). In evaluating the Euclidean on-shell action, we use $r_{\min} = r_H$. As elaborated in [31] with a toy model, the action of the probe that is inside the black hole contributes to the overall entropy of the background once the back-reaction of the probe is taken into account. We do not need to account for the part of the probe D-brane inside the horizon while computing the thermodynamic free energy of the probe sector.

Now, the degrees of freedom living on the probe brane are the open string degrees of freedom. In the presence of a background gauge field, *e.g.* an electric field on the probe world-volume, the effective geometry perceived by the fundamental sector can be different from the background geometry. As has been explicitly demonstrated in the seminal work in [32], in the presence of background gauge fields, the open string "feels" an effective geometry described by the so called open string metric. Let G be the induced metric on the probe and F be the constant electromagnetic field on its world-volume, then the open string metric, denoted by $\mathcal{S}$, is given by

$$\mathcal{S}_{ab} = G_{ab} - \left(FG^{-1}F\right)_{ab} \ . \tag{6.55}$$

This metric can be seen to naturally arise by expanding the DBI Lagrangian to quadratic order. In the presence of an electric field it can be explicitly shown that this open string metric $\mathcal{S}$ has a horizon at $r = r_*$. We have explicitly demonstrated this in Appendix C. In [33], using a similar set-up (studying D7-branes in AdS-Schwarzschild$\times S^5$-background) it has also been explicitly shown that the various conductivities can be determined by the data at $r = r_*$. This is reminiscent of the "membrane paradigm"; however the "fictitious" membrane is not located at the horizon, but at the pseudo-horizon.

Thus, as far as the fundamental degrees of freedom are considered, the pseudo-horizon plays an analogue role of the actual event-horizon of the space-time. Also, from the analysis of the different classes of embeddings in the presence of an electric field, we conclude that once the probe brane crosses $r = r_*$, it has to turn on a current j given by the formula in (6.54) and fall all the way through the horizon. Therefore, we propose to identify the Euclidean on-shell action evaluated up to $r = r_*$ with the thermodynamic free energy of the probe in the presence of an electric field. Notice, however, the pseudo-horizon has an important difference compared to an event-horizon: classically we cannot recover any information hidden behind an event-horizon; whereas information can propagate outside the pseudo-horizon. In analogy with the analysis done in [31], we conjecture that the part of the probe brane hidden behind $r = r_*$ contributes to the production of entropy of the background once the back-reaction of the probes are taken into account. It will be extremely interesting to verify this claim explicitly, but this is a non-trivial problem which we leave for future investigations.

Now, let us comment on a technical advantage of using $r_{\rm min} = r_*$. Recall that choosing $r_{\rm min} = r_H$ led to an IR log-divergence. It can now be explicitly checked that the action in (6.48) is perfectly IR-finite if we choose $r_{\rm min} = r_*$. Emboldened by all these observations, we propose the following prescription for computing the free energy in the presence of the electric field. We compute the on-shell action, but truncate it in the IR at $r = r_*$. Note that in determining r_* and j we can either use the on-shell action extended all the way to the horizon or we can simply impose reality condition for the solution of the gauge field in (6.47). The boundary term that we added in (6.48) can be interpreted as follows: for the part of the brane above r_*, this term simply acts as a boundary term; for the part of the brane below r_*, this acts as a source.

Now, with our conjectured proposal, we can easily verify that the parallel embeddings are always energetically favourable and chiral symmetry is always restored for the purely electric field case. We will get non-trivial phase structure in the presence of both electric and magnetic field at finite temperature, which we study in the next section.

1.7 Electric and Magnetic Field

We have argued and explicitly shown that an external magnetic field helps in chiral symmetry breaking whereas an external electric field restores the symmetry. Clearly electric and magnetic fields are two competing parameters as far as chiral symmetry breaking is considered. In this section we will explore the corresponding phase diagram when both of these competing parameters are present at finite temperature.

So far the dynamics of the flavours have been governed solely by the DBI action. In the presence of the electric and magnetic field (specifically the case when they are parallel to each other as we will see later), there will be a non-zero contribution coming from the Wess-Zumino term as well. This term takes the following general form

$$S_{\mathrm{WZ}} = \mu_7 \int \sum_p C_p \wedge e^{2\pi\alpha' F + B} \ , \tag{7.56}$$

where μ_7 is related to the 7-brane tension, F is the worldvolume 2-form field strength, B is the NS-NS 2-form and C_p is the p-form potential present in the background. The supergravity background given in (2.1) does not have any NS-NS field and F_5 is the only Ramond-Ramond field strength that is present. Thus the non-zero contribution coming from the Wess-Zumino term in this case takes the following general form

$$S_{\mathrm{WZ}} = \frac{\mu_7}{2}\int P[C_4]\wedge F\wedge F + \frac{\mu_7}{2}\int P[\tilde{C}_4]\wedge F\wedge F \ , \tag{7.57}$$

where P denotes the pull-back and the potentials C_4 and $\tilde{C}_4$ are defined by

$$F_5 = dC_4 \ , \tag{7.58}$$

$$\star F_5 = d\tilde{C}_4 \ . \tag{7.59}$$

Here $\star$ represents the 10-dimensional Hodge dual. The explicit form of the potentials are given by

$$C_4 = \frac{1}{g_s}\frac{r^4}{R^4} dt\wedge dx\wedge dy\wedge dz \ , \tag{7.60}$$

$$\tilde{C}_4 = -\frac{R^4}{27 g_s}\cos\theta f_1\wedge f_2\wedge f_3\wedge d\phi \ . \tag{7.61}$$

It is clear from the expression in (7.57), since F has legs along the Minkowski directions only, the Wess-Zumino term (which is proportional to $F\wedge F$) gives a non-zero contribution when the Minkowski electric and magnetic fields are parallel and this contribution comes solely from the second term in (7.57). We will discuss the consequences of this term in a subsequent subsection.

At zero temperature, there are only two Lorentz invariants: $\vec{E}^2 - \vec{H}^2$ and $\vec{E}\cdot\vec{H}$. Thus it suffices to consider two configurations: $\vec{E}\perp\vec{H}$ and $\vec{E}||\vec{H}$. Non-zero finite temperature breaks this Lorentz invariance. For a generic configuration, both the DBI and the WZ contributions depend on the relative angle of the electric and the magnetic fields. For simplicity, here we will focus on two representative cases: $\vec{E}\perp\vec{H}$ and $\vec{E}||\vec{H}$. In view of our discussion earlier, the WZ piece will contribute only in the parallel configuration. In this process, we will obtain the corresponding formulae for the flavour conductivity for these two cases. As before, these formulae are identical to the ones obtained in [34].

1.7.1 The case of perpendicular fields

Let us first consider the case when the electric and the magnetic fields are perpendicular and the Chern–Sinons term vanishes. Our ansatz for the gauge fields is[16]

$$A_x = -Et + A(r) \ , \quad A_y = Hx \ . \tag{7.62}$$

and the probe action is given by

$$S \ = \ \mathcal{N}_T \left[\int drr^3 \left[\left(1 + \frac{h^2}{r^4} - \frac{e^2}{fr^4}\right)\left(1 + \frac{r^2}{6} f(\phi')^2\right) + f(a')^2 \right]^{1/2} - j \int dra' \right] , \tag{7.63}$$

where

$$e \ = \ (2\pi\alpha' E)R^2, \quad h = (2\pi\alpha' H)R^2, \quad a'(r) \ = \ 2\pi\alpha' \frac{dA}{dr} \, . \tag{7.64}$$

Note that e and h have dimensions length^2, so the phase structure of the theory depends on the dimensionless ratios $e/h = E/H$ and

$$\frac{h}{r_H^2} \ = \ \frac{H}{\sqrt{\bar{\lambda}} T^2} \tag{7.65}$$

where $\bar{\lambda} = (\pi^2/4)\lambda_{\mathrm{t\,Hooft}}$.

The first term on the action (7.63) is the DBI action while the second term is a total derivative which does not change the equations of motion but contributes to the net action of

---

[16] Note that in general one would expect the presence of a Hall current perpendicular to the electric field for this configuration; however, it can be shown explicitly (or see *e.g.* [34]) that this Hall current is proportional to the chemical potential in this system. We do not consider the theory at finite chemical potential, hence we are safe to ignore the Hall current.

the brane. As we saw in section 6, for the U-shaped brane embedding the boundary conditions at the two sides of the U lead to $a(r) = \text{const}$, but for the $||$ embedding there is $a'(r) \neq 0$. Solving the equation of motion for the $a(r)$, we obtain

$$a'(r) \;=\; \frac{j}{r^2 f}\left(\frac{(r^4+h^2)\,f - e^2}{r^6 f - j^2}\right)^{1/2} \tag{7.66}$$

where j is the constant determined from the reality of the action integral

$$S_{||} \;=\; \int_{r_{\min}}^{\infty} \mathcal{L}_{||} dr \;=\; \mathcal{N}_T \int_{r_{\min}}^{\infty} dr \left[r^4 \left(\frac{(h^2+r^4)\,f(r) - e^2}{r^6 f(r) - j^2}\right)^{1/2} \;-\; j a'(r)\right] . \tag{7.67}$$

As explained in section 6, the lowest poin $r_{\min}$ of this integral is the pseudohorizon r_*. For reality's sake, both the numerator and the denominator of the ratio under the square root must change signs at the same point $r = r_*$, hence

$$\begin{aligned} &\left(h^2+r^4\right) f(r) - e^2 = 0 \quad\Longrightarrow\quad r_*^4 = \frac{1}{2}\left(\left(e^2+r_H^4-h^2\right) + \sqrt{\left(e^2+r_H^4-h^2\right)^2 + 4h^2 r_H^4}\right) , \\ &j^2 = r_*^6 f(r_*) \; . \end{aligned} \tag{7.68}$$

The above result matches with [34] in the appropriate limit.

For the U-shaped embeddings $a' \equiv 0$ while the equation of motion for the $\phi'(r)$ is

$$\frac{(r^5/6)\left(1+\frac{h^2}{r^4}-\frac{e^2}{fr^4}\right)^{1/2} f\phi'}{\left(1+\frac{r^2}{6}f(\phi')^2\right)^{1/2}} \;=\; \text{const} \;=\; \frac{r_0^4}{\sqrt{6}}\sqrt{f(r_0)}\left(1+\frac{h^2}{r_0^4}-\frac{e^2}{f(r_0)r_0^4}\right)^{1/2} . \tag{7.69}$$

The on-shell action for this class of embeddings becomes

$$\begin{aligned} S_U \;&=\; \mathcal{N}_T \int_{r_0}^{\infty} dr \frac{r^3}{\sqrt{f(r)}} \left((r^4+h^2)f(r) - e^2\right) \left[\frac{1}{r^4\left((r^4+h^2)f(r)-e^2\right) - \left((1+h^2)f(1)-e^2\right)}\right]^{1/2} \\ &=\; \int_{r_0}^{\infty} \mathcal{L}_U dr \; . \end{aligned} \tag{7.70}$$

Now we have to resort to numerical analysis to find out the thermodynamically preferred embedding. According to our proposal for the free energy, the corresponding phase diagram is obtained by looking at the zeroes of the following energy difference

$$\Delta S \;=\; \int_{r_0}^{\infty} \mathcal{L}_U dr - \int_{r_*}^{\infty} \mathcal{L}_{||} dr \ . \tag{7.71}$$

Notice that our underlying theory was conformal. We have introduced three dimensionful scales in the system (the temperature, the electric and magnetic field), which explicitly break the conformal invariance. However, the only meaningful quantities we can talk about are two dimensionless ratios: E/H and $H/(\sqrt{\lambda}T^2)$. Thus our goal will be to study the dependence of $\Delta\phi_\infty$ as a function of each of these ratios for a fixed value of the other one.

Before proceeding further, let us investigate some important features of the asymptotic angle separation in this case. From equation (7.69), the asymptotic angle separation is given by

$$\Delta\phi_\infty = \frac{3c}{x_0}\int_1^{\infty} \frac{dy}{\sqrt{y(y-1)}} \frac{1}{\sqrt{y - \frac{r_H^4}{x_0}}} \frac{1}{\sqrt{y + 1 + \frac{\Delta}{x_0}}} \ , \tag{7.72}$$

where we have defined

$$x_0 = r_0^4 \ , \quad \Delta = h^2 - e^2 - r_H^4 \ , \quad y = \frac{r^4}{r_0^4} \ , \tag{7.73}$$

and

$$3c = \sqrt{\frac{3}{2}} \left(x_0^2 + x_0\Delta - r_H^4 h^2\right)^{1/2} \ . \tag{7.74}$$

In the limit of large c, which translates to the limit of large x_0, we can obtain the following formula:[17]

$$\Delta\phi_\infty = \frac{\sqrt{6}\pi}{4} - \sqrt{\frac{3}{2}}\frac{e^2 - h^2}{2x_0} + \dots \ . \tag{7.75}$$

The formula in (7.75) implies if $e > h$, then asymptotically $\Delta\phi_\infty < \sqrt{6}\pi/4$; on the other hand if $e < h$, then asymptotically $\Delta\phi_\infty < \sqrt{6}\pi/4$. The first case is similar to the behaviour observed in fig. 1.3 and the second case is similar to the behaviour observed in fig. 1.7. Thus we expect no phase transition for $e > h$ and any non-trivial phase transition will take place only in the limit $e < h$. These features are pictorially demonstrated in fig. 1.12. We have numerically verified that the qualitative features demonstrated in fig. 1.12 are completely generic for both $e/h > 1$ and $e/h < 1$.

Alternatively, from the definition of the on-shell action in (7.70) and the asymptotic angle separation obtained from (7.69) we can obtain

$$\frac{S_U}{\mathcal{N}_T} - \frac{1}{2}c\Delta\phi_\infty = \int_{r_0}^{\infty} \frac{1}{r\sqrt{f}}\left(r^8 f Q^2 - 6c^2\right)^{1/2} \ , \quad Q = \left(1 + \frac{h^2}{r^4} - \frac{e^2}{r^4 f}\right)^{1/2} \ . \tag{7.76}$$

$$\begin{aligned}
&\implies \frac{\partial}{\partial c}\left(\frac{S_U}{\mathcal{N}_T} - \frac{1}{2}c\Delta\phi_\infty\right) = -\frac{1}{2}\Delta\phi_\infty \\
&\implies \frac{1}{\mathcal{N}_T}\frac{\partial S_U}{\partial c} = \frac{1}{2}c\frac{\partial \Delta\phi_\infty}{\partial c} \ .
\end{aligned} \tag{7.77}$$

Using the asymptotic expansion in (7.75) we get

$$\frac{1}{\mathcal{N}_T}S_U = \text{const.} + \sqrt{\frac{3}{2}}\frac{e^2 - h^2}{4}\log c + \dots \tag{7.78}$$

From (7.70) it is clear that in the limit $e > h$ the U-shaped embeddings become more and more energetic as c increases; on the other hand, in the limit $e < h$ increasing c decreases the energy of

---

[17] Interestingly, there is a term proportional to r_H^4 at the same order in $1/x_0$ but it's coefficient vanishes; thus there is no contribution coming from the background temperature. Non-zero effects of the background temperature is observed at the next order in $1/x_0$.

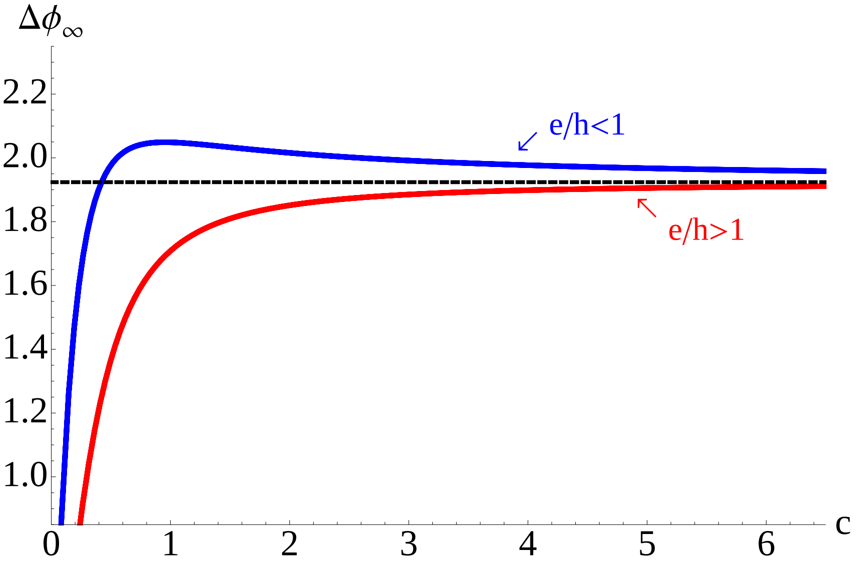

Figure 1.12: We have shown the dependence of the asymptotic angle separation as a function of c for both $e/h > 1$ and $e/h < 1$. It is clear that for $e/h > 1$, there is no phase transition and the interesting physics can happen only in the regime $e/h < 1$. The black (horizontal) dashed line represents the value $\sqrt{6}\pi/4$.

this class of embeddings. Thus we can conclude that for $e > h$, there will be no phase transition since the parallel shaped are always favoured and the interesting physics happens only in the regime where $e < h$.

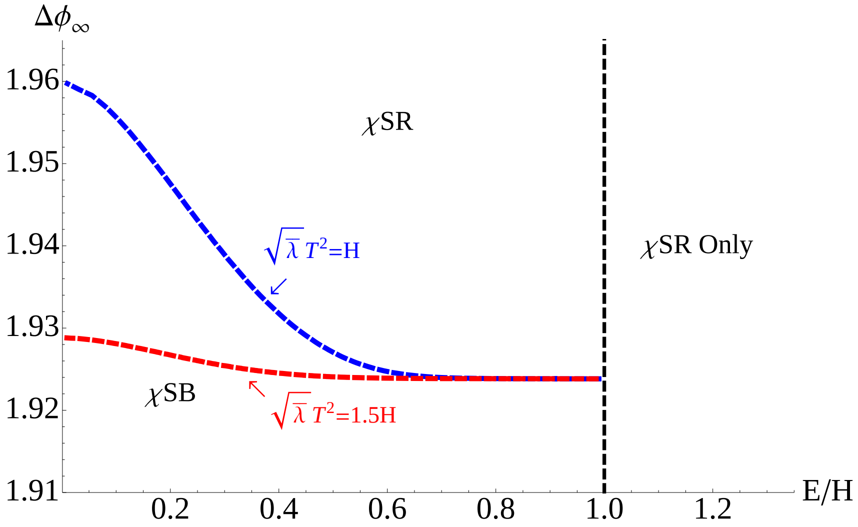

Figure 1.13: The phase diagram in the $(\Delta\phi_\infty - E/H)$-plane for various fixed values of the ratio $H/(\sqrt{\lambda}T^2)$. The non-trivial phase structure appears only in the limit $E/H < 1$ and in the regime $E > H$ only the chiral symmetry restored phase is available.

We have demonstrated a few representative phase diagrams in $\{\Delta\phi_\infty - E/H\}$-plane $\{\Delta\phi_\infty - H/(\sqrt{\lambda}T^2)\}$-plane and in fig. 1.13 and fig. 1.14 respectively. To avoid clumsiness, we have just presented the corresponding phase boundaries and have not appropriately labeled every region as in fig. 1.9. In fig. 1.13, we observe that for a fixed value of $H/(\sqrt{\lambda}T^2)$, increasing electric field decreases the asymptotic angle separation. On the other hand, for a fixed value of E/H, increasing $(\sqrt{\lambda}T^2)/H$ decreases $\Delta\phi_\infty$. This behavior is expected since both the electric field and temperature favour the restoration of chiral symmetry, whereas a magnetic field promotes symmetry breaking. Beyond the value $E/H = 1$, we do not have any chiral symmetry

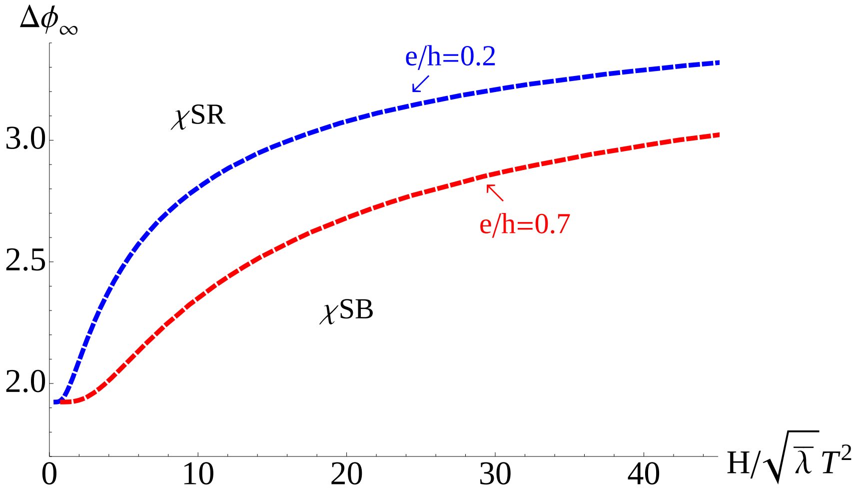

Figure 1.14: The phase diagram in the $\Delta\phi_\infty - H/(\sqrt{\lambda}T^2)$-plane for various fixed values of the ratio E/H. Again we restrict ourselves to the regime $E/H < 1$.

broken phase at all.

From fig. 1.14 we observe qualitatively similar physics. For a fixed value of e/h, increasing magnetic field increases the asymptotic angle separation, which is in keeping with the effect of magnetic catalysis in chiral symmetry breaking. We also observe that for a given value of $H/(\sqrt{\lambda}T^2)$, increasing e/h decreases $\Delta\phi_\infty$.

1.7.2 The case of parallel fields

For the parallel electric and magnetic fields, the vector potential takes form

$$A_x = -Et + A(r)\ , \quad A_z = Hy\ . \tag{7.79}$$

This time, there is a non-zero Wess–Zumino term, which pushes the D7 brane away from the equatorial $\theta = \pi/2$ plane of the S^2 sphere. Consequently, we need to parametrize the brane's geometry by two r-dependent angles $\theta(r)$ and $\phi(r)$, or equivalently by a unit 3-vector $\vec{n}(r)$. The DBI action is given by

$$S_{\rm DBI} \;=\; -\mathcal{N}\int dtdrr^3\left(1+\frac{h^2}{r^4}\right)^{1/2}\left[\left(1-\frac{e^2}{r^4 f}\right)\left(1+\frac{r^2}{6}f(r)\vec{n}'^2\right)+fa'^2\right]^{1/2} , \qquad (7.80)$$

where

$$h \;=\; (2\pi\alpha' H)\,R^2, \quad e \;=\; (2\pi\alpha' E)\,R^2, \quad \mathcal{N} \;=\; \tau_{D7}V_{\mathbb{R}^3}\frac{8\pi^2}{9}, \quad \frac{h}{r_H^2} = \frac{H}{\sqrt{\lambda}T^2} \qquad (7.81)$$

and

$$\vec{n}'^2 \;=\; \theta'^2 \;+\; \sin^2\theta\,\phi'^2 \qquad (7.82)$$

(where $'$ denotes d/dr), while the non-zero part of the Wess-Zumino term is

$$S_{\rm WZ} = \frac{\mu_7}{2}\int P\left[\tilde{C}_4\right]\wedge F\wedge F \ , \qquad (7.83)$$

for

$$P\left[\tilde{C}_4\right] = -\frac{R^4}{27g_s}\cos\theta(r)\phi'(r)f_1\wedge f_2\wedge f_3\wedge dr \ . \qquad (7.84)$$

Integrating the WZ term over the 3–space and the S^3 gives us

$$\begin{aligned} S_{\rm WZ} &= -\frac{eh\mu_7}{27g_s}\int \cos\theta\phi' dt\wedge dx\wedge dy\wedge dz\wedge dr\wedge f_1\wedge f_2\wedge f_3 \\ &= -\frac{2}{3}eh\mathcal{N}\int dtdr\vec{\mathcal{V}}(\vec{n})\cdot\vec{n}' \end{aligned} \qquad (7.85)$$

where $\vec{\mathcal{V}}(\vec{n})$ is a vector field on S^2 similar to the $\vec{A}$ field of a magnetic monopole,

$$\vec{\mathcal{V}}(\theta,\phi) \;=\; \cos\theta\,\nabla\phi \;=\; \cot\theta\,\hat{\phi} \quad (\hat{\phi}\text{ is a unit vector in the }\phi\text{ direction}). \qquad (7.86)$$

Altogether, the net Euclidean action for the probe brane takes form

$$S \;=\; S_{\rm DBI} \;+\; S_{\rm WZ} \;=\; \mathcal{N}_T \int dr\, \mathcal{L}_{\rm net}\,, \tag{7.87}$$

$$\mathcal{L}_{\rm net} \;=\; \left(1+\frac{h^2}{r^4}\right)^{1/2} \left[\left(1-\frac{e^2}{r^4 f}\right)\left(1+\frac{r^2}{6}f(r)\vec{n}'^2\right) \;+\; fa'^2\right]^{1/2} \;+\; \frac{2}{3}eh\vec{\mathcal{V}}\cdot\vec{n}'. \tag{7.88}$$

For the U-shaped solutions — where $a \to 0$ for $r \to \infty$ along both sides of the U — the action is clearly minimized for $a' \equiv 0$. Consequently, the remaining Lagrangian has form

$$\mathcal{L} = \mathcal{A}(r)\sqrt{1+\mathcal{B}(r)\,(\vec{n})^2} + k\vec{\mathcal{V}}(\vec{n})\cdot\vec{n}'\ , \tag{7.89}$$

— where

$$\mathcal{A}(r) \;=\; r^3\left(1+\frac{h^2}{r^4}\right)^{1/2}\left(1-\frac{e^2}{r^4 f(r)}\right)^{1/2}\ ,\quad \mathcal{B}(r) \;=\; \tfrac{1}{6}\,r^2 f(r)\ ,\quad k \;=\; \tfrac{2}{3}\,eh\ , \tag{7.90}$$

— which resembles Lagrangian of a charged particle moving in magnetic field of a monopole combined with a central electric potential. As explained in Appendix A, such particle has a modified conserved angular momentum

$$\mathbf{L} \;=\; \mathbf{r}\times m\mathbf{v} \;+\; Mq\frac{\mathbf{r}}{r} \tag{7.91}$$

where M is the magnetic charge of the monopole and q is the electric charge of the particle. When the ordinary angular momentum $\mathbf{r}\times m\mathbf{v}$ is conserved, the particles moves in a plane $\perp \mathbf{L}$. But for the conserved angular momentum of the form (7.91) the particle moves along a cone making fixed angle with the $\mathbf{L}$ vector. In spherical coordinates (where $\mathbf{L}$ points to the North pole) the radius r and the longitude ϕ change with time while the latitude remains constant, $\theta = \text{const} \neq \pi/2$.

Likewise, we show in Appendix B that for the U-shaped D7 brane $\theta(r) = \theta_c = \text{const} \neq \pi/2$ (in some coordinate system) while the longitudinal profile $\phi(r)$ depends on the functions $\mathcal{A}(r)$ and $\mathcal{B}(r)$. Specifically,

$$\cos\theta \;\equiv\; \frac{k}{L} \quad \text{while} \quad \frac{\mathcal{A}\mathcal{B}\,\phi'}{\sqrt{1+\mathcal{B}(\sin\theta\,\phi')^2}} \;\equiv\; L. \tag{7.92}$$

Assuming the U-shaped brane is smooth at its lowest point r_0 (where the D7 brane connects to the $\overline{\text{D7}}$ antibrane), we have $\phi'(r_0) = \infty$, hence

$$\mathcal{A}(r_0)\sqrt{\mathcal{B}(r_0)} \;=\; L\sin\theta_c \quad \text{while} \quad L\cos\theta_c \;=\; k \tag{7.93}$$

and therefore

$$\theta_c \;=\; \arctan\frac{\mathcal{A}(r_0)\sqrt{\mathcal{B}(r_0)}}{k}\,, \tag{7.94}$$

$$\frac{d\phi}{dr} \;=\; \sqrt{\frac{\mathcal{A}^2(r_0)\mathcal{B}(r_0)\,+\,k^2}{\left[\mathcal{A}^2(r)\mathcal{B}(r)\,-\,\mathcal{A}^2(r_0)\mathcal{B}(r_0)\right]\mathcal{B}(r)}}\,. \tag{7.95}$$

Plugging this solution into the Lagrangian (7.89), we obtain the net on-shell Euclidean action for the U-shaped solution as

$$\begin{aligned} S_U^E \;&=\; \mathcal{N}_T\int_{r_0}^{\infty}\frac{dr}{\sqrt{\mathcal{B}(r)}}\,\frac{\mathcal{A}^2(r)\mathcal{B}(r)\,+\,k^2}{\sqrt{\mathcal{A}^2(r)\mathcal{B}(r)\,-\,\mathcal{A}^2(r_0)\mathcal{B}(r_0)}} \\ &=\; \mathcal{N}_T\int_{r_0}^{\infty}\frac{dr}{r\sqrt{f(r)}}\,\frac{(r^4+h^2)(fr^4-e^2)\,+\,\frac{8}{3}e^2h^2}{\sqrt{(r^4+h^2)(fr^4-e^2)\,-\,(r_0^4+h^2)(f_0r_0^4-e^2)}}\,. \end{aligned} \tag{7.96}$$

On the other hand, for the parallel-shaped profile, the equation of motion for the gauge field can be solved to give

$$a' = \frac{j}{r^2 f}\sqrt{\frac{r^4 f - e^2}{(r^6+r^2h^2)\,f - j^2}}\,, \tag{7.97}$$

from which we determine

$$r_*^4 = r_H^4 + e^2 \ , \quad j^2 = \left(r_*^6 + r_*^2 h^2\right) f(r_*) \ . \tag{7.98}$$

The on-shell Euclidean action for this class of solutions is given by

$$S_{||}^E = \mathcal{N}_T \int_{r_*}^{\infty} dr \left[\left(r^4 + h^2\right) \sqrt{\frac{r^4 f - e^2}{\left(r^6 + r^2 h^2\right) f - j^2}} - j a' \right] \ . \tag{7.99}$$

The corresponding phase diagram is obtained by looking at the zeroes of

$$\Delta S = S_U^E - S_{||}^E \ . \tag{7.100}$$

Before proceeding further, let us again investigate the asymptotic angle separation — or rather the asymptotic longitude separation $\Delta\phi_\infty$ — in some details. Our goal here is to estimate when a phase transition is possible depending on the relative strength of the electric and the magnetic field. From (7.95) we obtain:

$$\Delta\phi_\infty = \frac{3L}{x_0} \int_1^\infty \frac{dy}{\sqrt{y\left(y - \frac{r_H^4}{x_0}\right)}} \frac{1}{\left[\left(y + \frac{h^2}{x_0}\right)\left(y - \frac{r_H^4+e^2}{x_0}\right) - \left(1 + \frac{h^2}{x_0}\right)\left(1 - \frac{r_H^4+e^2}{x_0}\right)\right]^{1/2}} \ , \tag{7.101}$$

where we have again defined

$$x = r^4 \ , \quad x_0 = r_0^4 \ . \tag{7.102}$$

It can again be shown that in the large L (hence the large x_0) limit, the asymptotic longitude separation is given by

$$\Delta\phi_\infty \ = \ \frac{\sqrt{6}\pi}{4} - \sqrt{\frac{3}{2}} \frac{e^2 - h^2}{2x_0} + \ldots \ , \tag{7.103}$$

Interestingly, this is the exact expression we obtained for the perpendicular case in (7.75) as well. As before it can also be checked that in this case we get

$$\frac{1}{\mathcal{N}_T}\frac{\partial S_U}{\partial c} = \frac{1}{2}c\frac{\partial \Delta\phi_\infty}{\partial c} + \dots \ , \tag{7.104}$$

where we now have

$$c = L\sin^2\theta_c \ . \tag{7.105}$$

Unlike (7.78), the above relation in (7.104) holds only in the limit $c \to \infty$. Taking everything together our general conclusion is similar as before: for $e > h$ we will not have any phase transition and chiral symmetry restored phase is the only available phase, but for $e < h$ we will have non-trivial physics and corresponding phase diagrams.

Before presenting the phase diagram a few words about the asymptotic angle separation are in order. Since in this case we have to fix some constant value of $\theta = \theta_c$, which is non-equatorial, the physical angle separation is the three-dimensional one instead of just $\Delta\phi_\infty$. If we denote this 3-d angle separation by $\Delta\Omega$, then in terms of θ_c and $\Delta\phi_\infty$ this is given by[18]

$$\cos\Delta\Omega = \cos^2\theta_c + \sin^2\theta_c\cos\Delta\phi_\infty \ . \tag{7.107}$$

The relevant coupling in the dual field theory corresponds to $\Delta\Omega$. We will use $\Delta\Omega$ in the corresponding phase diagrams.

---

[18] This formula is obtained by considering the dot product of two vectors represented by: $x_i = \sin\theta_c\cos\phi_i$, $y_i = \sin\theta_c\sin\phi_i$, $z_i = \cos\theta_c$, with $i = 1, 2$. Here $\{x, y, z\}$ represent the Cartesian coordinates. Now, taking the dot product we get

$$\cos\Delta\Omega = x_1x_2 + y_1y_2 + z_1z_2 = \cos^2\theta_c + \sin^2\theta_c\cos\Delta\phi_\infty \ , \tag{7.106}$$

where $\Delta\phi_\infty = \phi_1 - \phi_2$.

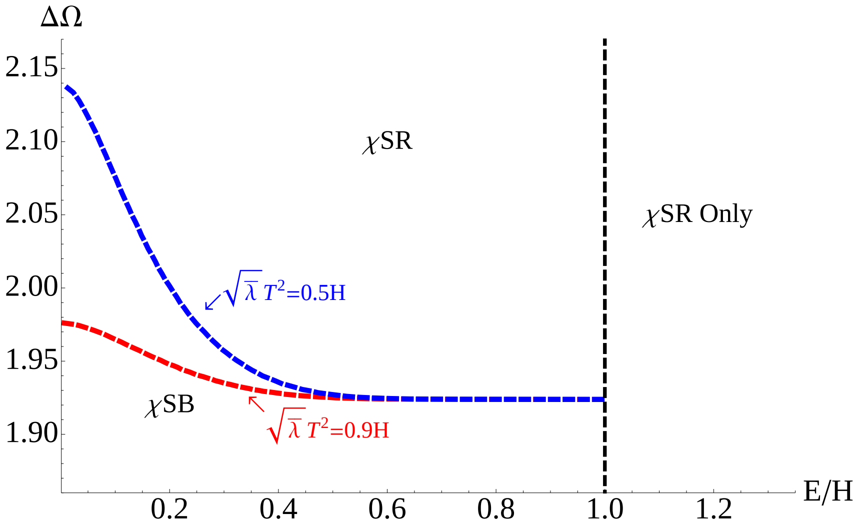

Figure 1.15: The phase diagram in the $(\Delta\Omega - E/H)$-plane for various fixed values of the ratio $(\sqrt{\lambda}T^2)/H$. The non-trivial phase structure appears in the regime $E/H < 1$ and in the regime $E/H > 1$ only the chiral symmetry restored phase is available.

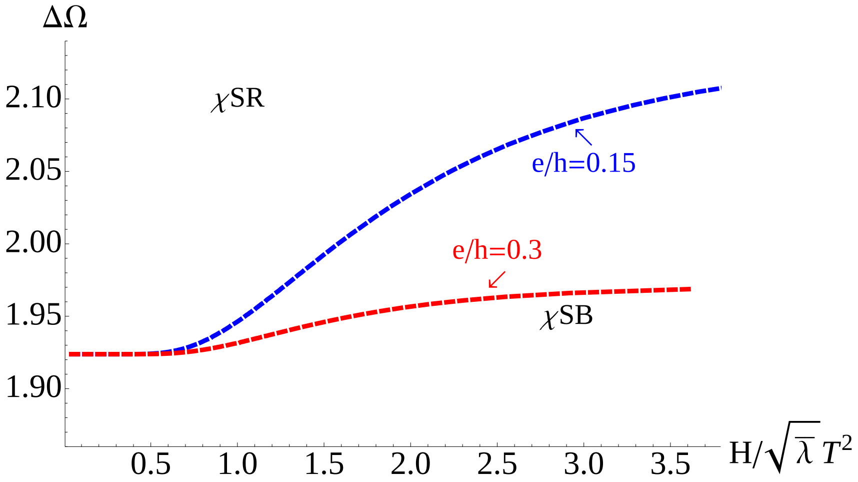

Figure 1.16: The phase diagram in the $\Delta\Omega - H/(\sqrt{\lambda}T^2)$-plane for various fixed values of the ratio E/H. We have restricted ourselves to the interesting regime $E < H$.

A few of the representative phase boundaries has been presented in fig. 1.15 in the $(\Delta\Omega - E/H)$-plane and in fig. 1.16 in the $\{\Delta\Omega - H/(\sqrt{\lambda}T^2)\}$-plane. As before, in these phase diagrams we have presented just the phase boundaries and have for simplicity. The qualitative features of these phase boundaries are similar to what we have observed for the perpendicular case. For a fixed value of $H/(\sqrt{\lambda}T^2)$, increasing e/h decreases $\Delta\Omega$, where for a fixed value of e/h increasing $H/(\sqrt{\lambda}T^2)$ increases $\Delta\Omega$. As we have already explained before, this is the expected general behavior.

1.8 Conclusions

We have studied in detail the Kuperstein-Sonnenschein model in the presence of temperature and a constant electromagnetic field. We have explicitly demonstrated the effect of *magnetic catalysis* in chiral symmetry breaking in this model adding to the claim of this universal phenomenon in various systems. The basic mechanism behind this is the fact that at strong magnetic field the fundamental matter populates the lowest Landau level and the dynamics of flavours effectively becomes $(1+1)$-dimensional. We have also obtained a detailed phase diagram in the temperature vs magnetic field plane. It is interesting and amusing to compare our phase diagram to the ones obtained earlier from various other holographic models. Such phase diagrams may be relevant for magnetars (neutron stars with a large magnetic field).

Based on our conjectured proposal of free energy in the presence of an electric field, we have also studied in detail the phase diagram when both electric and magnetic fields are present. Two representative situations that we have studied are parallel and perpendicular electric and magnetic fields. Not surprisingly, the qualitative features of these phase diagrams are similar. It is interesting to note that our analysis of a strongly coupled system conforms to weakly coupled field theory intuitions and hence hints towards some robust universal features of such non-Abelian gauge theories. Furthermore, the geometric manifestations of such gauge theory phenomena provide new and interesting outlook.[19]

It is worthwhile to remark here that in what we have considered, the magnetic catalysis (or the effects of the electric field) affects some scalar function which represents the embedding function of the probe brane. Such a bulk scalar field is dual to a single trace fermion bilinear

---

[19] For example, within a similar framework a holographic calculation of Schwinger effect has been recently carried out in [35].

in the dual boundary theory. Recently in [36] the magnetic catalysis of a bulk fermion field has been analyzed, which corresponds to a double trace operator in the boundary theory. Although the construction in [36] is not embedded within string theory, it is interesting to speculate such a possibility and its connection with our work.

There are many avenues for future work. It will be interesting to study the meson spectrum by studying the fluctuations of the probe brane around its classical profile in the presence of these external parameters to supplement our analysis of the various phases. The magnetic field produces interesting effects in the meson spectrum, *e.g.* Zeeman splitting, level mixing and enhancing the stability of mesons[96, 37] and thus it will be interesting to identify and study such features.

We have not considered the effect of a chemical potential or a non-zero baryon number in this model. A chemical potential can be realized by exciting the time component of the gauge field living on the probe brane worldvolume. The presence of a magnetic field and the baryon number is known to produce novel phases and interesting effects both in the so called $\mathrm{D3}-\mathrm{D7}$-model[38, 39] and in the Sakai-Sugimoto model[40, 41, 42, 43]. Thus it will be very interesting to further study the Kuperstein-Sonnenschein model in the presence of a non-zero baryon number.[20] Having both a magnetic field and a chemical potential gives rise to a non-zero Chern-Simons contribution through an $F \wedge F \wedge C_4$ term. This term has radial dependence through the profile function $\theta(r)$ as well as the gauge field excited on the worldvolume of the probe. This makes the problem technically more challenging as we will no longer be able to consider some constant θ-embedding and will have two coupled differential equations to solve for the profile. Thus we

---

[20] Baryon interactions based on non-supersymmetric $\mathrm{D7}/\overline{\mathrm{D7}}$-brane in the Klebanov-Strassler background has been studied in [94].

leave this for future work.

Note that one can place the probe D7-branes in the Klebanov-Witten background in two ways: the supersymmetric embeddings discussed in [45] and the non-supersymmetric ones which we have studied here. The former embedding does not have any spontaneous chiral symmetry breaking at zero temperature. Moreover, the global "flavour" symmetry for the supersymmetric embeddings is simply a $U(1)$. These embeddings are in close analogue of the Karch-Katz type embedding of D7-branes in the $\mathrm{AdS}_5 \times S^5$-background, which we have called the $\mathrm{D3}-\mathrm{D7}$-model earlier. It is quite interesting that the Klebanov-Witten background allows for both Karch-Katz type and a Sakai-Sugimoto type construction, although with different global "flavour" symmetry group and different physics as far as chiral symmetry is considered. Nonetheless, it would be interesting to investigate whether within the Klebanov-Witten background one could perhaps capture the rich phenomenology of both the $\mathrm{D3}-\mathrm{D7}$-model and the Sakai-Sugimoto model by considering these two different kinds of D7-embeddings.

It is noteworthy to remark that the Klebanov-Witten background has a conifold singularity at the origin where both the S^2 and the S^3 shrinks to zero size. This singularity is resolved in the Klebanov-Strassler background[46] by considering a deformed conifold and threading an NS-NS three-form flux through the S^3. This background corresponds to the confining phase of the dual field theory. Adding non-supersymmetric $\mathrm{D7}/\overline{\mathrm{D7}}$-branes in this background has been studied in [57]. To study non-trivial phase diagrams in the presence of external parameters, one needs to know the finite temperature version of the Klebanov-Strassler background which is currently not known in the literature in a closed form. For large temperature, an approximate solution is obtained in [48]. It will be interesting to study at least a part of the phase diagram in this large temperature background.

Our analysis is valid in the so called probe limit where the gravitational backreaction of the flavour branes are ignored. One crucial but technically challenging direction is to consider the backreaction of the probe branes and determine the resulting gravitational background. Some earlier works along these lines have been nicely summarized in *e.g.* [67]. Such an exercise with the non-supersymmetric branes in the Kuperstein-Sonnenschein model could also be a fruitful direction for future work. It is also interesting to speculate how the probe sector physics would be affected in such a back-reacted geometry. Some work along similar directions have been pursued recently in the so called D3–D7 model in [100, 51].

Our proposal of the thermodynamic free energy in the presence of the electric field and the boundary current, albeit a physically appealing one, is a conjecture. It would be extremely interesting if it could be directly verified in some simplifying model or argued further. One obvious direction is to consider the backreaction of the probe branes in the presence of the electric field and explicitly demonstrate our claim, which however is a technically difficult task. Some work along similar direction has been carried out in *e.g.* [52].

It is interesting to note that introducing an electric field and consequently having a non-zero current naturally realizes a system out of equilibrium. In the probe limit, according to our proposed definition of thermodynamic free energy, we seem to be able to perform sensible thermodynamics even outside the realm of equilibrium physics. For a system in thermal equilibrium, fluctuation-dissipation theorem relates the fluctuations of the system at equilibrium and its response to applied perturbations. Using our system, we can explore what might be the analogue of such a theorem for systems which are steady-state instead of at strict thermal equilibrium. Towards this end, we need to analyze the gauge field fluctuations around their classical configurations. We leave this for future investigations.

Finally we conclude by saying that although we do not pretend these models resemble QCD in the microscopic details, many macroscopic (qualitative) properties seem to be universal for these class of strongly coupled large N_c gauge theories (such as the *magnetic catalysis*). Thus within this approach we hope to continue to learn interesting and useful lessons relevant to the physics of quarks and gluons.

Appendix A. Charged particle in a monopole field

In section 7.2 we saw that the effect of the Wess-Zumino term on the motion of the D7 brane on the S^2 is similar to the effect of a monopole magnetic field on the motion of a charged particle. So as a warm-up exercise, let us consider the motion of a charged non-relativistic particle in a magnetic monopole field $\mathbf{B} = (M/r^2)\mathbf{n}$ superimposed on a central electrostatic potential $V(r)$.

When the Coulomb electric field of the charged particle is superimposed on the monopole magnetic field, the Poynting vector $\mathbf{E} \times \mathbf{B}$ has vorticity and hence non-zero angular momentum

$$\mathbf{L}_{\text{EM}} = \int d^3\mathbf{x}\, \mathbf{x} \times \mathbf{E} \times \mathbf{B} = -qM\, \mathbf{n} \tag{A.1}$$

where q is the electric charge of the particle, M is the magnetic charge of the monopole, and $\mathbf{n} = \mathbf{r}/r$ is the unit vector in the direction from the monopole to the particle. Consequently, the net angular momentum of the particle and the EM fields is

$$\mathbf{L} = \mathbf{L}_{\text{particle}} + \mathbf{L}_{\text{EM}} = \mathbf{r} \times m\mathbf{v} - qM\, \mathbf{n}\,. \tag{A.2}$$

Note that this is the net angular momentum that is conserved by the particle's motion while the $\mathbf{L}_{\text{particle}}$ and $\mathbf{L}_{\text{EM}}$ vary due to magnetic torques on the particle. Indeed, particle's equation of motion

$$m\mathbf{a} \;=\; \mathbf{F}_{\rm net} \;=\; -q\nabla V \;+\; q\mathbf{v}\times\mathbf{B} \;=\; -qV'\mathbf{n} \;+\; \frac{qM}{r^2}\,(\mathbf{v}\times\mathbf{n}) \tag{A.3}$$

leads to

$$\frac{d}{dt}(\mathbf{r}\times m\mathbf{v}) \;=\; \mathbf{r}\times\mathbf{F}_{\rm net} \;=\; 0 \;+\; \frac{qM}{r^2}\,\mathbf{r}\times(\mathbf{v}\times\mathbf{n}) \;=\; \frac{qM}{r}\Big(\mathbf{v} \,-\, (\mathbf{vn})\mathbf{n}\Big) \;=\; qM\,\frac{d\mathbf{n}}{dt} \tag{A.4}$$

and hence

$$\frac{d\mathbf{L}}{dt} \;=\; 0. \tag{A.5}$$

When the ordinary angular momentum $\mathbf{r}\times m\mathbf{v}$ is conserved, the particle moves in the central plane $\perp$ to the $\mathbf{L}$ vector. In the monopole magnetic field the conserved angular momentum is (A.2), so instead of a central plane the particle moves along a cone at fixed angle $\theta = \text{const} \neq \pi/2$ to the $\mathbf{L}$ vector. Indeed,

$$\mathbf{n}\cdot\mathbf{L} \;=\; \mathbf{n}\cdot(\mathbf{r}\times m\mathbf{v}) \;-\; \mathbf{n}\cdot(qM\,\mathbf{n}) \;=\; 0 \;-\; qM \;=\; \text{const} \tag{A.6}$$

and therefore

$$\cos\theta \;=\; \frac{\mathbf{n}\cdot\mathbf{L}}{|\mathbf{L}|} \;=\; -\frac{qM}{L} \;=\; \text{const}. \tag{A.7}$$

In the spherical coordinate system with North pole in the $\mathbf{L}$ direction, this constant θ is the particle's latitude angle, while the particle's motion in the longitudinal direction ϕ is governed by L,

$$mr^2\frac{d\phi}{dt} \;=\; L \;=\; \text{const}. \tag{A.8}$$

Finally, the radial motion is governed by the energy conservation,

$$E \;=\; \frac{m}{2}\left(\frac{dr}{dt}\right)^2 \;+\; V(r) \;+\; \frac{L^2\sin^2\theta \;=\; L^2-(qM)^2}{2mr^2} \;=\; \text{const}. \tag{A.9}$$

Appendix B. Brane Profile for Parallel E and B Fields

In section 7.2 we saw that when a D7 brane carries both electric and magnetic fields that are parallel to each other (or more generally when $\mathbf{E}\cdot\mathbf{B}\neq 0$), the action governing the brane's geometry included a non-trivial Wess–Zumino term. Consequently, the path of the brane on the S^2 as a function of the radius r does not follow the equator (or any other great circle) but involves both dimensions of the S^2. In this Appendix we shall see that the brane lies along a latitude circle $\theta = \text{const} \neq \pi/2$ and derive its longitudinal profile $\phi(r)$.

The effective action for the profile of a U-shaped brane is spelled out in eq. (7.89). In terms of r-dependent unit 3-vector $\vec{n}(r)$,

$$S \;=\; \int dr\Big(\mathcal{A}(r)\sqrt{1+\mathcal{B}(r)\vec{n}'^2}\;+\;k\vec{\mathcal{V}}(\vec{n})\cdot\vec{n}'\Big) \tag{B.1}$$

where $\vec{n}' \overset{\text{def}}{=} d\vec{n}/dr$, $\mathcal{A}$ and $\mathcal{B}$ are functions of r — they are spelled out in eq. (7.90), but their form is not important for the present argument, — and $\vec{\mathcal{V}}(\vec{n})$ is a vector field on the S^2 similar to the $\mathbf{A}$ field of a magnetic monopole,

$$\vec{\mathcal{V}}(\theta,\phi)\;=\;\cos\theta\,\nabla\phi\;=\;\cot\theta\,\hat{\phi},\quad \nabla\times\vec{\mathcal{V}}(\vec{n})\;=\;-\vec{n}\;. \tag{B.2}$$

Indeed, the effect of the WZ term $k\vec{\mathcal{V}}\cdot\vec{n}'$ on the brane profile is similar to the effect of a magnetic monopole field on the motion of a charged particle discussed in Appendix A — there is an extra $k\vec{n}$ term in the conserved (*i.e.*, r-independent) angular momentum of the brane.

To see how this works, let's develop the analogy between the brane profile $\vec{n}(r)$ and the particle's motion $\mathbf{r}(t)$. For the brane, there is no radial motion, and the radial coordinate r itself plays the role of time for the angular motion on the S^2. Thus, the first term in the brane's

Lagrangian (B.1) acts as a non-quadratic r-dependent kinetic energy for the angular motion, hence the analogue of the particle's mechanical momentum $\mathbf{p} = m\mathbf{v}$ is

$$\vec{P} \;=\; \frac{\partial(\text{first term in (B.1)})}{\partial\vec{n}'} \;=\; \frac{\mathcal{A}\mathcal{B}\,\vec{n}'}{\sqrt{1+\mathcal{B}\,\vec{n}'^2}} \tag{B.3}$$

while the canonical momentum is

$$\vec{P}_{\text{can}} \;=\; \frac{\partial\mathcal{L}}{\partial\vec{n}'} \;=\; \vec{P} \;+\; k\mathcal{V}(\vec{n})\,. \tag{B.4}$$

Consequently, the Euler–Lagrange equation for the brane is

$$\frac{d}{dr}\vec{P} \;=\; \frac{\partial\mathcal{L}}{\partial\vec{n}} \;-\; k\,\frac{d\vec{\mathcal{V}}(\vec{n})}{dr} \;=\; k\,\frac{\partial\mathcal{V}_j}{\partial\vec{n}}\,n'_j \;-\; k\,\frac{\partial\vec{\mathcal{V}}}{\partial n_j}\,n'_j \;=\; k\,\vec{n}'\times(\nabla\times\vec{\mathcal{V}}) \;=\; -k\,\vec{n}'\times\vec{n}\;, \tag{B.5}$$

where the right hand side is analogous to the Lorentz force in a monopole magnetic field. Finally, the analogy of the conserved net angular momentum is

$$\vec{L} \;=\; \vec{n}\times\vec{P} \;+\; k\vec{n}, \quad \frac{d\vec{L}}{dr} \;=\; 0. \tag{B.6}$$

Indeed,

$$\frac{d}{dr}(\vec{n}\times\vec{P}) \;=\; \vec{n}'\times\vec{P} \;+\; \vec{n}\times\vec{P}' \;=\; 0 \;-\; \vec{n}\times(k\vec{n}'\times\vec{n}) \;=\; -k\vec{n}' \quad\Longrightarrow\quad \vec{L}' \;=\; 0. \tag{B.7}$$

Conservation of the angular momentum (B.6) containing the $k\vec{n}$ term leads to constant angle $\Theta = \text{const}$ between the brane and the $\vec{L}$ vector. Specifically,

$$\vec{n}\cdot\vec{L} \;=\; k \;=\; \text{const} \quad\Longrightarrow\quad \cos\Theta \;=\; \frac{k}{|L|} \;=\; \text{const}. \tag{B.8}$$

Thus, the brane's path on the S^2 lies along a circle, but it's not a great circle since $\cos\Theta \neq 0$.[21]

---

[21] The brane does follow a great circle $\perp \vec{L}$ (which can be identified as the equator in some coordinate system) when the Wess–Zumino term vanishes, $k = 0 \implies \cos\Theta = 0$. This happens when there is only the magnetic field but $\mathbf{E} = 0$, or when there is only the electric field but $\mathbf{B} = 0$, or when the $\mathbf{E}$ and $\mathbf{B}$ fields are $\perp$ to each other. But when both the electric and the magnetic fields are present and $\mathbf{E} \not\perp \mathbf{B}$, there is non-zero WZ term $k \propto \mathbf{E}\cdot\mathbf{B}$ which moves the brane away from a great circle on the S^2, $\cos\Theta \neq 0$.

Instead, we may identify it as a constant-latitude circle

$$\theta(r) \;\equiv\; \Theta \;=\; \arccos\frac{k}{L} \;\neq\; \frac{\pi}{2} \tag{B.9}$$

in a spherical coordinate system where the North pole is in the direction of $\vec{L}$.

As to the motion in the longitudinal direction $\phi(r)$, in 3-vector notations we have $\vec{n}' = \vec{\omega}\times\vec{n}$ where $\vec{\omega}$ is a vector of magnitude ϕ' pointing due North (same direction as $\vec{L}$). Thus,

$$\begin{aligned}
\vec{n}'^2 \;&=\; (\vec{\omega}\times\vec{n})^2 \;=\; \omega^2\sin^2\theta\ , && \text{(B.10)}\\
\vec{P} \;&=\; \frac{\mathcal{A}\mathcal{B}}{\sqrt{1+\mathcal{B}\,\omega^2\sin^2\theta}}\,\vec{\omega}\times\vec{n}\ , && \text{(B.11)}\\
\vec{L} \;&=\; \frac{\mathcal{A}\mathcal{B}}{\sqrt{1+\mathcal{B}\omega^2\sin^2\theta}}\,\vec{n}\times(\vec{\omega}\times\vec{n}) \;+\; k\vec{n}, && \text{(B.12)}\\
&\Downarrow\\
\vec{L} \;-\; (L\cos\theta)\vec{n} \;&=\; \frac{\mathcal{A}\mathcal{B}}{\sqrt{1+\mathcal{B}\,\omega^2\sin^2\theta}}\Big(\vec{\omega} \;-\; (\omega\cos\theta)\vec{n}\Big)\ , && \text{(B.13)}
\end{aligned}$$

and consequently

$$\frac{\mathcal{A}\mathcal{B}\,\omega}{\sqrt{1+\mathcal{B}\,\omega^2\sin^2\theta}} \;\equiv\; L\ . \tag{B.14}$$

Solving this equation for the $\omega = \phi'$, we obtain

$$\frac{d\phi}{dr} \;=\; \frac{L}{\sqrt{\mathcal{B}(r)}\times\sqrt{\mathcal{A}^2(r)\mathcal{B}(r) \;-\; L^2\sin^2\theta}}\ . \tag{B.15}$$

Appendix C. The Open String Metric

In [32], the authors studied open strings in the presence of a constant electromagnetic field. One of the upshots of this is the definition of the open string metric which is different from just the spacetime metric in the presence of such background fields. Let G be the background spacetime metric, F be the constant electromagnetic field; then the open string metric, denoted by $\mathcal{S}$, is given by

$$\mathcal{S}^{ab} = \left[(G+F)^{-1}_{\rm symm}\right]^{ab} = \left[(G+F)^{-1}\, G\, (G-F)^{-1}\right]^{ab} \ , \tag{C.1}$$

$$\mathcal{S}_{ab} = G_{ab} - \left(FG^{-1}F\right)_{ab} \ , \tag{C.2}$$

$$\mathcal{A}^{ab} = \left[(G+F)^{-1}_{\rm anti-symm}\right]^{ab} = -\left[(G+F)^{-1}\, F\, (G-F)^{-1}\right]^{ab} \ , \tag{C.3}$$

where $\mathcal{A}$ is the purely anti-symmetric part. As argued in [32], the open string metric $\mathcal{S}$ simply describes the effective metric seen by the open strings.

The ten-dimensional background geometry is given in (2.1). Following [56], we place the D7/anti-D7 brane at $\theta = \pi/2$ and their profile is described by the scalar function $\phi(r)$. With this information, the induced metric on the worldvolume of the probe can be calculated to be given by

$$\begin{aligned} ds^2_{D7} &= \frac{r^2}{R^2}\left(-f(r)dt^2 + d\vec{x}^2\right) + \frac{R^2}{r^2 f(r)}\left(1 + \frac{r^2}{3}(\phi')^2\right) dr^2 \\ &+ \frac{R^2}{3}\left[\frac{1}{2}\left(f_1^2 + f_2^2\right) + \frac{1}{3}f_3^2 - \phi' dr f_1\right] \\ &= g_{tt}dt^2 + g_{xx}d\vec{x}^2 + g_{rr}dr^2 + g_{11}f_1^2 + g_{22}f_2^2 + 2g_{r1}dr f_1 \ . \end{aligned} \tag{C.4}$$

Our goal here is to compute the open string metric (for an open string ending on the D7-brane) taking G to be the induced metric in (C.4) in the presence of D7-brane worldvolume gauge fields. We consider two particular cases: perpendicular and parallel electric and magnetic field. Not surprisingly, our results will match the corresponding results in [33].

- **Perpendicular electric and magnetic field:**

The world volume gauge field ansatz is given by:

$$A_x = -Et + A(r) \ , \quad A_y = Hx \ . \tag{C.5}$$

The open string metric evaluated using the formula in (C.1) is given by

$$\begin{aligned}
ds^2 &= \frac{g_{tt}g_{xx}+e^2}{g_{xx}}d\tilde{t}^2 + \left(\frac{e^2}{g_{tt}} + g_{xx} + \frac{h^2}{g_{xx}} + \frac{g_{11}(a')^2}{g_{11}g_{rr}-g_{r1}^2}\right)dx^2 + \left(g_{xx}\left(g_{tt}g_{xx}+e^2\right)+h^2g_{tt}\right)d\tilde{y}^2 \\
&+ dr^2\left(g_{rr} + \frac{g_{tt}g_{xx}(a')^2}{g_{xx}\left(g_{tt}g_{xx}+e^2\right)+h^2g_{tt}}\right) \\
&+ g_{xx}dz^2 + g_{11}f_1^2 + g_{22}f_2^2 + g_{33}f_3^2 + g_{r1}drf_1 \ , \qquad (\mathrm{C.6}) \\
d\tilde{t} &= dt + \frac{eh}{g_{tt}g_{xx}+e^2}dy - \frac{ea'}{g_{tt}g_{xx}+e^2}dr \ , \qquad (\mathrm{C.7}) \\
d\tilde{y} &= \frac{1}{\sqrt{g_{tt}g_{xx}+e^2}}\left(dy + \frac{ha'g_{tt}}{g_{xx}\left(g_{tt}g_{xx}+e^2\right)+h^2g_{tt}}dr\right) \ . \qquad (\mathrm{C.8})
\end{aligned}$$

Here $g_{\alpha\beta}$ denotes the induced metric on the probe D7/anti-D7 brane. As we have seen before, only the parallel embeddings have a non-trivial $a(r)$. For this class of embeddings, the open string metric has an event horizon (denoted by $r = r_*$) which is different from the event horizon on the induced probe metric. The position of the open string metric event horizon is determined from

$$\mathcal{S}^{rr} = \left(g_{rr} + \frac{g_{tt}g_{xx}(a')^2}{g_{xx}\left(g_{tt}g_{xx}+e^2\right)+h^2g_{tt}}\right)^{-1} = \frac{j^2+g_{tt}g_{xx}}{g_{tt}g_{rr}g_{xx}^2} = 0 \ , \tag{C.9}$$

$$\implies j^2 + g_{tt}g_{xx} = 0 \qquad \implies \qquad g_{tt}\left(g_{xx}^2+h^2\right) + g_{xx}e^2 = 0 \ . \tag{C.10}$$

where we have used the equation of motion of the gauge field to substitute $a'(r)$ in favour of the constant j and also used the relation from which we fix j. It is clear from above that for this class of embeddings the corresponding phase in the dual field theory feels an effective temperature set by the pseudo-horizon. Thus in analogy with the purely finite temperature story, the appropriate "free energy" in this phase is defined as the on-shell action of the probe D7/anti-D7 brane which goes from $r = r_*$ to $r = \infty$.

On the other hand, for the U-shaped embeddings we have $a' = 0$ and thus the open string metric event horizon and the event horizon on the induced probe brane coincide.

- **Parallel electric and magnetic field:**

For parallel electric and magnetic fields, we take the following ansatz for the gauge fields

$$A_x = -Et + A(r) \ , \quad A_z = Hy \ . \tag{C.11}$$

In this case, the open string metric is given by

$$\begin{aligned} ds^2 &= \frac{g_{tt}g_{xx} + e^2}{g_{xx}} d\tilde{t}^2 + \frac{g_{xx}^2 + h^2}{g_{xx}} \left(dy^2 + dz^2\right) + \left(\frac{e^2}{g_{tt}} + g_{xx} + \frac{g_{11}(a')^2}{g_{11}g_{rr} - g_{r1}^2}\right) dx^2 \\ &+ dr^2 \left(g_{rr} + \frac{g_{tt}(a')^2}{g_{tt}g_{xx} + e^2}\right) + g_{11}f_1^2 + g_{22}f_2^2 + g_{33}f_3^2 + g_{r1}f_1 dr \ , \end{aligned} \tag{C.12}$$

$$d\tilde{t} = dt - \frac{ea'}{g_{tt}g_{xx} + e^2} \ . \tag{C.13}$$

For the parallel embeddings, the open string metric event horizon is determined from the following relation

$$\begin{aligned} &\mathcal{S}^{rr} = \left(g_{rr} + \frac{g_{tt}(a')^2}{g_{tt}g_{xx} + e^2}\right)^{-1} = \left(\frac{g_{rr}g_{tt}\left(g_{xx}^2 + h^2\right)}{g_{tt}\left(g_{xx}^2 + h^2\right) + j^2}\right)^{-1} = 0 \ , \\ &\Longrightarrow \quad g_{tt}\left(g_{xx}^2 + h^2\right) + j^2 = 0 \quad \Longrightarrow \quad g_{tt}g_{xx} + e^2 = 0 \ , \end{aligned} \tag{C.14}$$

where we have again used the equation of motion for the gauge field and the relation from which we fix the current j. Once again we see the emergence of an effective temperature for the conducting phase which is set by the pseudo-horizon. In this case as well we propose a similar definition of free energy as in the previous section.

Chapter 2

Backreaction and Phase Transitions

2.1 Introduction

[1] We saw evidence in the previous chapter that the use of holography, and in particular the AdS/CFT correspondence[53, 54, 55], has provided us with a powerful analytical tool to address strong coupling dynamics of certain gauge theories. Over the years it has become possible to capture some qualitative but key features of Quantum Chromodynamics (QCD), which so far has eluded the standard lore of conventional field theory methods.

In this chapter we will discuss one such aspect: the physics of the chiral symmetry breaking within the flavour sector of a large N_c gauge theory, with the hope that we learn at least qualitatively useful lessons about QCD and therefore the strongly coupled matter created at the Relativistic Heavy Ion Collider (RHIC) and the Large Hadron Collider (LHC). We will rely on a model proposed in [56][2], which we will henceforth refer to as the Kuperstein-Sonnenschein model.

The standard way of discussing the flavour physics is to introduce a set of probe branes in a particular gravity background which is sourced by some stack of D-branes. This method was pioneered in [58]. In the Kuperstein-Sonnenschein model, a pair of probe D7 and anti-D7

---

[1] This chapter is based on previous work done with Arnab Kundu, Matthias Ihl and Sandipan Kundu.

[2] See also [57].

brane is placed in the $\mathrm{AdS}_5 \times T^{1,1}$ background which is popularly known as the Klebanov-Witten background[59]. The probe branes wrap a three cycle inside the internal manifold $T^{1,1} \cong S^2 \times S^3$ and extend along the rest of the conifold $\mathbb{R}^+ \times S^2$. The zero temperature physics of the probes realizes a spontaneous breaking of the chiral symmetry by having the branes join smoothly in the IR and thus leading to: $U(N_f)_L \times U(N_f)_R \to U(N_f)_{\mathrm{diag}}$. In [60], we have explored the dynamics of the flavours in this model in the presence of a temperature and an external electro-magnetic field and found an interesting and rich phase structure.

The physics explored in the probe limit teaches us interesting lessons about the dynamics of flavours in such models, however they are also limited by the probe approximation. It is an interesting question in its own right to consider going beyond this approximation. Such an exercise is also physically relevant for QCD, where the number of colours and the number of flavours are of the same order. To consider back-reaction by the probes on the background geometry, one has to solve for the equations of motion obtained from an action consisting of supergravity and Dirac-Born-Infeld pieces. Typically, to facilitate the technical challenges, such an undertaking is carried out within the so called "smearing" approximation, where the probes are smeared along their transverse directions such that the full symmetry of the original background is recovered.

Work along this direction has been carried out in [61]-[66] in related models and summarized in the review [67]. However, most of these efforts rely on supersymmetry and become technically simpler than solving the equations of motion. The Kuperstein-Sonnenschein model is non-supersymmetric to begin with and thus one needs to consider a system of coupled second order non-linear differential equations to make any progress. We explored this system of equations in [68] and found an analytic solution at the leading order in the back-reaction, measured in powers of N_f/N_c.

When the flavour back-reaction is taken into account, the underlying conformal theory is deformed by higher dimensional irrelevant operators of dimension 6 and dimension 8 respectively. Furthermore, the gauge coupling runs and the theory acquires a Landau pole in the UV: the resulting theory is not UV-complete. Interestingly, these generic properties are very similar to the back-reacted backgrounds which do preserve some supersymmetry. In [68] we have also demonstrated that an additional probe sector in this back-reacted background now undergoes a chiral phase transition, which is otherwise absent when the back-reaction vanishes. This is simply because the Landau pole now gives a scale and there is a clear notion of small and large temperature regimes.

Let us offer a few more comments. It is not possible to observe a finite temperature phase transition in a theory whose underlying description is conformal. However, if one introduces another scale in the system (other than the temperature), as we have explored in [60], this possibility opens up. Typically, any such scale is an "infrared property" of the system since we are probing the system at low energies, *e.g.* at room temperatures. This is often summarized by saying that thermodynamics is an infrared property of a system, which means it does not care about the energy-scales that lie much higher than what is explored in an experimental set-up.

On the other hand, we have an example, demonstrated in [68], where such a phase transition happens because the Landau pole provides a scale other than the temperature. The theory is valid well below the Landau pole; and we have shown in [68] that within the regime of its validity there is now a phase transition. Thus the thermodynamics of the system is not quite just an "infrared property" of the system anymore. If we had an UV-complete description of the back-reacted system, the Landau pole would disappear yielding a more fundamental microscopic description which is not conformal. Thus it is not a surprising fact that a finite temperature phase transition takes place in such a fundamentally non-conformal system.

Before proceeding further, let us remark on a possible limitation[3] of our approach as far as exploring the physics in the flavour sector is concerned. We will introduce an additional probe sector and discuss the phase structure of this additional probe sector in the back-reacted background. Note, however, that our back-reacted background is obtained by considering back-reaction by the parallel shaped embeddings only. Thus, if we observe a phase transition from the parallel-shaped to the U-shaped embeddings in this additional probe sector, perhaps this is an indication that we need to actually consider back-reaction by both parallel-shaped and the U-shaped profiles separately and then compare the free energies of these two backgrounds. This is a very interesting yet technically more involved problem subject to ongoing research. For present purposes, we will adhere to a simpler analysis and pretend that the additional probe sector and the back-reacting probe sector are distinguishable, which should be viewed as a first attempt towards exploring the actual issue.

In the present article we will explore more aspects of the flavour sector by introducing additional probe branes in the back-reacted background and exciting a constant electro-magnetic field on this additional probe system. Our focus is to study the flavour dependence on the phase structure obtained in [60]. This effort, the reader should note, is merely a first attempt to understand how the QCD phase diagram might depend on the number of flavour degrees of freedom. Using lattice simulations, current understanding of flavour dependence of the QCD phase diagram at vanishing chemical potential is usually summarized in the so called "Columbia

---

[3] We thank Jacques Distler and Vadim Kaplunovsky for raising this point.

plot" (see for example fig 1 in [69]).[4] However, there is no general understanding about the phase structure in the presence of external fields such as the ones considered in this article. Thus our hope is to learn about robust qualitative features which may be relevant to QCD; although we have to remember that since we account for the back-reaction only up to the leading order in N_f/N_c, the flavour dependence that we will find within this framework is, by definition, weak. Nonetheless, the fact that this back-reaction breaks the conformal invariance of the background will result in some drastic changes as compared to the case when the back-reaction vanishes.

This article is divided in the following sections: Section 2 reviews the most relevant results on the back-reacted background obtained in [68]. In section 3, we discuss some interesting physical aspects of the perturbative back-reacted solution, while in section 4, electro-magnetic fields are introduced in the probe sector and their effects are investigated thoroughly, including their impact on holographic renormalization of UV divergences of the on-shell DBI action. Moreover, section 4 contains an exhibition of the most pertinent effects associated with the introduction of a chemical potential, studied both in the grand-canonical and canonical ensembles. Finally, section 5 offers concluding remarks and an outlook on future research.

2.2 Review of previous results

2.2.1 The back-reacted background

Let us begin with a brief review of the earlier results based on which we will continue to explore similar physical effects in our current work. Before taking any back-reaction into account, the model we consider is described in [56]. The authors introduced probe D7/anti-D7 branes in

---

[4] We thank Massimo D'Elia for very useful correspondence and the reference.

the $\mathrm{AdS}_5 \times T^{1,1}$ background, which is obtained as the near-horizon limit of a stack of D3-branes placed at the tip of the conifold. The D7/anti-D7 branes wrap a 3-cycle in the internal manifold $T^{1,1} \cong S^2 \times S^3$ and are extended along the rest of the conifold.

Before introducing the flavours, the dual field theory is given by an $\mathcal{N} = 1$ superconformal quiver gauge theory in $(3 + 1)$-dimensions with a gauge group $SU(N_c) \times SU(N_c)$ and a global $SU(2) \times SU(2) \times U(1)_R$ symmetry group. The degrees of freedom are contained in two bi-fundamental chiral superfields which transform in the $\big(N_c, \bar{N}_c\big)$ and $\big(\bar{N}_c, N_c\big)$ representations of the gauge group.

Introducing the probe branes corresponds, in the dual field theory, to introducing flavour degrees of freedom in an analogue of the so called "quenched approximation". This amounts to introducing a global $U(N_f)_L \times U(N_f)_R$ flavour symmetry group, where N_f denotes the number of flavours. The zero temperature physics of this system captures a geometric realization of the spontaneous breaking of chiral symmetry: the brane–anti-brane pair joins in the IR breaking the aforementioned flavour symmetry group down to a diagonal $U(N_f)$. On the other hand, the finite temperature physics of this system is rather trivial: since the background is conformal, there is no scale in the system and hence no phase transition can happen. Chiral symmetry is always restored in this case [60]. Nonetheless, the system exhibits interesting phase structure and some interesting phenomenon, such as the effect of *magnetic catalysis* in chiral symmetry breaking, when more control parameters are introduced [60]. In this article we will analyze the effect of the back-reaction by flavours on the physics observed and analyzed in [60].

Towards that end, we need to find the back-reacted background. Such a background can be found by sourcing the supergravity equations of motion by the Dirac-Born-Infeld (DBI) contribution coming from the probe flavour degrees of freedom. It turns out that, employing the "smearing technique", we can find an analytical solution of these back-reacted equations of motion at the leading order in the N_f/N_c correction [68]. In Einstein frame, the most general form of the back-reacted background is given by

$$\begin{aligned} ds^2 &= h(r)^{-1/2}\left(-b(r)dt^2 + d\vec{x}^2\right) + h(r)^{1/2}\left[\frac{dr^2}{b(r)} + \frac{e^{2g(r)}}{6}\sum_{i=1,2}\left(d\theta_i^2 + \sin^2\theta_i d\phi_i^2\right)\right. \\ &+ \left.\frac{e^{2f(r)}}{9}\left(d\psi + \sum_{i=1,2}\cos\theta_i d\phi_i\right)^2\right] , \qquad (C.1) \\ F_5 &= k(r)h(r)^{3/4}\left(e^t \wedge e^{x^1} \wedge e^{x^2} \wedge e^{x^3} \wedge e^r + e^\psi \wedge e^{\theta_1} \wedge e^{\phi_1} \wedge e^{\theta_2} \wedge e^{\phi_2}\right) , \qquad (C.2) \end{aligned}$$

where the vielbeins are given by

$$e^t = h^{-1/4}b^{1/2}dt \ , \quad e^{x^i} = h^{-1/4}dx^i \ , \quad e^r = h^{1/4}b^{-1/2}dr \ , \qquad (C.3)$$

$$e^\psi = \frac{1}{3}h^{1/4}e^f\left(d\psi + \cos\theta_1 d\phi_1 + \cos\theta_2 d\phi_2\right) \ , \qquad (C.4)$$

$$e^{\theta_{1,2}} = \frac{1}{\sqrt{6}}h^{1/4}e^g d\theta_{1,2} \ , \quad e^{\phi_{1,2}} = \frac{1}{\sqrt{6}}h^{1/4}e^g \sin\theta_{1,2}d\phi_{1,2} \ . \qquad (C.5)$$

Here $k(r)$ is a function that we can determine from the relation

$$k(r)h(r)^2 e^{4g(r)+f(r)} = 27\pi g_s^* N_c l_s^4 = 4L^4 \ , \qquad (C.6)$$

where g_s^* is the string coupling defined at $r = r_*$, which is a UV cut-off that we need to introduce since we have a running dilaton; l_s is the string length and L is the AdS-radius. The various metric functions are given by

$$b(r) = 1 - \frac{r_H^4}{r^4} \ , \tag{C.7}$$

$$\Phi(r) = \frac{\epsilon}{4} \log\left(\frac{r}{r_*}\right) \ , \tag{C.8}$$

$$h(r) = \frac{L^4}{r^4}\left(1 + \frac{\epsilon}{8}\right) + \epsilon\alpha\left(2 - \frac{r_H^4}{r^4}\right) \ , \tag{C.9}$$

$$e^{f(r)} = r\left[1 + \epsilon\left(-\frac{1}{24} + 4^{-2}\left(\frac{r_H^4}{r^2}\right)K\left(1 - \frac{r_H^4}{r^4}\right) - 8^{-2}r^2E\left(1 - \frac{r_H^4}{r^4}\right)\right)\right] \ , \tag{C.10}$$

$$e^{g(r)} = r\left[1 + \epsilon\left(-\frac{1}{48} -^{-2}\left(\frac{r_H^4}{r^2}\right)K\left(1 - \frac{r_H^4}{r^4}\right) + 2^{-2}r^2E\left(1 - \frac{r_H^4}{r^4}\right)\right)\right] \ , \tag{C.11}$$

with

$$\epsilon = \frac{3}{2\pi^2}\left(\frac{\lambda N_f}{N_c}\right) \ . \tag{C.12}$$

Here r_H is the location of the event-horizon, α and are two constants which correspond to — in the dual field theory — the couplings of a dimension 6 and a dimension 8 operator, respectively.[5] The temperature of the background can be identified with the inverse period of the Euclidean time direction. This yields [68],

$$T = \frac{r_H}{\pi L^2}\left(1 - \frac{\epsilon}{16}\right) \ . \tag{C.13}$$

Before proceeding further, let us comment on the regime of validity of the solution given in (C.7)-(C.11). To avoid the Landau pole coming from the diverging dilaton field we need to impose $r_* \ll \infty$, where r_* is the UV cut-off. Now the perturbative solution for various other

---

[5] Note that the constant α is denoted by c_3 in [68]. The general solution in [68] contains another constant which is denoted by c_5; however, since the coupling corresponding to the dimension 8 operator is a linear combination of these two constants, we have set $c_5 = 0$ without the loss of any generality.

functions will hold provided

$$\epsilon\left|\log\left(\frac{r_H}{r_*}\right)\right| \ll \mathcal{O}(1)\ , \quad \epsilon\left|\mathfrak{m}^{-2}\left(\frac{r_H^4}{r_*^2}\right)\right| \ll \mathcal{O}(1)\ , \quad \epsilon\left|\mathfrak{m}^{-2}r_*^2\right| \ll \mathcal{O}(1)\ , \tag{C.14}$$

$$\text{and} \quad 2\epsilon\left|\alpha\left(\frac{r_*^4}{L^4}\right)\right| \ll \mathcal{O}(1)\ . \tag{C.15}$$

In this article, we will often be interested in a simpler case where $\alpha = 0$ and $\mathfrak{m}^{-2} = 0$, in which case we only need to ensure that the first condition of the inequalities written above is satisfied.

2.2.2 Introducing an additional probe sector

In [68], we have explored the phase diagram of an additional probe sector in the background given in (C.1) and (C.7)-(C.11) imposing $\alpha = 0$, *i.e.* setting the source for the dimension 8 operator to zero. The inclusion of the back-reaction breaks the conformal invariance of the background and we found that the additional probe sector now undergoes a chiral phase transition. This phase transition is, in a very precise sense, caused by the existence of the Landau pole: this pole is located at $r \to \infty$ at the leading order in ϵ, which means we need to use a momentum UV cut-off. In what follows, we will discuss the phase structure in the additional probe sector including more control parameters such as a constant electro-magnetic field. For simplicity, we will mostly consider the case with $^{-2} = 0$ and $\alpha = 0$.

Before going further, let us revisit the phase structure in more details. Following [68], we introduce N_f' additional probe D7 and anti-D7 branes such that $N_f' \ll N_f$. These N_f' probes are aligned in a way similar to the back-reacting flavour branes. The dynamics of the N_f' flavours are given by

$$S_{\text{DBI}} = \mathcal{N}_T \int dr e^{f(r)+2g(r)+\Phi(r)}\sqrt{1+\frac{1}{6}b(r)e^{2g(r)}\phi'^2}\ , \quad \mathcal{N}_T = N_f'\tau_7 V_{\mathbb{R}^3}\frac{8\pi^2}{9T}\ , \tag{C.16}$$

where τ_7 is the tension of the probe, $V_{\mathbb{R}^3}$ denotes the volume along the three spatial directions and T is the background temperature. We have denoted $\phi \equiv \phi_1$ and also used the fact that it is consistent to set $\theta_1 = \pi/2$.

The equation of motion admits two classes of solutions: the parallel-shaped solutions denoted by

$$\phi(r) = \text{const} \ , \tag{C.17}$$

and the U-shaped solutions given by

$$\phi'(r) = \frac{6c}{\sqrt{b(r)^2 e^{2f(r)+8g(r)+2\Phi(r)} - 6c^2 b(r) e^{2g(r)}}} \ , \quad c^2 = \frac{1}{6} b(r) e^{2f(r)+6g(r)+2\Phi(r)}\bigg|_{r=r_0} \ , \tag{C.18}$$

where r_0 is the point where the brane–anti-brane pair joins smoothly. The parallel-shaped solutions correspond to the chiral symmetry restored phase and the U-shaped solutions correspond to the chiral symmetry broken phase.

Before discussing the phase transition, let us comment on the dependence of the coupling on the expansion parameter ϵ. For simplicity we will discuss the case when $\mathfrak{m}^{-1} = 0 = \alpha$. In this case the asymptotic angular separation is given by

$$(\epsilon) = (0) + \epsilon\, (r_0, r_H) \ , \quad \text{where} \quad (r_0, r_H) < 0 \ . \tag{C.19}$$

Thus at the leading order in ϵ the angular separation decreases linearly with ϵ with a slope which is determined by r_0 and r_H. The dependence of with ϵ is schematically shown in fig. 2.1. It is clear that, for the U-shaped profiles, increasing the effect of the back-reaction reduces the maximum value attained by the angular separation, denoted by $^{\max}$. In fact there is more physics in fig. 2.1: it displays the various available phases of the system for a given value of the coupling

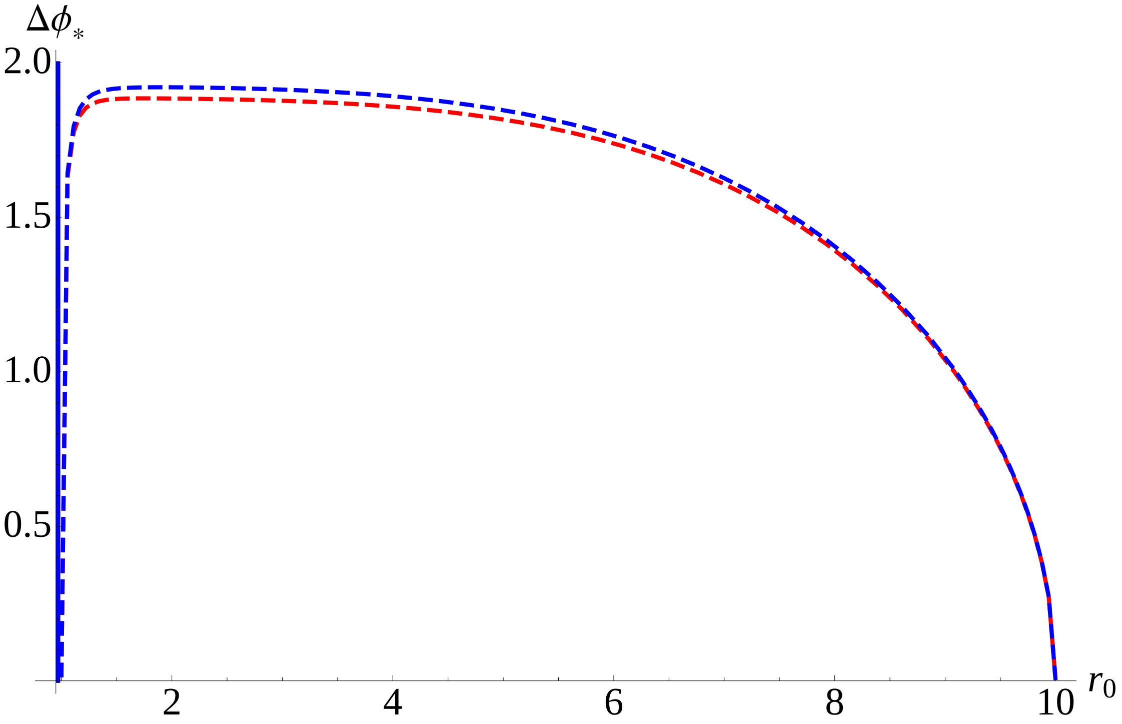

Figure 2.1: The blue and the red dashed curves correspond to $\epsilon = 0.01$ and $\epsilon = 0.5$ respectively corresponding the U-shaped embeddings. We have set $\mathfrak{m}^{-2} = 0$ and $r_H = 1$ and $r_* = 10$. The solid vertical blue line correspond to the parallel embeddings.

. For any $>^{\rm max}$, we only have the chiral symmetry restored phase available. On the other hand, for any $<^{\rm max}$, we have three available points in the phase space: one on the vertical solid line and two on the dashed curves. Comparing this situation with the more familiar $\{P - V\}$-diagram of the Van der Waals gas, we can conclude that there exists a first order phase transition from a point on the solid vertical line (*i.e.* the chiral symmetry restored phase) to a point on the dashed line (*i.e.* the chiral symmetry broken phase) for some critical value of .

The energetics of the two classes of embeddings will now decide the phase of the system. One has to look at the Euclidean on-shell action — which is identified with the thermodynamic free energy of the system — for these two types of embeddings and compute their difference

$$\Delta S = S_U - S_{||} \ . \tag{C.20}$$

Now depending whether $\Delta S > 0$ or $\Delta S < 0$, we will get a chiral symmetry restored or a chiral symmetry broken phase. This results in a non-trivial phase structure analyzed in [68], which we have shown in fig. 2.2. The phase diagram is presented in the vs m^2 plane, where m^2 is defined as

$$m^2 = \pi L^4 \left(\frac{T}{\mathfrak{m}}\right)^2 \left(1 + \frac{\epsilon}{8}\right) \ . \tag{C.21}$$

As can be observed from (C.16) this result is independent of α. We want to emphasize two main features here: First, in the absence of the back-reaction, no such phase structure exists at finite temperature. The underlying theory is conformal and only the chiral symmetry restored phase exists. Taking back-reaction into account breaks the conformal invariance by introducing a UV Landau pole and also deforming the CFT by higher dimensional irrelevant operators. In the leading order back-reacted solution described here, the UV Landau pole is located at $r \to \infty$ and the couplings corresponding to the irrelevant operators of dimension 6 and 8 respectively are denoted by α and $\mathfrak{m}$.

From the phase diagram shown in fig. 2.2 it is clear that $m^2 = 0$ is not a special point as far as the existence of the phase transition is considered. Thus we can conclude that the non-trivial phase structure and the associated thermodynamics that we obtain in this back-reacted model is caused by the existence of the Landau pole. We will now move on to discuss the effect of the back-reaction on some bulk properties of the background as well as the phase structure of an additional probe sector in the spirit of [60].

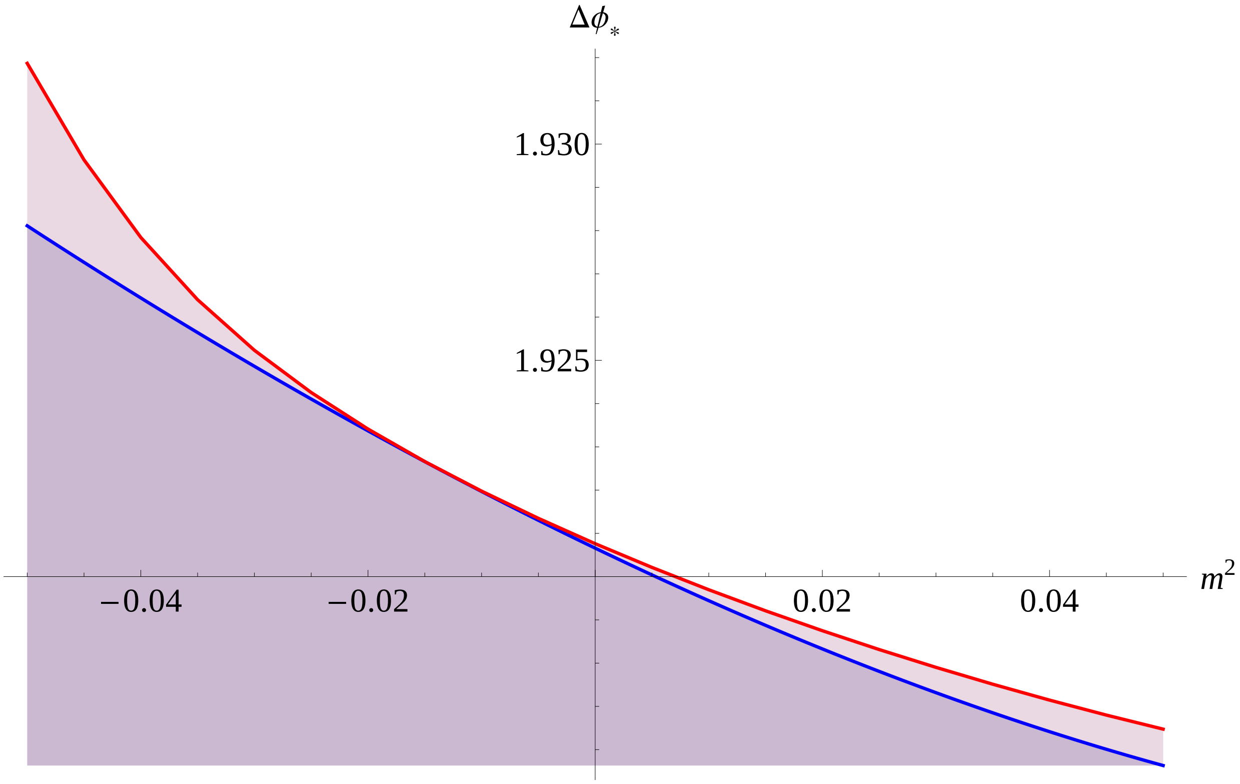

Figure 2.2: The phase diagram in the $\Delta\phi_\star$ vs m^2 plane. The blue line separates the χSB $\equiv$ chiral symmetry broken phase (below the line) from the χSR $\equiv$ chiral symmetry restored phase (above the line). Between the blue and the red line, we also have a metastable χSB phase. Above the red line we have only the χSR phase.

2.3 The back-reacted background: some physical aspects

Let us briefly comment on a few physical properties that we can extract from the solution in (C.7)-(C.11). To begin with, let us focus on the physics of the energy loss of the plasma. In the presence of the black hole, *i.e.*, introducing a non-zero temperature in the dual field theory, dissipation will occur due to the presence of the black hole in the bulk. We can now investigate how the back-reaction of the flavours affect the physics of dissipation at least when the back-reaction is taken into account perturbatively. Within such a "stringy" framework, there are two[6] canonical ways to explore this: First, in a perturbative description, the mechanism of energy loss of a parton moving in a plasma is usually characterized by the so called jet quenching parameter [72], usually denoted by $\hat{q}$. In [73], it was proposed that a non-perturbative description of the jet quenching parameter is given by a light-like Wilson loop, which one can use to perform computations at strong coupling. Second, within the "stringy" framework, the energy loss of a moving quark (parton) can be easily modeled by considering a fundamental string moving with a constant velocity. The force required to drag the string at a constant velocity is essentially the energy that is being lost in the plasma. This was first proposed and explored in [74, 75]. Here we will explore both these cases.

2.3.1 Jet quenching parameter

Let us begin with the jet quenching parameter. Using the general formula in [76], the jet quenching parameter is given by

$$\hat{q}^{-1} = \pi\alpha' \int_{r_H}^{r_*} e^{-\Phi/2} \frac{\sqrt{G_{rr}}dr}{G_{xx}\sqrt{G_{xx}+G_{tt}}} \ , \tag{C.22}$$

---

[6] See also [70, 71].

where G denotes the spacetime metric in the Einstein frame and the dilaton enters because of the conversion factor between the string frame and the Einstein frame. This gives

$$\begin{aligned} \hat{q}^{-1} &= I_0 + \epsilon I_1 + \epsilon\alpha I_2 \ , \quad \text{where} \\ I_0 &= \frac{L^4}{r_H^3}\int_1^{r_*/r_H} \frac{d\rho}{\sqrt{\rho^4-1}} \ , \qquad \text{(C.23)} \\ I_1 &= \frac{L^4}{8r_H^3}\int_1^{r_*/r_H} \frac{d\rho}{\sqrt{\rho^4-1}} \left[1-\log\left(r_H/r_*\right)-\log\rho\right] \ , \qquad \text{(C.24)} \\ I_2 &= \frac{1}{r_H}\int_1^{r_*/r_H} \frac{d\rho}{\sqrt{\rho^4-1}} \left[2\rho^4-1\right] \ . \qquad \text{(C.25)} \end{aligned}$$

Let us now offer a few comments: First, notice that although the integrals $I_0, I_2 > 0$, $I_1 < 0$. Thus the parameter $\hat{q}$ receives a correction of the form

$$\hat{q} = I_0^{-1} - \epsilon\frac{I_1}{I_0^2} - \epsilon\alpha\frac{I_2}{I_0^2} \ . \qquad \text{(C.26)}$$

The sign of the parameter α, which is hitherto unconstrained, determines whether the flavour contribution to the jet quenching parameter is positive or negative. The α-independent contribution is always positive. Note that, in [77] the parameter α is set to zero and thus the flavour contribution turns out to be always positive. The inclusion of the back-reaction breaks the underlying conformal symmetry by introducing a dimension 8 operator, which *a priori* can have both positive or negative contribution. The dimension 6 operator, however, does not play any role here.

2.3.2 Drag force computation

We will keep our discussion brief and follow [78] closely as far as notations are concerned. To discuss the drag force computation, we need to consider the following: let us start from the back-reacted background and consider a string that is hanging from the boundary, which in this case is located at $r = r_*$. The end point of the string describes a quark moving in the plasma as the string propagates in the bulk space-time. The ansatz for such a moving string takes the form

$$x(\sigma,\tau) = r(\sigma) + v\tau \ , \tag{C.27}$$

where $\{\tau, \sigma\}$ represents the string worldsheet and v denotes the velocity of the quark.

Due to the constant velocity, the string worldsheet develops a horizon that can be obtained from the following formula:

$$G_{tt} + G_{xx}v^2\big|_{r=r_c} = 0 \ , \quad \Longrightarrow \quad r_c = r_H \left(1 - v^2\right)^{-1/4} \ , \tag{C.28}$$

where r_c denotes the location of the horizon and G once again denotes the background spacetime. The momentum transfer is given by [78]

$$\frac{dp}{dt} = -\frac{1}{2\pi\alpha'}C \ , \quad \text{with} \quad e^{\Phi}G_{tt}G_{xx} + C^2\big|_{r=r_c} = 0 \ , \tag{C.29}$$

where the dilaton Φ enters the above formula since G is presented in the Einstein frame. Thus we finally get

$$C = \frac{L^2\pi^2T^2v}{\sqrt{1-v^2}}\left[1 + \frac{\epsilon}{16} + \frac{\epsilon}{8}\log\left(\frac{L^2\pi T}{r_*\left(1-v^2\right)^{1/4}}\right) - \frac{\epsilon}{2}L^4\pi^4T^4\alpha\frac{1+v^2}{1-v^2}\right] \ . \tag{C.30}$$

Once more we observe that for $\alpha \leq 0$, the energy loss is enhanced by the presence of the back-reaction. This is consistent with what we obtained for the jet quenching parameter.

2.3.3 Quark–anti-quark potential

We can use the background found in (C.7)-(C.11) to explore some of the non-perturbative aspects of the dual theory. The dual theory in this case is a non-supersymmetric theory which consists of the Klebanov-Witten theory coupled with a chiral flavour sector. We can investigate how the interaction between the flavours is affected by the presence of the adjoint as well as the fundamental degrees of freedom in this non-supersymmetric theory. To explore this, we can consider a massive quark anti-quark pair such that the mass of the pair is very small compared to the Landau pole. The corresponding bound state is given by a string worldsheet ending on a probe flavour brane that extends from r_0 to r_*, where r_0 is some infrared scale satisfying $r_0 \geq r_H$.

To parametrize the worldsheet of the string we can choose: $\tau = t, \sigma = x^1$ and $r = r(x^1)$, where x^1 is one of the spatial directions ranging from $-\ell/2$ to $+\ell/2$; and $\{\tau, \sigma\}$ represents the string worldsheet parameters. The quark–anti-quark distance, denoted by ℓ, and the renormalized potential, denoted by V, are then given by[79, 80]

$$\ell\left(r_0\right) = 2\int_{r_0}^{r_*} \frac{GP_0}{P\sqrt{P^2 - P_0^2}} dr \ , \tag{C.31}$$

$$V\left(r_0\right) = \frac{1}{\pi\alpha'}\left[\int_{r_0}^{r_*} \frac{GP}{\sqrt{P^2 - P_0^2}} dr - \int_{r_H}^{r_*} G dr\right] \ , \tag{C.32}$$

$$\text{with} \quad P = e^{\Phi/2}\sqrt{G_{tt}G_{xx}} \ , \quad G = e^{\Phi/2}\sqrt{G_{tt}G_{rr}} \ . \tag{C.33}$$

Once again, G above represents the background metric and the dilaton enters the above formulae since we are working in the Einstein frame. Our task here is to study the potential V as a function of the quark–anti-quark separation ℓ.

Recall that at zero temperature, in the absence of any back-reaction, the quark–anti-quark potential is Coulombic [81]; at finite temperature it undergoes a phase transition depending on the value of $T\ell$, as observed in [82, 83]. In the presence of the back-reaction, this phase transition will continue to exist and will receive ϵ order corrections. Thus we do not expect any qualitative change in the thermal physics of the system. Therefore we will consider the case when $T\ell \ll 1$

and explore how the Coulomb potential is affected by the back-reaction.[7] A representative plot is shown in fig. 2.3. It is evident that the Coulomb behaviour of the potential does not change in the presence of the back-reaction. Although we have not explicitly presented it, this behaviour does not change when $\alpha \neq 0$. This is in accord with what has been observed in *e.g.* [84].

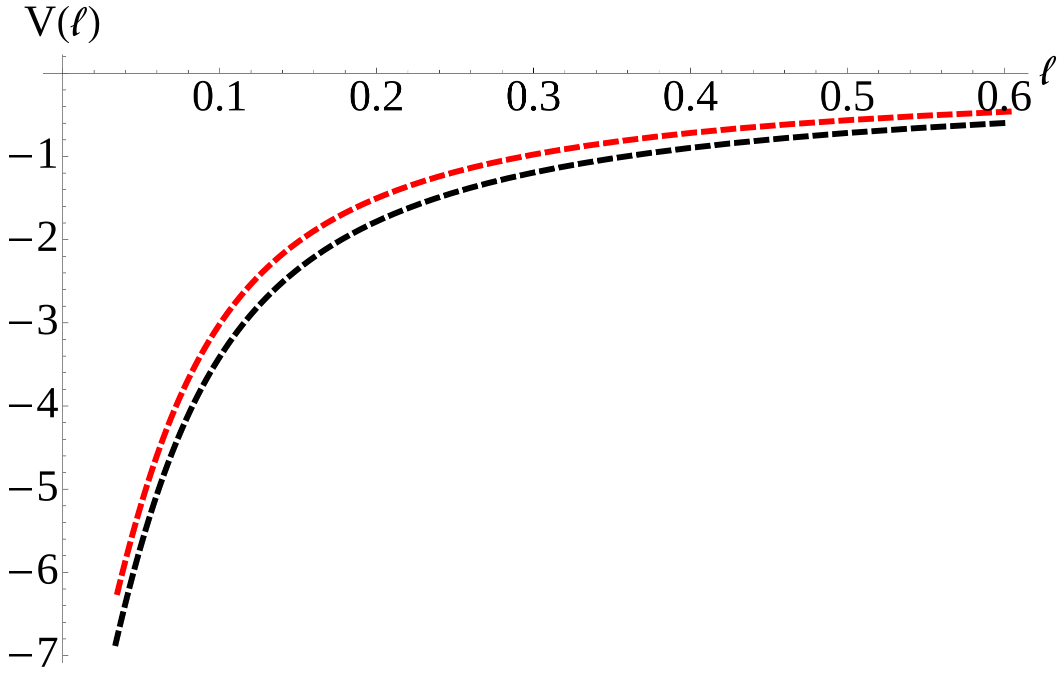

Figure 2.3: The quark–anti-quark potential obtained from (C.31) and (C.32). The black dashed line corresponds to $\epsilon = 0$ and the red dashed line correspond to $\epsilon = 0.5$. We have further set $L = 1$, $r_H \ll 1$, $\alpha = 0$.

---

[7] For some related studies in similar models, see *e.g.* [84].

2.3.4 Entanglement entropy

Entanglement entropy is a measure of quantum entanglement of a given system. It is defined as the von Neumann entropy of a reduced density matrix. For a given system, let us imagine dividing it into two parts denoted by A and B. For an observer who is restricted to access the information of the subsystem A only, the system will be described by the reduced density matrix $\rho_A = \mathrm{tr}_B \rho_{\mathrm{tot}}$, where ρ_{tot} denotes the total density matrix of the full system. Now, the entanglement entropy of the subsystem A is defined as

$$S_A = -\mathrm{tr}_A \rho_A \log \rho_A \ . \tag{C.34}$$

In the context of AdS/CFT correspondence, a proposal to compute the entanglement entropy was suggested in [85, 86]. Suppose we divide the system into two regions: one "rectangular" strip of length ℓ along x^1-direction (denoted by A) and its complement. The "rectangular" strip obviously has an infinite dimension along the x^2 and the x^3-directions. In such a scenario, the entanglement entropy is obtained by computing the minimal area surface whose boundary coincides with the boundary of the region A.

In the 10-dimensional Einstein frame metric, the Ryu-Takayanagi proposal yields

$$S_A = \frac{1}{4G_{10}} \int d^8\xi \sqrt{\mathrm{det} G} = \frac{2}{27 G_{10}} V_{\mathbb{R}^2} \int \sqrt{h} e^{f+4g} \left(x'^2 + \frac{h}{b} \right)^{1/2} \ , \tag{C.35}$$

where $V_{\mathbb{R}^2}$ denotes the area of the "rectangular" strip along the $\{x^2, x^3\}$-direction. The minimal area surface is parametrized by $x^1(r) \equiv x(r)$ with the boundary conditions $x(r_*) = \pm \ell/2$. Before going further, let us note that for the perturbative solution presented in (C.7)-(C.11) the quantity $(f + 4g)$ is independent of the coupling $\mathfrak{m}$. Hence the dimension 6 operator will have vanishing contribution to the entanglement entropy at least at the leading order in ϵ. This is not true for the dimension 8 operator, whose coupling is denoted by α.

The equation of motion resulting from minimizing the volume functional is given by

$$\sqrt{h}e^{f+4g}\frac{x'}{\sqrt{x'^2+\frac{h}{b}}} = \text{const} = \sqrt{h_0}e^{f_0+4g_0} \ , \tag{C.36}$$

where we have imposed the condition that at $r = r_0$ the minimal area surface turns over and have defined: $h_0 = h(r_0)$, $f_0 = f(r_0)$ and $g_0 = g(r_0)$. Substituting back the profile of the minimal area surface in (C.35), we get

$$S_A = S_A^{(0)} + \epsilon S_A^{(1)} \ , \tag{C.37}$$

at the leading order in ϵ.

One crucial property of the entanglement entropy is the so called "area law", *i.e.* S_A scales as the area of the sub-region A: $S_A \sim (\partial A)/a^2$, where a is an infrared cut-off in the dual field theory. It is easy to check that $S_A^{(0)} \sim (\partial A)/a^2$ and there are no sub-leading divergent pieces, as was previously alluded to in [86];[8] the new term here is $S_A^{(1)}$. Using the explicit functions for the background in (C.7)-(C.11), it is straightforward to check that

$$S_A^{(1)} \sim (\partial A)\frac{r_*^2}{24}\left(8r_*^4\alpha - L^4\right) + \text{finite} \ , \tag{C.38}$$

where r_* is the UV cut-off and we can identify $a^{-1} \equiv r_*$. Note that the term $\epsilon\alpha r_*^4$ has to be small because of the condition in (C.15). Hence, the divergence structure is the same as in the case where the back-reaction vanishes. It is nonetheless an interesting question whether going beyond a leading order perturbative solution in ϵ changes the divergence structure of the entanglement entropy.

---

[8] For the finite part of the entanglement entropy and physics related to it see [87, 88].

2.4 Physics on the probe brane

We will investigate the effects of introducing a constant electromagnetic field on the additional probe sector in this model. Let us begin by discussing the case of a purely electric field.

2.4.1 Purely electric field

Let us introduce a gauge field in the additional probe sector of the form

$$A_{x^1} = -Et + A_1(r) \ , \tag{C.39}$$

where E is the electric field along the x^1-direction. The function $A_1(r)$ encodes the possibility of a non-zero current which results from applying the electric field. The Euclideanized DBI action is given by

$$\begin{aligned} S_{\rm DBI} &= \mathcal{N}_T \int dr e^{f+2g+\Phi} \left[\left(1 - \frac{e^2 h}{b}\right) \left(1 + \frac{b}{6} e^{2g} \phi'^2\right) + b a_1'^2 \right]^{1/2} \ , && \text{(C.40)} \\ e &= (2\pi\alpha')\, E \ , \quad a_1 = (2\pi\alpha')\, A_x \ . && \text{(C.41)} \end{aligned}$$

As discussed in [60], for a non-trivial $\phi(r)$, the action is minimized for $a_1' = 0$. To have a non-trivial a_1', we focus on the parallel-shaped profiles which are given by $\phi = \text{const}$. For the parallel-shaped profiles the equation of motion for the gauge field is given by

$$\begin{aligned} e^{f+2g+\Phi} \frac{b a_1'}{\left(1 - \frac{e^2 h}{b} + b a_1'^2\right)^{1/2}} &= j \ , \\ \Longrightarrow \ a_1' &= \frac{j}{b} \left(\frac{b - e^2 h}{b e^{2f+4g+2\Phi} - j^2} \right)^{1/2} \ . \end{aligned} \tag{C.42}$$

Asymptotically, the solution for the gauge field takes the following form

$$a_1(r) = -\frac{j}{2r^2} \left(1 + \epsilon \frac{1 - 32\alpha e^2}{32} \right) + \epsilon \left(3j\mathfrak{m}^{-2}\right) \log r + \dots \ , \tag{C.43}$$

The condition that the solution for the gauge field given in equation (C.42) remain real ultimately determines the constant j in terms of the electric field and other parameters of the theory.

First, the location of the pseudo-horizon — which is where the numerator of the right hand side of (C.42) vanishes — is given by

$$r_{\rm ph}^4 \;=\; \left(e^2L^4+r_H^4\right)+\frac{\epsilon}{8}e^2\left[8r_H^4\alpha+L^4\left(1+16e^2\alpha\right)\right]+\mathcal{O}(\epsilon^2)\ . \tag{C.44}$$

Note that in the above formula the coupling $\mathfrak{m}$ does not enter. In general, depending on the sign of the constant α, the location of the pseudo-horizon can increase or decrease compared to the location in the case of vanishing back-reaction. If we set $\alpha=0$, then the pseudo-horizon receives a positive contribution coming from the back-reaction. Now the constant j can be fixed by demanding

$$j(\alpha,\mathfrak{m},e,r_H)=b(r)^{1/2}e^{f(r)+2g(r)+\Phi(r)}\Big|_{r=r_{\rm ph}}\ . \tag{C.45}$$

In general the correction to the constant j at the leading order in ϵ has a complicated algebraic form. For illustrative purposes, we can present one simplifying case in the limit $r_H^2/(eL^2)\ll 1$. We get

$$j^2=\left(eL^2\right)^3\left[1+\frac{\epsilon}{48}-8\epsilon\left(eL^2\right)\mathfrak{m}^{-2}+3\epsilon e^2\alpha+\frac{\epsilon}{8}\log\left(\frac{r_{\rm ph}}{r_*}\right)\right]+\mathcal{O}\left(\frac{r_H}{\sqrt{e}L}\right)\ , \tag{C.46}$$

where we have used equation (C.44) above.

To recast the above formula in terms of the quantities defined on the boundary field theory, let us recall a few basic definitions: First, the overall constant $\mathcal{N}$ that appears in front of the DBI action leaving out the integral over the time direction

$$\mathcal{N}=N_f'\tau_7\left(8\pi^2\right)\ ,\quad \text{and}\quad \tau_7=\frac{1}{g_s^*}\left(2\pi\right)^{-7}\alpha'^{-4}\ , \tag{C.47}$$

where we have set the volume of the three Minkowski spatial directions, $V_{\mathbb{R}^3} = 1$. If we also set the radius of the deformed AdS-space, $L = 1$ then using equation (C.6) and the above definitions we get

$$\mathcal{N} = \overline{\lambda} N_f' N_c \ , \quad \text{where} \quad \overline{\lambda} = \frac{3^4}{2^6}\lambda = \frac{3^4}{2^6}\left(4\pi g_s^* N_c\right) \ , \tag{C.48}$$

where λ denotes the 't Hooft coupling. The current density in the boundary gauge theory, denoted by $\langle J_x \rangle$, can be obtained as (see equation (C.69))

$$\langle J_x \rangle = \mathcal{N}\left(2\pi\alpha'\right) j \ . \tag{C.49}$$

For simplicity, setting ${}^{-1} = 0 = \alpha$ we get

$$\langle J_x \rangle = \overline{\lambda} N_f' N_c E \sqrt{2\pi\alpha' E}\left(1 + \frac{\epsilon}{96} + \frac{\epsilon}{16}\log\left(\frac{r_{\text{ph}}}{r_*}\right)\right) \ . \tag{C.50}$$

Here we can define an effective 't Hooft coupling absorbing all ϵ dependences in it, which will leave us with a simple formula for the conductivity much like for the case of vanishing back-reaction.

Notice that now, even for the purely electric field case, we will have a non-trivial phase structure. To demonstrate the existence of this phase transition, in fig. 2.4 we have shown the behaviour of as a function of r_0, the radial position where the brane–anti-brane pair joins, for different values of e/r_H^2. On the other hand our expectation is that increasing the electric field will favour a restoration of the chiral symmetry. Thus we should observe a monotonically decreasing behaviour of the phase boundary curve in the vs e/r_H^2 plane. This is demonstrated in fig. 2.5. We should note that only for $\epsilon \neq 0$ there is a non-trivial phase structure and the qualitative features are similar for various values of ϵ.

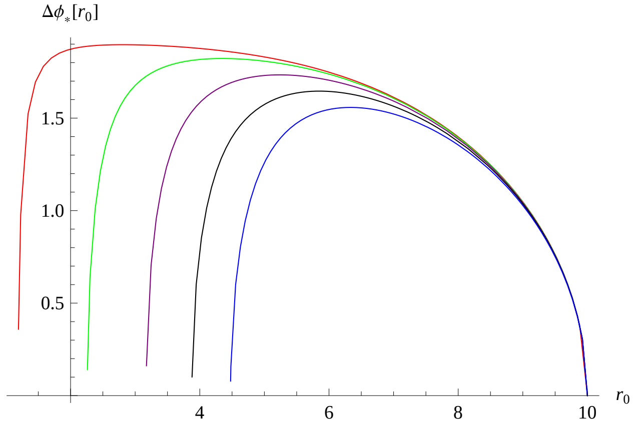

Figure 2.4: (r_0) for $r_H = 1, \epsilon = 0.01, m^2 = 0.05$, $\alpha = 0$ and $e = 1$ (red), $e = 5$ (green), $e = 10$ (purple), $e = 15$ (black) and $e = 20$ (blue). Clearly e is measured in units of r_H^2.

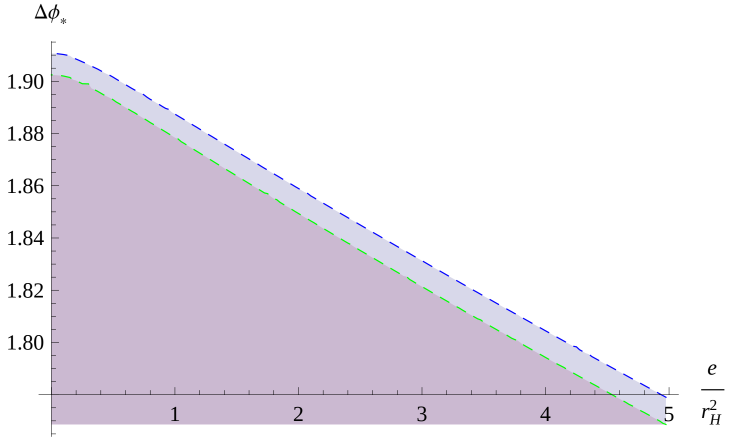

Figure 2.5: The critical $\left(\frac{e}{r_H^2}\right)$ for $m^2 = 0.001$ and $\epsilon = 0.01$ (blue) or $\epsilon = 0.1$ (green). The shaded region below the respective dashed lines corresponds to the χSB or metastable χSR phase and the region above the respective dashed lines represents the χSR or metastable χSB phase.

2.4.2 Purely magnetic field

Now we will introduce a constant magnetic field on the worldvolume of the additional probe D7 and anti-D7 branes. The ansatz for the gauge field is

$$A_3 = Hx^2 \; , \tag{C.51}$$

which represents a constant magnetic field $F_{23} = H$ along the x^1-direction. With this gauge field the DBI action is given by:

$$S_{\text{DBI}} = \mathcal{N}_T \int dr e^{f(r)+2g(r)+\Phi(r)} \left(1 + 4\pi^2\alpha'^2 H^2 h(r)\right)^{1/2} \sqrt{1 + \frac{1}{6} b(r) e^{2g(r)} \phi'(r)^2} \ . \tag{C.52}$$

Defining $B := 2\pi\alpha' H$, we obtain

$$\frac{e^{f+4g+\Phi}\sqrt{1+B^2h(r)}\frac{b}{6}\phi'}{\sqrt{1+\frac{1}{6}be^{2g}\phi'^2}} = c_H \ . \tag{C.53}$$

Equivalently,

$$\phi'(r) = \frac{6c_H}{\sqrt{b(r)^2\left(1+B^2h(r)\right)e^{2f(r)+8g(r)+2\Phi(r)} - 6c_H^2 b(r) e^{2g(r)}}} \ , \tag{C.54}$$

where we have defined

$$c_H^2 = \frac{e^{2f(r_0)+6g(r_0)+2\Phi(r_0)}}{6} b(r_0)\left(1 + B^2 h(r_0)\right) \ . \tag{C.55}$$

To demonstrate how this constant magnetic field affects the coupling , we can make a plot in the vs r_0 plane for different values of B. This is shown in fig. 2.6. The existence of a phase transition is self-evident from this diagram and the corresponding phase structure is shown in fig. 2.7, which is consistent with the phenomenon of magnetic catalysis.

2.4.3 Holographic renormalization

In the context of the AdS/CFT correspondence, the on-shell action S_{DBI} of the additional probe sector corresponds to the generating functional of the additional flavour sector that has been introduced in the dual field theory. This on-shell action contains UV divergences. Holographic renormalization is the rigorous procedure to regulate such divergences by adding

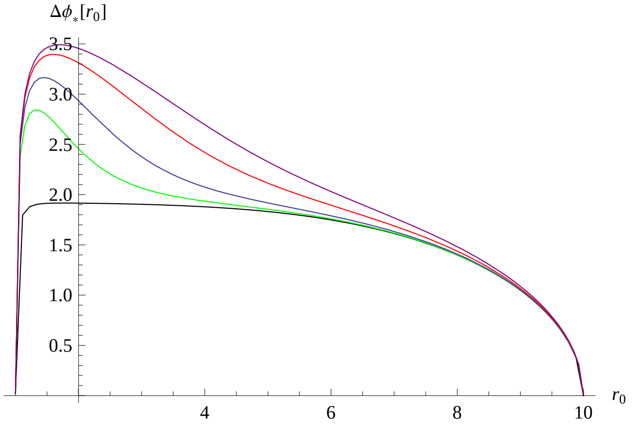

Figure 2.6: (r_0) for $r_H = 1, \epsilon = 0.01, m^2 = 0.05$, $\alpha = 0$ and $B = 0$ (black), $B = 5$ (green), $B = 10$ (blue), $B = 20$ (red) and $B = 30$ (purple).

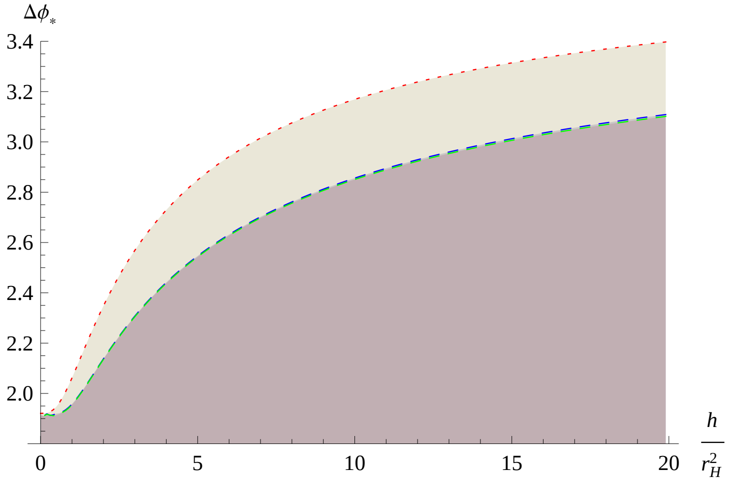

Figure 2.7: The critical (blue and green, dashed) and maximal (red, dotted) $\Delta\phi_*(h/r_H^2)$ for $m^2 = 0.001$ and $\epsilon = 0.01$ (blue, red) or $\epsilon = 0.05$ (green). The shaded region below the dashed line corresponds to the χSB or metastable χSR phase and the region between the dashed and dotted lines represents the χSR or metastable χSB phase. Above the dotted line, χSR is the only possible configuration.

covariant counter-terms on a cut-off surface and then taking the cut-off to infinity. In our current scenario, we have a cut-off surface r_* already in the problem and we need to restrict this cut-off surface to a position much below the Landau pole, which in our case is located at infinity. For a review on the procedure of holographic renormalization, see *e.g.* [89].

Let us apply the procedure of holographic renormalization to our current case. Here we will work with Euclidean signature. To procede, we need the following data: $\Lambda \equiv$ cut-off; γ_{ij} is the induced metric on the $r = \Lambda$ slice and $\gamma := \det\gamma_{ij}$. After the counter-terms are introduced, we need to take $\Lambda \to r_*$, which is the actual cut-off surface.

Firstly, we shall discuss the case of the parallel embeddings. We will review and elaborate on the discussion presented in [68]. In the absence of any external fields, the on-shell Euclidean action for the parallel embeddings is given by

$$S_{||} = \mathcal{N}_T \int_{r_H}^{r_*} dr e^{f(r)+2g(r)+\Phi(r)} \ . \tag{C.56}$$

The divergent pieces in $S_{||}$ can be arranged as follows:

$$S_{||}^{\rm div} = \mathcal{N}_T \left[-\frac{2r_*^6\left({}^{-2}\epsilon\right)}{3} + \frac{1}{192} r_*^4 \left(-7\epsilon + 48\right) + \frac{1}{2}^{-2} r_*^2 \epsilon r_H^4 - \frac{1}{16} \epsilon r_H^4 \log\left(\frac{r_H}{r_*}\right) \right] + {\rm finite} \ . \tag{C.57}$$

Of course, the ϵ dependent terms are parametrically much smaller compared to order one numbers and thus the leading order divergent behaviour is identical to the pure AdS-case, which contains only a quartic term. In addition to that there is another divergent piece proportional to (ϵr_*^6). The remaining terms in the above expression are actually not divergent under the conditions written in equations (C.14) and (C.15) and will eventually be absorbed in an effective 't Hooft coupling which receives correction due to the presence of the back-reaction and the temperature. It is worthwhile to remark that the "potentially divergent" term proportional to $\log(r_H/r_*)$ stems from the infrared part of the geometry. This can be understood by noticing that this term will not arise if one first expands the integrand in (C.56) in inverse powers of r_* and then integrates;

instead one needs to first integrate (C.56) and then expand the result in inverse powers of r_*. Note that the on-shell action does not depend on the warp factor $h(r)$ and hence the divergences are also insensitive to the constant α.

It was shown in [68] that we need only one counter-term to regulate the divergences of this on-shell action; however, the α-dependent contribution (which will be present in the counter-term) was not included there. In the most general case, we need the following counter-term

$$\begin{aligned} S_{\rm ct} &= -\mathcal{N}_T \frac{L}{4}\left(1 - \epsilon\frac{1}{32} + \frac{4}{3}\epsilon r_*^{2-2} + \frac{\alpha}{2L^4}\epsilon r_*^4\right)\sqrt{\det\gamma} \\ &= \mathcal{A}\left(\epsilon^{-2} r_*^2, \epsilon\alpha r_*^4\right)\sqrt{\det\gamma}\ . \end{aligned} \tag{C.58}$$

The constant $\mathcal{A}$ receives *finite* correction coming from the presence of the back-reaction and the irrelevant operators in the theory. This leaves us with the two “potentially divergent” pieces which can be absorbed in the definition of an effective ’t Hooft coupling:

$$\lambda_{\rm eff}(T) = \lambda\left[1 + \frac{1}{4}\epsilon\log\left(\frac{r_H}{r_*}\right) + \frac{1}{3}\epsilon^{-2}r_*^2\right] + \mathcal{O}(\epsilon^2)\ , \tag{C.59}$$

where $\lambda = 4\pi g_s^* N_c$ is the ’t Hooft coupling. Note that the effective ’t Hooft coupling also receives finite corrections due to the presence of the back-reaction, the deformations of the original CFT and the background temperature. This exercise demonstrates that the presence of the back-reaction does not call for a new counter-term, at least at the leading order in ϵ. Let us now discuss the case when there is a constant electro-magnetic field on the worldvolume of the probe sector. We will discuss the electric and the magnetic cases separately.

Case I: electric field

We will first discuss some subtleties that occur in the presence of an electric field as elaborated in [60]. First, the on-shell action in this case for the parallel embeddings should be supplemented by a boundary term due to the variation of the gauge field itself. Second, the lower limit of the integration is where the pseudo-horizon is located rather than the actual event-horizon of the background. The latter is motivated by a couple of facts, most prominently the fact that the open string metric, which is the metric the open string degrees of freedom should sense, possesses an event-horizon which is the pseudo-horizon; and hence it is natural to cut-off the integral at this location. This prescription also has the technical advantage of avoiding an IR singularity coming from the location of the event-horizon [60]. Altogether, we arrive at the following form for the on-shell action,

$$S_{||} = \mathcal{N}_T \int_{r_{\rm ph}}^{r_*} dr \left[e^{2f(r)+4g(r)+2\Phi(r)} \frac{\left(b(r) - e^2 h(r)\right)^{1/2}}{\left(b(r) e^{2f(r)+4g(r)+2\Phi(r)} - j^2\right)^{1/2}} - j a_1' \right] , \tag{C.60}$$

where $r_{\rm ph}$ was determined in equation (C.44). Subsequently the constant j is determined from equation (C.45) and the gauge field can be obtained from equation (C.42).

It is straightforward to see that the boundary term due to the gauge field contributes a finite quantity and there will be no divergences associated with it. All divergences will come from the DBI-piece. Let us comment on the case of vanishing back-reaction. The presence of the background gauge field introduces a new logarithmic divergence,

$$S_{||}^{\rm div} = -\mathcal{N}_T \left(\frac{r_*^4}{4} - \frac{1}{2} e^2 L^4 \log r_* \right) + \text{finite} , \tag{C.61}$$

where r_* is the cut-off surface. The above divergences can be regulated by adding a counter-term on the $r = $ const. slice

$$\begin{aligned} S_{\rm ct} &= \mathcal{N}_T \frac{L}{4} \left(\sqrt{\det\gamma} - (2\pi\alpha')^2 \sqrt{\det\gamma}\, \gamma^{ij} \gamma^{kl} F_{ik} F_{jl} \log r_* \right) \\ &= \mathcal{A} \sqrt{\det\gamma} + \mathcal{B} \sqrt{\det\gamma}\, \gamma^{ij} \gamma^{kl} F_{ik} F_{jl} \log r_* \ , \end{aligned} \tag{C.62}$$

where $\mathcal{A}$ and $\mathcal{B}$ are the coefficients of the counter-terms.

Now — including the effect of the back-reaction — the divergences take the following form:

$$\begin{aligned} S_{||}^{\rm div}/\mathcal{N}_T &= \frac{r_*^4}{4}\left(1-\frac{7\epsilon}{48}\right)-\frac{1}{2}e^2L^4\log r_*\left(1+\frac{\epsilon}{24}\right) \\ &+ \epsilon\left[-\frac{2}{3}^{-2}r_*^6+\frac{1}{2}^{-2}r_*^2\left(r_{\rm ph}^4+e^2L^4\right)-\frac{1}{4}e^2\alpha r_*^4+\left(2\jmath^{2-2}-\frac{1}{2}\alpha e^2 r_{\rm ph}^4\right)\log\left(\frac{r_*}{r_{\rm ph}}\right)\right] \\ &+ \frac{\epsilon}{16}e^2L^4\left(\log(r_*/r_{\rm ph})\right)^2+\mathcal{J}(r_{\rm ph},e,r_*)+\text{finite}\ , \end{aligned} \tag{C.63}$$

which is true at the leading order in ϵ. The term $\mathcal{J}$ is a "potentially divergent" term coming from the IR of the geometry, which in this case is located at $r = r_{\rm ph}$. This term gives

$$\mathcal{J}\left(r_{\rm ph},e,r_*\right)=\frac{\epsilon}{2}\int_{r_{\rm ph}}\frac{x^5}{\sqrt{4x^4+2e^2L^4}}\log\left(\frac{x}{r_*}\right)dx\ , \tag{C.64}$$

which can be integrated analytically; however, we refrain from doing so since the result is algebraically complicated and not particularly illuminating. Note that, when $e \to 0$, we get

$$\mathcal{J}(r_{\rm ph},0,r_*)=\mathcal{J}(r_H,0,r_*)=-\frac{\epsilon}{16}r_H^4\log\left(\frac{r_H}{r_*}\right)\ , \tag{C.65}$$

which is exactly what we had in [68]. Ultimately, the term $\mathcal{J}$ contributes to an effective 't Hooft coupling as explicitly demonstrated in [68].

We will now introduce appropriate counter-terms to take care of the divergences. Note that the leading order divergences in (C.63) are again a quartic one and a logarithmic one. There is an r_*^6 divergence supported purely by the back-reaction. The rest of the terms — which depend on r_* — are nonetheless parametrically finite within the regime of validity of our solution. Since the physics should not depend on the cut-off surface r_*, we will define an effective coupling which will receive corrections due to the presence of the horizon, the electric field and the cut-off surface.

The counter-term turns out to be:

$$\begin{aligned} S_{\rm ct} &= -\mathcal{N}_T \frac{L}{4}\left[\left(1-\frac{\epsilon}{32}+\frac{\epsilon}{2L^4}\alpha r_*^4+\frac{4\epsilon^{-2}}{3}r_*^2+3\alpha e^2\epsilon\log(r_*/r_{\rm ph})\sqrt{\det\gamma}\right)\right. \\ &\quad \left.-\left(1+4\epsilon^{-2}r_*^2-\frac{\epsilon}{8}\log(r_*/r_{\rm ph})\right)(2\pi\alpha')^2\sqrt{\det\gamma}\,\gamma^{ij}\gamma^{kl}F_{ik}F_{jl}\log(r_*/r_{\rm ph})\right] \\ &= \mathcal{A}\sqrt{\det\gamma}+\mathcal{B}\sqrt{\det\gamma}\,\gamma^{ij}\gamma^{kl}F_{ik}F_{jl}\log r_*\ . \end{aligned} \tag{C.66}$$

which again implies that there is no need for any additional counter-term as compared to the case of vanishing back-reaction. The presence of the back-reaction and other relevant parameters in the theory, such as the temperature or the electric field, yields a finite contribution to the coefficients of the counter-terms.

To obtain the boundary current, one can follow the procedure outlined in [90]. We will briefly review this process and argue that the presence of the back-reaction does not change the identification of the boundary current. To this end, we go back to Minkowski signature and write the on-shell action for the probes as

$$S_{D7} = -\mathcal{N}\int dtdr\mathcal{L}_{\rm on-shell} + \mathcal{N}\int dt\mathcal{L}_{\rm ct}\ , \tag{C.67}$$

where $\mathcal{L}_{\rm on-shell}$ denotes the on-shell Lagrangian (presented in equation (C.60)) and $\mathcal{L}_{\rm ct}$ denotes the counter-terms given in equation (C.66) and $\mathcal{N} = T\mathcal{N}_T$, where T is the background temperature.

The variation of the on-shell regularized action is

$$\delta S_{D7} = -\mathcal{N}\left[\int dtdr\left(\frac{\delta\mathcal{L}_{\rm on-shell}}{\delta\partial_r A_x}\partial_r\delta A_x+\frac{\delta\mathcal{L}_{\rm on-shell}}{\delta\partial_t A_x}\partial_t\delta A_x\right)-\int dt\frac{\delta\mathcal{L}_{\rm ct}}{\delta\partial_t A_x}\partial_t\delta A_x\right]\ . \tag{C.68}$$

There will be no contribution coming from the counter-term since we impose $\int dt\partial_t \delta A_x = 0$. The only contribution will come from the first variation of the on-shell Lagrangian and thus we get

$$\langle J_x \rangle := \frac{\delta S_{D7}}{\delta A_x} = \mathcal{N}\left(2\pi\alpha'\right) j \ , \tag{C.69}$$

where we have used the definition of j from equation (C.75).

Case II: magnetic field

Since the divergence structure is identical for the parallel and the U-shaped embeddings, we will discuss the parallel case in detail. The on-shell action with a purely magnetic field is given by

$$S_{||} = \mathcal{N}_T \int dr e^{f(r)+2g(r)+\Phi(r)} \left(1 + B^2 h(r)\right)^{1/2} \ . \tag{C.70}$$

The divergences of the on-shell action takes the following form

$$\begin{aligned} S_{||}/\mathcal{N}_T &= \frac{r_*^4}{4}\left(1 - \frac{7\epsilon}{48}\right) + \frac{1}{2}B^2 L^4 \log r_* \left(1 + \frac{\epsilon}{24}\right) \\ &+ \epsilon\left[-{\frac{2}{3}}^{-2} r_*^6 + \frac{1}{4}B^2\alpha r_*^4 + {\frac{1}{2}}^{-2} r_*^2\left(r_H^4 - 2B^2L^4\right) - \frac{1}{2}\alpha r_H^4 B^2 \log\left(\frac{r_*}{r_H}\right)\right. \\ &- \left.\frac{1}{16}B^2L^4\left(\log(r_*/r_H)\right)^2\right] + \mathcal{J}\left(r_*, B, r_H\right) + \text{finite} \ , \end{aligned} \tag{C.71}$$

where $\mathcal{J}$ is the "potentially divergent" term that arises from the IR of the background, which is explicitly given by

$$\mathcal{J} = \frac{\epsilon}{4}\int_{r_H} dx x\sqrt{x^4 + B^2L^4}\log\left(\frac{x}{r_*}\right) \ . \tag{C.72}$$

Note that the divergences in equation (C.71) are very similar to the ones encountered for purely electric case in equation (C.63); in fact, equation (C.71) can be obtained from equation (C.63) by $j \to 0$ and $e^2 \to -B^2$, which of course makes sense since in the absence of a finite temperature Lorentz symmetry allows one to the identify the physics by sending $e^2 \to -B^2$. This means that the divergence structure does not depend on the finite temperature. However, the presence of the finite temperature affects the effective 't Hooft coupling in inequivalent ways for the electric and the magnetic cases.

2.4.4 Electromagnetic fields

At zero temperature, in the presence of an electric and magnetic field, denoted by E and H respectively, there are two Lorentz invariants: $\vec{E}^2 - \vec{H}^2$ and $\vec{E} \cdot \vec{H}$. Therefore, when the temperature vanishes, it is sufficient to analyze the cases when the electric and the magnetic fields are parallel or perpendicular. However, it was demonstrated in [60] that these two situations yield qualitatively similar results; hence in order to keep our discussions simple, we will consider the perpendicular case only.

Let us introduce

$$A_{x^1} = -Et + A_1(r) \ , \quad A_{x^2} = Hx^1 \ , \tag{C.73}$$

which yields

$$S_{\rm DBI} = \mathcal{N}_T \int dr e^{f(r)+2g(r)+\Phi(r)} \left[\left(1 + B^2 h(r) - e^2 \frac{h(r)}{b(r)}\right) \right.$$
$$\left. \left(1 + \frac{1}{6} b(r) e^{2g(r)} \phi'(r)^2\right) + b(r) \left(\frac{\partial a_1(r)}{\partial r}\right)^2\right]^{1/2} \ .$$

For convenience, we have again introduced the following:

$$e := 2\pi\alpha' E \ , \quad B := 2\pi\alpha' H \ , \quad a_1 := 2\pi\alpha' A_1 \ . \tag{C.74}$$

Of course, the action should be supplemented by the boundary term discussed in [60], but we have not written it explicitly since it does not affect the equations of motion. The boundary term becomes relevant only for the computation of the free energy and the discussion of the phase diagrams. The basic structure of the probe profile functions remain qualitatively the same as discussed in [60]. In the case of a non-trivial profile $\phi(r)$, the action is clearly minimized when $a_1'(r) = 0$.

For the parallel embeddings we find,

$$\begin{aligned} a' &= \pm \frac{j}{\sqrt{b(r)}} \frac{\sqrt{1 + B^2 h(r) - e^2 \frac{h(r)}{b(r)}}}{\sqrt{b(r) e^{2f(r)+4g(r)+2\Phi(r)} - j^2}} \ , & \text{(C.75)} \\ &= \pm \left[\frac{j}{r^3} + \mathcal{O}(r^{-7}) + \epsilon \left(\frac{4j\mathfrak{m}^{-2}}{r} + \mathcal{O}(r^{-3}) \right) \right] + \ldots \ . & \text{(C.76)} \end{aligned}$$

The second line above is valid as $r \to r_*$, the UV cut-off. As it was pointed out in [60], imposing the ingoing boundary condition singles out the solution in (C.75) with positive sign.

The location of the the pseudo-horizon, denoted by $r_{\rm ph}$, is now obtained by solving the following algebraic equation

$$1 + B^2 h(r) - e^2 \frac{h(r)}{b(r)} \bigg|_{r=r_{\rm ph}} = 0 \ , \tag{C.77}$$

which then fixes the response-current

$$j = b(r) e^{2f(r)+4g(r)+2\Phi(r)} \big|_{r=r_{\rm ph}} \ . \tag{C.78}$$

The current in the dual field theory is proportional to this constant j, with the proportionality constant determined in (C.69). It is not particularly illuminating to present the formulae explicitly in terms of all the variables of the system; therefore we refrain from doing so. The formula above gives an N_f/N_c correction of the conductivity formula discussed in [90, 91]. Note that in [92] an analogous N_f/N_c correction to the conductivity formula has been obtained for a probe sector which is different from what we are discussing here. So, although in the limit of vanishing back-reaction, both our result and the result of [92] coincide with [90], the N_f/N_c correction is different.

As far as the possibility of a phase transition is considered, let us investigate (along the lines of [60]) the angular separation for the U-shaped embeddings. The angular separation in this case is given by

$$= 12c \int_{r_0}^{r_*} \frac{dr}{e^{g}\sqrt{b}} \frac{1}{\sqrt{e^{2f+6g+2\Phi}\left[b + h(B^2 b - e^2)\right] - 6c^2}} \ , \tag{C.79}$$

where

$$c = \frac{1}{\sqrt{6}} e^{f+3g+\Phi} \left[b + h\left(B^2 b - e^2\right)\right]^{1/2}\Big|_{r=r_0} \ . \tag{C.80}$$

It can be checked from the above expression that the large r_0 limit corresponds to large c limit. Our task is to investigate what happens to this angular separation as $c \to \infty$. Using the solutions in (C.7)-(C.11), it can be shown that in the limit $c \to \infty$ we get

$$= \int_1^{r_*/r_0} dy \, {}_1(y,\epsilon) - \frac{1}{r_0^4}\left(e^2 - B^2\right) \int_1^{r_*/r_0} dy \, {}_2(y,\epsilon) + \dots \ , \tag{C.81}$$

where we have defined $y = r/r_0$. Here we will not present the functional forms of ${}_1$ or ${}_2$ since they are not particularly illuminating; however, we will remark that the resulting integrals, performed over the variable y, are positive numbers. For large values of r_0, we can have two physically different regimes to consider: one where $r_* \gg r_0$ and one where $r_0 \sim r_*$. In the former regime, the angular separation tends to asymptote to a constant value and the behaviour is similar to what is discussed in [60]; however as r_0 increases, we enter the second regime and $\to 0$ eventually. Thus, in this case, irrespective of the relative magnitudes of the electric and the magnetic fields, there will always be a corresponding phase transition.

To make connection with our earlier work in [60] with a vanishing back-reaction, let us recall that there we found an upper limit on the electric field $e < B$, beyond which no phase transitions happen. We can recover this result from the above expression. To do so, let us set $\epsilon = 0$, which restores the conformal symmetry and we will have $r_*/r_0 \to \infty$ now. In that case, $< \sqrt{6}\pi/4$ for $e > B$ and therefore no phase transition takes place.

2.4.5 Including a chemical potential

There are two types of chemical potential we can introduce: U(1) (baryonic) and isospin[9]. We can explore their effect in both the back-reacted and non-back-reacted backgrounds. We find that the effects are very nearly the same in any of these cases, *i.e.* back-reaction does not significantly alter the results. Also an isospin chemical potential yields results that are qualitatively similar to the ones obtained in the U(1) case. Thus for simplicity, we will discuss the U(1) chemical potential case in the absence of back-reaction.

The canonical way to realize a chemical potential is to excite the time-component of the gauge field $A_t(r)$, which will give rise to a bulk field strength F_{tr}. The corresponding DBI action

---

[9] In this case, one will require two flavour branes. See *e.g.* [93] introducing an isospin chemical potential in the Sakai-Sugimoto model.

takes the form

$$S = \mathcal{N}_T \int drr^3 \left(1 + \frac{r^2}{6} b(r) \phi'^2 - a_t'^2\right)^{1/2} = \mathcal{N}_T \int dr \mathcal{L} \ , \tag{C.82}$$

$$b(r) = 1 - \left(\frac{r_H}{r}\right)^4 \ , \quad a_t := (2\pi\alpha') \, A_t \ . \tag{C.83}$$

Once again we remind the reader that we are considering the case when the back-reaction vanishes, *i.e.* $\epsilon = 0$ limit of the background in (C.7)-(C.11).

The equations of motion that result from the above action are given by

$$\left(\frac{r^2}{6}\right) \frac{r^3 b(r) \phi'}{\left(1 + \frac{r^2}{6} b(r) \phi'^2 - a_t'^2\right)^{1/2}} = c \ , \tag{C.84}$$

$$\frac{r^3 a_t'}{\left(1 + \frac{r^2}{6} b(r) \phi'^2 - a_t'^2\right)^{1/2}} = d \ , \tag{C.85}$$

where we have seen the constant c appear before and d denotes a new constant of motion. Before going further, let us discuss these equations in more details. Note that, in order for the U-shaped profiles to join smoothly at some $r = r_0$, we need to impose $\phi'(r_0) \to \infty$.[10] From the above equations of motion we can conclude that this condition leads to set $d = 0$ identically, or demand that $a_t'(r_0) \to \infty$ as well. In order to keep the norm of the bulk vector field F_{tr} finite, we conclude that for the U-shaped profiles we have $d = 0$ and they will not be affected by the inclusion of the chemical potential. This is expected on physical grounds since the bulk radial field has nowhere

---

[10] Note that, if we relax the condition $\phi'(r_0) \to \infty$, then the physics is richer. One will have to consider including explicit sources which can support the radial field strength on the U-shaped profiles. Usually there are two candidates for such sources: a baryon vertex and a bunch of fundamental string attached to the probe brane at r_0. The qualitative picture is similar to [94], which analyzes baryons in the Klebanov-Strassler set-up[57]. In the Klebanov-Witten case, we have one candidate for explicit source: a bunch of fundamental strings that stretch from $r = r_0$ to $r = r_H$. However, we will not discuss the physics when such explicit sources are included.

to go for the U-shaped profiles. On the other hand, for the parallel embeddings there will be a non-trivial gauge field.

For the parallel shaped case, the asymptotic behaviour of the gauge field takes the form

$$a_t(r) \simeq (2\pi\alpha')\mu - \frac{2d}{r^2} + \ldots \ , \tag{C.86}$$

where the constant μ is related to the chemical potential and the constant d is related to the charge density of the system. Let us denote the charge density in the probe sector by

$$\rho = \frac{\delta S}{\delta F_{rt}} \qquad \Longrightarrow \qquad \rho = (4\mathcal{N}_T)\,(2\pi\alpha')\,d \ , \tag{C.87}$$

where we have used the asymptotic expansion in (C.86) and the definition of S from (C.82). On the other hand, the chemical potential of the system can be obtained by

$$\mu = \frac{1}{2\pi\alpha'}\int_{r_H}^{\infty} a_t'(r)dr = \frac{d}{(2\pi\alpha')r_H^2}\,\frac{{}_2F_1\left(\frac{1}{3},\frac{1}{2};\frac{4}{3};-(d^2/r_H^6)\right)}{2} \ , \tag{C.88}$$

where we have utilized the solution of $a_t'(r)$ in terms of d from equation (C.85) and ${}_2F_1$ is a hypergeometric function. Our task henceforth will be to determine the favoured phase among the U-shaped and the parallel profiles. To determine this, we need to evaluate and compare the corresponding thermodynamic free energies of the individual phases. In this context, we can address this in two inequivalent ways, *i.e.* in grand canonical and canonical ensembles respectively.

2.4.5.1 Grand Canonical Ensemble

Let us first work in the grand canonical ensemble. If we take the action in (C.82) in its full generality and evaluate the corresponding variation on-shell, then we are left with the following boundary term

$$\delta S = \mathcal{N}_T\left[\frac{\partial\mathcal{L}}{\partial\phi'}\delta\phi + \frac{\partial\mathcal{L}}{\partial a_t'}\delta a_t\right]_{r_{\min}}^{r_{\max}} \ , \tag{C.89}$$

where $r_{\rm min}$ denotes the lowest point in the infrared, $r_{\rm max}$ denotes the UV-cutoff and $\mathcal{L}$ denotes the Lagrangian density in (C.82). Using the equations of motion in (C.84) and (C.85), we get

$$\delta S = \mathcal{O}_\phi \delta\left(\Delta\phi_\infty\right) + \mathcal{O}_\mu \delta\mu \ , \tag{C.90}$$

$$\mathcal{O}_\phi = \mathcal{N}_T c \ , \quad \mathcal{O}_\mu = \mathcal{N}_T \left(2\pi\alpha'\right) d \ , \tag{C.91}$$

which implies that the natural thermodynamic variables in the corresponding ensemble are $\Delta\phi_\infty$ and μ. This means that the on-shell action defines the corresponding Gibbs free energy in the grand canonical ensemble. The corresponding canonically conjugate variables are c, which is a condensate-like object, and d, which is related to the charge density *via* (C.87).

In the grand canonical ensemble it is straightforward to check that at finite temperature, the chiral symmetry restored phase is always favoured for any value of the chemical potential, which qualitatively is the same physics we observe at vanishing chemical potential as well [60]. In the absence of any back-reaction, we can only obtain a non-trivial phase structure after the inclusion of a magnetic field. This can be easily achieved as before, see *e.g.* equation (C.51). Introducing this field will deform the DBI Lagrangian and we will get

$$\mathcal{L} = r^3 \left(1 + \frac{r^2}{6} b(r) \phi'^2 - a_t'^2\right)^{1/2} \left(1 + B^2 L^4 / r^4\right)^{1/2} \ . \tag{C.92}$$

The analysis of the solutions proceeds as before and one can conclude that a non-trivial chemical potential will exist only for the parallel shaped case. For a fixed value of the chemical potential one can now explore the phase diagram, which is shown in fig. 2.8. From the phase diagram it is clear that the effect of magnetic catalysis observed in [60] for vanishing chemical potential survives here. Here we have presented only a representative diagram, but have checked explicitly that the qualitative behaviour remains similar for a wide range of values for the chemical potential.

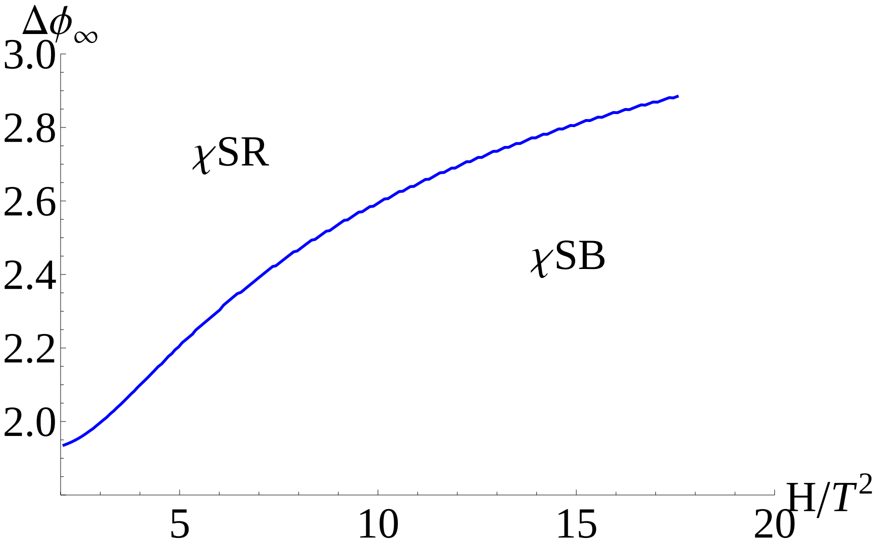

Figure 2.8: The phase diagram in the non-backreacted background with a U(1) chemical potential for $(2\pi\alpha')\mu = 1.0$ in the grand canonical ensemble.

Evidently, one can also explore the phase diagram (even without any magnetic field) resulting from the non-trivial dynamics once back-reaction is included. However we will not attempt this here, because, as should be noted, once the back-reaction is taken into account, the qualitative nature of fig. 2.8 will not change since we treat the back-reaction perturbatively. Thus, the physics will remain unchanged at the leading order.

2.4.5.2 Canonical Ensemble

Let us now switch gear and discuss the physics in the canonical ensemble, which is characterized by the charge density rather than the chemical potential. The corresponding free energy is the so called Helmholtz free energy that can be obtained by a Legendre transformation of the Gibbs free energy. In terms of the on-shell action of the probe, we now need to consider the following quantity (see *e.g.* [95])

$$\tilde{\mathcal{L}} = \mathcal{L} - \frac{\partial \mathcal{L}}{\partial a_t'} a_t' \ . \tag{C.93}$$

Clearly, since the U-shaped profiles do not support a non-trivial a_t', the Legendre transformation will change the corresponding free energy for the parallel shaped profiles only. It can be checked that in the canonical ensemble we have a non-trivial phase diagram when a non-zero charge density is introduced. We obtain a phase transition both at vanishing and at non-zero magnetic field. The corresponding diagram is shown in fig. 2.9. Moreover, we can also explore the physics in the presence of a magnetic field. A representative phase diagram in shown in fig. 2.5, which again demonstrates the effect of magnetic catalysis that we have observed and commented on several times by now. Before concluding this section let us remark that the inclusion of the back-reaction again does not have a significant effect on the qualitative physics, as expected.

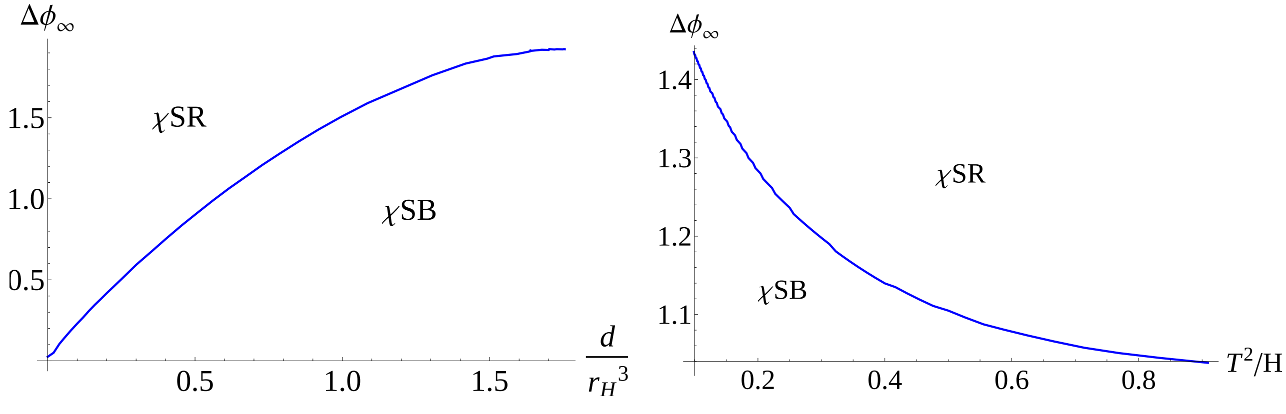

(a)

(b)

Figure 2.9: Panel (a): Phase diagram at vanishing magnetic field, in the canonical ensemble. Note that there is no corresponding phase transition in the grand canonical ensemble. Panel (b): A representative phase diagram in the presence of a magnetic field. Here we have fixed $d = 2$.

2.5 Discussion of results

In this chapter, we investigated various aspects of the back-reacted solution that we obtained in [68]. In keeping with our perturbative approach, we find that the physics is qualitatively similar to the original background both w.r.t. the back-reacted background and the additional probe sector. We observe the familiar magnetic catalysis effect[11], and the emergence of a pseudo-horizon in the probe sector. We also initiated a study of the corresponding phase structure introducing a chemical potential in this model.

There are various directions for future work. When the back-reaction is included, the presence of the phase transition in the additional probe sector demands a more thorough study of the model. This phase transition is perhaps signaling that we need to obtain backgrounds back-reacted by both the parallel and the U-shaped profiles and compare their energetics to decide whether the true picture is richer in physics. This is a rather intriguing possibility that we hope to address in the future.

For our current work, it was convenient to consider the additional probe sector and exciting various fields restricted to this sector. In principle, it should not be possible to distinguish between the additional probe sector and the back-reacting probe sector and thus what we have analyzed here is at best an approximate situation, however, it would be very instructive to consider the back-reaction including such worldvolume gauge fields: The back-reaction by a probe magnetic field will induce anisotropy in the system, a chemical potential will induce a charged black hole background, an electric field will induce a time-dependent background where

---

[11] See *e.g.* [96, 97, 98, 99] for similar effects in other models in the probe limit and in [100] beyond the probe limit.

the actual bulk event-horizon will be increasing with time. Such results would be exciting to further analyze and understand.

Note that our analysis of the model with the chemical potential is rather rudimentary in the sense that we did not include any source terms. We observed that the phenomenon of magnetic catalysis persists and is independent of the chemical potential. On the other hand, it has been observed in *e.g.* [101] that an inverse magnetic catalysis effect exists for the Sakai-Sugimoto model. It will be very interesting to see whether it is possible to find a similar physical effect in this model once sources are included. We leave such interesting research opportunities for future work.

Chapter 3

Instanton Crystals

3.1 Introduction

In this chapter, we investigate lattices of instantons. In a large class of holographic models of QCD, baryons are represented by instantons of the $U(N_f)$ gauge theory residing on the flavor branes. In this way, cold nuclear matter is represented by a crystalline lattice of instantons. We take the Sakai-Sugimoto model as a prototype model for our investigation. However, the same arguments could be applied for any holographic model in which baryons arise as instantons of the flavor gauge theory. The geometry as well as the dimensionality of the instanton lattice varies as the instanton density. At low to moderate densities, the baryons (or the flavor instantons) are confined to form a $3D$ lattice in the $x_4 = 0$ hyperplane. At high densities, the baryons are pushed out into the x_4 direction and form a $4D$ lattice. This $3D \to 4D$ transition is conjectured to be dual to the baryonic to quarkyonic phase transition of nuclear matter. In the baryonic phase, quarks are confined to individual baryons. In the quarkyonic phase, the quarks fill the Fermi sea but the excitations near the Fermi surface are not free quarks or holes but rather meson-like quark-hole pairs or baryon-like bound states of N_c quarks rather than free quarks or holes themselves.

Instead of trying to solve the $3D \to 4D$ transition, we focus our attention here on the $1D \to 2D$

transition as a first step in trying to solve the much more complicated problem. We put the instantons in a harmonic potential that rises at different rates along three of the four space coordinates. In terms of the $5D$ gauge coupling,

$$\frac{8\pi^2}{g_5^2} \quad = \quad N_c\lambda M \left(1 + \sum_{i=1}^{3} M_i^2 x_i^2 + O(M^4 x_{2,3,4}^4)\right) \tag{C.1}$$

with three independent parameters M_2, M_3 and M_4. Our investigations are in the regime $M_2 \ll M_3 \sim M_4$ but $M_3 < M_4$. Under this approximation, the instantons line up along the x_1 axis for low densities, or rather low external pressure. As we increase the pressure, the instanton lattice starts spreading out in the x_2 direction. Depending on the M_3/M_4 ratio, we obtain a rich variety of $2D$ crystalline lattices whose details we present below.

Apart from the motivation to use gauge/gravity duality to investigate the baryonic to quarkyonic phase transition, one could also view this work as the description of a hypothetical condensed matter system. There are limitations inherent to the large N_c limite of gauge/gravity duality that constrain us from accurately modeling the above mentioned phase transition. For example, in ordinary $N_c = 3$ QCD, cold nuclear matter forms a quantum liquid but for large N_c it becomes a crystalline solid since the ratio of the kinetic to potential energy decreases with N_c. Indeed, in the large N_c limit the two-baryon potential [105] becomes

$$\begin{aligned} V \quad \sim \quad & N_c \cdot A_C(r) + N_c \cdot A_S(r)(\mathbf{I}_1 \cdot \mathbf{I}_2)(\mathbf{J}_1 \cdot \mathbf{J}_2) \\ & + N_c \cdot A_T(r)(\mathbf{I}_1 \cdot \mathbf{I}_2)(3(\mathbf{n} \cdot \mathbf{J}_1)(\mathbf{n} \cdot \mathbf{J}_2) - (\mathbf{J}_1 \cdot \mathbf{J}_2)) + O(1/N_c) \end{aligned} \tag{C.2}$$

for some N_c-independent profiles $A_C(r)$, $A_S(r)$ and $A_T(r)$ for the central, spin-spin and tensor forces, with overall magnitudes $A \sim \Lambda_{QCD}$ for $r \sim 1/\Lambda_{QCD}$. Classically, such a potential tends to organize the baryons into a crystalline structure such that the distance between baryons is independent of N_c but the binding energy per baryon scales like $N_c O(\Lambda_{QCD})$. Quantum mechanically, the baryons in such a crystal oscillate in their potential wells with zero-point kinetic energies K, just as atoms in ordinary crystals

$$K \sim \frac{\pi}{2m_B d^2} \sim \frac{\Lambda_{QCD}}{N_c}\frac{1}{d^2} \tag{C.3}$$

where $d \sim 1/\Lambda_{QCD}$ is the N_c-independent diameter of the potential well. Consequently, at zero temperature the ratio of kinetic to potential energy scales as

$$\frac{K}{V} \sim \frac{1}{N_c^2} \tag{C.4}$$

which becomes very small as N_c grows large. At high enough temperature, the kinetic energies of the baryons does become larger, $K \sim T$, but in the confined phase we are constrained to $T < T_d < \Lambda_{QCD}$ so that $K < O(\Lambda_{QCD})$, in which case the ratio of kinetic to potential energy scales as

$$\frac{K}{V} \sim \frac{1}{N_c} \tag{C.5}$$

which is larger than $1/N_c^2$ but still tends to zero as N_c tends to infinity. Therefore, for large N_c neither zero-point quantum motion nor the thermal motion of baryons are able to melt the baryon crystal into a liquid, and the large N_c nuclear matter remains solid all the way upto the deconfining temperature.

Moreover, in gauge/gravity duality, we typically take not only the large N_c limit but also the large t'hooft coupling $\lambda = N_c g_{YM}^2$ limit. In this limit, the baryons become heavy[103]: in units of the mesonic mass scale $M \sim \Lambda_{QCD}$, the baryon mass is $M_b \sim \lambda N_c M$. On the other hand, the interactions between baryons do not grow with λ. Even for baryons very close to each other, the mutual repulsive potential is only $V \sim N_c M \sim M_b/\lambda$. The potential grows weaker as the distance between them grows large as the hard-core radius of a holographic baryon shrinks with λ as $R_b \sim M^{-1}\lambda^{-1/2}$. Outside of this radius, the repulsive potential decreases as $1/r^2$ until $r \sim M^{-1}$, at which point the potential becomes model dependent. In some cases, the potential becomes attractive for $r \sim M^{-1}$ while in others it remains repulsive for all values of r, as depicted below.

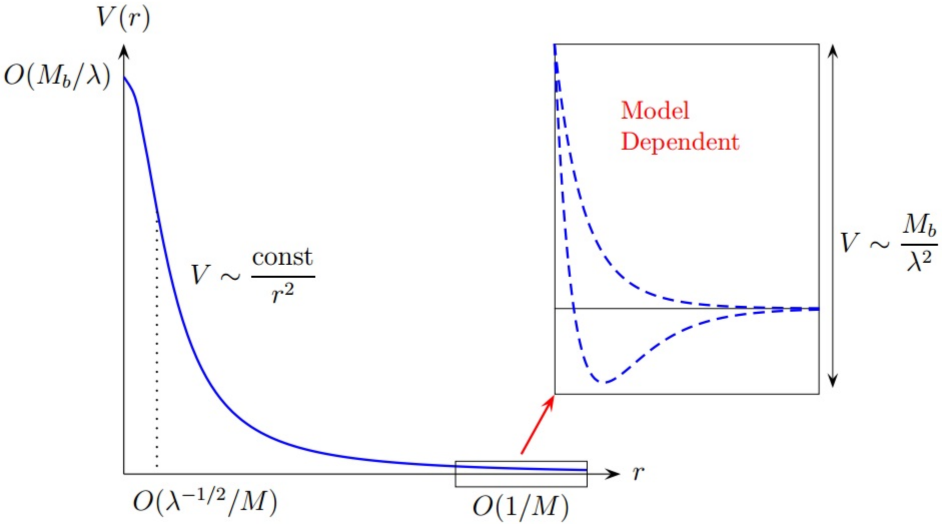

Figure 3.1: Two-body nuclear potential in holographic QCD.

Apart from nuclear matter, one could instead also take the approach of viewing this as a many-body problem. If we take $N_f = 2$ in the holographic model, we are essentially exploring lattices of $SU(2)$ instantons. The interactions between these instantons are stringy in origin, and depend not only on the positions of instantons in the physical space, but also on their orientation in the internal isospace. Moreover, the interaction energy of the instantons depend on a mixing of orientations in isospace and positions in physical space. This serves as an interesting many-body problem in its own right, and the techniques employed here may be applied to other types of non-abelian crystals. To make everything concrete, we specifically use the Sakai-Sugimoto model[106] although our considerations can be applied to a larger class of models.

3.2 Instantons in the Sakai-Sugimoto Model and their interactions

We now describe the Sakai-Sugimoto, or the $D4/D8$, model in some detail. Starting with the space $\mathbb{R}^{3,1} \times S^1 \times S^4 \times \mathbb{R}^+$ (radial coordinate), we place N_c coincident $D4$ branes spanning the Minkowski directions $\times S^1$. The circle has antiperiodic boundary conditions for the fermions which breaks the $\mathcal{N} = 4$ SUSY down to $\mathcal{N} = 0^\star$. In the field theory limit $\lambda \ll 1 \Rightarrow \Lambda_{QCD} \ll M_{KK}$ and the effective low-energy theory is pure $U(N_c)$ Yang-Mills. On the $\lambda \gg 1$ side of the duality, the $D4$ branes merge into a black brane which warps the $10D$ geometry. Instead of flat spacetime, we now have a warped product of $\mathbb{R}^{3,1}$ Minkowski space, the S^4 sphere (which originally surrounds the $D4$ branes), and a $2D$ cigar that spans the radial direction transverse to the brans, and finally the S^1 circle. The radial coordinate u runs from $u_\Lambda > 0$ to infinity. At u_Λ the S^1 shrinks to a point, hence the cigar shaped geometry. Altogether we have

$$ds^2 = \left(\frac{u}{R_{D4}}\right)^{3/2} \left[-dt^2 + \delta_{ij} dx^i dx^j + f(u) dx_4^2\right] + \left(\frac{R_{D4}}{u}\right)^{3/2} \left[\frac{du^2}{f(u)} + u^2 d\Omega_4^2\right] \tag{C.6}$$

with

$$\begin{aligned} F_4 &= 3\pi l_s^3 N_c \times \text{volume form}(S^4) \\ e^{\phi} &= g_s \left(\frac{u}{R_{D4}}\right)^{3/4} \end{aligned} \tag{C.7}$$

where x_4 was originally the coordinate along the S^1 circle but is now the polar angle on the $2D$ cigar,

$$\begin{aligned} R_{D4}^3 &= \pi g_s l_s^3 N_c \\ f(u) &= 1 - \left(\frac{u_\Lambda}{u}\right)^3 \end{aligned} \tag{C.8}$$

such that $l_s = \sqrt{\alpha'}$ is the string length scale and g_s is the string coupling, while u_Λ, which is the minimal value of the radial coordinate u at the tip of the cigar, is related to the original radius R of the S^1 circle as

$$2\pi R = \frac{4\pi}{3}\left(\frac{R_{D4}^3}{u_\Lambda}\right)^{1/2} \tag{C.9}$$

The 4D gauge coupling and hence also the t'Hooft coupling λ also depend on R. Analytically continuing from $\lambda \ll 1$ to $\lambda \gg 1$ we must have

$$\lambda = g_{4D}^2 N_c = \frac{g_{5D}^2}{2\pi R} N_c = \frac{2\pi g_s l_s}{R} N_c \tag{C.10}$$

Next, we add the flavor degrees of freedom by adding N_f D8 and anti-D8 branes in the probe approximation $N_f \ll N_c$. The flavor branes span the Minkowski space $\times S^4 \times$ a line on the 2D cigar. The topology of the cigar demands that the brane/anti-brane pair merge into a single brane at some point $u_0 \geq u_\Lambda$, which can be seen more explicitly from minimizing the brane action. The result is that the $U(N_f)_L \times U(N_f)_R$ symmetry breaks down to a diagonal $U(N_f)$ symmetry, resulting in chiral symmetry breaking, simlilar to the situation in the previous chapters.

As was the case there, the low energy dynamics of the flavor degrees of freedom living on the D8 branes is governed by the effective action consisting of the DBI + CS terms

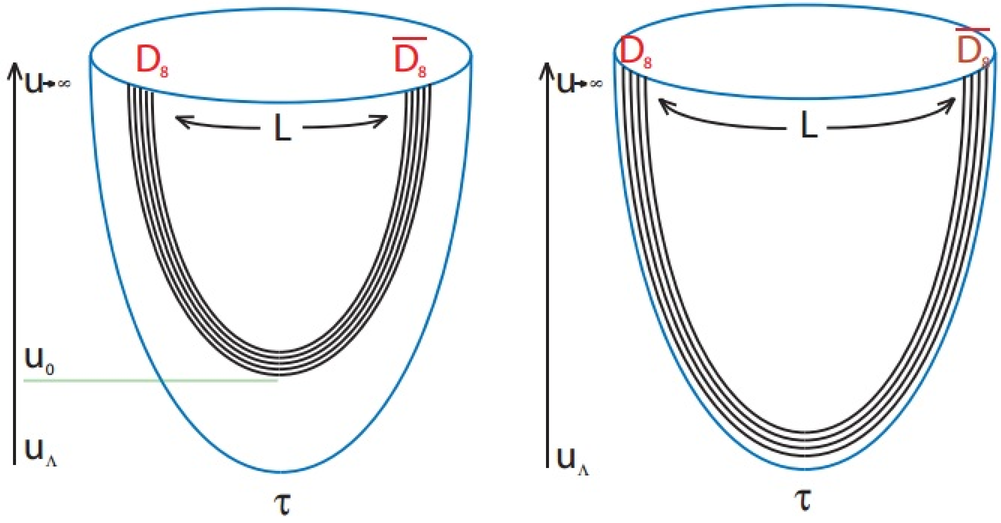

Figure 3.2: The U-shaped profile of the brane/anti-brane pair on the 2D cigar of the Sakai-Sugimoto model merging together to give rise to spontaneous breaking of chiral symmetry. The figure on the right depicts the antipodal configuration where the branes merge at the tip of the cigar $u = u_\Lambda$, while the figure on the left depicts the non-antipodal configuration where the branes merge at some point $u_0 > u_\Lambda$.

$$S = S_{DBI} + S_{CS} \tag{C.11}$$

where

$$S_{DBI} \;=\; T_8 \int_{D8+\overline{D8}} d^9x e^{-\phi} \mathrm{Str}\left(\sqrt{-\det(g_{mn} + 2\pi\alpha' \mathcal{F}_{mn})}\right) \tag{C.12}$$

where $T_8 = (2\pi)^{-p} l_s^{-(p+1)}$ is the D8 brane tension, g_{mn} is the 9-dim induced metric on the flavor brane, $\mathcal{F}_{mn}$ is the $U(N_f)$ gauge field strength, and Str denotes the symmetrized trace over flavor indices.

In the limit of fixed brane geometry and weak gauge fields, the DBI action reduces to the YM action

$$S_{DBI}[\mathcal{F}] \;=\; \text{const.} + S_{YM}[\mathcal{F}] + O(\mathcal{F}^4) \tag{C.13}$$

The low-energy field modes we are interested in are constant along the S^4 while the vector fields directions are transverse to the S^4. We therefore dimensionally reduce to 5 dimensions: the 4 Minkowski directions and a coordinate z along the U-shaped line of the cigar. It is convenient to choose a particular z coordinate that makes the 5D metric conformal

$$ds^2 \;=\; A(z)(-dt^2 + d\mathbf{x}^2 + dz^2), \;\; A(z) = \left(\frac{u(z)}{R_{D4}}\right)^{3/2} \tag{C.14}$$

In the (x^0, x^1, x^2, x^3, z) coordinates, the 5D YM action for the flavor gauge fields becomes

$$S_{YM} \;\approx\; \int d^4x \int dz \frac{1}{2g_{YM}^2(z)} \mathrm{tr}\left(\mathcal{F}_{mn}^2\right) \tag{C.15}$$

Besides the $U(N_f)$ gauge fields, the effective low-energy 5D theory also contains scalar fields $\Phi^a(x, z)$ that describes small fluctuations of the D8 branes in the transverse directions. These scalars form the adjoint multiplet of the $U(N_f)$ gauge symmetry. The action for these scalar fields follows from the DBI action for the pull-backed metric of the fluctuation branes. For the $\Phi(x,z)$ fields normalized to have similar kinetic energies to the vector fields, the scalar action is

$$\begin{aligned} S_{scalar} &= \int d^4x \int dz \frac{1}{2g^2_{YM}(z)} \mathrm{tr}\left((D_M\Phi)^2 + V(\Phi)\right) \\ &\quad + \frac{N_c}{16\pi^2} \int d^4x \int dz C(z) \mathrm{tr}\left(\Phi \mathcal{F}_{MN}\mathcal{F}^{MN}\right) \end{aligned} \tag{C.16}$$

For $C(z) \neq 0$, which characterizes the non-antipodal models, the second term leads to attractive nuclear forces[103]. Meanwhile, the Chern-Simons term arises from the couplings of the gauge fields on the D8 brane to the bulk RR field. In 9 dimensions,

$$S_{CS} = T_8 \int_{D8+\overline{D8}} C_3 \wedge \mathrm{tr} e^{2\pi\alpha'\mathcal{F}} \tag{C.17}$$

After integrating over the S^4 and dimensionally reducing to 5D, the CS term becomes

$$S_{CS} = \frac{N_c}{24\pi^2} \int_{5D} \mathrm{tr}\left(\mathcal{A}\mathcal{F}^2 - \frac{\imath}{2}\mathcal{A}^3\mathcal{F} - \frac{1}{10}\mathcal{A}^5\right) \tag{C.18}$$

In the case of $N_f = 2$, it is convenient to separate the $U(2)$ gauge fields $\mathcal{A}_M$ into their $SU(2)$ components A_M and the $U(1)$ components $\hat{A}_M$. In terms of these components, the CS action becomes

$$S_{CS} = \frac{N_c}{16\pi^2} \int \hat{A} \wedge \mathrm{tr} F^2 + \frac{N_c}{96\pi^2} \int \hat{A} \wedge \hat{F}^2 \tag{C.19}$$

The first term above implies that the instanton number density

$$I(x,z) = \frac{\epsilon^{\kappa\lambda\mu\nu} F^a_{\kappa\lambda} F^a_{\mu\nu}}{32\pi^2} \tag{C.20}$$

acts as electric charge density for the abelian field $\hat{A}_0$, so that the net electric charge of an instanton is $Q_{el} = N_c/2$.

To identify the instantons as baryons of the holographic model, we need to construct a baryon vertex. This is generally given by wrapping D_p branes on compact cycles carrying $O(N_c)$ Ramond-Ramond fluxes. In the Sakai-Sugimoto model, the baryon vertex is realized as a D4 brane wrapping the S^4, which carries N_c units of RR flux

$$\frac{1}{(2\pi)^3 l_s^3} \int_{S^4} F_4 \quad = \quad N_c \tag{C.21}$$

so the Chern-Simons coupling of this flux to the $U(1)$ gauge field $\mathcal{B}$ on the D4 brane world-volume acts as N_c units of the net electric charge for the B_0

$$T_4 \int_{D4} C_3 \wedge e^{2\pi\alpha' dB} \quad = \quad N_c \int B_0 dt \tag{C.22}$$

In a compact space such as the S^4, the net electric charge must equal zero. To cancel the above charge, we need to connect the D4 brane to open strings. The tail-end of an oriented open string carries charge -1, so we connect the D4 to the tail-end of N_c such open strings. The front-ends of the open strings connect to the D8 flavor branes and act as N_c quarks. For $N_f > 1$, each of the N_c strings connecting the vertex to the flavor branes possesses electric charge $1/N_f$ under the abelian $U(1)$ subgroup of the $U(N_f)$, so that the entire baryon has abelian charge N_c/N_f.

In principle, we could place the D4 brane anywhere on the cigar. However, the S^4 volume increases with the u coordinate and the brane action tends to pull it down to the cigar tip $u = u_\Lambda$. On the other hand, the strings connected to the baryon vertex tend to pull it towards the flavor D8 branes, competing against the gravity like force that tends to place the brane at the cigar tip. In some models, the forces reach equilibrium for the baryon vertex hanging on strings somewhere below the flavor branes, while in many others such as the non-antipodal Sakai-Sugimoto model (in which the D8 branes do not reach the cigar's tip but rather $u = u_0$) which we consider, the string forces win and pull the baryon vertex all the way to lowest point u_0 of the flavor branes.

In all such models, the baryonic vertex is a D_p brane completely embedded in a stack of D_{p+4} flavor branes, so it is equivalent to zero-radius Yang-Mills instanton of the $U(N_f)$ gauge symmetry of the flavor branes, and for $N_f > 1$ this could be smoothly inflated to finite-radius instanton[107, 108, 109, 110, 111]. In $p + 5$ dimensions of the flavor branes, this instanton is a D_p brane wrapping some compact cycle, and once we dimensionally reduce to 5 dimensions, the instanton becomes a finite size particle. Consequently, in the low-energy effective 5D theory, a baryon is realized as a finite-size instanton of the $U(N_f)$ gauge theory.

Correspondingly, a static system of N baryonss corresponds to a time-independent configuration of the non-abelian magnetic flavor fields $F^a_{\mu\nu}(\mathbf{x}, z)$ $(\mu, \nu = 1, 2, 3, z)$ of net instanton number N,

$$\int d^3\mathbf{x}dz \frac{\epsilon^{\kappa\lambda\mu\nu}}{16\pi^2}\mathrm{tr}(F_{\kappa\lambda}F_{\mu\nu}) \tag{C.23}$$

accompanied by the Coulomb electric $A^a_0(\mathbf{x}, z)$ and scalar $\Phi^a(\mathbf{x}, z)$ potentials induced by their CS and ΦFF couplings to the magnetic fields. The entire configuration should minimize the net DBI + CS energy of the system subject to the constraint (C.23).

Now the 5D gauge coupling is given by

$$\frac{1}{g^2_{YM}(z)} = \frac{N_c\lambda M_{KK}}{216\pi^3} \cdot \frac{u(z)}{u_\Lambda} \tag{C.24}$$

We have already noted that the baryon vertex resides at the bottom of the U-shaped flavor branes, $u = u_0$. In this region,

$$\frac{1}{g_{YM}^2(z)} \simeq \frac{N_c \lambda M_{KK}}{216\pi^3}\left(\zeta + \frac{8\zeta^3 - 5}{9\zeta} M_{KK}^2 z^2 + O(M_{KK}^2 z^4)\right) \tag{C.25}$$

To constrain the instantons to form 1 or 2 dimensional lattices in the (x_1, x_2) plane, we curve the x_2 and x_3 dimensions of the flavor brane similar to the $x_4 \equiv z$ coordinate. In terms of the effective 5D theory, this essentially corresponds to the 5D gauge coupling acquiring a dependence on the x_2 and x_3 directions as well as the $x_4 \equiv z$,

$$\frac{8\pi^2}{g_5^2(x)} = N_c \lambda M \left(1 + M_2^2 x_2^2 + M_3^2 x_3^2 + M_4^2 x_4^2\right) \tag{C.26}$$

Therefore, the gauge coupling acts as a harmonic potential for the instantons tends to align them along the x_1 axis. At higher densities, the instantons push away from the x_1 axis to form higher dimensional lattices.

Now, in principle, the net energy of a multi-instanton system could have significant n-body forces besides the 2-body force,

$$\xi^{net} = \sum_{n=1}^{N} \xi^{(1)}(n) + \frac{1}{2}\sum_{n\neq m=1,\ldots,N} \xi^{(2)}(n,m) + \frac{1}{6}\sum_{n\neq m\neq l=1,\ldots,N} \xi^{(3)}(n,m) + \ldots \tag{C.27}$$

Indeed, at very high densities such that the instanton cores overlap, we should expect all the n-body forces to have comparable strengths. However, it was shown in [102] that in the low-density regime where instantons are separated by distance much larger than their radii, the 2-body forces dominate the interactions while the higher n-body forces are smaller by powers of $(a/D)^2$, where

D is the inter-instanton distance, and a the radius. Consequently, in the regime $D \gg a$, which is what we work under, the net energy reduces to

$$E = \sum_{\mu=2,3,4} N_c \lambda M M_\mu^2 (X_n^\mu)^2 + \frac{1}{2}\left(\frac{2N_c}{5\lambda M}\right) \sum_{n \neq m} \frac{Q(n,m)}{|X_n - X_m|^2} \tag{C.28}$$

where $M \equiv M_4$ is a constant times M_{KK} and

$$Q(n,m) = \frac{1}{2} + \mathrm{tr}^2(Y_n^\dagger Y_m) + \sum_{\mu=2,3,4} C_\mu \left(\eta^a_{\mu\nu} N^\nu_{nm} \mathrm{tr}(Y_n^\dagger Y_m(-\imath\tau^a))\right)^2 \tag{C.29}$$

In the above, $\eta^a_{\mu\nu}$ is the 't Hooft tensor

$$\eta^a_{44} = 0, \;\; \eta^a_{4i} = -\delta^a_i, \;\; \eta^a_{i4} = \delta^a_i, \;\; \eta^a_{ij} = \epsilon^{aij}, \quad a, i, j = 1, 2, 3 \tag{C.30}$$

and

$$N^\mu_{nm} \equiv (\vec{N}_{nm}, N^4_{nm}) = \frac{X^\mu_n - X^\mu_m}{|X_n - X_m|} \tag{C.31}$$

while

$$C_\mu \equiv \frac{M_\mu^2}{M_4^2 + M_3^2 + M_2^2}, \;\; C_4 + C_3 + C_2 = 1 \tag{C.32}$$

and the Y_n are $SU(2)$ matrices specifying the instanton orientations (for $N_f = 2$). Note that only the relative orientations $Y_n^\dagger Y_m$ carry any physical significance, and the overall sign of $Y_n^\dagger Y_m$ does not matter. We work in the approximation $M_2 \ll M_3 \sim M_4$ (but $0 < M_3/M_4 < 1$), so that the instanton lattice originally forced by the harmonic potentials to line up along the X^1 axis push out in the X^2 direction to form 2D lattices. In this approximation, the first term in (C.28) reduces to $N_c \lambda M M_2^2 \sum_n (X_n^2)^2$. Moreover, for instantons confined to the (X^1, X^2) plane so that $N^\mu_{nm} = (\star, \star, 0, 0)$, Eq. (C.29) reduces to

$$\begin{aligned} Q(n,m) &= \frac{1}{2} + \mathrm{tr}^2\left(Y_n^\dagger Y_m\right) + C_3 \sum_{a=1,2} \mathrm{tr}^2\left(Y_n^\dagger Y_m(-\imath\tau_a)\right) \\ &\quad + (1 - 2C_3)\mathrm{tr}^2\left(Y_n^\dagger Y_m(-\imath\vec{\tau} \cdot \vec{N}_{nm})\right) \end{aligned} \tag{C.33}$$

It is evident from the above expression that the interaction energy of the instanton lattice depends not only on the instantons' position in the physical 2D space, but also on their orientations Y_n in the $SU(2)$ space. Moreover, the $Y_n^\dagger Y_m(\vec{\tau}\cdot\vec{N})$ term mixes the instantons' orientations in $SU(2)$ with their positions in the physical 2D space.

Let us conclude this section with the following observation. Suppose we consider a 1D lattice constrained to lie along the X^1 axis so that $N^\mu_{nm} = (\pm 1, 0, 0, 0)$. In this case, (C.29) reduces to

$$\begin{aligned} Q(n,m) &= \frac{1}{2} + \mathrm{tr}^2(Y_n^\dagger Y_m) + C_4 \mathrm{tr}^2(Y_n^\dagger Y_m(-\imath\tau_1)) \\ &\quad + C_3 \mathrm{tr}^2(Y_n^\dagger Y_m(-\imath\tau_2)) + C_2 \mathrm{tr}^2(Y_n^\dagger Y_m(-\imath\tau_3)) \end{aligned} \tag{C.34}$$

Under the assumption $M_4 > M_3 > M_2$ (and hence $C_4 > C_3 > C_2$), which we work with, the lowest energy configuration is for the relative orientation for an instanton pair (n,m) of $Y_n^\dagger Y_m = \pm\imath\tau_3$. If this orientation is unachievable, the next best option is a linear combination of $\imath\tau_3$ and $\imath\tau_2$. If this too is unachievable, the third best option is a linear combination all three $\imath\tau_3$, $\imath\tau_2$ and $\imath\tau_1$. In $SO(3)$ terms, this corresponds to a 180° rotation (or a $\pi/2$ rotation in $SU(2)$ terms) about a generic axis. Rotations other than 180° are energetically the least attractive option which an instanton pair would rather avoid unless forced upon by interactions with other instantons. Indeed, as will become obvious in the calculations, two instantons with similar orientations repel each other 9 times stronger than instantons at the same distance from each other but whose orientations differ by a 180° rotation.

3.3 Simulation

In this section, we present the results of the simulation we run to find the lowest-energy pattern of instanton orientations. Once we find all the patterns, we use them to form an ansatz for which we analytically calculate the interaction energy as a function of a few parameters. We focus exclusively on the 1D to 2D transition.

The instantons naturally want to spread out in three dimensions due to the Coulomb repulsion. In order to force them to form a 1D lattice, we may curve the x_2 and x_3 directions of the flavor brane similar to the $x_4 \equiv z$ direction. In terms of the effective $4+1$-dimensional theory, this corresponds to the 5D flavor gauge coupling gaining a dependence on these directions as well.

$$\frac{8\pi^2}{g_5^2(x)} \quad = \quad N_c \lambda M \left(1 + \sum_{i=1}^{3} M_i^2 x_i^2 + O(M^4 x^4)\right) \qquad \text{(C.35)}$$

The (inverse) gauge coupling (squared) therefore acts as a harmonic potential along the x_2, x_3 and x_4 directions. This tends to align the instantons along the x_1 direction so that indeed, for low enough densities, we only obtain a straight chain of instantons aligned along the x_1 direction. At higher densities, the Coulomb repulsion tends to push the instantons away from the x_1 axis to form more complicated 2D patterns. We choose $M_2 \ll M_3 \sim M_4$, but allow for different values for M_3 and M_4. As a result, the instantons push out towards the x_2 direction. We allow for general values of the ratio M_3/M_4, constrained to $0 \leq M_3/M_4 \leq 1$. In doing so, we obtain a rich variety of instanton crystals through the simulation.

To begin with, we do not assume any particular pattern for the orientations or rather the relative orientations $y_n^\dagger y_m$. Instead, we perform a numerical simulation to find what patterns might emerge. Typically, we use a lattice of about 200 instantons, each of which form the nodes of the lattice. We begin with completely arbitrary SU(2) matrix y_n for each instanton, apply an external pressure along the x_2 direction, and let the y_n evolve to a minimum of the energy function (C.28) according to

$$\frac{dy_n(t)}{dt} \quad = \quad -K\,\frac{\delta\xi}{\delta y_n} \tag{C.36}$$

where K is a constant mobility factor and the derivative with respect to the $SU(2)$ matrix y_n is defined as

$$\frac{\delta\xi}{\delta y_n} \quad \equiv \quad y_n\Big((-\imath\vec{\tau})\cdot\nabla_s\xi(y_n \to y_n(1+\imath\vec{s}\cdot\vec{\tau}))|_{\vec{s}=0}\Big) \tag{C.37}$$

We conclude each run when all the y_n have seemed to converge to their equilibrium values and their derivatives (C.36) become negligible. Strictly speaking, this method only allows us to obtain a local minimum of the energy function (C.28). However, after several runs for the same values of the relevant parameters, we may be reasonably confident that the patterns we obtain are indeed the lowest energy configurations for those values of the parameters.

Instead of the absolute orientations y_n at each node, what is physically relevant are the relative orientations between instantons $y_n^\dagger y_m$. These are represented by links between the instanton nodes. Within the energy function (C.28), the over all sign of the relative orientations $y_n^\dagger y_m$ does not carry any physical significance. Therefore, the moduli space we are really interested in is the space $S^3/\mathbb{Z}_2$. We would like to assign each distinct point in this space to some particular color. However the color RBG cube, which is homeomorphic to the 3-ball B^3 is topologically inequivalent to $S^3/\mathbb{Z}_2 \simeq \mathbb{RP}^3$, and so we cannot uniquely color each point in $S^3/\mathbb{Z}_2$. Instead, we employ various coloring schemes to illustrate different properties of the simulated patterns we find.

For Figs. 3.3, 3.5, 3.6, 3.10, 3.11 and 3.12, a relatively simple color scheme was employed in which we search for 180° twists about some axis. Red links represent twists around τ_1, blue around τ_2 and green around τ_3. For Figs. 3.7, 3.8 and 3.9 on the other hand, we emply a more complicated scheme, without which these phases might have been missed.

This scheme is as follows. Let (R, I, J, K) be the $(1, \tau_1, \tau_2, \tau_3)$ components of the $SU(2)$ twist $y_m^\dagger y_n$ respectively. Then the color of the link has

$$\begin{aligned}\text{Lightness:}\quad L &= 0.5 + 0.4(R^2 - K^2)\\ \text{Chroma:}\quad C &= I^2 + J^2\\ \text{Saturation:}\quad S &= C/\max(2L, 2-2L)\end{aligned}\tag{C.38}$$

Meanwhile the Hue depends on the J/I ratio. In the ‘absolute’ scheme,

$$\text{Hue:}\quad H = 2\text{ArcTan}(J/I) - 60^\circ \tag{C.39}$$

while in the ‘relative’ scheme,

$$\text{Hue:}\quad H = 2\text{ArcTan}(J/I) - 60^\circ - 2\text{ArcTan}(\Delta y/\Delta x) \tag{C.40}$$

In other words, the ‘absolute’ scheme colors the SU(2) twists between the two instantons with no knowledge of the link's direction in space, while the ‘relative’ scheme colors the SU(2) twists relative to the space direction of the link. In both these schemes, a 180° (or $\pi/2$ in $SU(2)$ terms) twist about the τ_3 axis is denoted by dark gray color, while a 180° twist about any axis perpendicular to the τ_3 axis is denoted by a bright saturated color whose hue indicates the axis's direction in the (τ_1, τ_2) plane, a 180° twist about some general axis is denoted by a saturated but darker color, and a trivial 0° (or 360°) twist is denoted by a very light gray. For Figs. 3.7, 3.8 and 3.9, we have used the 'absolute' scheme for illustrative purposes.

The simplest lattice we obtain in this way is the anti-ferromagnetic pattern aligned along the x_1 axis, which occurs for low enough values of the external pressure. For large enough M_3/M_4 but at low pressure, we observe a wave-like pattern periodically repeating itself after every 3 instantons. For low pressure and also low to moderate M_3/M_4 we observe two distinct types of zig-zag patterns following non-abelian orders. For high enough pressure, we observe a square pattern following a non-abelian order. For high enough pressure but higher M_3/M_4, we observe a triangular lattice following a non-abelian order. For high enough pressure and even higher M_3/M_4 we observe a square pattern following an anti-ferromagnetic order. These are depicted in the diagrams below. We find square patterns with increasingly many layers as we go to higher pressure. In addition, we also find non-abelian square patterns rotated by 45°, but these are not to be confused with the non-abelian triangular lattice.

In real life crystals, there may also be impurities such as crystalline defects, or edge effects. We encounter such impurities in our simulation. To get rid of the defects, we often resort to increasing the 'temperature' of the lattice so the instanton nodes can jostle around, and then let the whole lattice 'cool down' so that the instantons reassemble themselves into a more uniform lattice. This 'temperature' is *not* to be confused with the temperature that the lattice actually experiences. Instead, it is simply noise as written in the simulation code. The background we work with is in reality at zero temperature. We can often get rid of defects in this way, but we allow for the possibility of edge effects. Indeed, for the triangular non-abelian lattice, we form an ansatz for the edge effects and calculate the interaction energy which is generically different from the same lattice without any edge effects.

Figure 3.3: The anti-ferromagnetic chain in which all the instantons are aligned along the x_1 axis. In this coloring scheme, the green links represent 180° twists about the τ_3 axis.

Figure 3.4: A wave like pattern which periodically repeats itself after every three instantons. The links represent 180° twists about the τ_3 axis.

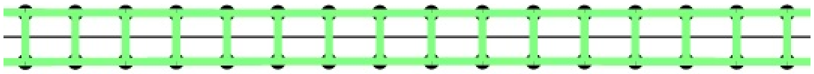

Figure 3.5: The Anti-Ferromagnetic Square lattice. In this coloring scheme, as in the case of the straight line and the period 3 wave, the green links represent 180° twists about the τ_3 axis.

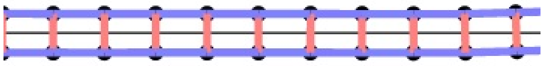

Figure 3.6: The Non-Abelian Square lattice in which all links represent a 180° twist albeit about different axes. In this coloring scheme, horizontal links represent twists about the τ_2 axis and vertical links about the τ_1 axis.

Figure 3.7: Non-Abelian Zig-Zag pattern. In this coloring scheme, both kind of diagonal links are 180° twists, but the direction of rotation alternates between two different axes in the (12) plane.

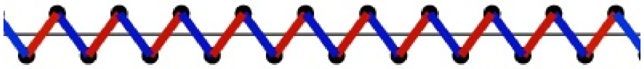

Figure 3.8: Another Non-Abelian Zig-Zag pattern. In this coloring scheme, both kind of diagonal links are 180° twists, but the direction of rotation no longer lie in the (12) plane.

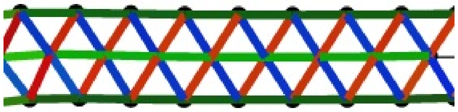

Figure 3.9: Triangular pattern following a non-abelian order.

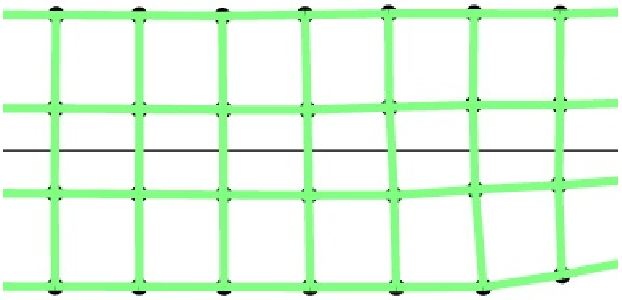

Figure 3.10: Square Anti-ferromagnetic lattice with three layers.

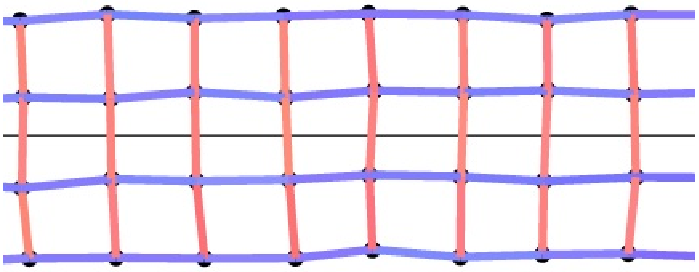

Figure 3.11: Square Non-Abelian lattice with three layers.

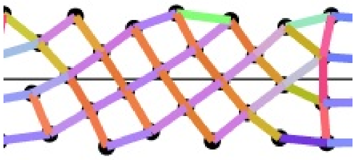

Figure 3.12: Square Non-Abelian pattern rotated by 45°.

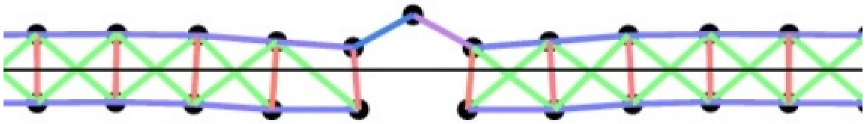

Figure 3.13: A crystalline defect observed in the simulation of a Square Non-Abelian lattice.

3.4 Thin Crystals

In this section, we explore crystals that extend infinitely long along the x_1 axis but typically a few layers along the x_2 direction. Based on the results of the simulation, we form ansatz for the instanton orientations for each of the various patterns we find. The simplest pattern we found is a 1D chain, in which neighboring instantons undergo a 180° (in $SO(3)$ terminology which really corresponds to $\pi/2$ in $SU(2)$ terminology) twist about the τ_3 axis.

$Y_1 \quad Y_2 \quad Y_1 \quad Y_2 \quad Y_1 \quad Y_2 \quad ...$

where $Y_1 = \pm 1$, $Y_2 = \pm \imath\tau_3$. For instantons labelled by n and m, we have that $|X_n - X_m| = (n-m)D$, where D is the distance between any two neighboring instantons. For odd $n-m$, we have $Y_n^\dagger Y_m = \pm\imath\tau_3$ so that using Eq. (C.29), we find $Q = 1/2$. On the other hand, for even $n-m$, we have $Y_n^\dagger Y_m = \pm 1$ so that in this case $Q = 9/2$. This illustrates the general rule that instantons having the same orientation will repel each other 9 times stronger than those differing by a relative orientation of 180° about some axis (in this case the τ_3 axis, which is the most favored one), for the same physical separation. We define $F \equiv \sum_{n\neq m} Q(n,m)/|X_n - X_m|^2$, and for this lattice we have

$$\begin{aligned} F &= \frac{1}{2}\sum_{n\ odd}\frac{1}{(nD)^2} + \frac{9}{2}\sum_{n\ even}\frac{1}{(nD)^2} \\ &= \frac{\pi^2}{2D^2} \end{aligned} \tag{C.41}$$

In general, the F function for other lattices will have the form $\pi^2/2D^2+$ other terms.

The non-abelian zigzag pattern # 1 (NAZ1) follows the arrangement such that the relative orientation between neighboring instantons is through an 180° angle, but the direction of rotation alternates between two different axes in the (τ_1, τ_2) plane, one axis for the odd-numbered instantons and the other for even-numbered ones. In $SU(2)$ terms,

$$\begin{aligned} Y_{2k}^{\dagger} Y_{2k+1} &= \exp\left(\frac{\imath\pi}{2}\vec{n}_e \cdot \vec{\tau}\right) = \imath\vec{n}_e \cdot \vec{\tau} = \imath A\tau_1 + \imath B\tau_2 \\ Y_{2k+1}^{\dagger} Y_{2k+2} &= \exp\left(\frac{\imath\pi}{2}\vec{n}_o \cdot \vec{\tau}\right) = \imath\vec{n}_o \cdot \vec{\tau} = \imath A\tau_1 - \imath B\tau_2 \end{aligned} \tag{C.42}$$

for some $A, B \neq 0$ such that $A^2 + B^2 = 1$.

On the other hand, the non-abelian zigzag pattern # 2 (NAZ2)follows the pattern such that the relative orientation between neighboring instantons is always through a 180° angle, but this time the direction of rotation alternates between two different axes that are no longer constrained to just the (τ_1, τ_2) plane. In $SU(2)$ terms,

$$\begin{aligned} Y_{2k}^{\dagger} Y_{2k+1} &= \imath A\tau_1 + \imath B\tau_2 + \imath C\tau_3 \\ Y_{2k+1}^{\dagger} Y_{2k+2} &= \imath A\tau_1 - \imath B\tau_2 + \imath C\tau_3 \end{aligned} \tag{C.43}$$

where $A, B, C \neq 0$ such that $A^2 + B^2 + C^2 = 1$.

Both the zigzag patterns can be fit into a single ansatz

$$\begin{aligned} Y_n &= \exp\left(\imath n\frac{\phi}{2}\tau_2\right) \times \exp\left(\imath\left(\frac{\alpha}{2} + (-1)^n\frac{\beta}{2}\right)\tau_1\right), \\ Y_n^{\dagger} Y_{n+1} &= \cos\frac{\phi}{2}\cos\beta \times 1 - (-1)^n\cos\frac{\phi}{2}\sin\beta \times \imath\tau_1 \\ &\quad +\sin\frac{\phi}{2}\cos\alpha \times \imath\tau_2 + \sin\frac{\phi}{2}\sin\alpha \times \imath\tau_3 \end{aligned} \tag{C.44}$$

for some angles ϕ, α and β. The NAZ1 phase is characterized by $0 < \phi < \pi$, $\alpha = 0$, $\beta = \pi/2$, while the NAZ2 phase is characterized by $0 < \phi < \pi$, $0 < \alpha < \pi/2$, $\beta = \pi/2$. The F function for such a lattice was already calculated in [102], and here we present the result

$$\begin{aligned} F \;=\; & \frac{\pi^2}{4D^2}\left[\frac{3}{2}+\left(-1+C_3(\cos^2\alpha\cos^2\beta+\sin^2\alpha\sin^2\beta)\right)\cdot\Sigma_0(\phi)\right. \\ & +\left(\frac{5}{2}+\cos^2\alpha-\sin^2\beta\right)\cdot\Sigma_1(\nu)+\left(2-\cos^2\alpha-\sin^2\beta\right)\cdot\Sigma_2(\phi,\nu) \\ & +(1-2C_3)(\sin^2\beta-\cos^2\alpha)\cdot\Sigma_3(\nu) \\ & +(1-2C_3)(\sin^2\beta+\cos^2\alpha)\cdot\Sigma_4(\phi,\nu) \\ & \left.+2(2C_3-1)\cos\alpha\sin\beta\cdot\Sigma_5(\phi,\nu)\right] \end{aligned} \tag{C.45}$$

where $\nu = L/2D$, such that D is the distance between neighboring instantons in any one layer (upper or lower), while L is the vertical distance between the upper and lower layers of the zigzag pattern, and the Σ_i are given by

$$\begin{aligned} \Sigma_0 &= \frac{4\phi(\pi-\phi)}{\pi^2} \\ \Sigma_1 &= \frac{\tanh(\pi\nu)}{\pi\nu} \\ \Sigma_2 &= \frac{\sinh((\pi-2\phi)\nu)}{(\pi\nu)\cosh(\pi\nu)} \\ \Sigma_3 &= \frac{1}{\cosh^2(\pi\nu)} \\ \Sigma_4 &= \frac{\cosh(2\phi\nu)}{\cosh^2(\pi\nu)}-\frac{2\phi}{\pi}\cdot\frac{\cosh((\pi-2\phi)\nu)}{\cosh(\pi\nu)} \\ \Sigma_5 &= \frac{\sinh(2\phi\nu)}{\cosh^2(\pi\nu)}+\frac{2\phi}{\pi}\cdot\frac{\sinh((\pi-2\phi)\nu)}{\cosh(\pi\nu)} \end{aligned} \tag{C.46}$$

The F functions for the rest of the lattices we obtain are calculated in Appendix A. Here, we gather the main results.

First, the wave-like pattern periodic after every 3 instantons consists of the following pattern

$$\begin{array}{cccccccccccccc}
Y_1 & & & Y_2 & & & Y_1 & & & Y_2 & & .. & & \\
& Y_2 & & & Y_1 & & & Y_2 & & & Y_1 & & .. & \\
& & Y_1 & & & Y_2 & & & Y_1 & & & Y_2 & & ..
\end{array}$$

where $Y_1 = \pm 1$ and $Y_2 = \pm \imath \tau_3$. For this lattice arrangement, we have

$$F[P3] = \frac{\pi^2}{18D^2} + \frac{\pi}{3DL} \left(\frac{2\sinh(\nu)}{3} \cdot \frac{5\cosh(\nu) - 2}{\cosh^2(\nu) - \frac{1}{4}} + \frac{\sinh(2\nu)}{6} \cdot \frac{5\cosh(2\nu) - 2}{\cosh^2(2\nu) - \frac{1}{4}} \right) \tag{C.47}$$

for $\nu = \pi L/3D$. Generically, ν is the (inverse) aspect ratio L/D times some constant, whose definition we change according to convenience for the various lattices.

The square anti-ferromagnetic lattice consists of the following pattern

$$\begin{array}{ccccccccccc}
Y_1 & Y_2 & Y_1 & Y_2 & Y_1 & Y_2 & Y_1 & Y_2 & Y_1 & Y_2 & .. \\
Y_2 & Y_1 & Y_2 & Y_1 & Y_2 & Y_1 & Y_2 & Y_1 & Y_2 & Y_1 & .. \\
Y_1 & Y_2 & Y_1 & Y_2 & Y_1 & Y_2 & Y_1 & Y_2 & Y_1 & Y_2 & ..
\end{array}$$

where $Y_1 = \pm 1$ and $Y_2 = \pm \imath \tau_3$. With two lines of instantons, this lattice arrangement has

$$F_{2-lines}[\Box AF] = \frac{\pi}{2DL} \left(2\nu + \frac{5\cosh(2\nu) - 4}{\sinh(2\nu)} \right) \tag{C.48}$$

where $\nu = \pi L/D$. For three lines, we have

$$F_{3-lines}[\Box AF] \;=\; \frac{\pi^2}{2D^2}\left(1+\frac{17\coth(\nu/2)+81\tanh(\nu/2)}{12\nu}+\frac{\tanh(\nu)}{6\nu}\right) \tag{C.49}$$

and more generally, for N lines, we have

$$F_{N-lines}[\Box AF] \;=\; \frac{\pi^2}{2D^2}+\sum_{k=1}^{N-1}\frac{2(N-k)}{N}\cdot\frac{\pi}{2DkL}\left[\frac{5\cosh(k\nu)+4(-1)^k}{\sinh(k\nu)}\right] \tag{C.50}$$

The square non-abelian lattice consists of the following pattern:

$$\begin{array}{ccccccccc}
Y_1 & Y_2 & Y_1 & Y_2 & Y_1 & Y_2 & Y_1 & Y_2 & .. \\
Y_3 & Y_4 & Y_3 & Y_4 & Y_3 & Y_4 & Y_3 & Y_4 & .. \\
Y_1 & Y_2 & Y_1 & Y_2 & Y_1 & Y_2 & Y_1 & Y_2 & ..
\end{array}$$

where $Y_1 = \pm 1,\ Y_2 = \pm\imath\tau_2,\ Y_3 = \pm\imath\tau_1,\ Y_4 = \pm\imath\tau_3$. With two lines of instantons, this lattice has

$$F_{2-lines}[\Box NA] \;=\; \frac{\pi^2}{2D^2}\left[2C_3+1+\frac{2C_3-1}{\sinh^2(\nu)}+\frac{5\coth(\nu)+\tanh(\nu)}{4\nu}\right] \tag{C.51}$$

where $\nu = \pi L/2D$. For three lines,

$$\begin{aligned} F_{3-lines}[\Box NA] \;&=\; \frac{\pi^2}{2D^2}\left[(2C_3+1) + \frac{2}{3}(2C_3-1)\left(\frac{2}{\sinh^2(\nu)} + \frac{1}{\cosh^2(2\nu)}\right)\right. \\ &\qquad\qquad \left. + \frac{49\mathrm{coth}(\nu) + 17\mathrm{tanh}(\nu) + 10\mathrm{tanh}(2\nu)}{24\nu}\right] \end{aligned} \tag{C.52}$$

and more generally for N lines,

$$\begin{aligned} F_{N-lines}[\Box NA] \;&=\; (1+2C_3)\frac{\pi^2}{2D^2} \\ &\qquad + \sum_{k=1}^{N-k} \frac{2(N-k)}{N} \cdot F_k[\Box NA] \end{aligned} \tag{C.53}$$

where

$$\begin{aligned} F_k[\Box NA] \;&=\; \frac{\pi}{4DkL}\Big([7+2(-1)^k]\mathrm{coth}(k\nu) + [3+2(-1)^k]\mathrm{tanh}(k\nu)\Big) \\ &\qquad + \frac{\pi^2}{D^2} \cdot \frac{(2C_3-1)}{\cosh(2k\nu) + (-1)^k} \end{aligned} \tag{C.54}$$

The triangular non-abelian lattice consists of the following pattern:

$$\begin{array}{ccccccccccccccc} & Y_3 & & Y_4 & & Y_3 & & Y_4 & & Y_3 & & Y_4 & .. & & \\ Y_1 & & Y_2 & & Y_1 & & Y_2 & & Y_1 & & Y_2 & & Y_1 & .. & \\ & Y_4 & & Y_3 & & Y_4 & & Y_3 & & Y_4 & & Y_2 & .. & & \end{array}$$

where

$$\begin{aligned} Y_1 &= \pm 1 \\ Y_2 &= \pm \imath \tau_3 \\ Y_3 &= \pm \frac{\imath}{\sqrt{2}}(\tau_1 - \tau_2) \\ Y_4 &= \pm \frac{\imath}{\sqrt{2}}(\tau_1 + \tau_2) \end{aligned} \tag{C.55}$$

With three lines, this lattice has

$$F_{3-lines}[\triangle NA] = \frac{\pi^2}{2D^2}\left[1 + \frac{\coth(\nu) + 49\tanh(\nu)}{6\nu} + \frac{16(2C_3 - 1)\sinh(\nu)}{3\cosh^2(\nu)}\right] \tag{C.56}$$

where $\nu = \pi L/D$. More generally, for N lines we have

$$\begin{aligned} F_{N-lines}[\triangle NA] = \frac{\pi^2}{2D^2} + \sum_{k=1}^{N-1} \frac{2(N-k)}{N} \Big[&(k \bmod 2) \cdot F_{k\ odd}[\triangle NA] \\ &+ ((k+1) \bmod 2) \cdot F_{k\ even}[\triangle NA] \Big] \end{aligned} \tag{C.57}$$

where

$$F_{k\ even}[\triangle NA] = \frac{\pi}{2DkL}\left[\frac{5\cosh(k\nu) + 4(-1)^{k/2}}{\sinh(k\nu)}\right] \tag{C.58}$$

and

$$F_{k\ odd}[\triangle NA] = \frac{\pi}{2DkL}\Big(5 + 4k\nu(-1)^{\frac{k+1}{2}}(1 - 2C_3)\mathrm{sech}(k\nu)\Big)\tanh(k\nu) \tag{C.59}$$

A treatment of the triangular lattice with edge effects is also presented in Appendix A.

3.5 Infinite Crystals

In this section, we present the results for lattices extending for infinite extent in both the x_1 and x_2 directions. Nevertheless, in practice, we have to cutoff one of the directions at some width W. For simplicity we assume that the (inverse) aspect ratio $L/D = 1$. The calculations are presented in Appendix B, and here we simply gather the main results. Instead of presenting the F functions, we directly write the net interaction energy of the lattice per instanton, ξ.

For the square anti-ferromagnetic lattice, we have

$$\xi[\square AF] \;=\; \frac{\pi N_c}{\lambda M D^2}\left(\log\frac{W}{D} + \gamma_E + A\right) \tag{C.60}$$

where γ_E is the Euler Gamma constant and $A \approx 0.247$.

For the square non-abelian lattice, we have

$$\xi[\square NA] \;=\; \frac{\pi N_c}{\lambda M D^2}\left(\log\frac{W}{D} + \gamma_E + R_1 - R_2\zeta\right) \tag{C.61}$$

where R_1 and R_2 are numerical constants

$$\begin{aligned} R_1 &\approx 0.389 \\ R_2 &\approx 0.438 \end{aligned} \tag{C.62}$$

and

$$\zeta \;=\; 1 - 2C_3 = \frac{M_4^2 - M_3^2}{M_4^2 + M_3^2} \tag{C.63}$$

while for the triangular non-abelian lattice, we have

$$\xi[\triangle] \;=\; \frac{\pi N_c \rho}{\lambda M} \cdot \left(\log(W\sqrt{\rho}) + \gamma_E + T_1 - T_2\zeta\right) \tag{C.64}$$

where the constants T_1 and T_2 are

$$\begin{aligned} T_1 &\approx 0.3319 \\ T_2 &\approx 0.3252 \end{aligned} \tag{C.65}$$

A comparison of the energetics of these three lattices is presented in Appendix B.

3.6 Phase Diagram

In order to stabilize the instanton density ρ, we need to supply an external pressure P which acts as a compressive force in the x_1 direction. It could be argued that one could instead simply constrain the overall volume of the lattice of instantons. However, this approach has problems. As an analogous situation, consider a fluid governed by a Van-der-Waals equation of state. Up to some upper bound, this equation allows for a uniform fluid to have any density. However, at sub-critical temperatures one could have a low-density gas or a high-density liquid, but no uniform fluid with intermediate densities. Instead, we find some domains with high-density liquid while others with low-density gas. For instantons, we could fix the length of the fluid to some amount V such that the average density $\rho = N/L$ falls into the intermediate range, however we would then have L split into domains of two different lattices, one denser than N/L and the other less dense, as this configuration would then minimize the energy.

In order to keep ρ uniform for the instanton lattice then, we instead control the P (or the net compression force $\mathbf{F}$) rather than the lattice spacing D or the net length L. Therefore, the phase diagram follows from minimizing the free enthalpy $G = E - ST + \mathbf{F}L$ rather than the internal energy E. But since our background is at $T = 0$, what we really need is the ordinary enthalpy $H = E + \mathbf{F}L$, or in our case $H = E + P \times \text{Length}$. Equivalently, we minimize the non-relativistic chemical potential

$$\begin{aligned}
\hat{\mu} &= \mu_{rel} - M_{baryon} \\
&= \xi(\rho, \nu, \mathcal{M}) + \frac{P}{\rho} \\
&= \frac{P}{\rho} + N_c \lambda M M_2^2 \frac{\nu^2}{\rho^2} + \frac{N_c}{5\lambda M} \rho^2 k F(\nu, \mathcal{M}, C_3) \qquad \text{(C.66)}
\end{aligned}$$

Note that in the above we define $\nu = L/D$ where L is the RMS x_2 amplitude, whereas in the preceding calculations, we have typically taken ν to be some constant that depends on the lattice geometry times L/D. The above expression is to be understood as absorbing that overall factor into the constant k.

At fixed external pressure P, the entire system seeks to minimize the chemical potential (C.66) with respect to all the parameters of the lattice geometry. The $\mathcal{M}$ parameters constitute all the parameters other than the linear density ρ and the RMS x_2 amplitude $L = \nu/\rho$. We minimize the chemical potential with respect to the $\mathcal{M}$ parameters at fixed ν, so that the optimal values of the $\mathcal{M}$ parameters becomes function of ν. As the ν parameter changes in response to the external pressure P, the $\mathcal{M}$ parameters change accordingly, $\mathcal{M} = \mathcal{M}(\nu(P))$.

Next, in the case $\nu = 0$, the lattice is simply a straight line. For any $\nu > 0$, minimizing the chemical potential with respect to ν requires

$$\rho = \rho(\nu) = \left[\sqrt{10}\lambda M M_2\right]^{1/2} \left[-\frac{k}{\nu}\frac{\partial F}{\partial \nu}\right]^{-1/4} \qquad \text{(C.67)}$$

Minimizing with respect to the density ρ requires

$$P = \frac{kN_c}{5\lambda M} 2\rho^3 \cdot F(\nu) - (N_c \lambda M M_2^2) \frac{2\nu^2}{\rho} \tag{C.68}$$

In order to determine ν and ρ as functions of the external pressure P we should solve the combined equations (C.67) and (C.68). It could occur that (C.67) and (C.68) have multiple solutions for $\nu(P)$ and $\rho(P)$. In such a situation, we choose the solution which has the lowest value for

$$\hat{\mu} = \frac{3kN_c}{5M\lambda} \rho^2 F(\nu, \mathcal{M}, C_3) - (N_c \lambda M M_2^2) \frac{\nu^2}{\rho^2} \tag{C.69}$$

which follows from combining (C.66) and (C.68). Using these rules, we obtain the phase diagram.

In the following figures,

Z, Z' : Two layer zigzags, Z represents NAZ1, while Z' represents NAZ2.

$\blacksquare n$: Square lattice, n-layer regular slice, anti-ferromagnetic orientations.

$\Box n$: Square lattice, n-layer regular slice, non-abelian orientation.

$\Diamond n$: Square lattice, n-layer diagonal slice, non-abelian orientation.

$\triangle n$: Triangular lattice, n layers, non-abelian orientation.

Black lines between phases indicate first order phase transitions while white lines indicate second order phase transitions. Gray areas on the third diagram do not correspond to any stable uniform lattices.

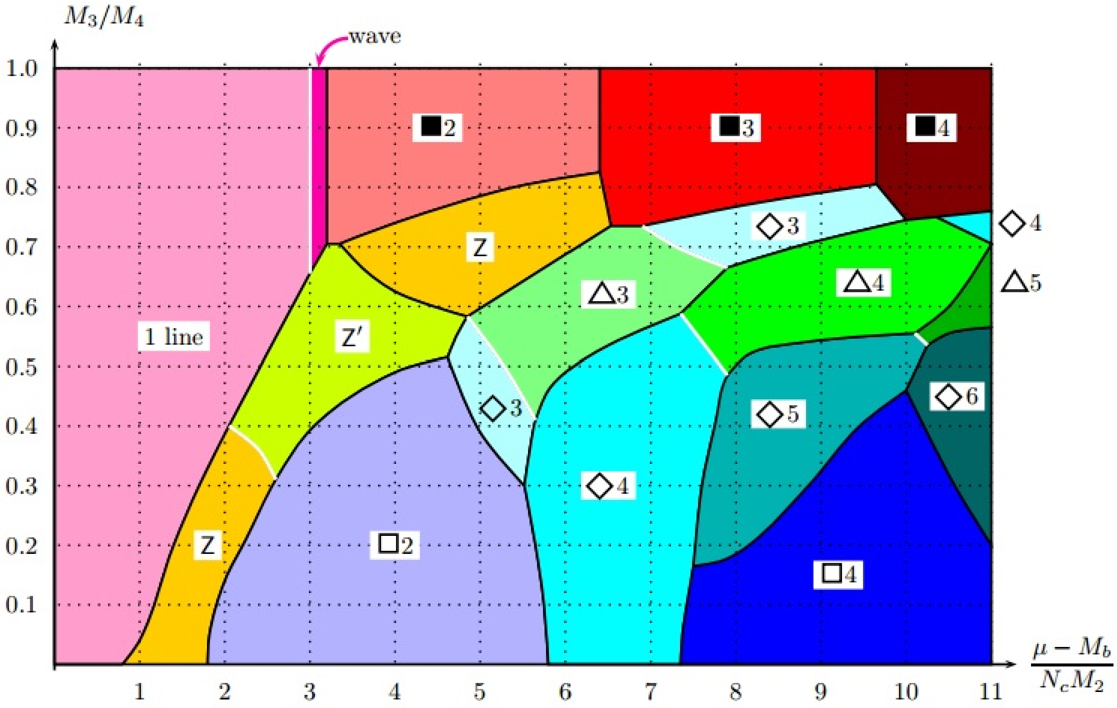

Figure 3.14: M_3/M_4 vs. non-relativistic chemical potential $\hat{\mu}$ (in units of $N_c M_2$).

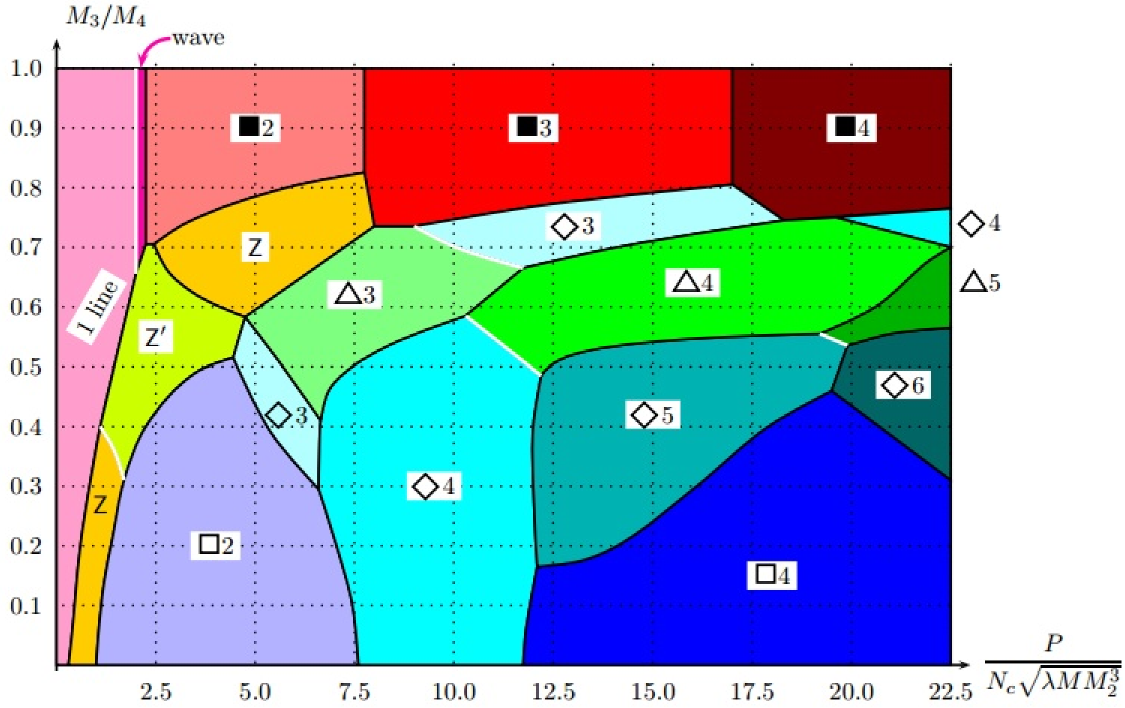

Figure 3.15: M_3/M_4 vs. 1D pressure P (in units of $N_c\sqrt{\lambda M M_2^3}$).

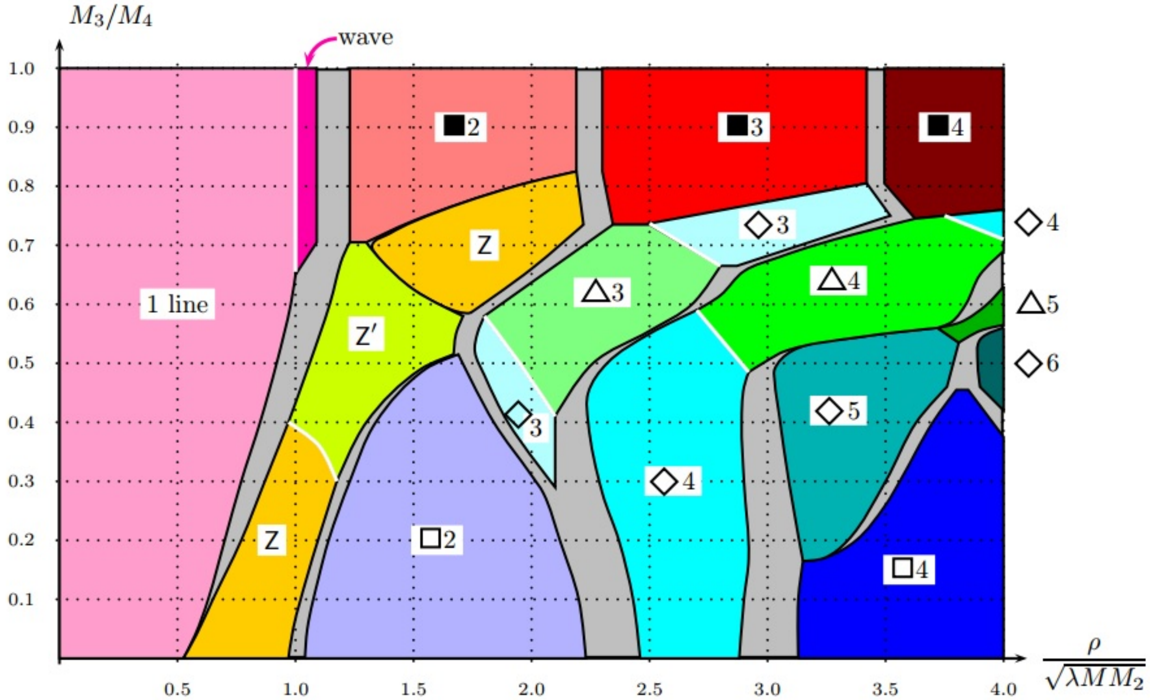

Figure 3.16: M_3/M_4 vs. linear density ρ (in units of $\sqrt{\lambda M M_2}$).

3.7 Conclusion and Outlook

We have investigated 1D and 2D lattices of $SU(2)$ instantons whose interactions arise from the gauge/gravity duality in a string theory setting. An obvious next step is to generalize this exploration to higher dimensional instanton lattices, 3D and eventually the 4D. Indeed, from the perspective of understanding the baryonic to quarkyonic phase transition of nuclear matter, it is the 3D to 4D transition that is ultimately conjectured to be dual to this phase transition. Another direction one could take is to generalize these results from $N_f = 2$ to $N_f = 3$. In such a case, the instantons would also acquire non-abelian electric charges in addition to the abelian electric charge [102].

Seen as a description of a hypothetical condensed matter system however, one could ask another question. The interaction energy of the crystalline lattice we have investigated was schematically of the form

$$\begin{aligned} E \;\sim\;& A(r) + B(r)(\text{relative orientation}) \\ & + C(r)\Big((\text{relative orientation}) \cdot (\text{distance in physical space})\Big) \end{aligned} \tag{C.70}$$

where $A(r)$, $B(r)$ and $C(r)$ are terms that generically depend on the relative distance between interacting objects. Can the techniques we have developed here describe other systems that schematically carry this form for the energy? Can the system we describe here, or some close cousin of it, be realized experimentally in the lab? We leave these as open questions to be explored in the future.

This material is based upon work supported by the National Science Foundation under Grant Number PHY-1316033.

3.8 Appendix A: Thin Crystals

In this section, we calculate the net energies of the various instanton chains we have encountered earlier. Recall that the energy of a general 2D configuration of instantons in a background characterised by $M_2 \ll M_3 \sim M_4$ is given by

$$E = N_c \lambda M M_2^2 \sum_n (X_n^2)^2 + \frac{N_c}{5\lambda M} \sum_{n \neq m} \frac{Q(n,m)}{|X_n - X_m|^2} \tag{C.71}$$

where

$$\begin{aligned} Q(n,m) &= \frac{1}{2} + \mathrm{tr}^2\left(Y_n^\dagger Y_m\right) + C_3 \sum_{a=1,2} \mathrm{tr}^2\left(Y_n^\dagger Y_m(-\imath\tau_a)\right) \\ &\quad + (1-2C_3)\mathrm{tr}^2\left(Y_n^\dagger Y_m(-\imath\vec{\tau}\cdot\vec{N}_{nm})\right) \end{aligned} \tag{C.72}$$

and $C_3 = M_3^2/(M_3^2 + M_4^2)$, $0 \leq C_3 \leq \frac{1}{2}$, and $N_{nm}^\mu = (X_n^\mu - X_m^\mu)/|X_n - X_m|$. We focus our attention on the two-body interaction term. Specifically, we calculate $F \equiv \sum_{n\neq m} Q(n,m)/|X_n - X_m|^2$ for the various instanton crystals.

In summing over $n \neq m$, it is convenient to fix $m = 0$ so that we sum over all n except zero. Alternatively, one could think of this as a redefinition of the variable n in the sum. Note that all the terms in the Q-function except for the constant 1/2 are squares of a trace (or sums thereof), so that the overall sign of $Y_n^\dagger Y_m$ does not matter. To spell it out,

$$\begin{aligned}
\mathrm{tr}^2\left(Y_n^\dagger Y_m\right) &= \left[\mathrm{tr}\left(Y_n^\dagger Y_m\right)\right]^2 \\
\sum_{a=1,2} \mathrm{tr}^2\left(Y_n^\dagger Y_m(-\imath\tau_a)\right) &= \left[\mathrm{tr}\left(Y_n^\dagger Y_m(-\imath\tau_1)\right)\right]^2 + \left[\mathrm{tr}\left(Y_n^\dagger Y_m(-\imath\tau_2)\right)\right]^2 \\
\mathrm{tr}^2\left(Y_n^\dagger Y_m(-\imath\vec{\tau}\cdot\vec{N}_{nm})\right) &= \left[\mathrm{tr}\left(Y_n^\dagger Y_m(-\imath\vec{\tau}\cdot\vec{N}_{nm})\right)\right]^2 \qquad \text{(C.73)}
\end{aligned}$$

which makes it explicit that the overall sign of $Y_n^\dagger Y_m$ does not matter. We will use this fact extensively.

3.8.1 Square Anti-Ferromagnetic

This is a relatively simple lattice

$$\begin{array}{ccccccccccc}
Y_1 & Y_2 & Y_1 & Y_2 & Y_1 & Y_2 & Y_1 & Y_2 & Y_1 & Y_2 & .. \\
Y_2 & Y_1 & Y_2 & Y_1 & Y_2 & Y_1 & Y_2 & Y_1 & Y_2 & Y_1 & ..
\end{array}$$

where the orientations are given by $Y_1 = \pm 1,\ Y_2 = \pm\imath\tau_3$. There are two types of F functions here: one in which we sum over instantons within the same line, and the other in which we sum over instantons that are out of line from one another by one line (strictly speaking, there are two of each in this case). In general, it is useful to define F_k as the F function that sums over instantons differing by k lines. Thus, we denote the first F function as F_0 and the other as F_1.

For the in-line function F_0, we have $X_n - X_m = (n-m)D$. For even $n-m$, the relevant orientations are $Y_1^\dagger Y_1 \sim Y_2^\dagger Y_2 = \pm 1$ (where $\sim$ denotes equality upto a $\pm$ sign) and $X_n - X_m = (n-m)D$ (where D is the horizontal lattice spacing) for even $n-m$, while for odd $n-m$ we have $Y_1^\dagger Y_2 \sim Y_2^\dagger Y_1 = \pm\imath\tau_3$.

Thus, we obtain

$$
\begin{aligned}
& Y_1^\dagger Y_1 \sim Y_2^\dagger Y_2 = \pm 1 \\
\Rightarrow \quad & \mathrm{tr}^2\left(Y_n^\dagger Y_m\right) = 4 \\
& \sum_{a=1,2}\left(Y_n^\dagger Y_m(-\imath\tau_a)\right) = 0 \\
& (1-2C_3)\mathrm{tr}^2\left(Y_n^\dagger Y_m(-\imath\vec{\tau}\cdot\vec{N}_{nm})\right) = 0 \qquad \text{(C.74)}
\end{aligned}
$$

and consequently $Q_{even} = 9/2$ for F_0. Similarly,

$$
\begin{aligned}
& Y_1^\dagger Y_2 \sim -Y_2^\dagger Y_1 = \pm\imath\tau_3 \\
\Rightarrow \quad & \mathrm{tr}^2\left(Y_n^\dagger Y_m\right) = 0 \\
& \sum_{a=1,2}\left(Y_n^\dagger Y_m(-\imath\tau_a)\right) = 0 \\
& (1-2C_3)\mathrm{tr}^2\left(Y_n^\dagger Y_m(-\imath\vec{\tau}\cdot\vec{N}_{nm})\right) = 0 \qquad \text{(C.75)}
\end{aligned}
$$

so that $Q_{odd} = 1/2$ for F_0. In all we obtain

$$
\begin{aligned}
F_0 &= \frac{9}{2}\sum_{n\ even}\frac{1}{(nD)^2} + \frac{1}{2}\sum_{n\ odd}\frac{1}{(nD)^2} \\
&= \frac{9}{2}\sum_{k\neq 0}\frac{1}{(2kD)^2} + \frac{1}{2}\sum_{k}\frac{1}{((2k+1)D)^2} \\
&= \frac{\pi^2}{2D^2} \qquad \text{(C.76)}
\end{aligned}
$$

where we have used

$$
\begin{aligned}
\sum_{n\ even}\frac{1}{n^2} &= \sum_{k\neq 0}\frac{1}{(2k)^2} = 2\left(\sum_{k=1}^{\infty}\frac{1}{(2k)^2}\right) = \frac{\pi^2}{12} \\
\sum_{n\ odd}\frac{1}{n^2} &= \sum_{k=-\infty}^{+\infty}\frac{1}{(2k+1)^2} = \frac{\pi^2}{4} \qquad \text{(C.77)}
\end{aligned}
$$

For the out-of-line function F_1, we have $\vec{\tau}\cdot(\vec{X}_n-\vec{X}_m)=(n-m)D\tau_1\pm L\tau_2$ where L is the vertical lattice spacing (it is $+$ in $\pm$ if instanton m is one line below instanton n, and $-$ if it's the other way round). The Q-functions switch their respective values from the ones they had in F_0. Thus, for F_1 we obtain

$$F_1 \;=\; \frac{1}{2}\sum_{n\ even}\frac{1}{(nD)^2+L^2}+\frac{9}{2}\sum_{n\ odd}\frac{1}{(nD)^2+L^2} \tag{C.78}$$

In general, we have that

$$\begin{aligned}\sum_{n=-\infty}^{n=+\infty}\frac{1}{(n\gamma+x)^2+\kappa^2} &= \frac{\pi}{\gamma|\kappa|}\left[1+\frac{\eta}{1-\eta}+\frac{\eta^*}{1-\eta^*}\right]\\ &= \frac{\pi}{\gamma|\kappa|}\left[\frac{1-|\eta|^2}{1-2Re(\eta)+|\eta|^2}\right]\\ &= \frac{\pi}{\gamma|\kappa|}\left[\frac{\sinh\left(\frac{2\pi|\kappa|}{\gamma}\right)}{\cosh\left(\frac{2\pi|\kappa|}{\gamma}\right)-\cos\left(\frac{2\pi x}{\gamma}\right)}\right]\end{aligned} \tag{C.79}$$

where $\eta=e^{-2\pi|\kappa|/\gamma}e^{-2\pi\imath x/\gamma}$. Using this, we obtain

$$\begin{aligned}F_1 &= \frac{1}{2}\cdot\frac{\pi}{2DL}\left(\frac{\sinh(\pi L/D)}{\cosh(\pi L/D)-1}\right)+\frac{9}{2}\cdot\frac{\pi}{2DL}\left(\frac{\sinh(\pi L/D)}{\cosh(\pi L/D)+1}\right)\\ &= \frac{\pi}{4DL}\Big(\coth(\nu/2)+9\tanh(\nu/2)\Big)\\ &= \frac{\pi}{2DL}\left(\frac{5\cosh(\nu)-4}{\sinh(\nu)}\right)\end{aligned} \tag{C.80}$$

where $\nu=L\pi/D$ (or π times the inverse aspect ratio, L/D). To obtain the final F function for this lattice, we may simply sum up F_0 and F_1. As a general rule, which is relevant for more complicated lattices, we calculate the F function as the average of all the F_ks (recall that in this case, there are two each of F_0 and F_1).

Thus, in all we have

$$F = \frac{\pi}{2DL}\left(2\nu + \frac{5\cosh(2\nu) - 4}{\sinh(2\nu)}\right) \tag{C.81}$$

3.8.2 Square Non-Abelian

This is the following array

$$\begin{array}{ccccccccc} Y_1 & Y_2 & Y_1 & Y_2 & Y_1 & Y_2 & Y_1 & Y_2 & .. \\ \\ Y_3 & Y_4 & Y_3 & Y_4 & Y_3 & Y_4 & Y_3 & Y_4 & .. \end{array}$$

where $Y_1 = \pm 1,\ Y_2 = \pm \imath\tau_2,\ Y_3 = \pm\imath\tau_1,\ Y_4 = \pm\imath\tau_3$. For F_0, we have $X_n - X_m = (n-m)D$, and the relevant orientations give us

$$\begin{aligned} & Y_1^\dagger Y_2 \sim Y_3^\dagger Y_4 = \pm\imath\tau_2 \\ \Rightarrow\ & \mathrm{tr}^2\left(Y_n^\dagger Y_m\right) = 0 \\ & \sum_{a=1,2}\left(Y_n^\dagger Y_m(-\imath\tau_a)\right) = 4C_3 \\ & (1-2C_3)\mathrm{tr}^2\left(Y_n^\dagger Y_m(-\imath\vec{\tau}\cdot\vec{N}_{nm})\right) = 0 \end{aligned} \tag{C.82}$$

so that $Q = (4C_3 + 1/2)$ for odd $n-m$, and

$$\begin{aligned} & Y_1^\dagger Y1 \sim Y_2^\dagger Y_2 = \pm 1 \\ \Rightarrow\ & \mathrm{tr}^2\left(Y_n^\dagger Y_m\right) = 4 \\ & \sum_{a=1,2}\left(Y_n^\dagger Y_m(-\imath\tau_a)\right) = 0 \\ & (1-2C_3)\mathrm{tr}^2\left(Y_n^\dagger Y_m(-\imath\vec{\tau}\cdot\vec{N}_{nm})\right) = 0 \end{aligned} \tag{C.83}$$

so that $Q = 9/2$ for even $n - m$. In all we have

$$\begin{aligned} F_0 &= \left(4C_3 + \frac{1}{2}\right) \sum_{n\ odd} \frac{1}{(nD)^2} + \frac{9}{2} \sum_{n\ even} \frac{1}{(nD)^2} \\ &= (1 + 2C_3) \frac{\pi^2}{2D^2} \end{aligned} \tag{C.84}$$

For the out-of-line function F_1, we have the relevant orientations

$$\begin{aligned} Y_1^\dagger Y_3 \sim Y_2^\dagger Y_4 &= \pm \imath \tau_1 \\ \mathrm{tr}^2 \left(Y_n^\dagger Y_m\right) &= 0 \\ \sum_{a=1,2} \left(Y_n^\dagger Y_m (-\imath \tau_a)\right) &= 4C_3 \end{aligned} \tag{C.85}$$

while for the last term we note that since $\vec{\tau} \cdot (\vec{X}_n - \vec{X}_m) = (n - m) D \tau_1 \pm L \tau_2$ here,

$$(1 - 2C_3) \mathrm{tr}^2 \left(Y_n^\dagger Y_m (-\imath \vec{\tau} \cdot \vec{N}_{nm})\right) = \frac{4(1 - 2C_3)(n - m)^2 D^2}{(n - m)^2 D^2 + L^2} \tag{C.86}$$

for even $n - m$. Meanwhile, for odd $n - m$ we have for F_1

$$Y_1^\dagger Y_4 \sim Y_2^\dagger Y_3 = \pm \imath \tau_3 \tag{C.87}$$

and our previous analysis from the last section carries over to show that $Q = 1/2$ for odd $n - m$ in F_1.

As in the previous section, we can simply sum up the two F functions to obtain the complete F

function for this lattice, *i.e.* $F = F_0 + F_1$. All together, we have

$$\begin{aligned} F &= \left(4C_3 + \frac{1}{2}\right)\sum_{n\ odd}\frac{1}{(nD)^2} + \frac{9}{2}\sum_{n\ even}\frac{1}{(nD)^2} + \frac{1}{2}\sum_{n\ odd}\frac{1}{(nD)^2+L^2} \\ &\quad + \left(4C_3 + \frac{1}{2}\right)\sum_{n\ even}\frac{1}{(nD)^2+L^2} + 4(1-2C_3)\sum_{n\ even}\frac{(nD)^2}{\left[(nD)^2+L^2\right]^2} \end{aligned} \tag{C.88}$$

Using (C.79), we obtain

$$\begin{aligned} \sum_{n\ odd}\frac{1}{(nD)^2+L^2} &= \sum_k \frac{1}{(2kD+D)^2+L^2} \\ &= \frac{\pi}{2DL}\left(\frac{\sinh(\pi L/D)}{\cosh(\pi L/D)+1}\right) \end{aligned} \tag{C.89}$$

and

$$\begin{aligned} \sum_{n\ even}\frac{1}{(nD)^2+L^2} &= \sum_k \frac{1}{(2kD)^2+L^2} \\ &= \frac{\pi}{2DL}\left(\frac{\sinh(\pi L/D)}{\cosh(\pi L/D)-1}\right) \end{aligned} \tag{C.90}$$

We also have in general that

$$\begin{aligned} \sum_{n=-\infty}^{n=+\infty}\frac{\kappa^2-(n\gamma+x)^2}{\left[(n\gamma+x)^2+\kappa^2\right]^2} &= \frac{2\pi^2}{\gamma^2}\left[\frac{\eta}{(1-\eta)^2}+\frac{\eta^\star}{(1-\eta^\star)^2}\right] \\ &= \frac{2\pi^2}{\gamma^2}\left[\frac{2Re(\eta)+2|\eta|^2Re(\eta)-4|\eta|^2}{1+2(Re(\eta)^2-Im(\eta)^2)-4Re(\eta)+|\eta|^4-4|\eta|^2Re(\eta)+4|\eta|^2}\right] \\ &= \frac{2\pi^2}{\gamma^2}\left[\frac{2\cos\left(\frac{2\pi x}{\gamma}\right)\cosh\left(\frac{2\pi|\kappa|}{\gamma}\right)-2}{\cosh\left(\frac{4\pi|\kappa|}{\gamma}\right)+\cos\left(\frac{4\pi x}{\gamma}\right)-4\cos\left(\frac{2\pi x}{\gamma}\right)\cosh\left(\frac{2\pi|\kappa|}{\gamma}\right)+2}\right] \end{aligned} \tag{C.91}$$

We further note that

$$\frac{1}{(n\gamma+x)^2+\kappa^2} - \frac{\kappa^2-(n\gamma+x)^2}{\left[(n\gamma+x)^2+\kappa^2\right]^2} = \frac{2(n\gamma+x)^2}{\left[(n\gamma+x)^2+\kappa^2\right]^2} \tag{C.92}$$

which we can use to compute

$$\begin{aligned}
\sum_{n\ even} \frac{(nD)^2}{[(nD)^2+L^2]^2} &= \sum_k \frac{(2kD)^2}{[(2kD)^2+L^2]^2} \\
&= \frac{1}{2}\sum_k \frac{1}{(2kD)^2+L^2} - \frac{1}{2}\sum_k \frac{L^2-(2kD)^2}{[(2kD)^2+L^2]^2} \\
&= \frac{1}{2}\cdot\frac{\pi}{2DL}\left[\frac{\sinh(\pi L/D)}{\cosh(\pi L/D)-1}\right] \\
&\quad -\frac{1}{2}\cdot\frac{2\pi^2}{(2D)^2}\left[\frac{2\cosh(\pi L/D)-2}{\cosh(2\pi L/D)-4\cosh(\pi L/D)+3}\right] \\
&= \frac{\pi^2}{8D^2}\left[\frac{\coth(\nu)}{\nu}-\frac{1}{\sinh^2(\nu)}\right] \qquad \text{(C.93)}
\end{aligned}$$

where we define $\nu = \pi L/2D$ (differing by an overall factor of 1/2 from the previous section). Putting all the results together, we obtain the following expression for the F function for this lattice

$$F = \frac{\pi^2}{2D^2}\left[2C_3+1+\frac{2C_3-1}{\sinh^2(\nu)}+\frac{5\coth(\nu)+\tanh(\nu)}{4\nu}\right] \qquad \text{(C.94)}$$

3.8.3 Period 3 Wave

Here we have the array which follows a wave-like pattern periodically repeating itself after every three instantons.

Y_1 Y_2 Y_1 Y_2 ..
Y_2 Y_1 Y_2 Y_1 ..
Y_1 Y_2 Y_1 Y_2 ..

where $Y_1 = \pm 1$ and $Y_2 = \pm\imath\tau_3$. We take $3D$ as the distance between neighboring instantons in any one line, and L as the vertical spacing between horizontal layers. We have already encountered the relative orientations $Y_1^\dagger Y_2$ and $Y_1^\dagger Y_1 \sim Y_3^\dagger Y_3$ before, and these give $Q = 9/2$ and $Q = 1/2$ respectively (Note that if $Y_n^{\dagger|} Y_m$ had included a τ_1 or τ_2 term, we would have to be more careful in carrying over the previous analysis).

For the in-line function F_0, we have

$$\begin{aligned} F_0 &= \frac{1}{2}\sum_{n\ odd} \frac{1}{(n.3D)^2} + \frac{9}{2}\sum_{n\ even} \frac{1}{(n.3D)^2} \\ &= \frac{1}{2}\frac{\pi^2}{36D^2} + \frac{9}{2}\frac{\pi^2}{108D^2} = \frac{\pi^2}{18D^2} \end{aligned} \tag{C.95}$$

For out of line by one layer, we have

$$\begin{aligned} F_1 &= \frac{1}{2}\sum_{n\ even} \frac{1}{(D+n.3D)^2+L^2} + \frac{9}{2}\sum_{n\ odd} \frac{1}{(D+n.3D)^2+L^2} \\ &= \frac{\pi}{12DL}\left[\frac{1-e^{-\frac{2\pi L}{3D}}}{1-2e^{-\frac{\pi L}{3D}}\cos\left(\frac{\pi}{3}\right)+e^{-\frac{2\pi L}{3D}}}\right] + \frac{3\pi}{4DL}\left[\frac{1-e^{-\frac{2\pi L}{3D}}}{1-2e^{-\frac{\pi L}{3D}}\cos\left(\frac{4\pi}{3}\right)+e^{-\frac{2\pi L}{3D}}}\right] \\ &= \frac{\pi}{12DL}\left[\frac{\sinh\left(\frac{\pi L}{3D}\right)}{\cosh\left(\frac{\pi L}{3D}\right)-\cos\left(\frac{\pi}{3}\right)}\right] + \frac{3\pi}{4DL}\left[\frac{\sinh\left(\frac{\pi L}{3D}\right)}{\cosh\left(\frac{\pi L}{3D}\right)-\cos\left(\frac{4\pi}{3}\right)}\right] \end{aligned} \tag{C.96}$$

using the general result from the previous section. For out of line by two layers, we have

$$\begin{aligned} F_2 &= \frac{1}{2}\sum_{n\ odd} \frac{1}{(2D+n.3D)^2+(2L)^2} + \frac{9}{2}\sum_{n\ even} \frac{1}{(2D+n.3D)^2+(2L)^2} \\ &= \frac{\pi}{24DL}\left[\frac{1-e^{-\frac{4\pi L}{3D}}}{1-2e^{-\frac{2\pi L}{3D}}\cos\left(\frac{5\pi}{3}\right)+e^{-\frac{4\pi L}{3D}}}\right] + \frac{9\pi}{24DL}\left[\frac{1-e^{-\frac{4\pi L}{3D}}}{1-2e^{-\frac{2\pi L}{3D}}\cos\left(\frac{2\pi}{3}\right)+e^{-\frac{4\pi L}{3D}}}\right] \\ &= \frac{\pi}{24DL}\left[\frac{\sinh\left(\frac{2\pi L}{3D}\right)}{\cosh\left(\frac{2\pi L}{3D}\right)-\cos\left(\frac{5\pi}{3}\right)}\right] + \frac{9\pi}{24DL}\left[\frac{\sinh\left(\frac{2\pi L}{3D}\right)}{\cosh\left(\frac{2\pi L}{3D}\right)-\cos\left(\frac{2\pi}{3}\right)}\right] \end{aligned} \tag{C.97}$$

In principle, we should really calculate all possibilities for each of the F_k. If we label the horizontal layers a, b and c from top to bottom, we can calculate F_0 for the combinations (a,a), (b,b) and

(c,c), F_1 for the combinations (a,b), (b,a), (b,c), (c,b), and F_2 for the combinations (a,c) and (c,a). However, as can be checked, each of the possible combinations within each family of F_k yield identical results, so it is sufficient to calculate each F_k for any one possible combination. Nevertheless, we sum over all the possible contributions and then divide by the total number of horizontal lines to obtain the average F function. We then have $3F_{avg} = 3F_0 + 4F_1 + 2F_2$, using which we obtain

$$F_{avg} = \frac{\pi^2}{18D^2} + \frac{\pi}{3DL}\left(\frac{2\sinh(\nu)}{3}\cdot\frac{5\cosh(\nu)-2}{\cosh^2(\nu)-\frac{1}{4}} + \frac{\sinh(2\nu)}{6}\cdot\frac{5\cosh(2\nu)-2}{\cosh^2(2\nu)-\frac{1}{4}}\right) \tag{C.98}$$

where for convenience we redfine ν from the previous sections to be $\nu = \pi L/3D$, *i.e.* $\pi/3$ times the inverse aspect ratio, L/D.

3.8.4 Three Parallel Lines, Square Anti-Ferromagnetic

We now return to the earlier case of the square anti-ferromagnetic lattice, except now with three horizontal layers of instantons.

$$\begin{array}{ccccccccccc}
Y_1 & Y_2 & Y_1 & Y_2 & Y_1 & Y_2 & Y_1 & Y_2 & Y_1 & Y_2 & .. \\
Y_2 & Y_1 & Y_2 & Y_1 & Y_2 & Y_1 & Y_2 & Y_1 & Y_2 & Y_1 & .. \\
Y_1 & Y_2 & Y_1 & Y_2 & Y_1 & Y_2 & Y_1 & Y_2 & Y_1 & Y_2 & ..
\end{array}$$

where $Y_1 = \pm 1$ and $Y_2 = \pm \imath\tau_3$. Our results for F_1 and F_2 carry over from the earlier section. We still have that $Y_1^\dagger Y_2$ yields $Q = 1/2$ while $Y_1^\dagger Y_1 \sim Y_2^\dagger Y_2$ yields $Q = 9/2$. We have for the F_2 function

$$\begin{aligned} F_2 &= \frac{9}{2}\sum_{n\ even}\frac{1}{(nD)^2+(2L)^2}+\frac{1}{2}\sum_{n\ odd}\frac{1}{(nD)^2+(2L)^2} \\ &= \frac{\pi}{8DL}\left(9\mathrm{coth}(\nu)+\tanh(\nu)\right) \\ &= \frac{\pi}{4DL}\left(\frac{5\cosh(2\nu)+4}{\sinh(2\nu)}\right) \end{aligned} \qquad \text{(C.99)}$$

where as in the section with two horizontal layers, $\nu = \pi L/D$.

As in the section with the Period 3 Wave lattice, we take $3F_{avg} = 3F_0 + 4F_1 + 2F_2$. Using the results from the earlier section with two layers for F_0 and F_1, we obtain

$$F_{avg} = \frac{\pi^2}{2D^2}+\frac{2\pi}{3DL}\left(\frac{5\cosh(\nu)-4}{\sinh(\nu)}\right)+\frac{\pi}{6DL}\left(\frac{5\cosh(2\nu)+4}{\sinh(2\nu)}\right) \qquad \text{(C.100)}$$

which may also be rewritten as the less (or more – depending on taste) complicated expression

$$F_{avg} = \frac{\pi^2}{2D^2}\left(1+\frac{17\mathrm{coth}(\nu/2)+81\tanh(\nu/2)}{12\nu}+\frac{\tanh(\nu)}{6\nu}\right) \qquad \text{(C.101)}$$

3.8.5 Three Parallel Lines, Square Non-Abelian

Here we extend our case of the square non-abelian lattice to three layers of instantons. We have the following lattice

$$\begin{array}{ccccccccc} Y_1 & Y_2 & Y_1 & Y_2 & Y_1 & Y_2 & Y_1 & Y_2 & .. \\ Y_3 & Y_4 & Y_3 & Y_4 & Y_3 & Y_4 & Y_3 & Y_4 & .. \\ Y_1 & Y_2 & Y_1 & Y_2 & Y_1 & Y_2 & Y_1 & Y_2 & .. \end{array}$$

where $Y_1 = \pm 1,\ Y_2 = \pm\imath\tau_2,\ Y_3 = \pm\imath\tau_1,\ Y_4 = \pm\imath\tau_3$. The results for F_0 and F_1 carry over from the earlier section with two layers. For F_2, we have that $Y_1^\dagger Y_1 \sim Y_2^\dagger Y_2 \sim Y_3^\dagger Y_3 \sim Y_4^\dagger Y_4 = \pm 1$, so that for instantons separated by nD for even n along the horizontal axis, we have $Q = 9/2$.

For instantons separated by nD for odd n, the relative orientations give us

$$\begin{aligned} & Y_1^\dagger Y_2 \sim Y_3^\dagger Y_4 = \pm\imath\tau_2 \\ \Rightarrow\ & \mathrm{tr}^2\left(Y_n^\dagger Y_m\right) = 0 \\ & \sum_{a=1,2}\left(Y_n^\dagger Y_m(-\imath\tau_a)\right) = 4C_3 \end{aligned}$$

For F_2, we have that $\vec{\tau}\cdot(\vec{X}_n - \vec{X}_m) = (n-m)D\tau_1 \pm 2L\tau_2$, so that the last term in the Q-function is

$$(1-2C_3)\mathrm{tr}^2\left(Y_n^\dagger Y_m(-\imath\vec{\tau}\cdot\vec{N}_{nm})\right) = \frac{4(1-2C_3)(2L)^2}{(n-m)^2D^2 + L^2} \tag{C.102}$$

Thus, we obtain

$$\begin{aligned} F_2 = & \frac{9}{2}\sum_{n\ even}\frac{1}{(nD)^2+(2L)^2} + \left(4C_3 + \frac{1}{2}\right)\sum_{n\ odd}\frac{1}{(nD)^2+(2L)^2} \\ & +4(1-2C_3)\sum_{n\ odd}\frac{(2L)^2}{[(nD)^2+(2L)^2]^2} \end{aligned} \tag{C.103}$$

To calculate the last term above, we note that

$$\frac{1}{(n\gamma+x)^2+\kappa^2} + \frac{\kappa^2-(n\gamma+x)^2}{[(n\gamma+x)^2+\kappa^2]^2} = \frac{2\kappa^2}{[(n\gamma+x)^2+\kappa^2]^2} \tag{C.104}$$

so we can use (C.79) and (C.91) to obtain

$$\sum_{n\ odd}\frac{1}{(nD)^2+(2L)^2} = \frac{\pi}{8DL}\left(\frac{\sinh(4\nu)}{\cosh(4\nu)+1}\right) - \frac{\pi^2}{4D^2}\left(\frac{2\cosh(4\nu)+2}{\cosh(8\nu)+4\cosh(4\nu)+3}\right) \tag{C.105}$$

where as in the section with two layers, we have $\nu = \pi L/2D$. Following the prescription $3F_{avg} = 3F_0 + 4F_1 + 2F_2$, we obtain the following simplified expression for this lattice

$$\begin{aligned} F_{avg} &= \frac{\pi^2}{2D^2}\left[(2C_3+1) + \frac{2}{3}(2C_3-1)\left(\frac{2}{\sinh^2(\nu)} + \frac{1}{\cosh^2(2\nu)}\right)\right. \\ &\qquad \left. + \frac{49\coth(\nu) + 17\tanh(\nu) + 10\tanh(2\nu)}{24\nu}\right] \end{aligned} \tag{C.106}$$

3.8.6 Triangular Non-Abelian

Here we have the following lattice

$$\begin{array}{ccccccccccccccc} & Y_3 & & Y_4 & & Y_3 & & Y_4 & & Y_3 & & Y_4 & .. & & \\ Y_1 & & Y_2 & & Y_1 & & Y_2 & & Y_1 & & Y_2 & & Y_1 & .. & \\ & Y_4 & & Y_3 & & Y_4 & & Y_3 & & Y_4 & & Y_2 & .. & & \end{array}$$

where

$$\begin{aligned} Y_1 &= \pm 1 \\ Y_2 &= \pm \imath \tau_3 \\ Y_3 &= \pm \frac{\imath}{\sqrt{2}}(\tau_1 - \tau_2) \\ Y_4 &= \pm \frac{\imath}{\sqrt{2}}(\tau_1 + \tau_2) \end{aligned} \tag{C.107}$$

We start with the in-line F_0 function. We take D as the distance between neighboring instantons in any one horizontal layer, and L as the vertical distance between horiztonal layers. For instantons separated by nD within the same line for odd n, we have the relative orientations

$$\begin{aligned} & Y_1^\dagger Y_2 \sim Y_3^\dagger Y_4 = \pm\imath\tau_3 \\ \Rightarrow\quad & \mathrm{tr}^2\left(Y_n^\dagger Y_m\right) = 0 \\ & \sum_{a=1,2}\left(Y_n^\dagger Y_m(-\imath\tau_a)\right) = 0 \\ & (1-2C_3)\mathrm{tr}^2\left(Y_n^\dagger Y_m(-\imath\vec{\tau}\cdot\vec{N}_{nm})\right) = 0 \end{aligned} \tag{C.108}$$

which gives us $Q = 1/2$. For instantons separated by nD within the same line for even n, we have

$$\begin{aligned} & Y_1^\dagger Y_1 \sim Y_2^\dagger Y_2 \sim Y_3^\dagger Y_3 \sim Y_4^\dagger Y_4 = \pm 1 \\ \Rightarrow\quad & \mathrm{tr}^2\left(Y_n^\dagger Y_m\right) = 4 \\ & \sum_{a=1,2}\left(Y_n^\dagger Y_m(-\imath\tau_a)\right) = 0 \\ & (1-2C_3)\mathrm{tr}^2\left(Y_n^\dagger Y_m(-\imath\vec{\tau}\cdot\vec{N}_{nm})\right) = 0 \end{aligned} \tag{C.109}$$

which gives us $Q = 9/2$. Therefore, for F_0 we get the simple expression

$$\begin{aligned} F_0 &= \frac{9}{2}\sum_{n\ even}\frac{1}{(nD)^2} + \frac{1}{2}\sum_{n\ odd}\frac{1}{(nD)^2} \\ &= \frac{\pi^2}{2D^2} \end{aligned} \tag{C.110}$$

For F_1, we have $\vec{\tau}\cdot(\vec{X}_n-\vec{X}_m)=\left(\frac{D}{2}+(n-m)D\right)\tau_1\pm L\tau_2$. For odd n, we have

$$\begin{aligned}
& Y_3^\dagger Y_1 \sim Y_4^\dagger Y_2 = \pm\frac{\imath}{\sqrt{2}}(\tau_1-\tau_2) \\
\Rightarrow\quad & \mathrm{tr}^2\left(Y_n^\dagger Y_m\right)=0 \\
& C_3\sum_{a=1,2}\left(Y_n^\dagger Y_m(-\imath\tau_a)\right)=4C_3 \\
& (1-2C_3)\mathrm{tr}^2\left(Y_n^\dagger Y_m(-\imath\vec{\tau}\cdot\vec{N}_{nm})\right)=2(1-2C_3)\frac{\left(\frac{D}{2}+nD+L\right)^2}{\left(\frac{D}{2}+nD\right)^2+L^2}
\end{aligned} \tag{C.111}$$

while for even n, we have

$$\begin{aligned}
& Y_3^\dagger Y_2 \sim Y_4^\dagger Y_1 = \pm\frac{\imath}{\sqrt{2}}(\tau_1+\tau_2) \\
\Rightarrow\quad & \mathrm{tr}^2\left(Y_n^\dagger Y_m\right)=0 \\
& C_3\sum_{a=1,2}\left(Y_n^\dagger Y_m(-\imath\tau_a)\right)=4C_3 \\
& (1-2C_3)\mathrm{tr}^2\left(Y_n^\dagger Y_m(-\imath\vec{\tau}\cdot\vec{N}_{nm})\right)=2(1-2C_3)\frac{\left(\frac{D}{2}+nD-L\right)^2}{\left(\frac{D}{2}+nD\right)^2+L^2}
\end{aligned} \tag{C.112}$$

Thus, in all we have

$$\begin{aligned}
F_1 \;=\; & \left(\frac{1}{2}+4C_3\right)\sum_{n\ odd}\frac{1}{\left(\frac{D}{2}+nD\right)^2+L^2}+2(1-2C_3)\sum_{n\ odd}\frac{\left(\frac{D}{2}+nD+L\right)^2}{\left[\left(\frac{D}{2}+nD\right)^2+L^2\right]^2} \\
& +\left(\frac{1}{2}+4C_3\right)\sum_{n\ even}\frac{1}{\left(\frac{D}{2}+nD\right)^2+L^2}+2(1-2C_3)\sum_{n\ even}\frac{\left(\frac{D}{2}+nD-L\right)^2}{\left[\left(\frac{D}{2}+nD\right)^2+L^2\right]^2}
\end{aligned} \tag{C.113}$$

The first and third terms above can be combined under a single sum and solved using (C.79)

$$\sum_n \frac{1}{\left(\frac{D}{2}+nD\right)^2+L^2} = \frac{\pi}{DL}\left[\frac{\sinh\left(\frac{2\pi L}{D}\right)}{\cosh\left(\frac{2\pi L}{D}\right)+1}\right] \tag{C.114}$$

To evaluate the second and fourth terms above, we first note that

$$\frac{(n\gamma+x\pm\kappa)^2}{[(n\gamma+x)^2+\kappa^2]^2} = \frac{1}{(n\gamma+x)^2+\kappa^2} \pm \frac{2\kappa(n\gamma+x)}{[(n\gamma+x)^2+\kappa^2]^2} \tag{C.115}$$

Now we have in general that

$$\begin{aligned}\sum_{n=-\infty}^{+\infty} \frac{2\kappa(n\gamma+x)}{[(n\gamma+x)^2+\kappa^2]^2} &= \frac{2\pi^2}{\gamma^2}\left[\frac{-\imath\eta}{(1-\eta)^2}+\frac{\imath\eta^\star}{(1-\eta^\star)^2}\right]\cdot \operatorname{sign}(\kappa) \\ &= \frac{2\pi^2}{\gamma^2}\left[\frac{2Im(\eta)[1-|\eta|^2]}{1+2(Re(\eta)^2-Im(\eta)^2)-4Re(\eta)+|\eta|^4-4|\eta|^2Re(\eta)+4|\eta|^2}\right] \\ &\quad \times \operatorname{sign}(\kappa) \\ &= \frac{2\pi^2}{\gamma^2}\left[\frac{2\sinh\left(\frac{2\pi|\kappa|}{\gamma}\right)\sin\left(\frac{2\pi x}{\gamma}\right)}{\cosh\left(\frac{4\pi|\kappa|}{\gamma}\right)+\cos\left(\frac{4\pi x}{\gamma}\right)-4\cos\left(\frac{2\pi x}{\gamma}\right)\cosh\left(\frac{2\pi|\kappa|}{\gamma}\right)+2}\right] \\ &\quad \times \operatorname{sign}(\kappa)\end{aligned} \tag{C.116}$$

and we may use the above two equations to evaluate

$$\begin{aligned}\sum_{n\ odd} \frac{\left(\frac{D}{2}+nD+L\right)^2}{\left[\left(\frac{D}{2}+nD\right)^2+L^2\right]^2} &= \sum_{n\ even} \frac{\left(\frac{D}{2}+nD-L\right)^2}{\left[\left(\frac{D}{2}+nD\right)^2+L^2\right]^2} \\ &= \frac{\pi}{2DL}\tanh(\nu)-\frac{\pi^2}{D^2}\left(\frac{\sinh(\nu)}{\cosh(2\nu)+1}\right)\end{aligned} \tag{C.117}$$

where $\nu = L\pi/D$. Summing over all the terms, we obtain the simplified expression

$$F_1 = \frac{\pi^2}{2D^2}\left[\frac{5}{\nu}+\frac{4(2C_3-1)}{\cosh(\nu)}\right]\tanh(\nu) \tag{C.118}$$

Next, for F_2 we have $\vec{\tau} \cdot (\vec{X}_n - \vec{X}_m) = (n-m)D\tau_1 \pm (2L)\tau_2$. For instantons separated by nD for even n along the horizontal axis, the relative orientations are

$$\begin{aligned}
& Y_1^\dagger Y_2 \sim Y_3^\dagger Y_4 = \pm \imath \tau_3 \\
\Rightarrow\ & \mathrm{tr}^2\left(Y_n^\dagger Y_m\right) = 0 \\
& C_3 \sum_{a=1,2} \left(Y_n^\dagger Y_m(-\imath \tau_a)\right) = 0 \\
& (1-2C_3)\mathrm{tr}^2\left(Y_n^\dagger Y_m(-\imath \vec{\tau} \cdot \vec{N}_{nm})\right) = 0
\end{aligned}$$

so that $Q = 1/2$. Meanwhile, for instantons separated by nD for odd n along the horizontal axis, the relative orientations are

$$\begin{aligned}
& Y_3^\dagger Y_3 \sim Y_4^\dagger Y_4 \sim Y_2^\dagger Y_2 \sim Y_1^\dagger Y_1 = \pm 1 \\
\Rightarrow\ & \mathrm{tr}^2\left(Y_n^\dagger Y_m\right) = 4 \\
& C_3 \sum_{a=1,2} \left(Y_n^\dagger Y_m(-\imath \tau_a)\right) = 0 \\
& (1-2C_3)\mathrm{tr}^2\left(Y_n^\dagger Y_m(-\imath \vec{\tau} \cdot \vec{N}_{nm})\right) = 0
\end{aligned}$$

so that $Q = 9/2$. Altogether, we have

$$F_2 = \frac{1}{2}\sum_{n\ even} \frac{1}{(nD)^2 + (2L)^2} + \frac{9}{2}\sum_{n\ odd} \frac{1}{(nD)^2 + (2L)^2} \tag{C.119}$$

which upon employing (C.79) reduces to the expression

$$F_2 = \frac{\pi}{8DL}\left(\coth(\nu) + 9\tanh(\nu)\right) \tag{C.120}$$

Finally, following the prescription $3F_{avg} = 3F_0 + 4F_1 + 2F_2$, we obtain the simplified expression

$$F_{avg} = \frac{\pi^2}{2D^2}\left[1 + \frac{\coth(\nu) + 49\tanh(\nu)}{6\nu} + \frac{16(2C_3 - 1)\sinh(\nu)}{3\cosh^2(\nu)}\right] \tag{C.121}$$

3.8.7 Triangular Lattice, with Edge Effects

Here we include edge effects for the triangular lattice we encountered above. We have the following array

$$\begin{array}{ccccccccc}
Y_5 & & Y_6 & & Y_5 & & Y_6 & & Y_5 \\
 & Y_3 & & Y_4 & & Y_3 & & Y_4 & \\
Y_2 & & Y_1 & & Y_2 & & Y_1 & & Y_2 \\
 & Y_4 & & Y_3 & & Y_4 & & Y_3 & \\
- & - & - & - & - & - & - & - & - \\
Y_1 & & Y_2 & & Y_1 & & Y_2 & & Y_1 \\
 & Y_3 & & Y_4 & & Y_3 & & Y_4 & \\
Y_2 & & Y_1 & & Y_2 & & Y_1 & & Y_2 \\
 & Y_8 & & Y_7 & & Y_8 & & Y_7 &
\end{array}$$

where the orientations now acquire an additional phase and are given by

$$\begin{aligned}
Y_1 &= \pm e^{\imath(\gamma/2)\tau_1} \\
Y_2 &= \pm \imath\tau_3 \cdot e^{\imath(\gamma/2)\tau_1} \\
Y_3 &= \pm \imath\frac{\tau_1+\tau_2}{\sqrt{2}} \cdot e^{\imath(\gamma/2)\tau_1} \\
Y_4 &= \pm \imath\frac{-\tau_1+\tau_2}{\sqrt{2}} \cdot e^{\imath(\gamma/2)\tau_1}
\end{aligned} \tag{C.122}$$

while on the edges we have the orientations

$$\begin{aligned}
Y_5 &= \pm e^{\imath(\alpha+\gamma/2)\tau_1} \\
Y_6 &= \pm \imath\tau_3 \cdot e^{\imath(\alpha+\gamma/2)\tau_1} \\
Y_7 &= \pm \imath\frac{\tau_1+\tau_2}{\sqrt{2}} \cdot e^{\imath(\alpha+\gamma/2)\tau_1} \\
Y_8 &= \pm \imath\frac{-\tau_1+\tau_2}{\sqrt{2}} \cdot e^{\imath(\alpha+\gamma/2)\tau_1}
\end{aligned} \tag{C.123}$$

Taking (x, y) to be the coordinates in the 2D space for now, the relative orientations in the inner part of the lattice are given by

$$\begin{aligned}
Y_1^\dagger Y_2 \sim Y_3^\dagger Y_4 &= \imath\,(-\mathrm{sin}\gamma\cdot\tau_2+\mathrm{cos}\gamma\cdot\tau_3) \\
\Rightarrow Q &= \frac{1}{2}+2\mathrm{sin}^2\gamma+2(1-2C_3)\mathrm{sin}^2\gamma\cdot\frac{y^2-x^2}{y^2+x^2} \qquad \text{(C.124)} \\
Y_1^\dagger Y_4 \sim Y_2^\dagger Y_3 &= \pm\frac{\imath}{\sqrt{2}}\,(-\tau_1+\mathrm{cos}\gamma\cdot\tau_2+\mathrm{sin}\gamma\cdot\tau_3) \\
\Rightarrow Q &= \frac{5}{2}-\mathrm{sin}^2\gamma-(1-2C_3)\mathrm{sin}^2\gamma\cdot\frac{y^2-x^2}{y^2+x^2} \\
&\quad -2(1-2C_3)\mathrm{cos}\gamma\cdot\frac{2xy}{y^2+x^2} \qquad \text{(C.125)} \\
Y_1^\dagger Y_3 \sim Y_2^\dagger Y_4 &= \pm\frac{\imath}{\sqrt{2}}\,(\tau_1+\mathrm{cos}\gamma\cdot\tau_2+\mathrm{sin}\gamma\cdot\tau_3) \\
\Rightarrow Q &= \frac{5}{2}-\mathrm{sin}^2\gamma-(1-2C_3)\mathrm{sin}^2\gamma\cdot\frac{y^2-x^2}{y^2+x^2} \\
&\quad +2(1-2C_3)\mathrm{cos}\gamma\cdot\frac{2xy}{y^2+x^2} \qquad \text{(C.126)}
\end{aligned}$$

The relative orientations between the inner part of the lattice and the edge are given by

$$
\begin{aligned}
Y_1^\dagger Y_5 \sim Y_2^\dagger Y_6 \sim Y_3^\dagger Y_7 \sim Y_4^\dagger Y_8 &= \pm\left(\cos\alpha \cdot 1 + \sin\alpha \cdot \imath\tau_1\right) \\
\Rightarrow Q &= \frac{9}{2} - 2\sin^2\alpha - 2(1-2C_3)\sin^2\alpha \cdot \frac{y^2-x^2}{y^2+x^2} \\
Y_1^\dagger Y_6 \sim Y_2^\dagger Y_5 \sim Y_3^\dagger Y_8 \sim Y_4^\dagger Y_7 &= \pm\imath\left(-\sin(\alpha+\gamma)\tau_2 + \cos(\alpha+\gamma)\tau_3\right) \\
\Rightarrow Q &= \frac{1}{2} + 2\sin^2(\alpha+\gamma) + 2(1-2C_3)\sin^2(\alpha+\gamma) \cdot \frac{y^2-x^2}{y^2+x^2} \\
Y_1^\dagger Y_8 \sim Y_4^\dagger Y_5 \sim Y_3^\dagger Y_6 \sim Y_2^\dagger Y_7 &= \pm\frac{1}{\sqrt{2}}\left(\sin\alpha \cdot 1 - \cos\alpha \cdot \imath\tau_1 + \cos(\alpha+\gamma)\cdot\imath\tau_2 + \sin(\alpha+\gamma)\cdot\imath\tau_3\right) \\
\Rightarrow Q &= \frac{5}{2} + \sin^2\alpha - \sin^2(\alpha+\gamma) \\
&\quad +(1-2C_3)(\sin^2\alpha - \sin^2(\alpha+\gamma)) \cdot \frac{y^2-x^2}{y^2+x^2} \\
&\quad -2(1-2C_3)\cos\alpha\cos(\alpha+\gamma) \cdot \frac{2xy}{y^2+x^2} \\
Y_1^\dagger Y_7 \sim Y_3^\dagger Y_5 \sim Y_4^\dagger Y_6 \sim Y_2^\dagger Y_8 &= \pm\frac{1}{\sqrt{2}}\left(-\sin\alpha \cdot 1 + \cos\alpha \cdot \imath\tau_1\right. \\
&\qquad\qquad \left. + \cos(\alpha+\gamma)\cdot\imath\tau_2 + \sin(\alpha+\gamma)\cdot\imath\tau_3\right) \\
\Rightarrow Q &= \frac{5}{2} + \sin^2\alpha - \sin^2(\alpha+\gamma) \\
&\quad +(1-2C_3)\left(\sin^2\alpha - \sin^2(\alpha+\gamma)\right) \cdot \frac{y^2-x^2}{y^2+x^2} \\
&\quad +2(1-2C_3)\cos\alpha\cos(\alpha+\gamma) \cdot \frac{2xy}{y^2+x^2}
\end{aligned}
\tag{C.127}
$$

while the relative orientation along the edges are given by

$$\begin{aligned}
Y_5^\dagger Y_6 \sim Y_7^\dagger Y_8 &= \pm\imath\left(-\sin(\gamma+2\alpha)\tau_2+\cos(\gamma+2\alpha)\tau_3\right)\\
\Rightarrow Q &= \frac{1}{2}+2\sin^2(\gamma+2\alpha)+2(1-2C_3)\sin^2(\gamma+2\alpha)\cdot\frac{y^2-x^2}{y^2+x^2}\\
Y_5^\dagger Y_8 \sim Y_6^\dagger Y_7 &= \pm\frac{\imath}{\sqrt{2}}\left(-\tau_1+\cos(\gamma+2\alpha)\tau_2+\sin(\gamma+2\alpha)\tau_3\right)\\
\Rightarrow Q &= \frac{5}{2}-\sin^2(\gamma+2\alpha)-(1-2C_3)\sin^2(\gamma+2\alpha)\cdot\frac{y^2-x^2}{y^2+x^2}\\
&\quad -2(1-2C_3)\cos(\gamma+2\alpha)\cdot\frac{2xy}{y^2+x^2}\\
Y_5^\dagger Y_7 \sim Y_6^\dagger Y_8 &= \pm\frac{\imath}{\sqrt{2}}\left(\tau_1+\cos(\gamma+2\alpha)\tau_2+\sin(\gamma+2\alpha)\tau_3\right)\\
\Rightarrow Q &= \frac{5}{2}-\sin^2(\gamma+2\alpha)-(1-2C_3)\sin^2(\gamma+2\alpha)\cdot\frac{y^2-x^2}{y^2+x^2}\\
&\quad +2(1-2C_3)\cos(\gamma+2\alpha)\cdot\frac{2xy}{y^2+x^2} \qquad \text{(C.128)}
\end{aligned}$$

Let us now define $\nu = L/D$ as the (inverse) aspect ratio with D as the distance between neighboring instantons within a horizontal layer, so that $x = \left(n-\frac{1}{2}k\right)D$ and $y = k\nu D$, where k and n are integers, and k indexes the number of the horizontal line. Let us further define

$$\begin{aligned}
F(k) &\equiv \frac{2D^2}{\pi^2}\sum_n \frac{Q((0,0);(x,y))}{x^2+y^2}\\
&= \frac{2}{\pi^2}\sum_n \frac{Q(k=0,n)}{n^2} \qquad \text{(C.129)}
\end{aligned}$$

so that the net interaction energy per instanton becomes

$$\xi = \frac{E}{N_{inst.}} = \frac{\pi^2 N_c}{10\lambda M D^2}\cdot\frac{1}{N_{lines}}\sum_{k_1,k_2} F(k_1-k_2) \qquad \text{(C.130)}$$

In an infinitely long lattice, $F(k)$ only depends on the difference $k = k_1 - k_2$, which is the number of horizontal lines the interacting instantons are away from each other. However, in a lattice with a finite number of lines such that the edge effects make the outer lines different from the inner lines, $F(k)$ further depends on whether k_1 or k_2 are inner or outer (edge) lines.

In the case where $k_1 = k_2$ are both inner lines,

$$F_i(0) = \frac{2}{\pi^2} \sum_{n \neq 0} \frac{Q_i(n,0)}{n^2} \tag{C.131}$$

where the subscript i denotes inner line. In the case of even n, the interacting instanton pair separated by $(n, 0)$ have the same orientations so that $Q_{n\ even} = 9/2$, while for odd n the relative orientation is $Y_1^\dagger Y_2 \sim Y_3^\dagger Y_4$, so that

$$\begin{aligned} Q_{n\ odd} &= \frac{1}{2} + 2\sin^2\gamma + 2(1-2C_3)\sin^2\gamma \cdot \frac{y^2 - x^2}{y^2 + x^2} \\ &= \frac{1}{2} + 4C_3\sin^2\gamma \end{aligned} \tag{C.132}$$

Consequently,

$$\begin{aligned} F_i(0) &= \frac{9}{\pi^2} \sum_{n \neq 0\ even} \frac{1}{n^2} + \frac{1 + 8C_3\sin^2\gamma}{\pi^2} \sum_{n\ odd} \frac{1}{n^2} \\ &= 1 + 2C_3\sin^2\gamma \end{aligned} \tag{C.133}$$

In the case where $k_1 = k_2$ are both outer lines, we still have $Q_{even} = 9/2$ as before, but now for odd n the relative orientation is $Y_5^\dagger Y_6 \sim Y_7^\dagger Y_8$, so that

$$Q_{n\ odd} = \frac{1}{2} + 4C_3\sin^2(\gamma + 2\alpha) \tag{C.134}$$

so that

$$F_o(0) = 1 + 2C_3\sin^2(\gamma + 2\alpha) \tag{C.135}$$

where the subscript o denotes outer line. In the case where both k_1 and k_2 label inner lines, but we have odd $k = k_1 - k_2$, the relative orientations are either $Y_1^\dagger Y_4 \sim Y_2^\dagger Y_3$ (for even n) or $Y_1^\dagger Y_3 \sim Y_2^\dagger Y_4$ (for odd n), so that

$$Q = \frac{5}{2} - \sin^2\gamma - (1-2C_3)\sin^2\gamma \cdot \frac{y^2 - x^2}{y^2 + x^2} + (-1)^n 2(1-2C_3)\cos\gamma \cdot \frac{2xy}{y^2+x^2} \tag{C.136}$$

and as a result

$$\begin{aligned} F_{ii}(k\ odd) &= \frac{5 - 2\sin^2\gamma}{\pi^2} \sum_n \frac{1}{\left(n - \frac{1}{2}k\right)^2 + \nu^2 k^2} \\ &\quad - \frac{2(1-2C_3)\sin^2\gamma}{\pi^2} \sum_n \frac{\nu^2 k^2 - \left(n - \frac{1}{2}k\right)^2}{\left[\nu^2 k^2 + \left(n - \frac{1}{2}k\right)^2\right]^2} \\ &\quad + \frac{4(1-2C_3)\cos\gamma}{\pi^2} \sum_n \frac{2(-1)^n \nu k \left(n - \frac{1}{2}k\right)}{\left[\nu^2 k^2 + \left(n - \frac{1}{2}k\right)^2\right]^2} \\ &= (5 - 2\sin^2\gamma)\frac{\tanh \pi\nu k}{\pi\nu k} + 2(1-2C_3)\frac{\sin^2\gamma}{\cosh^2(\pi\nu k)} \\ &\quad - 4(1-2C_3)\cos\gamma \frac{\sinh(\pi\nu k)}{\cosh^2(\pi\nu k)}(-1)^{(k-1)/2} \end{aligned} \tag{C.137}$$

The case where both k_1 and k_2 are outer (edge) lines for odd $k = k_1 - k_2$ works similarly, and we obtain

$$\begin{aligned} F_{oo}(k\ odd) &= (5 - 2\sin^2(\gamma + 2\alpha))\frac{\tanh \pi\nu k}{\pi\nu k} + 2(1-2C_3)\frac{\sin^2(\gamma+2\alpha)}{\cosh^2(\pi\nu k)} \\ &\quad - 4(1-2C_3)\cos(\gamma+2\alpha)\frac{\sinh(\pi\nu k)}{\cosh^2(\pi\nu k)}(-1)^{(k-1)/2} \end{aligned} \tag{C.138}$$

In the case where k_1 is an inner line and k_2 is an outer (edge) line for odd $k = k_1 - k_2$, the relative orientation is $Y_3^\dagger Y_5$, $Y_4^\dagger Y_6$, $Y_1^\dagger Y_7$ or $Y_2^\dagger Y_8$ for even n; and $Y_4^\dagger Y_5$, $Y_3^\dagger Y_6$, $Y_1^\dagger Y_8$ or $Y_2^\dagger Y_7$ for odd n. Thus, we find

$$\begin{aligned} F_{io}(k\ odd) &= \left[5+2\sin^2\alpha-2\sin^2(\gamma+\alpha)\right]\cdot\frac{\tanh\pi\nu k}{\pi\nu k}+2(1-2C_3)\frac{\sin^2(\gamma+\alpha)-\sin^2\alpha}{\cosh^2(\pi\nu k)} \\ &\quad -4(1-2C_3)\cos\alpha\cos(\gamma+\alpha)\frac{\sinh(\pi\nu k)}{\cosh^2(\pi\nu k)}(-1)^{(k-1)/2} \end{aligned} \tag{C.139}$$

In the case where both k_1 and k_2 are inner lines, for even $k=k_1-k_2$, we have $Q=9/2$ for instantons separated by even n, while for odd n the relative orientation is $Y_1^\dagger Y_2 \sim Y_3^\dagger Y_4$, so proceeding along similar lines we find

$$\begin{aligned} F_{ii}(k\ even) &= \frac{9}{2}\cdot\frac{\cosh(\pi\nu k)+(-1)^{k/2}}{(\pi\nu k)\sinh(\pi\nu k)}+\frac{1+4\sin^2\gamma}{2}\cdot\frac{\cosh(\pi\nu k)-(-1)^{k/2}}{(\pi\nu k)\sinh(\pi\nu k)} \\ &\quad -2(1-2C_3)\sin^2\gamma\cdot\frac{(-1)^{k/2}}{\cosh(\pi\nu k)+(-1)^{k/2}} \end{aligned} \tag{C.140}$$

In the case where both k_1 and k_2 are outer lines, for even $k=k_1-k_2$, we get a similar result

$$\begin{aligned} F_{oo}(k\ even) &= \frac{9}{2}\cdot\frac{\cosh(\pi\nu k)+(-1)^{k/2}}{(\pi\nu k)\sinh(\pi\nu k)}+\frac{1+4\sin^2(\gamma+2\alpha)}{2}\cdot\frac{\cosh(\pi\nu k)-(-1)^{k/2}}{(\pi\nu k)\sinh(\pi\nu k)} \\ &\quad -2(1-2C_3)\sin^2(\gamma+2\alpha)\cdot\frac{(-1)^{k/2}}{\cosh(\pi\nu k)+(-1)^{k/2}} \end{aligned} \tag{C.141}$$

For the case of inner k_1 and outer k_2 (or vice versa), for even $k=k_1-k_2$, the relative orientation is $Y_1^\dagger Y_5 \sim Y_2^\dagger Y_6 \sim Y_3^\dagger Y_7 \sim Y_4^\dagger Y_8$ for even n, while the relative orientation is $Y_1^\dagger Y_6 \sim Y_2^\dagger Y_5 \sim Y_3^\dagger Y_8 \sim Y_4^\dagger Y_7$ for odd n. Consequently, we have

$$\begin{aligned} F_{io}(k\ even) &= \frac{9-4\sin^2\alpha}{2}\cdot\frac{\cosh(\pi\nu k)+(-1)^{k/2}}{(\pi\nu k)\sinh(\pi\nu k)} \\ &\quad -2(1-2C_3)\sin^2\alpha\cdot\frac{(-1)^{k/2}}{\cosh(\pi\nu k)-(-1)^{k/2}} \\ &\quad +\frac{1+4\sin^2(\gamma+\alpha)}{2}\cdot\frac{\cosh(\pi\nu k)-(-1)^{k/2}}{(\pi\nu k)\sinh(\pi\nu k)} \\ &\quad -2(1-2C_3)\sin^2(\gamma+\alpha)\cdot\frac{(-1)^{k/2}}{\cosh(\pi\nu k)+(-1)^{k/2}} \end{aligned} \tag{C.142}$$

Now we have that $F(k) = F(-k)$. We can use this fact to calculate the net F function

$$F_{net} \;=\; \sum_{k_1,k_2} F(k_1 - k_2) \tag{C.143}$$

where after counting pairs, we obtain

$$F_{net} \;=\; (N-2)F_i(0) + 2F_o(0) + 2\sum_{k=1}^{N-3}(N-2-k)F_{ii}(k) + 4\sum_{k=1}^{N-2}F_{io}(k) + 2F_{oo}(N-1) \tag{C.144}$$

in terms of which we have the net interaction energy of the lattice per instanton

$$\begin{aligned} \xi &= \frac{\pi^2 N_c}{10\lambda M D^2}\cdot\frac{F_{net}}{N} \\ &= \frac{\pi^2 N_c \rho^2}{10\lambda M}\cdot\frac{F_{net}}{N^3} \end{aligned} \tag{C.145}$$

where $\rho = N/D$ is the linear density. Meanwhile, the 1-body term $V^{1-body} = N_c\lambda M M_2^2 y^2$ averaged over the instanton lines gives us

$$\begin{aligned} \xi^{1-body} &= N_c\lambda M M_2^2\cdot\frac{1}{N}\sum_{k=1}^{N} y^2(k) \\ &= N_c\lambda M M_2^2(\nu D)^2\sum_{k=1}^{N}\frac{(2k-N-1)^2}{4N} \\ &= N_c\lambda M M_2^2\cdot\frac{N^2\nu^2}{\rho^2}\cdot\frac{N^2-1}{12} \end{aligned} \tag{C.146}$$

so that the net energy of the lattice per instanton becomes

$$\xi \;=\; \frac{\pi^2 N_c}{10\lambda M}\rho^2\frac{F_{net}(\nu,\alpha,\gamma)}{N^3} + N_c\lambda M M_2^2\cdot\frac{N^2(N^2-12)}{12}\frac{\nu^2}{\rho^2} \tag{C.147}$$

3.8.8 Generalization to N lines

Here, we generalize the results for a few lattices so that instead of two or three lines, the pattern consists of more generally N lines. We start with the relatively simple case of the square anti-ferromagnetic lattice. We already have that

$$F_0 = \frac{\pi^2}{2D^2} \tag{C.148}$$

Following our earlier notation, we use F_k to denote the F function calculated for interacting instantons separated by k lines. We have that for even k, instantons separated by nD along the x_1 axis for even n have $Q = 9/2$, while those for odd n have $Q = 9/2$. Therefore,

$$\begin{aligned} F_{k\ even} &= \frac{9}{2}\sum_{n\ even}\frac{1}{(nD)^2+(kL)^2} + \frac{1}{2}\sum_{n\ odd}\frac{1}{(nD)^2+(kL)^2} \\ &= \frac{\pi}{4DkL}\left[9\mathrm{coth}\left(\frac{k\nu}{2}\right) + \tanh\left(\frac{k\nu}{2}\right)\right] \\ &= \frac{\pi}{2DkL}\left[\frac{5\mathrm{cosh}(k\nu)+4}{\sinh(k\nu)}\right] \end{aligned} \tag{C.149}$$

where $\nu = \pi L/D$. For k odd, the Q's flip values so that we have

$$\begin{aligned} F_{k\ odd} &= \frac{1}{2}\sum_{n\ even}\frac{1}{(nD)^2+(kL)^2} + \frac{9}{2}\sum_{n\ odd}\frac{1}{(nD)^2+(kL)^2} \\ &= \frac{\pi}{4DkL}\left[\coth\left(\frac{k\nu}{2}\right) + 9\mathrm{tanh}\left(\frac{k\nu}{2}\right)\right] \\ &= \frac{\pi}{2DkL}\left[\frac{5\mathrm{cosh}(k\nu)-4}{\sinh(k\nu)}\right] \end{aligned} \tag{C.150}$$

Next, we note that in a lattice of N lines, there are a total of N number of F_0 functions and $2(N-k)$ number of F_k (for $k > 0$), but whose values are fixed (or rather functions of the parameters) for fixed k. Taking this into account, and generalizing our previous rule of finding the average net F function, we now have

$$F_{net} \;=\; F_0 + \sum_{k=1}^{N-1} \frac{2(N-k)}{N} F_k \tag{C.151}$$

using which we find for the square anti-ferromagnetic lattice

$$F_{N-lines}[\Box AF] \;=\; \frac{\pi^2}{2D^2} + \sum_{k=1}^{N-1} \frac{2(N-k)}{N} \cdot \frac{\pi}{2DkL} \left[\frac{5\cosh(k\nu) + 4(-1)^k}{\sinh(k\nu)} \right] \tag{C.152}$$

Next, for the square non-abelian lattice, we derived earlier that

$$F_0 \;=\; (1+2C_3)\frac{\pi^2}{2D^2} \tag{C.153}$$

For even k, we have that instantons separated by nD along the x_1 axis for odd n have a relative orientation of $Y^\dagger Y \sim \tau_2$, while for even n we have $Y^\dagger Y \sim 1 \Rightarrow Q = 9/2$. Consequently,

$$\begin{aligned} F_{k\ even} &= \left(\frac{1}{2} + 4C_3\right) \sum_{n\ odd} \frac{1}{(nD)^2 + (kL)^2} + 4(1-2C_3) \sum_{n\ odd} \frac{(kL)^2}{(nD)^2 + (kL)^2} \\ &\quad + \frac{9}{2} \sum_{n\ even} \frac{1}{(nD)^2 + (kL)^2} \\ &= \frac{\pi}{4DkL} \left(9\coth(k\nu) + 5\tanh(k\nu)\right) + \frac{\pi^2}{D^2} \cdot \frac{(2C_3 - 1)}{\cosh(2k\nu) + 1} \end{aligned} \tag{C.154}$$

where now $\nu = \pi L/2D$. For odd k, instantons separated by nD along x_1 for odd n have $Y^\dagger Y \sim \tau_3 \Rightarrow Q = 1/2$ while for even n they have $Y^\dagger Y \sim \tau_1$, so that we have

$$\begin{aligned} F_{k\ even} &= \left(\frac{1}{2} + 4C_3\right) \sum_{n\ odd} \frac{1}{(nD)^2 + (kL)^2} + 4(1-2C_3) \sum_{n\ odd} \frac{(kL)^2}{(nD)^2 + (kL)^2} \\ &\quad + \frac{1}{2} \sum_{n\ odd} \frac{1}{(nD)^2 + (kL)^2} \\ &= \frac{\pi}{4DkL} \left(5\coth(k\nu) + \tanh(k\nu)\right) + \frac{\pi^2}{D^2} \cdot \frac{(2C_3 - 1)}{\cosh(2k\nu) - 1} \end{aligned} \tag{C.155}$$

Putting these results together we have that

$$F_{N-lines}[\square NA] = (1+2C_3)\frac{\pi^2}{2D^2} + \sum_{k=1}^{N-k}\frac{2(N-k)}{N}\cdot F_k[\square NA] \tag{C.156}$$

where

$$F_k[\square NA] = \frac{\pi}{4DkL}\Big([7+2(-1)^k]\coth(k\nu)+[3+2(-1)^k]\tanh(k\nu)\Big) + \frac{\pi^2}{D^2}\cdot\frac{(2C_3-1)}{\cosh(2k\nu)+(-1)^k} \tag{C.157}$$

Next, we consider the triangular non-abelian lattice. We already have that

$$F_0 = \frac{\pi^2}{2D^2} \tag{C.158}$$

For the F_k functions, we have to be a little more careful. Instead of organizing the F_k ($k \neq 0$) according to either even or odd k, we should rather sum them up according to k modulo 4. For odd $k = 1, 5, 9, ...$, we have

$$\begin{aligned} F_{k=1,5,9,..} &= \left(\frac{1}{2}+4C_3\right)\sum_n \frac{1}{\left(\frac{D}{2}+nD\right)^2+(kL)^2} + 2(1-2C_3)\sum_{n\ even}\frac{\left(\frac{D}{2}+nD-kL\right)^2}{\left[\left(\frac{D}{2}+nD\right)^2+(kL)^2\right]^2} \\ &\quad + 2(1-2C_3)\sum_{n\ odd}\frac{\left(\frac{D}{2}+nD+kL\right)^2}{\left[\left(\frac{D}{2}+nD\right)^2+(kL)^2\right]^2} \\ &= \frac{\pi}{2DkL}\Big(5+4k\nu(2C_3-1)\mathrm{sech}(k\nu)\Big)\tanh(k\nu) \end{aligned} \tag{C.159}$$

while for odd $k = 3, 7, 11, ...$, we have

$$\begin{aligned} F_{k=3,7,11,..} &= \left(\frac{1}{2} + 4C_3\right) \sum_n \frac{1}{\left(\frac{D}{2} + nD\right)^2 + (kL)^2} + 2(1-2C_3) \sum_{n\ even} \frac{\left(\frac{D}{2} + nD + kL\right)^2}{\left[\left(\frac{D}{2} + nD\right)^2 + (kL)^2\right]^2} \\ &\quad + 2(1-2C_3) \sum_{n\ odd} \frac{\left(\frac{D}{2} + nD + kL\right)^2}{\left[\left(\frac{D}{2} + nD\right)^2 + (kL)^2\right]^2} \\ &= \frac{\pi}{2DkL}\Big(5 - 4k\nu(2C_3 - 1)\text{sech}(k\nu)\Big)\tanh(k\nu) \end{aligned} \tag{C.160}$$

which we can write together as

$$F_{k\ odd}[\triangle NA] = \frac{\pi}{2DkL}\Big(5 + 4k\nu(-1)^{\frac{k+1}{2}}(1-2C_3)\text{sech}(k\nu)\Big)\tanh(k\nu) \tag{C.161}$$

For even $k = 2, 6, 10, ...$, we have

$$\begin{aligned} F_{k=2,6,10,..} &= \frac{1}{2} \sum_{n\ even} \frac{1}{(nD)^2 + (kL)^2} + \frac{9}{2} \sum_{n\ odd} \frac{1}{(nD)^2 + (kL)^2} \\ &= \frac{\pi}{4DkL}\Big(\coth\left(\frac{k\nu}{2}\right) + 9\tanh\left(\frac{k\nu}{2}\right)\Big) \end{aligned} \tag{C.162}$$

while for $k = 4, 8, 12, ...$, we have

$$\begin{aligned} F_{k=4,8,12,..} &= \frac{9}{2} \sum_{n\ even} \frac{1}{(nD)^2 + (kL)^2} + \frac{1}{2} \sum_{n\ odd} \frac{1}{(nD)^2 + (kL)^2} \\ &= \frac{\pi}{4DkL}\Big(9\coth\left(\frac{k\nu}{2}\right) + \tanh\left(\frac{k\nu}{2}\right)\Big) \end{aligned} \tag{C.163}$$

which we can simplify and write together as

$$F_{k\ even}[\triangle NA] = \frac{\pi}{2DkL}\left[\frac{5\cosh(k\nu) + 4(-1)^{k/2}}{\sinh(k\nu)}\right] \tag{C.164}$$

These F_k's cannot further be brought to a similar form, so our net F function is given by

$$\begin{aligned} F_{N-lines}[\triangle NA] &= \frac{\pi^2}{2D^2} + \sum_{k=1}^{N-1} \frac{2(N-k)}{N} \Big[(k \bmod 2) \cdot F_{k\,odd}[\triangle NA] \\ &\qquad + ((k+1) \bmod 2) \cdot F_{k\,even}[\triangle NA] \Big] \end{aligned} \tag{C.165}$$

3.9 Appendix B: Infinite Crystals

In this section, we adopt a slight change in notation for convenience, and express the orientations in unimodular quaternions. The two-body interaction energy is

$$E = \frac{4N_c}{5\lambda M} \sum_{i \neq j} \frac{Q}{|\vec{X}_i - \vec{X}_j|^2} \tag{C.166}$$

where the $\vec{X}_i$ denote the instantons' locations in 2D space, while Q depends on the orientations of the instantons here represented by unimodular quaternions ys

$$Q = \frac{1}{8} + \mathcal{R}^2\left(y_i^\dagger y_j\right) + \frac{1-\zeta}{2} \sum_{a=1,2} \mathcal{I}_a^2(y_i^\dagger y_j) + \zeta\left(\vec{N}_{ij} \cdot \vec{\mathcal{I}}(y_i^\dagger y_j)\right) \tag{C.167}$$

where $\mathcal{R}$ and $\mathcal{I}$ denote the real and pure quaternion components respectively, and

$$\vec{N}_{ij} = \frac{\vec{X}_i - \vec{X}_j}{|\vec{X}_i - \vec{X}_j|} \tag{C.168}$$

and

$$\zeta = 1 - 2C_3 = \frac{M_4^2 - M_3^2}{M_4^2 + M_3^2} \tag{C.169}$$

We seek to calculate the net interaction energy per instanton, $\xi = E/\#instantons$. This energy is IR divergent in two dimensions, and to regulate this divergence we introduce a cutoff in the

X^2 direction, *i.e.* $-W < X_i^2 < W$.

In calculating the interaction energy, we pick a single instanton, *e.g.* at $\vec{X} = (0,0)$, and first sum over the X^1 direction and then over the X^2 direction. In doing so, we make extensive use of (C.79), (C.91) and (C.116). Indeed, if we identify

$$\begin{aligned}
\Sigma_1 &= \sum_{n=-\infty}^{n=+\infty} \frac{1}{(n\gamma+x)^2+\kappa^2} = \frac{\pi}{\gamma|\kappa|}\left[1+\frac{\eta}{1-\eta}+\frac{\eta^*}{1-\eta^*}\right] \\
\Sigma_2 &= \sum_{n=-\infty}^{n=+\infty} \frac{\kappa^2-(n\gamma+x)^2}{[(n\gamma+x)^2+\kappa^2]^2} = \frac{2\pi^2}{\gamma^2}\left[\frac{\eta}{(1-\eta)^2}+\frac{\eta^\star}{(1-\eta^\star)^2}\right] \\
\Sigma_3 &= \sum_{n=-\infty}^{+\infty} \frac{2\kappa(n\gamma+x)}{[(n\gamma+x)^2+\kappa^2]^2} = \frac{2\pi^2}{\gamma^2}\left[\frac{-\imath\eta}{(1-\eta)^2}+\frac{\imath\eta^\star}{(1-\eta^\star)^2}\right]\cdot \mathrm{sign}(\kappa)
\end{aligned} \tag{C.170}$$

then we can reduce these sums for some special cases. For $\frac{x}{\gamma} \in \mathbb{Z}$, $\eta = \eta^\star = e^{-2\pi|\kappa|/\gamma}$ and the above sums simplify to

$$\begin{aligned}
\Sigma_1 &= \frac{\pi}{\gamma|\kappa|}\left[1+\frac{2e^{-2\pi|\kappa|/\gamma}}{1-e^{-2\pi|\kappa|/\gamma}}\right] \\
\Sigma_2 &= \frac{2\pi^2}{\gamma^2}\left[\frac{2e^{-2\pi|\kappa|/\gamma}}{\left(1-e^{-2\pi|\kappa|/\gamma}\right)^2}\right] \\
\Sigma_3 &= 0
\end{aligned} \tag{C.171}$$

For $\frac{x}{\gamma} \in \mathbb{Z}+\frac{1}{2}$, $\eta = \eta^\star = -e^{-2\pi|\kappa|/\gamma}$ and we have

$$\begin{aligned}
\Sigma_1 &= \frac{\pi}{\gamma|\kappa|}\left[1-\frac{2e^{-2\pi|\kappa|/\gamma}}{1+e^{-2\pi|\kappa|/\gamma}}\right] \\
\Sigma_2 &= \frac{2\pi^2}{\gamma^2}\left[\frac{-2e^{-2\pi|\kappa|/\gamma}}{\left(1+e^{-2\pi|\kappa|/\gamma}\right)^2}\right] \\
\Sigma_3 &= 0
\end{aligned} \tag{C.172}$$

For $\frac{x}{\gamma} \in \mathbb{Z} + 14$, $\eta = \pm \imath e^{-2\pi|\kappa|/\gamma}$, $\eta^\star = -\eta = \mp \imath e^{-2\pi|\kappa|/\gamma}$, and thus

$$\begin{aligned}
\Sigma_1 &= \frac{\pi}{\gamma|\kappa|}\left[1 - \frac{2e^{-4\pi|\kappa|/\gamma}}{1+e^{-4\pi|\kappa|/\gamma}}\right] \\
\Sigma_2 &= \frac{2\pi^2}{\gamma^2}\left[\frac{-4e^{-4\pi|\kappa|/\gamma}}{\left(1+e^{-4\pi|\kappa|/\gamma}\right)^2}\right] \\
\Sigma_3 &= \frac{2\pi^2}{\gamma^2} \cdot \frac{2e^{-2\pi|\kappa|/\gamma}(1-e^{-4\pi|\kappa|/\gamma})}{[1+e^{-4\pi|\kappa|/\gamma}]^2} \cdot \mathrm{sign}(\kappa) \qquad \text{(C.173)}
\end{aligned}$$

A useful thing to note while summing over X^2 is

$$\sum_{n=1}^{N} \frac{1}{n} = \log(N) + \gamma_E + O(1/N) \qquad \text{(C.174)}$$

where γ_E is the Euler Gamma constant.

3.9.1 Square Antiferromagnetic

For simplicity, we will assume that this lattice is an honest-to-god square so that $D = L$. Thus, we take

$$\begin{aligned}
X^1 &= nD \\
X^2 &= mD \qquad \text{(C.175)}
\end{aligned}$$

and $y_n^\dagger y_m = \pm 1$ for even $n+m$, and $y_n^\dagger y_m = \pm k$, where k is the third imaginary quaternion unit (analogous to the third Pauli matrix, τ_3, used earlier). Much of our analysis carries over from the previous section, except for changes in overall factors. Thus, we have

$$Q((0,0),(n,m)) = \begin{cases} 9/8 & \text{for even } n+m \\ 1/8 & \text{for odd } n+m \end{cases} \qquad \text{(C.176)}$$

As a first step to calculate the interaction energy per instanton, we first sum over n with $m = 0$

$$\begin{aligned} S_0 &= \frac{9}{8}\sum_{n\ even}\frac{1}{n^2} + \frac{1}{8}\sum_{n\ odd}\frac{1}{n^2} \\ &= \frac{\pi^2}{8} \end{aligned} \tag{C.177}$$

Next, we sum over n for even $m \neq 0$.

$$\begin{aligned} S_{m\ even} &= \frac{9}{8}\sum_{n\ even}\frac{1}{n^2+m^2} + \frac{1}{8}\sum_{n\ odd}\frac{1}{n^2+m^2} \\ &= \frac{9}{8}\cdot\frac{\pi}{2|m|}\left(1+\frac{2e^{-\pi|m|}}{1-e^{-\pi|m|}}\right) + \frac{1}{8}\cdot\frac{\pi}{2|m|}\left(1-\frac{2e^{-\pi|m|}}{1+e^{-\pi|m|}}\right) \\ &= \frac{\pi}{|m|}\left(\frac{5}{8}+\frac{e^{-\pi|m|}}{1-e^{-2\pi|m|}}+\frac{5}{4}\cdot\frac{e^{-2\pi|m|}}{1-e^{-2\pi|m|}}\right) \end{aligned} \tag{C.178}$$

Quite similarly, the sum over n for odd m evaluates to

$$\begin{aligned} S_{m\ odd} &= \frac{1}{8}\sum_{n\ even}\frac{1}{n^2+m^2} + \frac{9}{8}\sum_{n\ odd}\frac{1}{n^2+m^2} \\ &= \frac{1}{8}\cdot\frac{\pi}{2|m|}\left(1+\frac{2e^{-\pi|m|}}{1-e^{-\pi|m|}}\right) + \frac{9}{8}\cdot\frac{\pi}{2|m|}\left(1-\frac{2e^{-\pi|m|}}{1+e^{-\pi|m|}}\right) \\ &= \frac{\pi}{|m|}\left(\frac{5}{8}-\frac{e^{-\pi|m|}}{1-e^{-2\pi|m|}}+\frac{5}{4}\cdot\frac{e^{-2\pi|m|}}{1-e^{-2\pi|m|}}\right) \end{aligned} \tag{C.179}$$

Next, if we take $\pm W$ as the cutoff in length in the X^2 direction, then the sum over m must be cutoff at the integer $\pm W/D$. Summing over all the contributions then, we obtain

$$\begin{aligned} \sum_{m=-W/D}^{+W/D} S_m &= \frac{\pi^2}{8} + 2\sum_{m=1}^{W/D}\frac{\pi}{m}\left(\frac{5}{8}+\frac{(-1)^m e^{-\pi|m|}}{1-e^{-2\pi|m|}}+\frac{5}{4}\cdot\frac{e^{-2\pi|m|}}{1-e^{-2\pi|m|}}\right) \\ &\approx \frac{\pi^2}{8} + \frac{5\pi}{4}\left(\log\frac{W}{D}+\gamma_E\right) + \frac{5\pi}{4}\sum_{m=1}^{\infty}\frac{1}{m}\cdot\frac{\frac{8}{5}(-\mu)^m+2\mu^{2m}}{1-\mu^{2m}} \end{aligned} \tag{C.180}$$

where $\mu = e^{-\pi} \approx 0.0432$. Seen as a function of m, the summand approaches the m-axis from below fairly rapidly, so we obtain a reliable numerical value for the sum after just a few terms

$$\sum_{m=1}^{\infty} \frac{1}{m} \cdot \frac{\frac{8}{5}(-\mu)^m + 2\mu^{2m}}{1-\mu^{2m}} \quad \approx \quad -0.0670647 \tag{C.181}$$

Thus we obtain

$$\sum_m S_m \quad = \quad \frac{5\pi}{4}\left(\log\frac{W}{D} + \gamma_E + \frac{\pi}{10} - 0.0670647\right) \tag{C.182}$$

and consequently the net interaction energy per instanton is

$$\xi[\Box AF] \quad = \quad \frac{\pi N_c}{\lambda M D^2}\left(\log\frac{W}{D} + \gamma_E + A\right) \tag{C.183}$$

where $A \approx 0.247$.

3.9.2 Square Non-Abelian

As in the previous section, we assume an aspect ratio of 1 so that in the physical 2D space, we have

$$\begin{aligned} X^1 &= nD \\ X^2 &= mD \end{aligned} \tag{C.184}$$

However, in this case, we have a non-abelian order for the orientations

$$y_n^\dagger y_m \quad = \quad \begin{cases} \pm 1 & \text{for even } n\text{, even } m, \\ \pm j & \text{for odd } n\text{, even } m, \\ \pm i & \text{for even } n\text{, odd } m, \\ \pm k & \text{for odd } n\text{, odd } m, \end{cases} \tag{C.185}$$

We may graphically represent the lattice as

$$\begin{array}{cccccccc}
y_1 & y_2 & y_1 & y_2 & y_1 & y_2 & y_1 & y_2 \\
y_3 & y_4 & y_3 & y_4 & y_3 & y_4 & y_3 & y_4 \\
y_1 & y_2 & y_1 & y_2 & y_1 & y_2 & y_1 & y_2 \\
y_3 & y_4 & y_3 & y_4 & y_3 & y_4 & y_3 & y_4 \\
y_1 & y_2 & y_1 & y_2 & y_1 & y_2 & y_1 & y_2 \\
y_3 & y_4 & y_3 & y_4 & y_3 & y_4 & y_3 & y_4
\end{array}$$

where the orientations are given by $y_1 = \pm 1$, $y_2 = \pm j$, $y_3 = \pm i$, $y_4 = \pm k$ (the only difference from the earlier section on thin crystals being the extent in 2D space, and the replacement of Pauli matrices with quaternions). The various possibilities for $Q(n, m)$ are now

$$\begin{aligned}
Q(even, even) &= \frac{9}{8} \\
Q(odd, even) &= \frac{5}{8} + \frac{\zeta}{2} \cdot \frac{m^2 - n^2}{m^2 + n^2} \\
Q(even, odd) &= \frac{5}{8} - \frac{\zeta}{2} \cdot \frac{m^2 - n^2}{m^2 + n^2} \\
Q(odd, odd) &= \frac{1}{8}
\end{aligned} \tag{C.186}$$

Now we sum over n for fixed m. The sum over n for $m = 0$ is

$$\begin{aligned}
S_0 &= \frac{9}{8} \sum_{n\ even} \frac{1}{n^2 + m^2} + \left(\frac{5}{8} - \frac{\zeta}{2} \right) \sum_{n\ odd} \frac{1}{n^2 + m^2} \\
&= \frac{\pi^2}{8} (2 - \zeta)
\end{aligned} \tag{C.187}$$

For even $m \neq 0$, we have

$$\begin{aligned}
S_{m\ even} &= \frac{9}{8} \sum_{n\ even} \frac{1}{n^2 + m^2} + \frac{5}{8} \sum_{n\ odd} \frac{1}{n^2 + m^2} + \frac{\zeta}{2} \sum_{n\ odd} \frac{m^2 - n^2}{[n^2 + m^2]^2} \\
&= \frac{9}{8} \cdot \frac{\pi}{2|m|} \left(1 + \frac{2e^{-\pi|m|}}{1 - e^{-\pi|m|}} \right) + \frac{5}{8} \cdot \frac{\pi}{2|m|} \left(1 - \frac{2e^{-\pi|m|}}{1 + e^{-\pi|m|}} \right) \\
&\quad + \frac{\zeta}{2} \cdot \frac{\pi^2}{2} \cdot \frac{-2e^{-\pi|m|}}{[1 + e^{-\pi|m|}]^2}
\end{aligned} \tag{C.188}$$

and likewise for odd m we have

$$\begin{aligned}
S_{m\ odd} &= \frac{1}{8}\sum_{n\ odd}\frac{1}{n^2+m^2}+\frac{5}{8}\sum_{n\ even}\frac{1}{n^2+m^2}-\frac{\zeta}{2}\sum_{n\ even}\frac{m^2-n^2}{[n^2+m^2]^2}\\
&= \frac{1}{8}\cdot\frac{\pi}{2|m|}\left(1-\frac{2e^{-\pi|m|}}{1+e^{-\pi|m|}}\right)+\frac{5}{8}\cdot\frac{\pi}{2|m|}\left(1+\frac{2e^{-\pi|m|}}{1-e^{-\pi|m|}}\right)\\
&\quad -\frac{\zeta}{2}\cdot\frac{\pi^2}{2}\cdot\frac{2e^{-\pi|m|}}{[1+e^{-\pi|m|}]^2}
\end{aligned} \tag{C.189}$$

Both the above expressions are expressible as

$$S_m = \frac{\pi}{2|m|}\left(\frac{5}{4}+\frac{(-1)^m}{2}+\frac{\mu^{|m|}}{1-(-\mu)^{|m|}}+\frac{5\mu^{2|m|}}{2(1-\mu^{2|m|})}\right)-\frac{\zeta\pi^2}{2}\cdot\frac{\mu^{|m|}}{[1+(-\mu)^{|m|}]^2} \tag{C.190}$$

where as in the previous section we have $\mu = e^{-\pi} \approx 0.0432$. Finally, summing over m we obtain

$$\begin{aligned}
\sum_{m=-W/D}^{+W/D} S_m &= \frac{\pi^2}{8}(2-\zeta)+\frac{5\pi}{4}\sum_{m=1}^{W/D}\frac{1}{m}\left(1+\frac{2}{5}(-1)^m+\frac{2\mu^{2m}}{1-\mu^{2m}}+\frac{4\mu^m}{5[1-(-\mu)^m]}\right)\\
&\quad -\frac{\zeta\pi^2}{2}\sum_{m=1}^{W/D}\frac{\mu^{|m|}}{[1+(-\mu)^{|m|}]^2}\\
&\approx \frac{\pi^2}{8}(2-\zeta)+\frac{5\pi}{4}\left(\log\frac{W}{D}+\gamma_E-\frac{2}{5}\log 2\right)\\
&\quad +\frac{5\pi}{4}\sum_{m=1}^{\infty}\frac{1}{m}\left(\frac{2\mu^{2m}}{1-\mu^{2m}}+\frac{4\mu^m}{5[1-(-\mu)^m]}\right)-\zeta\pi^2\sum_{m=1}^{\infty}\frac{\mu^{|m|}}{[1+(-\mu)^{|m|}]^2}
\end{aligned} \tag{C.191}$$

We may evaluate the last two sums above numerically to obtain the approximate values

$$\sum_{m=1}^{\infty}\frac{1}{m}\left(\frac{2\mu^{2m}}{1-\mu^{2m}}+\frac{4\mu^m}{5[1-(-\mu)^m]}\right) \approx 0.0377 \tag{C.192}$$

$$\sum_{m=1}^{\infty}\frac{\mu^{|m|}}{[1+(-\mu)^{|m|}]^2} \approx 0.0469 \tag{C.193}$$

so that

$$\sum_m S_m = \frac{5\pi}{4}\left(\log\frac{W}{D} + \gamma_E + R_1 - R_2\zeta\right) \tag{C.194}$$

where R_1 and R_2 are numerical constants

$$\begin{aligned} R_1 &\approx 0.389 \\ R_2 &\approx 0.438 \end{aligned} \tag{C.195}$$

Consequently, the net interaction energy per instanton for this lattice is

$$\xi[\Box NA] = \frac{\pi N_c}{\lambda M D^2}\left(\log\frac{W}{D} + \gamma_E + R_1 - R_2\zeta\right) \tag{C.196}$$

3.9.3 Comparison of Square Lattices

We can now compare the energies of the two kinds of square lattices we find. The net interaction energy per instanton for either lattice has the same IR divergence but different finite parts, so that the difference

$$\Delta\xi \equiv \xi[\Box NA] - \xi[\Box AF] = \frac{\pi N_c}{\lambda M D^2}(R_1 - A - R_2\zeta) \tag{C.197}$$

Note that $R_1 - A = 0.142$ is less than R_2, so the sign of $\Delta\xi$ depends on ζ. The non-abelian lattice has higher energy than the anti-ferromagnetic one for $\zeta < \zeta_c$ where

$$\zeta_c = \frac{R_1 - A}{R_2} \approx 0.324 \tag{C.198}$$

and lower energy for $\zeta > \zeta_c$. This critical value ζ_c corresponds to $(M_3/M_4)_c \approx 0.72$. Thus, the square lattice prefers the non-abelian order for $(M_3/M_4) < 0.72$ and the anti-ferromagnetic order for $(M_3/M_4) > 0.72$.

3.9.4 Triangular Non-Abelian Lattice

Here, we consider the triangular lattice of non-abelian order. Graphically, we may represent it as

$$\begin{array}{ccccccccccccc}
 & y_3 & & y_4 & & y_3 & & y_4 & & y_3 & & y_4 & \\
y_1 & & y_2 & & y_1 & & y_2 & & y_1 & & y_2 & & y_1 \\
 & y_4 & & y_3 & & y_4 & & y_3 & & y_4 & & y_2 & \\
y_2 & & y_1 & & y_2 & & y_1 & & y_2 & & y_1 & & y_2 \\
 & y_3 & & y_4 & & y_3 & & y_4 & & y_3 & & y_4 & \\
y_1 & & y_2 & & y_1 & & y_2 & & y_1 & & y_2 & & y_1 \\
 & y_4 & & y_3 & & y_4 & & y_3 & & y_4 & & y_2 & \\
y_2 & & y_1 & & y_2 & & y_1 & & y_2 & & y_1 & & y_2
\end{array}$$

where we take $y_1 = \pm 1$, $y_2 = \pm\alpha$, $y_3 = \pm\beta$, $y_4 = \pm\gamma$. Here, α, β and γ are imaginary unimodular quaternions that satisfy $\alpha\beta = \pm\gamma$, $\beta\gamma = \pm\alpha$, and $\gamma\alpha = \pm\beta$. As 3-vectors, they are all perpendicular to each other. To minimize the energy, α should be perpendicular to the X^1 axis, which we identify as the triangle's base, while β and γ should be perpendicular to the other two sides of the triangle. The following ansatz satisfies all these requirements

$$\begin{aligned}
\alpha &= 0 \cdot i + \sqrt{\frac{2}{3}} \cdot j + \sqrt{\frac{1}{3}} \cdot k \\
\beta &= \sqrt{\frac{1}{2}} \cdot i - \sqrt{\frac{1}{6}} \cdot j + \sqrt{\frac{1}{3}} \cdot k \\
\gamma &= -\sqrt{\frac{1}{2}} \cdot i - \sqrt{\frac{1}{6}} \cdot j + \sqrt{\frac{1}{3}} \cdot k
\end{aligned} \tag{C.199}$$

We take D as the distance between neighboring instantons within any one horizontal layer, but also as the diagonal distance between neighboring instantons within the triangle. In the 2D space then, the instantons' coordinates are given by

$$X^1 = nD + m\frac{D}{2}\ , \quad X^2 = m\frac{\sqrt{3}D}{2} \tag{C.200}$$

and their relative orientations are given by

$$y_n^\dagger y_m \quad = \quad \begin{cases} \pm 1 & \text{for even } n, \text{ even } m, \\ \pm\alpha & \text{for odd } n, \text{ even } m, \\ \pm\beta & \text{for even } n, \text{ odd } m, \\ \pm\gamma & \text{for odd } n, \text{ odd } m, \end{cases} \tag{C.201}$$

Consequently, the various possibilities for $Q(n,m)$ are

$$\begin{aligned} Q(even, even) &= \frac{9}{8} \\ Q(odd, even) &= \frac{11}{24} + \frac{\zeta}{3} \cdot \frac{\frac{3}{4}m^2 - (n+\frac{1}{2}m)^2}{\frac{3}{4}m^2 + (n+\frac{1}{2}m)^2} \\ Q(even, odd) &= \frac{11}{24} - \frac{\zeta}{6} \cdot \frac{\frac{3}{4}m^2 - (n+\frac{1}{2}m)^2}{\frac{3}{4}m^2 + (n+\frac{1}{2}m)^2} \\ & \quad -\frac{\zeta}{12} \cdot \frac{2(n+\frac{1}{2}m)\sqrt{\frac{3}{4}}m}{\frac{3}{4}m^2 + (n+\frac{1}{2}m)^2} \\ Q(odd, odd) &= \frac{11}{24} - \frac{\zeta}{6} \cdot \frac{\frac{3}{4}m^2 - (n+\frac{1}{2}m)^2}{\frac{3}{4}m^2 + (n+\frac{1}{2}m)^2} \\ & \quad +\frac{\zeta}{12} \cdot \frac{2(n+\frac{1}{2}m)\sqrt{\frac{3}{4}}m}{\frac{3}{4}m^2 + (n+\frac{1}{2}m)^2} \end{aligned} \tag{C.202}$$

using which we can calculate

$$\xi[\triangle] \quad = \quad \frac{4N_c}{5\lambda M D^2} \sum_{n,m} \frac{Q(n,m)}{\frac{3}{4}m^2 + (n+\frac{1}{2}m)^2} \tag{C.203}$$

We can perform these sums using (C.170) using

$$\eta \quad = \quad i^m (-1)^{n+1} \mu^{|m|} \tag{C.204}$$

where now $\mu = e^{-\sqrt{3}\pi/2} \approx 0.065$. In performing the sums, we need to be careful to distinguish whether $x = n + \frac{1}{2}m$ is integer or half-integer depending on m. For $m \neq 0$ divisible by 4, we obtain

$$\begin{aligned}
\sum_{n\ even} \frac{Q(n,m)}{\frac{3}{4}m^2 + (n+\frac{1}{2}m)^2} &= \frac{9}{8} \cdot \frac{\pi}{\sqrt{3}|m|}\left(1 + \frac{2\mu^{|m|}}{1-\mu^{|m|}}\right) \\
\sum_{n\ odd} \frac{Q(n,m)}{\frac{3}{4}m^2 + (n+\frac{1}{2}m)^2} &= \frac{11}{24} \cdot \frac{\pi}{\sqrt{3}|m|}\left(1 - \frac{2\mu^{|m|}}{1+\mu^{|m|}}\right) + \frac{\zeta}{3} \cdot \frac{\pi^2}{2} \frac{-2\mu^{|m|}}{[1+\mu^{|m|}]^2}
\end{aligned} \tag{C.205}$$

For even $m = 4l + 2$ for some integer l, we have

$$\begin{aligned}
\sum_{n\ even} \frac{Q(n,m)}{\frac{3}{4}m^2 + (n+\frac{1}{2}m)^2} &= \frac{9}{8} \cdot \frac{\pi}{\sqrt{3}|m|}\left(1 - \frac{2\mu^{|m|}}{1+\mu^{|m|}}\right) \\
\sum_{n\ odd} \frac{Q(n,m)}{\frac{3}{4}m^2 + (n+\frac{1}{2}m)^2} &= \frac{11}{24} \cdot \frac{\pi}{\sqrt{3}|m|}\left(1 + \frac{2\mu^{|m|}}{1-\mu^{|m|}}\right) + \frac{\zeta}{3} \cdot \frac{\pi^2}{2} \frac{2\mu^{|m|}}{[1-\mu^{|m|}]^2}
\end{aligned} \tag{C.206}$$

For odd $m = 4l + 1$ for some integer l, we have

$$\begin{aligned}
\sum_{n\ even} \frac{Q(n,m)}{\frac{3}{4}m^2 + (n+\frac{1}{2}m)^2} &= \frac{11}{24} \cdot \frac{\pi}{\sqrt{3}|m|}\left(1 - \frac{2\mu^{2|m|}}{1+\mu^{2|m|}}\right) - \frac{\zeta}{6} \cdot \frac{\pi^2}{2} \frac{-4\mu^{2|m|}}{[1+\mu^{2|m|}]^2} \\
&\quad - \frac{\zeta}{\sqrt{12}} \frac{\pi^2}{2} \frac{2\mu^{|m|}(1-\mu^{2|m|})}{[1+\mu^{2|m|}]^2} \cdot \mathrm{sign}(m) \\
\sum_{n\ odd} \frac{Q(n,m)}{\frac{3}{4}m^2 + (n+\frac{1}{2}m)^2} &= \frac{11}{24} \cdot \frac{\pi}{\sqrt{3}|m|}\left(1 - \frac{2\mu^{2|m|}}{1+\mu^{2|m|}}\right) - \frac{\zeta}{6} \cdot \frac{\pi^2}{2} \frac{-4\mu^{2|m|}}{[1+\mu^{2|m|}]^2} \\
&\quad + \frac{\zeta}{\sqrt{12}} \frac{\pi^2}{2} \frac{2\mu^{|m|}(1-\mu^{2|m|})}{[1+\mu^{2|m|}]^2} \cdot \mathrm{sign}(m)
\end{aligned} \tag{C.207}$$

For odd $m = 4l + 3$ for some integer l, we have

$$\begin{aligned}
\sum_{n\ even} \frac{Q(n,m)}{\frac{3}{4}m^2 + (n+\frac{1}{2}m)^2} &= \frac{11}{24} \cdot \frac{\pi}{\sqrt{3}|m|}\left(1 - \frac{2\mu^{2|m|}}{1+\mu^{2|m|}}\right) - \frac{\zeta}{6} \cdot \frac{\pi^2}{2} \frac{-4\mu^{2|m|}}{[1+\mu^{2|m|}]^2} \\
&\quad + \frac{\zeta}{\sqrt{3}} \frac{\pi^2}{2} \frac{-2\mu^{|m|}(1-\mu^{2|m|})}{[1+\mu^{2|m|}]^2} \cdot \mathrm{sign}(m) \\
\sum_{n\ odd} \frac{Q(n,m)}{\frac{3}{4}m^2 + (n+\frac{1}{2}m)^2} &= \frac{11}{24} \cdot \frac{\pi}{\sqrt{12}|m|}\left(1 - \frac{2\mu^{2|m|}}{1+\mu^{2|m|}}\right) - \frac{\zeta}{6} \cdot \frac{\pi^2}{2} \frac{-4\mu^{2|m|}}{[1+\mu^{2|m|}]^2} \\
&\quad - \frac{\zeta}{\sqrt{12}} \frac{\pi^2}{2} \frac{2\mu^{|m|}(1-\mu^{2|m|})}{[1+\mu^{2|m|}]^2} \cdot \mathrm{sign}(m)
\end{aligned} \tag{C.208}$$

After summing over both even and odd n for odd m we obtain

$$\begin{aligned}
S_{m\ odd} &= \sum_n \frac{Q(n,m)}{\frac{3}{4}m^2 + (n+\frac{1}{2}m)^2} \\
&= \frac{11\pi}{12\sqrt{3}} \frac{1}{|m|}\left(1 - \frac{2\mu^{2|m|}}{1+\mu^{2|m|}}\right) + \frac{2\pi^2\zeta}{3} \frac{\mu^{2|m|}}{[1+\mu^{2|m|}]^2} \\
&\quad - \frac{\pi^2\zeta}{\sqrt{3}} \frac{\mu^{|m|}(1-\mu^{2|m|})}{[1+\mu^{2|m|}]^2} (-1)^{(|m|-1)/2}
\end{aligned} \tag{C.209}$$

Similarly, summing over both even and odd n for even m we obtain

$$\begin{aligned}
S_{m\ even} &= \sum_n \frac{Q(n,m)}{\frac{3}{4}m^2 + (n+\frac{1}{2}m)^2} \\
&= \frac{\pi}{6\sqrt{3}} \frac{1}{|m|}\left(\frac{19}{2} + 19\frac{\mu^{2|m|}}{1-\mu^{2|m|}} + 8(-1)^{|m|/2}\frac{\mu^{|m|}}{1-\mu^{2|m|}}\right) \\
&\quad + \frac{\pi^2\zeta}{3} \frac{\mu^{|m|}}{[1-\mu^{|m|}]^2}
\end{aligned} \tag{C.210}$$

Meanwhile, the $m = 0$ line evaluates to

$$\begin{aligned} S_{m=0} &= \sum_{n\neq 0} \frac{Q(n,0)}{n^2} \\ &= \sum_{n\neq 0\ even} \frac{9}{8n^2} + \sum_{n\ odd} \frac{11-8\zeta}{24n^2} \\ &= \frac{\pi^2}{24}(5-2\zeta) \end{aligned} \tag{C.211}$$

We may now add up all the S_m, and as before the sum $\sum_m S_m$ carry IR divergences which come from the leading terms that are independent of μ

$$\begin{aligned} S^{lead}_{m\ even} &= \frac{\pi}{12\sqrt{3}} \cdot \frac{19}{|m|} \\ S^{lead}_{m\ odd} &= \frac{\pi}{12\sqrt{3}} \cdot \frac{11}{|m|} \end{aligned} \tag{C.212}$$

We identify $M = W/(\sqrt{\frac{3}{4}}D)$ as the cutoff for summing over m so that

$$\begin{aligned} sum^{+M}_{m=-M} S^{lead}_m &= S_{m=0} + 2\sum_{m=1}^{M} \frac{12}{\pi\sqrt{3}} \cdot \frac{15+4(-1)^m}{m} \\ &= \frac{\pi^2}{24}(5-2\zeta) + \frac{5\pi}{2\sqrt{3}}\left(\log M + \gamma_E - \frac{4}{15}\log 2\right) \end{aligned} \tag{C.213}$$

Consequently

$$\xi[\triangle] \;=\; \frac{4N_c}{5\lambda M D^2}\sum_m S_m = \frac{2\pi N_c}{\sqrt{3}\lambda M D^2} \cdot \log\frac{W}{D} + K \tag{C.214}$$

where K is a finite constant. Note that the coefficient of the IR divergence here is different from that of the square lattices, however this is an artifact of the different lattice spacings. The square lattices have density

$$\rho(\square) \;=\; \frac{1}{D^2} \tag{C.215}$$

while the triangle lattice has density

$$\rho(\triangle) \;=\; \frac{2}{\sqrt{3}D^2} \tag{C.216}$$

For the same density ρ, the triangular lattice has the same IR divergence as the square lattices

$$\xi[\triangle] \;=\; \frac{\pi N_c \rho}{\lambda M}\cdot \log(W\sqrt{\rho}) + \text{finite} \tag{C.217}$$

Including the finite terms we obtain

$$\xi[\triangle] \;=\; \frac{\pi N_c \rho}{\lambda M}\cdot (\log(W\sqrt{\rho}) + \gamma_E + T_1 - T_2\zeta) \tag{C.218}$$

where the constants are

$$\begin{aligned}
T_1 \;&=\; \frac{1}{4}\log\frac{4}{3} - \frac{4}{15}\log 2 + \frac{\pi}{4\sqrt{3}} - \frac{22}{15}\sum_{m>0\;odd}\frac{1}{m}\cdot\frac{\mu^{2m}}{1+\mu^{2m}} \\
&\quad + \frac{2}{15}\sum_{m>0\;even}\frac{1}{m}\cdot\frac{19\mu^{2m} + 8\mu^m(-1)^{m/2}}{1-\mu^{2m}} \\
&\approx\; 0.3319 \\
T_2 \;&=\; \frac{\pi}{10\sqrt{3}} + \frac{4\pi}{5\sqrt{3}}\sum_{m>0\;even}\frac{-\mu^m}{[1-\mu^m]^2} \\
&\quad + \frac{4\pi}{5\sqrt{3}}\sum_{m>0\;odd}\frac{-2\mu^{2m} + \sqrt{3}\mu^m(1-\mu^{2m})(-1)^{(m-1)/2}}{[1+\mu^{2m}]^2} \\
&\approx\; 0.3252
\end{aligned} \tag{C.219}$$

3.9.5 Comparison of Square Anti-ferromagnetic, Square Non-Abelian and Triangular Non-Abelian Lattices

We have noted that the IR divergences of all three lattices is the same for the same density, ρ. Subtracting this divergence, we obtain the finite parts of the net interaction energy per instanton for all three lattices

$$\begin{aligned} \hat{\xi} &\equiv \xi - \frac{\pi N_c \rho}{\lambda M}\left(\log(W\sqrt{\rho}) + \gamma_E\right) \\ &= \frac{\pi N_c \rho}{\lambda M} \cdot \begin{cases} A & \text{for the Square AF lattice} \\ R_1 - R_2\zeta & \text{for the Square NA lattice} \\ T_1 - T_2\zeta & \text{for the Triangular NA lattice} \end{cases} \end{aligned} \tag{C.220}$$

We may plot this finite part of the interaction energy per instanton as a function of the ζ parameter, as depicted below. Therefore, the lowest energy state is

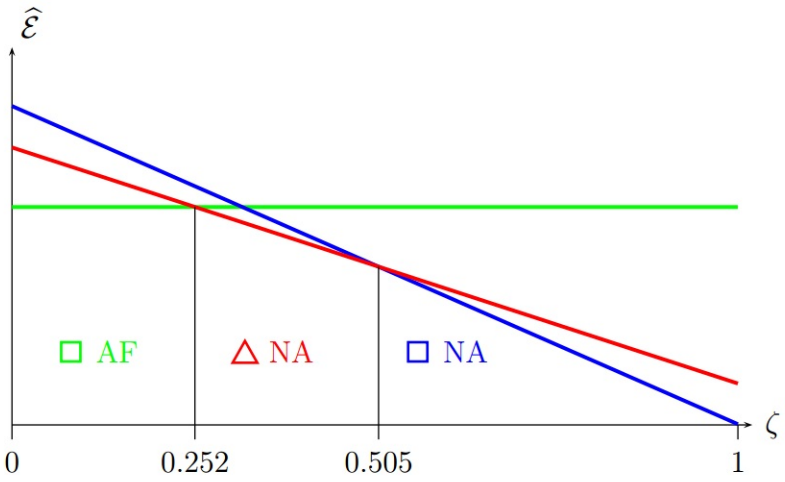

Figure 3.17: Dependence of the finite part of the net interaction energy per instanton of the □ AF and NA lattices, and the △ NA lattice.

(a) Square Anti-ferromagnetic lattice for

$$0 \le \zeta \le \zeta_{c1} = 0.252 \iff 0.77 \le M_3/M_4 \le 1 \tag{C.221}$$

(b) Triangular Non-Abelian lattice for

$$0.252 \leq \zeta \leq \zeta_{c2} = 0.505 \quad \Longleftrightarrow \quad 0.57 \leq M_3/M_4 \leq 0.77 \tag{C.222}$$

(c) Square Non-Abelian lattice for

$$0.505 \leq \zeta \leq 1 \quad \Longleftrightarrow \quad 0 \leq M_3/M_4 \leq 0.57 \tag{C.223}$$

Bibliography

[1] J. M. Maldacena, “The Large N limit of superconformal field theories and supergravity,” Adv. Theor. Math. Phys. **2**, 231-252 (1998). [hep-th/9711200].

[2] S. S. Gubser, I. R. Klebanov, A. M. Polyakov, “Gauge theory correlators from noncritical string theory,” Phys. Lett. **B428**, 105-114 (1998). [hep-th/9802109].

[3] E. Witten, “Anti-de Sitter space and holography,” Adv. Theor. Math. Phys. **2**, 253-291 (1998). [hep-th/9802150].

[4] O. Aharony, S. S. Gubser, J. M. Maldacena, H. Ooguri, Y. Oz, “Large N field theories, string theory and gravity,” Phys. Rept. **323**, 183-386 (2000). [hep-th/9905111].

[5] S. S. Gubser, A. Karch, “From gauge-string duality to strong interactions: A Pedestrian’s Guide,” Ann. Rev. Nucl. Part. Sci. **59**, 145-168 (2009). [arXiv:0901.0935 [hep-th]].

[6] A. Karch, E. Katz, “Adding flavor to AdS / CFT,” JHEP **0206**, 043 (2002). [hep-th/0205236].

[7] J. Babington, J. Erdmenger, N. J. Evans, Z. Guralnik and I. Kirsch, “Chiral symmetry breaking and pions in nonsupersymmetric gauge / gravity duals,” Phys. Rev. D **69**, 066007 (2004) [hep-th/0306018].

[8] J. Erdmenger, N. Evans, I. Kirsch and E. Threlfall, “Mesons in Gauge/Gravity Duals - A Review,” Eur. Phys. J. A **35**, 81 (2008) [arXiv:0711.4467 [hep-th]].

[9] T. Sakai, S. Sugimoto, "Low energy hadron physics in holographic QCD," Prog. Theor. Phys. **113**, 843-882 (2005). [hep-th/0412141].

[10] T. Sakai, S. Sugimoto, "More on a holographic dual of QCD," Prog. Theor. Phys. **114**, 1083-1118 (2005). [hep-th/0507073].

[11] S. Kuperstein and J. Sonnenschein, "A New Holographic Model of Chiral Symmetry Breaking," JHEP **0809**, 012 (2008) [arXiv:0807.2897 [hep-th]].

[12] I. R. Klebanov, E. Witten, "Superconformal field theory on three-branes at a Calabi-Yau singularity," Nucl. Phys. **B536**, 199-218 (1998). [hep-th/9807080].

[13] V. G. Filev, C. V. Johnson, R. C. Rashkov, K. S. Viswanathan, "Flavoured large N gauge theory in an external magnetic field," JHEP **0710**, 019 (2007). [hep-th/0701001].

[14] T. Albash, V. G. Filev, C. V. Johnson, A. Kundu, "Finite temperature large N gauge theory with quarks in an external magnetic field," JHEP **0807**, 080 (2008). [arXiv:0709.1547 [hep-th]].

[15] T. Albash, V. G. Filev, C. V. Johnson, A. Kundu, "Quarks in an external electric field in finite temperature large N gauge theory," JHEP **0808**, 092 (2008). [arXiv:0709.1554 [hep-th]].

[16] J. Erdmenger, R. Meyer, J. P. Shock, "AdS/CFT with flavour in electric and magnetic Kalb-Ramond fields," JHEP **0712**, 091 (2007). [arXiv:0709.1551 [hep-th]].

[17] N. Evans, T. Kalaydzhyan, K. -y. Kim and I. Kirsch, "Non-equilibrium physics at a holographic chiral phase transition," JHEP **1101**, 050 (2011) [arXiv:1011.2519 [hep-th]].

[18] O. Bergman, G. Lifschytz, M. Lippert, “Response of Holographic QCD to Electric and Magnetic Fields,” JHEP **0805**, 007 (2008). [arXiv:0802.3720 [hep-th]].

[19] C. V. Johnson, A. Kundu, “External Fields and Chiral Symmetry Breaking in the Sakai-Sugimoto Model,” JHEP **0812**, 053 (2008). [arXiv:0803.0038 [hep-th]].

[20] A. Kundu, “External Fields and the Dynamics of Fundamental Flavours in Holographic Duals of Large N Gauge Theories,” [arXiv:1012.5450 [hep-th]].

[21] N. Evans, A. Gebauer, K. -Y. Kim, “E, B, μ, T Phase Structure of the D3/D7 Holographic Dual,” JHEP **1105**, 067 (2011). [arXiv:1103.5627 [hep-th]].

[22] N. Evans, K. -Y. Kim, J. P. Shock, “Chiral phase transitions and quantum critical points of the D3/D7(D5) system with mutually perpendicular E and B fields at finite temperature and density,” JHEP **1109**, 021 (2011). [arXiv:1107.5053 [hep-th]].

[23] V. P. Gusynin, V. A. Miransky, I. A. Shovkovy, “Dimensional reduction and catalysis of dynamical symmetry breaking by a magnetic field,” Nucl. Phys. **B462**, 249-290 (1996). [hep-ph/9509320].

[24] G. W. Semenoff, I. A. Shovkovy, L. C. R. Wijewardhana, “Universality and the magnetic catalysis of chiral symmetry breaking,” Phys. Rev. **D60**, 105024 (1999). [hep-th/9905116].

[25] V. A. Miransky, “Dynamics of QCD in a strong magnetic field,” [hep-ph/0208180].

[26] A. Karch, A. O’Bannon, “Metallic AdS/CFT,” JHEP **0709**, 024 (2007). [arXiv:0705.3870 [hep-th]].

[27] T. Albash, V. G. Filev, C. V. Johnson, A. Kundu, “Global Currents, Phase Transitions, and Chiral Symmetry Breaking in Large N(c) Gauge Theory,” JHEP **0812**, 033 (2008). [arXiv:hep-th/0605175 [hep-th]].

[28] S. R. Das, T. Nishioka, T. Takayanagi, “Probe Branes, Time-dependent Couplings and Thermalization in AdS/CFT,” JHEP **1007**, 071 (2010). [arXiv:1005.3348 [hep-th]].

[29] L. J. Romans, “NEW COMPACTIFICATIONS OF CHIRAL N=2 d = 10 SUPERGRAVITY,” Phys. Lett. **B153**, 392 (1985).

[30] A. Karch, S. L. Sondhi, “Non-linear, Finite Frequency Quantum Critical Transport from AdS/CFT,” JHEP **1101**, 149 (2011). [arXiv:1008.4134 [cond-mat.str-el]].

[31] A. Karch, A. O’Bannon and E. Thompson, “The Stress-Energy Tensor of Flavor Fields from AdS/CFT,” JHEP **0904**, 021 (2009) [arXiv:0812.3629 [hep-th]].

[32] N. Seiberg, E. Witten, “String theory and noncommutative geometry,” JHEP **9909**, 032 (1999). [hep-th/9908142].

[33] K. -Y. Kim, J. P. Shock, J. Tarrio, “The open string membrane paradigm with external electromagnetic fields,” JHEP **1106**, 017 (2011). [arXiv:1103.4581 [hep-th]].

[34] A. O’Bannon, “Hall Conductivity of Flavor Fields from AdS/CFT,” Phys. Rev. **D76**, 086007 (2007). [arXiv:0708.1994 [hep-th]].

[35] G. W. Semenoff, K. Zarembo, “Holographic Schwinger Effect,” [arXiv:1109.2920 [hep-th]].

[36] S. Bolognesi, D. Tong, “Magnetic Catalysis in AdS4,” [arXiv:1110.5902 [hep-th]].

[37] C. V. Johnson, A. Kundu, "Meson Spectra and Magnetic Fields in the Sakai-Sugimoto Model," JHEP **0907**, 103 (2009). [arXiv:0904.4320 [hep-th]].

[38] N. Evans, A. Gebauer, K. -Y. Kim, M. Magou, "Holographic Description of the Phase Diagram of a Chiral Symmetry Breaking Gauge Theory," JHEP **1003**, 132 (2010). [arXiv:1002.1885 [hep-th]].

[39] K. Jensen, A. Karch, E. G. Thompson, "A Holographic Quantum Critical Point at Finite Magnetic Field and Finite Density," JHEP **1005**, 015 (2010). [arXiv:1002.2447 [hep-th]].

[40] O. Bergman, G. Lifschytz, M. Lippert, "Magnetic properties of dense holographic QCD," Phys. Rev. **D79**, 105024 (2009). [arXiv:0806.0366 [hep-th]].

[41] E. G. Thompson, D. T. Son, "Magnetized baryonic matter in holographic QCD," Phys. Rev. **D78**, 066007 (2008). [arXiv:0806.0367 [hep-th]].

[42] A. Rebhan, A. Schmitt, S. A. Stricker, "Meson supercurrents and the Meissner effect in the Sakai-Sugimoto model," JHEP **0905**, 084 (2009). [arXiv:0811.3533 [hep-th]].

[43] A. Rebhan, A. Schmitt, S. A. Stricker, "Anomalies and the chiral magnetic effect in the Sakai-Sugimoto model," JHEP **1001**, 026 (2010). [arXiv:0909.4782 [hep-th]].

[44] A. Dymarsky, D. Melnikov, J. Sonnenschein, "Attractive Holographic Baryons," [arXiv:1012.1616 [hep-th]].

[45] S. Kuperstein, "Meson spectroscopy from holomorphic probes on the warped deformed conifold," JHEP **0503**, 014 (2005). [hep-th/0411097].

[46] I. R. Klebanov, M. J. Strassler, “Supergravity and a confining gauge theory: Duality cascades and chi SB resolution of naked singularities,” JHEP **0008**, 052 (2000). [hep-th/0007191].

[47] A. Dymarsky, S. Kuperstein, J. Sonnenschein, “Chiral Symmetry Breaking with non-SUSY D7-branes in ISD backgrounds,” JHEP **0908**, 005 (2009). [arXiv:0904.0988 [hep-th]].

[48] S. S. Gubser, C. P. Herzog, I. R. Klebanov, A. A. Tseytlin, “Restoration of chiral symmetry: A Supergravity perspective,” JHEP **0105**, 028 (2001). [hep-th/0102172].

[49] C. Nunez, A. Paredes, A. V. Ramallo, “Unquenched flavor in the gauge/gravity correspondence,” Adv. High Energy Phys. **2010**, 196714 (2010). [arXiv:1002.1088 [hep-th]].

[50] V. G. Filev and D. Zoakos, “Towards Unquenched Holographic Magnetic Catalysis,” JHEP **1108**, 022 (2011) [arXiv:1106.1330 [hep-th]].

[51] J. Erdmenger, V. G. Filev and D. Zoakos, “Magnetic catalysis with massive dynamical flavours,” arXiv:1112.4807 [hep-th].

[52] B. Sahoo, H. -U. Yee, “Electrified plasma in AdS/CFT correspondence,” JHEP **1011**, 095 (2010). [arXiv:1004.3541 [hep-th]].

[53] J. M. Maldacena, “The Large N limit of superconformal field theories and supergravity,” Adv. Theor. Math. Phys. **2**, 231 (1998) [hep-th/9711200].

[54] E. Witten, “Anti-de Sitter space and holography,” Adv. Theor. Math. Phys. **2**, 253 (1998) [hep-th/9802150].

[55] S. S. Gubser, I. R. Klebanov and A. M. Polyakov, “Gauge theory correlators from noncritical string theory,” Phys. Lett. B **428**, 105 (1998) [hep-th/9802109].

[56] S. Kuperstein and J. Sonnenschein, “A New Holographic Model of Chiral Symmetry Breaking,” JHEP **0809**, 012 (2008) [arXiv:0807.2897 [hep-th]].

[57] A. Dymarsky, S. Kuperstein and J. Sonnenschein, “Chiral Symmetry Breaking with non-SUSY D7-branes in ISD backgrounds,” JHEP **0908**, 005 (2009) [arXiv:0904.0988 [hep-th]].

[58] A. Karch and E. Katz, “Adding flavor to AdS / CFT,” JHEP **0206**, 043 (2002) [hep-th/0205236].

[59] I. R. Klebanov and E. Witten, “Superconformal field theory on three-branes at a Calabi-Yau singularity,” Nucl. Phys. B **536**, 199 (1998) [arXiv:hep-th/9807080].

[60] M. S. Alam, V. S. Kaplunovsky and A. Kundu, “Chiral Symmetry Breaking and External Fields in the Kuperstein-Sonnenschein Model,” JHEP **1204**, 111 (2012) [arXiv:1202.3488 [hep-th]].

[61] F. Bigazzi, R. Casero, A. L. Cotrone, E. Kiritsis and A. Paredes, “Non-critical holography and four-dimensional CFT’s with fundamentals,” JHEP **0510**, 012 (2005) [hep-th/0505140].

[62] R. Casero, C. Nunez and A. Paredes, “Towards the string dual of N=1 SQCD-like theories,” Phys. Rev. D **73**, 086005 (2006) [hep-th/0602027].

[63] A. Paredes, “On unquenched N=2 holographic flavor,” JHEP **0612**, 032 (2006) [hep-th/0610270].

[64] F. Benini, F. Canoura, S. Cremonesi, C. Nunez and A. V. Ramallo, “Unquenched flavors in the Klebanov-Witten model,” JHEP **0702**, 090 (2007) [hep-th/0612118].

[65] F. Benini, F. Canoura, S. Cremonesi, C. Nunez and A. V. Ramallo, “Backreacting flavors in the Klebanov-Strassler background,” JHEP **0709**, 109 (2007) [arXiv:0706.1238 [hep-th]].

[66] E. Caceres, R. Flauger, M. Ihl and T. Wrase, “New supergravity backgrounds dual to N=1 SQCD-like theories with N(f) = 2N(c),” JHEP **0803**, 020 (2008) [arXiv:0711.4878 [hep-th]].

[67] C. Nunez, A. Paredes and A. V. Ramallo, “Unquenched Flavor in the Gauge/Gravity Correspondence,” Adv. High Energy Phys. **2010**, 196714 (2010) [arXiv:1002.1088 [hep-th]].

[68] M. Ihl, A. Kundu and S. Kundu, “Back-reaction of Non-supersymmetric Probes: Phase Transition and Stability,” JHEP **1212**, 070 (2012) [arXiv:1208.2663 [hep-th]].

[69] C. Bonati, P. de Forcrand, M. D’Elia, O. Philipsen and F. Sanfilippo, “Constraints on the two-flavor QCD phase diagram from imaginary chemical potential,” PoS LATTICE **2011**, 189 (2011) [arXiv:1201.2769 [hep-lat]].

[70] J. Casalderrey-Solana and D. Teaney, “Heavy quark diffusion in strongly coupled N=4 Yang-Mills,” Phys. Rev. D **74**, 085012 (2006) [hep-ph/0605199].

[71] S. S. Gubser, D. R. Gulotta, S. S. Pufu and F. D. Rocha, “Gluon energy loss in the gauge-string duality,” JHEP **0810**, 052 (2008) [arXiv:0803.1470 [hep-th]].

[72] R. Baier, Y. L. Dokshitzer, A. H. Mueller, S. Peigne and D. Schiff, “Radiative energy loss and p(T) broadening of high-energy partons in nuclei,” Nucl. Phys. B **484**, 265 (1997) [hep-ph/9608322].

[73] H. Liu, K. Rajagopal and U. A. Wiedemann, “Calculating the jet quenching parameter from AdS/CFT,” Phys. Rev. Lett. **97**, 182301 (2006) [hep-ph/0605178].

[74] C. P. Herzog, A. Karch, P. Kovtun, C. Kozcaz and L. G. Yaffe, "Energy loss of a heavy quark moving through N=4 supersymmetric Yang-Mills plasma," JHEP **0607**, 013 (2006) [hep-th/0605158].

[75] S. S. Gubser, "Drag force in AdS/CFT," Phys. Rev. D **74**, 126005 (2006) [hep-th/0605182].

[76] N. Armesto, J. D. Edelstein and J. Mas, "Jet quenching at finite 't Hooft coupling and chemical potential from AdS/CFT," JHEP **0609**, 039 (2006) [hep-ph/0606245].

[77] F. Bigazzi, A. L. Cotrone, J. Mas, A. Paredes, A. V. Ramallo and J. Tarrio, "D3-D7 Quark-Gluon Plasmas," JHEP **0911**, 117 (2009) [arXiv:0909.2865 [hep-th]].

[78] C. P. Herzog, "Energy Loss of Heavy Quarks from Asymptotically AdS Geometries," JHEP **0609**, 032 (2006) [hep-th/0605191].

[79] S. -J. Rey and J. -T. Yee, "Macroscopic strings as heavy quarks in large N gauge theory and anti-de Sitter supergravity," Eur. Phys. J. C **22**, 379 (2001) [hep-th/9803001].

[80] A. Brandhuber, N. Itzhaki, J. Sonnenschein and S. Yankielowicz, "Wilson loops, confinement, and phase transitions in large N gauge theories from supergravity," JHEP **9806**, 001 (1998) [hep-th/9803263].

[81] J. M. Maldacena, "Wilson loops in large N field theories," Phys. Rev. Lett. **80**, 4859 (1998) [hep-th/9803002].

[82] A. Brandhuber, N. Itzhaki, J. Sonnenschein and S. Yankielowicz, "Wilson loops in the large N limit at finite temperature," Phys. Lett. B **434**, 36 (1998) [hep-th/9803137].

[83] S. -J. Rey, S. Theisen and J. -T. Yee, “Wilson-Polyakov loop at finite temperature in large N gauge theory and anti-de Sitter supergravity,” Nucl. Phys. B **527**, 171 (1998) [hep-th/9803135].

[84] F. Bigazzi, A. L. Cotrone, A. Paredes and A. Ramallo, “Non chiral dynamical flavors and screening on the conifold,” Fortsch. Phys. **57**, 514 (2009) [arXiv:0810.5220 [hep-th]].

[85] S. Ryu and T. Takayanagi, “Holographic derivation of entanglement entropy from AdS/CFT,” Phys. Rev. Lett. **96**, 181602 (2006) [hep-th/0603001].

[86] S. Ryu and T. Takayanagi, “Aspects of Holographic Entanglement Entropy,” JHEP **0608**, 045 (2006) [hep-th/0605073].

[87] W. Fischler and S. Kundu, “Strongly Coupled Gauge Theories: High and Low Temperature Behavior of Non-local Observables,” JHEP **1305**, 098 (2013) [arXiv:1212.2643 [hep-th]].

[88] W. Fischler, A. Kundu and S. Kundu, “Holographic Mutual Information at Finite Temperature,” arXiv:1212.4764 [hep-th].

[89] K. Skenderis, “Lecture notes on holographic renormalization,” Class. Quant. Grav. **19**, 5849 (2002) [hep-th/0209067].

[90] A. Karch and A. O’Bannon, “Metallic AdS/CFT,” JHEP **0709**, 024 (2007) [arXiv:0705.3870 [hep-th]].

[91] T. Albash, V. G. Filev, C. V. Johnson and A. Kundu, “Quarks in an external electric field in finite temperature large N gauge theory,” JHEP **0808**, 092 (2008) [arXiv:0709.1554 [hep-th]].

[92] A. Magana, J. Mas, L. Mazzanti and J. Tarrio, “Probes on D3-D7 Quark-Gluon Plasmas,” JHEP **1207**, 058 (2012) [arXiv:1205.6176 [hep-th]].

[93] A. Parnachev, “Holographic QCD with Isospin Chemical Potential,” JHEP **0802**, 062 (2008) [arXiv:0708.3170 [hep-th]].

[94] A. Dymarsky, D. Melnikov, J. Sonnenschein, “Attractive Holographic Baryons,” JHEP **1106**, 145 (2011) [arXiv:1012.1616 [hep-th]].

[95] S. Kobayashi, D. Mateos, S. Matsuura, R. C. Myers, R. M. Thomson, “Holographic phase transitions at finite baryon density,” JHEP **0702**, 016 (2007) [hep-th/0611099].

[96] V. G. Filev, C. V. Johnson, R. C. Rashkov, K. S. Viswanathan, “Flavoured large N gauge theory in an external magnetic field,” JHEP **0710**, 019 (2007) [hep-th/0701001].

[97] T. Albash, V. G. Filev, C. V. Johnson, A. Kundu, “Finite temperature large N gauge theory with quarks in an external magnetic field,” JHEP **0807**, 080 (2008) [arXiv:0709.1547 [hep-th]].

[98] C. V. Johnson, A. Kundu, “External Fields and Chiral Symmetry Breaking in the Sakai-Sugimoto Model,” JHEP **0812**, 053 (2008) [arXiv:0803.0038 [hep-th]].

[99] V. G. Filev and M. Ihl, “Flavoured Large N Gauge Theory on a Compact Space with an External Magnetic Field,” JHEP **1301**, 130 (2013) [arXiv:1211.1164 [hep-th]].

[100] V. G. Filev, D. Zoakos, “Towards Unquenched Holographic Magnetic Catalysis,” JHEP **1108**, 022 (2011) [arXiv:1106.1330 [hep-th]].

[101] F. Preis, A. Rebhan, A. Schmitt, “Inverse magnetic catalysis in dense holographic matter,” JHEP **1103**, 033 (2011) [arXiv:1012.4785 [hep-th]].

[102] V. Kaplunovsky and J. Sonnenschein, JHEP **1404**, 022 (2014) [arXiv:1304.7540 [hep-th]].

[103] V. Kaplunovsky and J. Sonnenschein, JHEP **1105**, 058 (2011) [arXiv:1003.2621 [hep-th]].

[104] V. Kaplunovsky, D. Melnikov and J. Sonnenschein, JHEP **1211**, 047 (2012) [arXiv:1201.1331 [hep-th]].

[105] D. B. Kaplan and A. V. Manohar, Phys. Rev. C **56**, 76 (1997) [nucl-th/9612021].

[106] T. Sakai and S. Sugimoto, Prog. Theor. Phys. **113**, 843 (2005) [hep-th/0412141].

[107] E. Witten, J. Geom. Phys. **15**, 215 (1995) [hep-th/9410052].

[108] M. R. Douglas, In *Cargese 1997, Strings, branes and dualities* 267-275 [hep-th/9512077].

[109] M. R. Douglas, J. Geom. Phys. **28**, 255 (1998) [hep-th/9604198].

[110] M. R. Douglas and G. W. Moore, hep-th/9603167.

[111] K. -M. Lee and P. Yi, Phys. Rev. D **56**, 3711 (1997) [hep-th/9702107].